

Electrochemical systems for hydrogen fuel cell and battery electric vehicle infrastructure

Présentée le 11 décembre 2020

à la Faculté des sciences de base
Laboratoire d'électrochimie physique et analytique
Programme doctoral en énergie

pour l'obtention du grade de Docteur ès Sciences

par

Yorick LIGEN

Acceptée sur proposition du jury

Prof. J. Luterbacher, président du jury
Prof. H. Girault, H. Vrubel, directeurs de thèse
Dr A. Brisse, rapporteuse
Dr R. Réau, rapporteur
Prof. B. Buchmann, rapporteuse

*« Je tiens pour impossible de connaître le tout si je ne
connais les parties ni de connaître les parties si je ne
connais le tout »*

Blaise Pascal, *Les Pensées*, 1669-1670

*« For more than a century, we have been aware that changes
in the composition of the atmosphere could affect its ability
to trap the sun's energy for our benefit. We now have
incontrovertible evidence that the atmosphere is indeed
changing and that we ourselves contribute to that change. »*

Jule G. Charney et. al,
Carbon Dioxide and Climate: A Scientific Assessment, 1979

*« The first 1% takes forever; 1% to 5% is like waiting for a
sneeze – you know it's inevitable but it takes longer than you
think; then 5% to 50% happens incredibly fast. Clean energy
is entering this period of rapid transformation »*

Michael Liebreich, 14.10.2019

Acknowledgements

Working towards a dissertation is a long journey made of desillusions, patience and puzzling rewards. I'm very grateful to Professor Hubert Girault, Dr. Heron Vrubel and Dr. Véronique Amstutz, who welcomed me, a project engineer, to take a ride on the academic research roller coaster.

Prof. Hubert Girault has leveraged his extensive network and developed a vision on hydrogen following or even moving faster than the pace of my research, offering great opportunities for outreach. On the other side of my thesis direction tandem, Dr. Heron Vrubel largely contributed to the success of our demonstration project. The broad, and even abyssal spectrum of his technical skills enabled us to go beyond the initial scope of the project. Heron is a multiskilled scientist and engineer, and I have learned a lot from him.

I am also very grateful to my jury. Defending the work of 4 years with reknown experts is a fantastic chance. Even if they are, by definition, involved only in the very last step of the PhD, I very appreciated the exchange we had during the defense. Sadly, the health measures in place did not allow us to have a presential meeting, but hopefully our paths will cross again. Thanks to Dr. Annabelle Brisse, scientific advisor hydrogen solutions at EIFER. Thanks to Dr. Régis Réau, R&D scientific Director at Air Liquide. Thanks to Dr. Brigitte Buchmann, head of department Mobility, Energy and Environment at EMPA. And finally tanks to Dr. Jeremy Luterbacher, the jury president.

From the EPFL side I very much appreciated the support of Dr. Véronique Amstutz who welcomed me from the first day. Patricia Byron and Sandrine Jaussi, who always assist you with a large smile and supportive words. Same as Cecile Taverney from the doctoral school of Energy.

The LEPA is a very large team, and special thanks goes to the Martigny team with Dr. Alberto Battistel, Dr. Christopher Denisson and Danick Reynard. I will remember our lunch break discussions and our team work to move massive equipments. I have spent less time in Sion, but still valuable moments with Dr. Sunny Maye, Dr. Elena Zanzola, Dr. Solene Gentil, Dr. Gregoire Gschwend, Dr. Victor Battistel, Dr. Yingdi Zhu, Imen Fourzai, Prof. Andreas Lesch, Dr. Astrid Olaya. I do not forget Dr. Lucie Rivier, a solid support even years after leaving the lab.

Because this thesis involved a lot of engineering, I have to thank the workshops both in Lausanne and Sion and the chemical stores. I also had the chance to discuss about our projects and hydrogen in general with the groups of Prof. François Marechal and Prof. Jan Van Herle.

On the academic side I don't want to miss the opportunity to thank also the Professors I've met for teaching duties, in particular Prof. Kevin Sivula, Dr. Anne-Sophie Chauvin and Dr. Sylvain Bréchet. Teaching is part of the PhD journey, and I have worked with great master students: Johnny Arlettaz and Numa Gueissaz.

This thesis would not have been possible without our strong project partners such as Dr. Jakob Rager from the CREM, Jonathan Caron from Sinergy and Dr. Stefan Oberholzer from the Swiss Federal Office for Energy. Fruitful exchanges of experience also occurred with Urs Cabalzar and Patrick Stadelman from EMPA.

I am very glad to have met GreenGT with its visionary founder Jean-François Weber, and its fantastic managers, engineers and technicians: Dr. Jean-Marc Le Canut, Frédéric Veloso, Matthieu Charrier, Bertrand Steulet and many more... I can also mention the inspirational encounters with Thierry Lassus from ABB, and André Borschberg from H55.

And finally, a clear sign of the democratisation and outreach of our work was given by the International Olympic Committee when they asked us to assist them in the definition and selection of their hydrogen refilling infrastructure. Thank you to Marie Sallois Dambreville, to Lise Van-Long and to Jose Diamanto to have involved me in this project. This triggered further discussions on larger scale with SIG, Tamoil, SEFA, SATOM, the Canton of Valais and finally with Alain Thébault and SeaBubbles with whom I have now the chance to enlarge the perspective for hydrogen powertrains.

This acknowledgment section is already long but would be truncated if I omit the personal support I received from my loved ones, and first of all from Thuy-An. Sorry that I have said so many times “There is nothing new here”, but I guess that’s what science is sometimes. Hopefully, back in the industry, I will be more talkative about my working day routines! To my parents, my grand parents and my sisters: how you managed your respective life paths, how brave you faced difficulties, and how available you are when needed, was, is and will remain a very valuable support and inspiration.

3E12 buddies: endless whatsapp chats, relaxing (or not) holidays, weddings, ski touring trips... always too few events but always the same joy to be together. Also a special thought to my ETH schoolmates, crazy enough or not to also do a PhD. From all of you I received support and cheering: thank you.

Closing this chapter of academic education, I have a kind and loving regard for my nephew, who is just starting school, Noham, you don’t have to stay at school until 31, just be curious to learn, but if you are too curious you may end up doing a PhD!

Martigny, September 2020

Abstract

Thermodynamics and heat engines are the core disciplines which enabled the development of the thermo-industrial society during the 20th century. Liquid hydrocarbon fuels are one of the easiest and most convenient solutions offered by the thermophysical constraints of our world. However, an alternative to these dense energy carriers is required to enable a transition to a low carbon transport sector. Climate change mitigation, local air pollution reduction and energy independency are some of the key advantages that hydrogen fuel cell and battery electric vehicles can bring in this context.

Beyond a shift from fossil fuels, the entire value chain, from primary energy to powertrains must be reconsidered, redesigned and redeployed to include renewable energies, robust powergrids, charging stations and electric powertrains. The prominent role of the infrastructure in terms of energy efficiency is demonstrated in chapter 2, introducing a grid to mobility segmentation for life cycle studies. In addition, the shortcomings of local and off-grid solutions are highlighted in the same chapter. Nevertheless, the grid integration also requires innovative solutions to comply with the physical constraints of current networks. In particular, the role and the sizing of stationary buffer batteries is detailed in chapter 3. The stochastic nature of charging events is used to develop a battery sizing algorithm including grid tie constraints.

This research was intrinsically motivated by the perspective of infrastructure operators. A full scale demonstrator is at the core of the scientific questioning of this thesis. The design, the construction and the operation of a grid to mobility demonstrator is reported in chapter 4. Including a 200 kW / 400 kWh Vanadium redox flow battery, a 50 kW alkaline electrolyser, and a hydrogen refueling station, this demonstrator enabled a better understanding and characterization of process engineering, of control and programming and of electrochemical phenomenons. In particular, the data analysis on the electrolysis side and purification solutions are reported in chapter 5. Finally, the intrinsic characteristics of air driven gas boosters, a robust small scale compression solution, are analyzed in chapter 6 and the challenges for a full scale hydrogen mobility are discussed with an economic and logistics perspective.

Keywords: Hydrogen, Battery, Water electrolysis, Energy Storage, Electric Mobility

Zusammenfassung

Thermodynamik und Wärmekraftmaschinen sind die Kerndisziplinen, die im 20. Jahrhundert die Entwicklung der thermo-industriellen Gesellschaft ermöglicht haben. Die Anwendung von flüssigen Kohlenwasserstoffen bietet angesichts der thermophysikalischen Gesetze unserer Welt einfache Lösungen. Eine Alternative zu diesen dichten Energieträgern ist jedoch erforderlich, um die Energiewende und einen kohlenstoffarmen Verkehr zu ermöglichen. Die Bekämpfung des Klimawandels, die Verringerung der lokalen Luftverschmutzung und die Energieunabhängigkeit sind einige der wichtigsten Vorteile, die Wasserstoff-Brennstoffzellen und batterieelektrische Fahrzeuge in diesem Zusammenhang bringen können.

Neben dem Ausstieg aus fossilen Kraftstoffen, muss die gesamte Wertschöpfungskette, von der Primärenergie bis zum Antriebsstrang neu gestaltet und umgestellt werden, um erneuerbare Energien, robuste Stromnetze, Ladestationen und Elektroantriebe einzusetzen. Die herausragende Rolle der Infrastruktur in Bezug auf die Energieeffizienz wird in Kapitel 2 aufgezeigt. Eine Energiebilanz vom Stromnetz bis zur Mobilität ist eingeführt. Darüber hinaus werden im selben Kapitel die Mängel der lokalen und netzunabhängigen Lösungen aufgezeigt. Ausserdem erfordert die Netzintegration auch innovative Lösungen, um die physikalischen Zwänge der derzeitigen Netze zu überwinden. Insbesondere die Rolle und die Dimensionierung von stationären Pufferbatterien werden in Kapitel 3 beschrieben. Die stochastische Natur von Ladesessionen wird verwendet, um einen Algorithmus zur Batteriegrößenbestimmung zu entwickeln, der die Netzkopplungseinschränkungen berücksichtigt.

Die Perspektive der Infrastrukturbetreiber ist ein wichtiger Aspekt dieser Dissertation. Ein vollwertiger Demonstrator steht im Mittelpunkt der wissenschaftlichen Hinterfragung dieser Arbeit. Über den Design, den Aufbau und den Betrieb eines «von Netz zur Mobilität» - Demonstrator wird in Kapitel 4 berichtet. Mit einer 200 kW / 400 kWh Vanadium-Redox-Flow-Batterie, einem 50 kW alkalischen Elektrolyseur und einer Wasserstofftankstelle ermöglichte dieser Demonstrator ein besseres Verständnis der Verfahrenstechnik, der Steuerung und Programmierung und der elektrochemischen Phänomene, die stattfinden. Insbesondere wird die Datenanalyse der Elektrolyseure und der Reinigungslösungen in Kapitel 5 berichtet. Schließlich werden in Kapitel 6 die Eigenschaften von druckluftbetriebenen Gasboostern, einer robusten Kompressionslösung im kleinen Maßstab, analysiert und die Herausforderungen für eine Wasserstoffmobilität im großen Maßstab unter wirtschaftlichen und logistischen Gesichtspunkten erörtert.

Stichwörter: Wasserstoff, Batterie, Elektrolyse, Energiespeicher, Elektromobilität

Résumé

La thermodynamique et les machines thermiques sont les disciplines clefs qui ont permis le développement de la société thermo-industrielle au cours du 20^{ème} siècle. Les hydrocarbures liquides font partie des solutions les plus simples à mettre en oeuvre compte tenu des lois physiques de notre monde. Cependant, une alternative à ces carburants denses en énergie est nécessaire pour permettre une transition vers un secteur des transports bas carbone. La lutte contre le réchauffement climatique, l'amélioration de la qualité de l'air et l'indépendance énergétique sont quelques-uns des avantages majeurs que les véhicules électriques à batterie et à hydrogène peuvent apporter dans ce contexte.

Au-delà de l'abandon des carburants fossiles, la chaîne de valeur entière, de l'énergie primaire aux groupes motopropulseurs, doit être repensée, reconçue et redéployée pour inclure des énergies renouvelables, des réseaux électriques robustes, des stations de recharge et des chaînes de traction électriques. Le rôle majeur de l'infrastructure en termes d'efficacité énergétique est mis en évidence dans le chapitre 2. Une segmentation du réseau à la mobilité est introduite pour les analyses de cycle de vie. De plus, les faiblesses des solutions locales et découplées du réseau sont mises en évidence dans ce chapitre. Néanmoins, l'intégration au réseau nécessite aussi des solutions innovantes pour faire face aux contraintes physiques des réseaux existants. En particulier, le rôle et le dimensionnement de batteries tampon stationnaires est détaillé dans le chapitre 3. La nature stochastique des sessions de recharge est utilisée pour développer un algorithme de dimensionnement de batteries stationnaires, prenant en compte les contraintes de puissance d'un raccordement au réseau.

Ces travaux de recherche ont été profondément motivés par la perspective des opérateurs d'infrastructure de recharge. Un démonstrateur à échelle 1 : 1 est au cœur de l'approche scientifique de cette thèse. La conception, la construction et l'opération d'un démonstrateur du réseau électrique à la mobilité est relatée dans le chapitre 4. Ce démonstrateur, incluant une batterie Vanadium à flux redox 200 kW / 400 kWh, un électrolyseur alcalin de 50 kW et une station de remplissage d'hydrogène, a permis une meilleure compréhension et caractérisation de l'ingénierie des procédés, des systèmes de contrôle et leur programmation et des phénomènes électrochimiques en jeu. En particulier les données d'exploitation de l'électrolyseur et les solutions de purification des gaz sont approfondies dans le chapitre 5. Enfin, le chapitre 6 couvre l'étude du fonctionnement des boosters à air comprimé, une solution robuste de compression à petite échelle, ainsi que les défis à relever pour une mobilité hydrogène à pleine échelle avec une perspective économique et logistique.

Mots-clés: Hydrogène, Batterie, Electrolyse de l'eau, Stockage d'énergie, Mobilité électrique

Abbreviations

AC	Alternating Current
ATEX	EXplosive ATmosphere (from French)
BEV	Battery Electric Vehicle
BMS	Battery Management System
<i>ca.</i>	<i>circa</i>
CAPEX	Capital Expenditures
CHF	Swiss Franc
CNG	Compressed Natural Gas
CO ₂ eq	CO ₂ equivalent
CSO	Charging Station Operator
DC	Direct Current
DCFC	Direct Current Fast Charger
DoE	Department of Energy (US)
EMPA	Swiss Federal Laboratories for Materials Science and Technology
EPA	Environmental Protection Agency (US)
EPFL	Ecole Polytechnique Fédérale de Lausanne
<i>et al.</i>	<i>et alii</i>
<i>e.g.</i>	<i>exempli gratia</i>
ESS	Energy Storage System
EV	Electric Vehicle
FC	Fuel Cell
FCEV	Fuel Cell Electric Vehicle
FCH-JU	Fuel Cell and Hydrogen Joint Undertaking (EU)
GC	Gas Chromatography
HEV	Hybrid Electric Vehicle
HHV	Higher Heating Value
HMI	Human Machine Interface
HRS	Hydrogen Refueling Station
ICEV	Internal Combustion Engine Vehicle
IPCC	Intergovernmental Panel on Climate Change
IR	Infra-Red
IRES	Intermittent Renewable Energy Sources
ISO	International Organization for Standardization
<i>i.e.</i>	<i>id est</i>

LCA	Life Cycle Assessment
LCOH	Levelized Cost of Hydrogen
LEL	Lower Explosive Limit
LEPA	Laboratory of Physical and Analytical Electrochemistry
LH ₂	Liquid Hydrogen
LHV	Lower Heating Value
LOHC	Liquid Organic Hydrogen Carrier
LPG	Liquefied Petroleum Gas
MOF	Metal Organic Framework
MS	Mass Spectrometry
OPEX	Operational Expenditures
PEM	Proton Exchange Membrane or Polymer Electrolyte Membrane
PHEV	Plug-in Hybrid Electric Vehicle
PID	Proportional Integral Derivative controller
PLC	Programmable Logic Controller
ppm	parts per million
PSA	Pressure Swing Adsorption
SAE	Society of Automotive Engineers
SFOE	Swiss Federal Office of Energy (OFEN in French or BFE in German)
SHE	Standard Hydrogen Electrode
SMR	Steam Methane Reforming
SoC	State of Charge
SOEC	Solid Oxyde Electrolysis
TCO	Total Cost of Ownership
TRL	Technology Readiness Level
TSA	Temperature Swing Adsorption
TtW	Tank to Wheel
UPS	Uninterruptible Power Supply
VPSC	Vacuum and Pressure Swing Adsorption
VRFB	Vanadium Redox Flow Battery
Wp	Watt peak
wt	weight
WtW	Well to Wheel

Table of contents

Acknowledgements.....	ii
Abstract.....	iv
Zusammenfassung.....	v
Résumé.....	vi
Abbreviations.....	vii
Chapter 1 Introduction.....	1
1.1. Energy and transport sector	1
1.2. Electric powertrains	2
1.2.1. Vehicle architecture.....	2
1.2.2. On-board energy storage.....	3
1.2.3. Market deployment of BEVs and FCEVs	7
1.3. Infrastructure for e-mobility	8
1.3.1. BEV chargers.....	8
1.3.2. Hydrogen refueling stations	9
1.4. Hydrogen production modes.....	11
1.5. Thesis goals and scope	14
References	15
Chapter 2 Grid to mobility.....	21
2.1. Grid to mobility efficiencies	22
2.1.1. Grid to mobility segmentation.....	24
2.1.2. BEV charging.....	26
2.1.3. FCEV refueling.....	27
2.1.4. Results and discussion	29
2.2. E-mobility and renewables.....	31
2.2.1. Production profiles of intermittent renewable energies	32
2.2.2. Energy demand from charging stations	35
2.3. Conclusion.....	37
References	39

Chapter 3	Buffering charging demand	45
3.1.	Problem setting	46
3.2.	Stochastic demand and charging points	48
3.2.1.	Method	48
3.2.2.	Results	51
3.3.	ESS operation and sizing	53
3.3.1.	Method	53
3.3.2.	Results	56
3.4.	Case study	58
3.5.	Conclusion	62
	References	63
Chapter 4	Building a e-mobility infrastructure demonstrator	67
4.1.	Grid to mobility demonstrator layout	68
4.2.	Redox Flow battery and DC charger	69
4.2.1.	VRFB fundamentals	69
4.2.2.	Installation	71
4.3.	Hydrogen Refueling Station	73
4.3.1.	Design	73
4.3.2.	HRS installation	76
4.3.3.	HRS programming	77
4.3.4.	HRS PLC wiring diagram	83
4.3.5.	Dynamic refuelling model on MATLAB	84
4.3.6.	Others uses of the HRS	86
4.3.7.	Hyundai ix35 Fuel Cell car	87
4.3.8.	Costs and hardware suppliers	87
4.4.	Electrolyser	89
4.4.1.	Installation	89
4.4.2.	Design and construction	90
4.4.3.	Electrolyser programming	94
4.4.4.	Electrolyser PLC wiring diagram	99
4.4.5.	Component failures and corrective measures	102
4.4.6.	Costs and hardware suppliers	103
4.5.	Hazard identification	104
4.6.	Conclusion	105

References	107
Chapter 5 Electrolysis and purification.....	109
5.1. Thermodynamics of alkaline water electrolysis	110
5.2. Alkaline electrolysis, data collection	112
5.2.1. Preliminary remarks	112
5.2.2. Power data.....	113
5.2.3. Cell performance and temperature data	115
5.2.4. Process control observations	118
5.3. Electrolytic hydrogen purification	119
5.3.1. Contaminants	120
5.3.2. Removal methods and quantification.....	124
5.3.3. Contaminant removal performance	128
5.4. Conclusion.....	133
References	134
Chapter 6 Hydrogen at scale and booster modelling.....	139
6.1. Hydrogen storage modes and release.....	140
6.1.1. Compressed gaseous hydrogen.....	141
6.1.2. Liquid hydrogen	142
6.1.3. Liquid Organic Hydrogen Carriers.....	143
6.2. Gas booster modelling	144
6.2.1. Context.....	144
6.2.2. Method.....	146
6.2.3. Variables of interest and governing parameters	150
6.2.4. Results and discussion	152
6.2.5. Integration of the results and engineering variables for HRS	155
6.3. Hydrogen at scale.....	157
6.3.1. Levelized cost of hydrogen production	157
6.3.2. Refueling stations	161
6.3.3. Hydrogen dispensing and transport logistics	163
6.4. Conclusion.....	165
References	167

Concluding remarks and perspectives	173
Numbers and orders of magnitude	176
Mass and pressure equilibrium plot	182
Conference posters	183
Curriculum Vitae.....	186

Chapter 1

Introduction

1.1 Energy and transport sector

Energy, by definition, is the enabler of any physical flow. Available in various forms in the environment, primary energy sources are converted into heat, movement or light in order to satisfy the needs of human activities. Currently, hydrocarbons represent more than 80% of our primary energy supply [1]. International governmental and non-governmental organisations are regularly publishing scenarii to explore the future composition of our energy mix. Demographic trends and carbon emissions pathways are at the core of these prospective studies [2]. From an estimated 7.7 billion people worldwide in 2019, the global population is projected to grow to around 9.7 billions in 2050 [3]. In the same time, the Intergovernmental Panel on Climate Change (IPCC) has determined that the current anthropogenic CO₂ emissions of *ca.* 42 GtCO₂eq/year need to reach a net zero by 2050 in order to limit global warming to 1.5°C [4]. Consequently, mitigation strategies are developed around remaining carbon budgets and necessary technologies and/or lifestyle changes [5,6].

With 8 GtCO₂eq emitted in 2017 [7], the transport sector is directly targeted in 3 out of the 17 Sustainable Development Goals of the United Nations (Goal 7 – Affordable and Clean Energy, Goal 11 – Sustainable Cities and Communities and Goal 13 – Climate Action) [8]. In addition, the transport sector is the only sector to have increased its emissions since 1990 in Europe [9]. Following the Avoid-Shift-Improve framework [10], three approaches are concomitantly pursued for transport's emission reduction: a reduction of the transport demand, a modal shift to low carbon modes and a technological change to more efficient powertrains. The latter being the one investigated in this thesis, with a focus on road transport. Depending on the implemented policies, the rolling stock of electric vehicles (excluding two-wheelers) is expected to reach 130 to 250 million units by 2030 [11]. With new energy carriers to deliver, the supply infrastructure will also undergo a drastic transformation. The technological aspects are presented in the following sections.

1.2 Electric powertrains

The potential advantages of electric powertrains result in three major cornerstones: no tailpipe emissions (air quality), the availability of a low carbon energy carrier (CO₂ emissions), and finally a greater energy independence (geopolitical exposure). The corresponding technological options and commercial deployments are discussed in the following subsections.

1.2.1 Vehicle architecture

Electric vehicles (EVs) are defined by the presence of one or more electric motors delivering mechanical energy to the wheels. A hybrid powertrain consists in a propulsion system featuring at least two independent sources of power. The presence of multiple energy sources and corresponding conversion devices enables a large set of variants as presented in **Table 1.1**.

Table 1.1 - Nomenclature of vehicle powertrains.

Vehicle type	Acronym	Battery Capacity	Fuel Cell Power	Example
Internal Combustion Engine	ICEV	-	-	Ford F-150
Hybrid Electric	HEV	1 – 2 kWh	-	Toyota Prius
Plug-In Hybrid Electric	PHEV	5 – 20 kWh	-	Chevrolet Volt
Battery Electric	BEV	25 – 100 kWh	-	Tesla Model 3
Battery Electric with H₂ range extender	-	30 – 60 kWh	5 – 20 kW	Renault Kangoo ZE H2
Fuel Cell Electric	FCEV	1 – 2 kWh	>80 kW	Toyota Mirai
Fuel Cell Plug-In Hybrid Electric	-	10 – 20 kWh	>50 kW	Mercedes GLC F-Cell

Regarding BEVs, the energy storage device is directly used to power the electric motor. Contrarywise, in FCEVs, in addition to the energy storage, a conversion device, the fuel cell, is needed to transform the chemical energy into electricity. Battery and hydrogen fuel cell systems are discussed hereinafter.

1.2.2 On-board energy storage

Energy storage encompass a large set of technologies, for example, we can mention potential energy stored in water reservoirs, kinetic energy stored in flywheels, thermal energy stored in phase-change materials or chemical energy in hydrocarbons. For automotive energy storage, liquid hydrocarbon fuels are widely used: they offer high energy densities and easy handling. The physical properties of various energy carriers used in road vehicles are presented in **Table 1.2**. The electrochemical processes enabling the release of energy in the form of electricity for batteries and hydrogen are detailed below.

Table 1.2 – Energy carriers in road vehicles, physical properties¹.

	Energy storage system / Fuel					
Property	Gasoline	LPG propane	CNG methane	Gaseous H ₂	Li-ion Battery [12]	Lead Acid Battery [13]
Gravimetric density*, kWh/kg	11.9	12.9	13.2	33.3 (1.6 incl. 5w% tank)	0.1 -0.2	0.03-0.05
Volumetric density*, kWh/L	8.9	6.6	2.5 (25 MPa)	0.87 – 1.3 (35 – 70 MPa)	0.2-0.6	0.06-0.1
Vapour density to air	4.0	1.52	0.55	0.07	N/A	N/A
Flammability range	1.4 – 7.6 %	2.1 – 10.1 %	5.0 – 15 %	4.0 – 75 %	N/A	N/A

Batteries

A large variety of battery chemistries are used to store energy. In the case of mobility applications, lithium-ion represents the current technology adopted by the car manufacturers. This specific chemistry, was rewarded by the 2019 Nobel Prize in Chemistry and we report hereinafter its main characteristics [14]. Lithium-ion batteries have the advantage of a charge/discharge roundtrip energy efficiency >90% and a life time >1000 cycles [15]. The working principle is presented in **Figure 1.1**. The cathode (positive electrode) is made from a metal oxide which contains lithium in its cristal lattice. Common oxides are LiCoO₂ (LCO), LiFePO₄ (LFP), LiMn₂O₄ (LMO), LiNiMnCoO₂ (NMC).

¹ https://www.engineeringtoolbox.com/alternative-fuels-d_1221.html

*Lower Heating Value

The anode (negative electrode) is typically made of porous carbon materials (*e.g.* graphite). When the battery is charged, lithium ions are stored in the anode. During discharge, they move back to the cathode, through the electrolyte (ethylene carbonate or analog solvent with dissolved lithium salts). A separator (polymer, *e.g.* polyethylene or polypropylene) is present to avoid the direct contact between cathode and anode materials and thus prevents the direct flow of electrons.

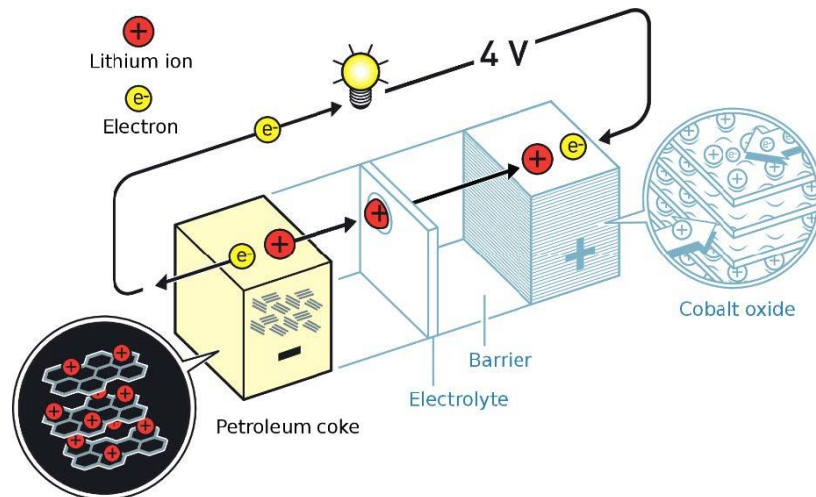


Figure 1.1 – Ion transfer mechanisms in a lithium Battery [14].

Lithium-ion battery manufacturing is an energy intensive process due to the extraction of raw materials and the cell assembly. Depending on the studies, the manufacturing of 1 kWh of battery capacity requires an energy input of 100 to 300 kWh [16,17]. This translates currently to 61 to 146 kg CO₂ eq per kWh of battery capacity, with a high sensitivity to the electricity mix used.

The development of BEVs is closely related to the evolution of lithium-ion battery price which were above 1100 \$/kWh in 2010 and have fallen below 200 \$/kWh in 2019 [12]. Based on these numbers, the battery pack in a BEV can be assumed to cost between 4000 \$ and 20 000 \$. For reference, the 50 kWh battery pack in a Peugeot e-208 weighs 330 kg, and is sold for about 10 000 CHF more than the equivalent ICE version.

Hydrogen and Fuel Cells

Since the mid-1960's, hydrogen is used in fuel cells for the NASA space program. Nowadays, the global hydrogen use is *ca.* 70 Mton, mostly for oil refining and ammonia production [18]. Hydrogen production pathways, and their corresponding carbon intensities are discussed in section 1.4. Due to its low volumetric density, gaseous hydrogen must be compressed to be used as an automotive energy carrier (see **Figure 1.2**). Higher densities of up to 70g/L can be obtained with liquid hydrogen at -253 °C. Hydrogen storage in liquid organic carriers, hydrides, or cryo-compressed is also an

option [19], but with no commercial applications in the automotive sector yet. Specific storage tanks are available for high pressure gaseous hydrogen, the typology is the following [20]:

- Type I: metal vessel (steel or aluminium)
- Type II: metal vessel with filament windings
- Type III: fully composite wrapped vessel with a metallic liner, usually aluminium
- Type IV: fully composite wrapped vessel with a non metallic liner, usually high-density polyethylene

For weight constraints, Type I and Type II cylinders are only used for stationary applications. Type III and Type IV mainly differ by their weight and ability to dissipate the heat during fast refueling (higher thermal conductivity of the liner in Type III). Bladder tanks and conformable reservoirs are still in development stage² (TRL 4 -5), as well as Type V (or linerless) composite reservoirs.

The gravimetric capacity of an automotive Type IV cylinders is *ca.* 5w%, and costs about 600\$/kg of stored hydrogen [21]. Specific on tank valves include safety features (Temperature and Pressure Relief Device, Excess Flow Valve, Bleed port, solenoids...) and pressure reducers to feed the fuel cell.

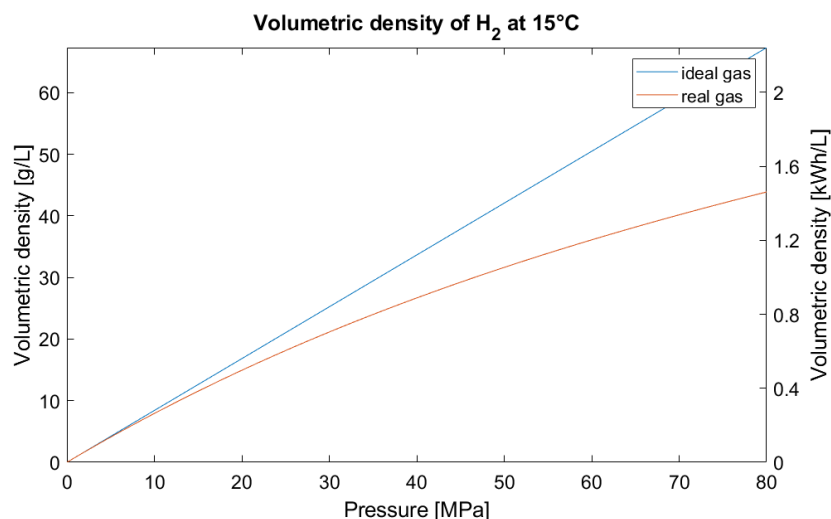


Figure 1.2 – Volumetric density of hydrogen, and non-ideal gas behavior (data calculated from SAE J 2601 [25]).

The non-ideal behaviour of hydrogen gas clearly appears in **Figure 1.2**. Various equations of state were developed to approach the real behaviour [22–24]. In this thesis, if not stated differently, the polynomial expression proposed in the SAE J2601 was used [25] (see **Equation 1.1**).

² <http://www.h2ref.eu/>

$$\begin{aligned}
\rho = & (-1.1671 \times 10^{-16} P^4 + 3.5429 \times 10^{-14} P^3 - 3.80467 \times 10^{-12} P^2 + 1.51947 \times 10^{-10} P - 3.76254 \times 10^{-12}) \cdot T^4 \\
& + (1.59364 \times 10^{-13} P^4 - 4.91286 \times 10^{-11} P^3 + 5.38378 \times 10^{-9} P^2 - 2.22007 \times 10^{-7} P + 5.12189 \times 10^{-9}) \cdot T^3 \\
& + (-8.26768 \times 10^{-11} P^4 + 1.6014 \times 10^{-8} P^3 - 2.93356 \times 10^{-6} P^2 + 1.2714 \times 10^{-4} P - 2.63185 \times 10^{-6}) \cdot T^2 \\
& + (1.95877 \times 10^{-8} P^4 - 6.34261 \times 10^{-6} P^3 + 7.478 \times 10^{-4} P^2 - 3.54828 \times 10^{-2} P + 6.08078 \times 10^{-4}) \cdot T \\
& + (-1.8437 \times 10^{-6} P^4 + 6.23884 \times 10^{-4} P^3 - 7.98237 \times 10^{-2} P^2 + 4.77618 P - 5.36549 \times 10^{-3})
\end{aligned}$$

Equation 1.1 – Hydrogen density ρ in kg/m³.

In **Equation 1.1**, P represents the pressure in MPa and T the temperature in degrees Kelvin.

The optimal pressure level for automotive applications was discussed in the literature [26], but the industry has retained two pressure levels, 350 and 700 bar [25], as reducing the heterogeneity of standards favors economies of scale.

In order to convert the hydrogen stored on-board to electricity, proton exchange membrane fuel cells (PEMFC) are used. The working principle and cell components are detailed in **Figure 1.3**.

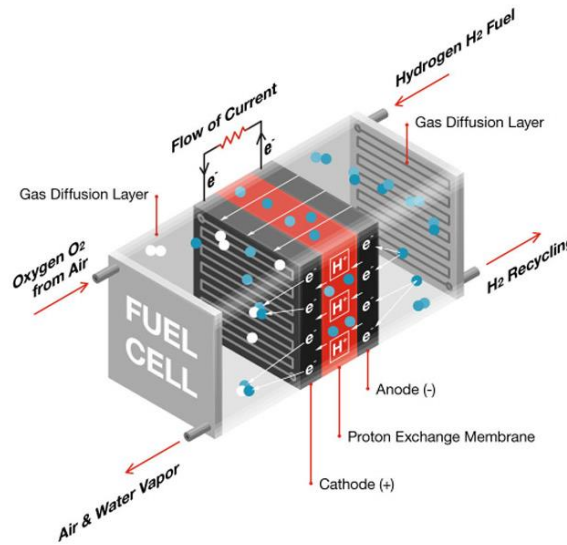
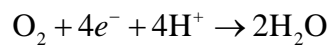
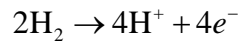


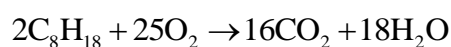
Figure 1.3 – Hydrogen fuel cell, working principle (image from www.cummins.com).

The electrochemical half reactions are the following:



³ <https://www.cummins.com/news/2019/10/08/five-key-questions-about-next-frontier-hydrogen-fuel-cells>

For reference, in an internal combustion engine (average formula for gasoline) we have the following ideal reaction:



In **Table 1.3**, atmospheric emissions and consumptions are compared for ICE and FCEVs.

Table 1.3 – Comparative emissions and consumptions per 100 km for ICE and FCEV.

	ICE	FCEV
Consumption per 100km		
Gasoline	4.5 kg (<i>ca.</i> 6L)	0
H₂	0	1 kg
O₂ (from ambient air)	15.8 kg	8 kg
Direct emissions per 100 km		
H₂O	6.4 kg	9 kg
CO₂	13.9 kg	0
Others	Partial combustion residues (NO _x , SO _x , PM...)	None (from the fuel cell)

In the past ten years, a 60% cost reduction has been achieved for PEMFC and they are currently at about 50\$/kW for large volume production (100 - 500 000 units per year, current prices above 1000 \$/kW)) [27]. Finally, for a typical passenger car, a 100 kW fuel cell and a 5 kg hydrogen storage cost *ca.* 10 000 \$.

1.2.3 Market deployment of BEVs and FCEVs

Policies have a major influence on the development of electric mobility. In EU, from January 1st 2020, the fleet average emission target was set at 95 g CO₂/km down from the average of 120.4 g CO₂/km measured in 2018 [28]. These targets can be reached with electric vehicles [29]. However, within electric vehicles, the market uptake of BEV and FCEV differs significantly.

One of the first mass produced modern BEV, with a Li-ion battery, is the Nissan Leaf, introduced in 2010, which reached 200 000 units sold in 2015 [30]. The same year, the 1 million electric vehicle milestone (BEV and PHEV) was crossed. In 2018, the global BEV and PHEV fleet exceeded 5.1 million units [11]. BEVs models are now available in all car segments. Interestingly, the first companies to

produce a million EVs were Tesla and BYD in early 2020⁴ (after *ca.* 6 year since the first car produced). For reference, one can note that each of the major automakers (VW, Toyota and Renault Nissan⁵) are producing *ca.* 10 million conventional cars per year. The numbers of electric vehicles produced in Europe is expected to surge to 4 millions units per year in 2025 [31].

In 2015, the Hyundai ix35 Fuel Cell and the Toyota Mirai, were the first commercially produced FCEV available. The Honda Clarity Fuel Cell was introduced the following year. In late 2019, about 10'000 Toyota Mirai were produced [32]. A ramp-up to 30'000 units per year is projected for newer model versions (Hyundai Nexo and Toyota Mirai). Nevertheless, the EU Roadmap plan for 2030 aims at 5.7 million FCEV on the road, 500'000 light commercial vehicles and 45'000 trucks and buses [33].

1.3 Infrastructure for e-mobility

With new energy carriers, the traditional layout of refueling stations, together with the upstream fuel supply chain, needs a different perspective. An average gasoline refueling station in Switzerland typically has half-a-dozen of stalls, with one or several 50'000 L fuel tanks, and delivers 2500 L of gasoline per day (2018 average from the 3367 fuel stations in Switzerland⁶ [34]). In order to offer the same level of service as the current network of service station, the e-mobility infrastructure needs to be developed, as recognized in the EU directive 2014/94 [35]. The technical characteristics of BEV chargers and hydrogen refueling stations (HRS) are explained below, together with network deployment perspectives.

1.3.1 BEV chargers

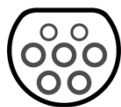

With electricity as the energy carrier, a large variety of charging points topology exists. Inductive, conductive, with plug, catenary, or even battery swap [36,37]. Standardized solutions nowadays are the fast DC charging (DCFC), and level 2 AC charging, as presented in **Table 1.4**. The technical details are specified in the SAE J1772 standard [38]. Inductive charging, at up to 11 kW, is also developed but with limited commercial deployments as yet [39]. The SAE J1772 addresses only vehicles with a maximum curb weight of 6000 lb (2720kg). 1-3 MW chargers are under investigation by the Charging Interface Initiative e.V. (CharIN) with up to 1500 V DC and 3000 A [40].

⁴ <https://cleantechnica.com/2019/12/10/tesla-passes-byd-in-global-ev-sales-the-history-behind-byd-teslas-efforts-at-global-ev-domination/>

⁵ <https://www.reuters.com/article/us-automakers-sales-japan/renault-nissan-group-sold-most-cars-last-year-but-vws-no-1-including-trucks-idUSKCN1PO0R1>

⁶ 2'342'285 tons of gasoline sold in 2018, average density of 0.7489 assumed

Table 1.4 – BEV charger topology.

Charging type	Nominal supply voltage	Max current	Power range	Cost [41]	Plug type (EU)
Level 2 residential	240 V AC (1 phase)	32 A	2.9 – 7.7 kW	400 – 700 \$	
Level 2 commercial	240 V AC	80 A	7.7 – 22 kW	2500 – 5000 \$	
DCFC	400 V DC	400 A	50 - 150 kW	20 000 – 100 000 \$	
	800 V DC		up to 350 kW	150 000 \$	

It is estimated that 80% of the recharging events will occur at slow charging rates at home or at the workplace [42]. However, long travels, vehicle availability constraints and current housing statistics⁷, justify the need for a DCFC network. Charging speed is discussed in Chapter 3.

Publicly accessible fast chargers numbered 144'000 worldwide by the end of 2018 [11], and the recommended target is to maintain a ratio higher than 1 charger per 10 electric cars. Several companies are working on transnational or transcontinental fast charging corridors (Ionia™, Tesla™, Ultra-E™, VW Electrify™, Fastned™...).

1.3.2 Hydrogen Refueling Stations

A hydrogen refueling station (HRS) consists of five main components (the scale of some components can be seen on **Figure 1.4**):

- Hydrogen production/delivery system, supply storage
- Hydrogen compression
- Gaseous hydrogen buffer storage (medium pressure and high pressure), also named cascade storage or fueling storage (usually combined with the compressor within a container)
- Pre-cooling device (below the filling point), also named Temperature Cooling Unit
- Gaseous hydrogen dispensing system

⁷ In 2017, 42% of the EU population lived in flats. https://ec.europa.eu/eurostat/statistics-explained/index.php/Living_conditions_in_Europe_-_housing_quality

The refilling process for passenger vehicles is standardized and documented in the SAE J2601 [25], with a reference fueling target of 3 minutes. This standard covers filling protocols for vehicles with hydrogen storage system sizes from 49.7 to 248.6 L corresponding to *ca.* 2 to 10 kg at 700 bar and 15°C. Protocols for larger tanks are not yet standardized, but the characteristics of high flow nozzles (up to 120 g H₂/s) are detailed in ISO 17268 [43]. If any deviation from the fuelling protocol arises, a stop within 5 seconds is required [44].

Specific safety regulations are in place to take into account the risks associated with pressurized hydrogen. Notably, all pressure components should sustain at least 10 cycling to 150 % Hydrogen Service Level (HSL); they should be functional and without physical deformation after a test at 210% HSL; and the burst pressure should be at least 330% of HSL [44].

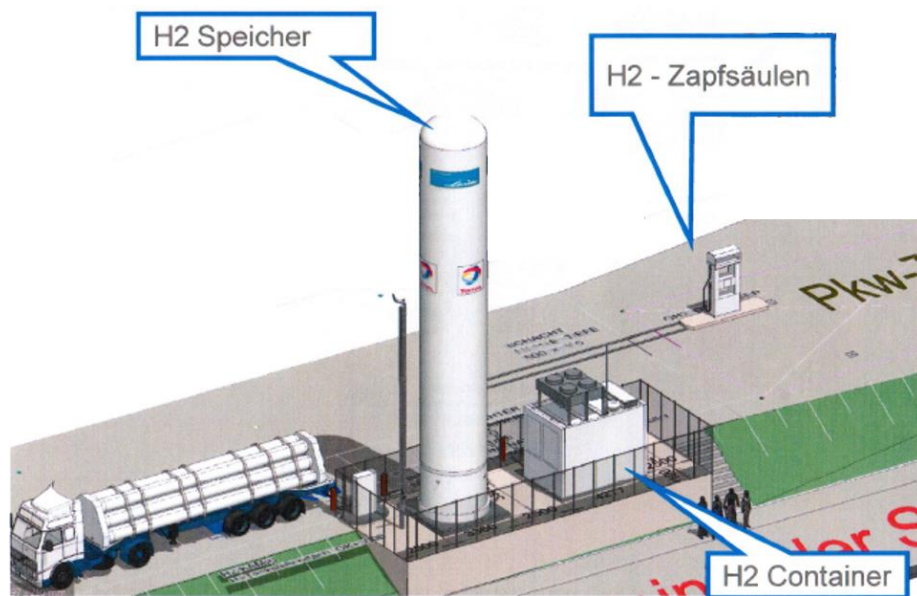


Figure 1.4 – Components of a hydrogen refilling station, with a tube trailer delivery (example from Total, Geiselwind, Germany, https://www.now-gmbh.de/content/1-aktuelles/1-presse/20150608-vollversammlung-statusseminar-brennstoffzelle/bacelli_h2tankstellen_total.pdf).

Depending on the daily capacity of hydrogen delivered and the required safety components, an HRS can cost between 0.8 to 2.1 MCHF in EU [45]. High pressure storage banks and compressors are the key cost contributors with 40 to 60% of the total components costs [46–48]. Systems at a lower cost, in the 0.3-0.5 MCHF range, are only used for demonstration purposes with a daily capacity below 20 kg/day. Thus, deploying a network of HRS involves capital intensive programs often supported by public funding (FCHJU, BMVI, DOE) together with strategic roadmaps.

With 330 public HRS in operation worldwide at the end of 2019, the hydrogen mobility infrastructure is still at an early deployment stage. Japan, Germany and California are among the leading regions

with respectively 114, 87 and 48 stations in operation⁸. In Switzerland, the first public HRS was opened in 2016, and is, to date, the only one. However, significant deployments are forecasted in the next years in all regions [45]. In 2019, a target of 10 million fuel cell vehicles, 10 thousand refueling stations in the 10 years until 2030 was set by the Hydrogen Council [49]. However, the forecasting exercise remains a difficult task, with the same working group, in November 2017, aiming at 1'100 HRS in 2020 and 15'000 by 2030 [50].

1.4 Hydrogen production modes

Electricity is a commodity with large and established industrial players for production, transport and distribution. Low carbon electricity generation technologies are already available at large scale and their deployment is independent from the electrification of the transport sector. On the other hand, the use of hydrogen in the transport sector is expected to trigger significant transformations in hydrogen supply chains. Some of the main hydrogen production modes are reviewed here.

Applications for hydrogen go far beyond the transport sector as shown in **Figure 1.5** [18]. Hydrogen is a commodity with large industrial consumers, especially for ammonia synthesis and oil refining, or as a mixture with other gases, for steel and methanol production. The use of liquid hydrogen as rocket fuel remains marginal. Therefore, with cost as the primary objective, thermochemical routes based on fossil fuels are largely deployed and represent the vast majority of industrial hydrogen production.

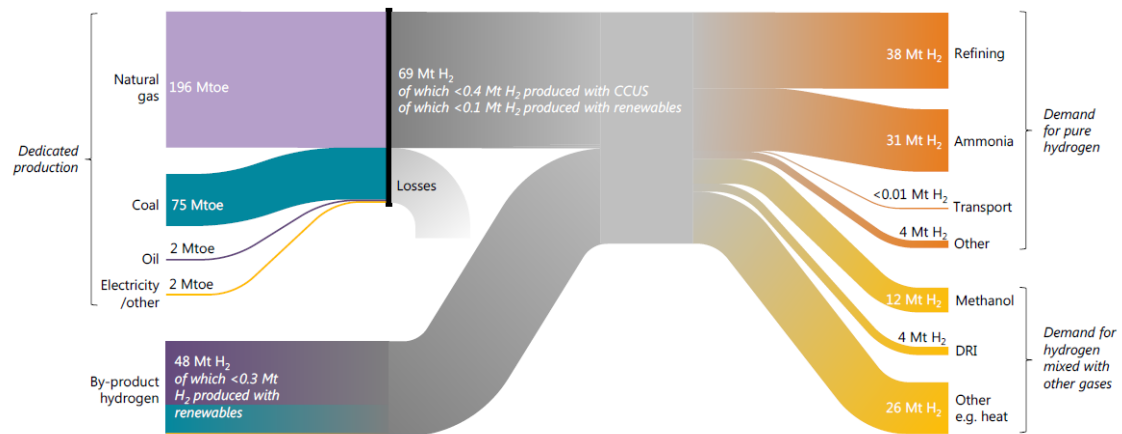


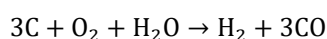
Figure 1.5 – Today's hydrogen value chains ([18]).

⁸ <https://www.tuvsud.com/en/press-and-media/2020/february/83-new-hydrogen-refuelling-stations-worldwide> (Accessed February 27, 2020)

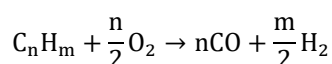
These processes, based on natural gas or coal, are responsible for 0.83 Gt of CO₂ emissions per year [18]. Indeed, each kilogram of hydrogen produced *via* Steam Methane Reforming (SMR), releases 9 kg of CO₂. SMR is a two step reaction, as detailed below [51]:

- Reforming $\text{CH}_4 + \text{H}_2\text{O (g)} \xrightarrow{\text{Ni cat.}} \text{CO} + 3\text{H}_2$ at 700 – 900 °C
- Water-gas shift $\text{CO} + \text{H}_2\text{O} \rightarrow \text{CO}_2 + \text{H}_2$ at 250 – 450 °C depending on the catalysts

Other routes based on hydrocarbons and biomass include gasification and partial oxidation. During gasification, solid fuels (coal, wood...) are heated, dried and then react with steam and oxygen:



Partial oxidation is the reaction of hydrocarbons with a constrained amount of oxygen. It is usually performed at temperatures of up to 1600 °C.



Alternatively, electrochemistry is a way to produce hydrogen without direct carbon emissions or so-called green hydrogen with a corresponding low carbon electricity supply. In most hydrogen roadmaps, green hydrogen (<https://www.certifyhy.eu/>) is considered as a must for large scale deployments (Europe Roadmap⁹, US Roadmap¹⁰, Japan Roadmap¹¹). Green hydrogen production relies on water splitting which can be divided in two semi-reactions:

- Oxygen evolution reaction (OER): $2\text{H}_2\text{O} \rightarrow \text{O}_2 + 4\text{H}^+ + 4\text{e}^-$
- Hydrogen evolution reaction (HER): $2\text{H}^+ + 2\text{e}^- \rightarrow \text{H}_2$

The main candidate for water splitting at industrial scale is water electrolysis, which can be performed with three main technologies as presented in **Table 1.5**. The required amount of electricity to produce 1 kg of hydrogen is in the range of 50 to 65 kWh at the system level due to overpotentials (see Chapter 2 and Chapter 5).

⁹ https://www.fch.europa.eu/sites/default/files/Hydrogen%20Roadmap%20Europe_Report.pdf

¹⁰ https://cafc.org/sites/default/files/Road-map-to-a-US-hydrogen-economy_Executive-Summary.pdf

¹¹ https://www.meti.go.jp/english/press/2017/pdf/1226_003b.pdf

Table 1.5 – Water electrolysis techniques.

Technology	Alkaline	PEM	SOEC
Temperature	50 – 80 °C	50 – 80 °C	700 – 900 °C
Anode reaction	$2\text{OH}^- \rightarrow 0.5\text{O}_2 + \text{H}_2\text{O} + 2\text{e}^-$	$\text{H}_2\text{O} \rightarrow 0.5\text{O}_2 + 2\text{H}^+ + 2\text{e}^-$	$2\text{O}^{2-} \rightarrow \text{O}_2 + 4\text{e}^-$
Cathode reaction	$2\text{H}_2\text{O} + 2\text{e}^- \rightarrow \text{H}_2 + 2\text{OH}^-$	$2\text{H}^+ + 2\text{e}^- \rightarrow \text{H}_2$	$2\text{H}_2\text{O} + 4\text{e}^- \rightarrow 2\text{O}^{2-} + 2\text{H}_2$
Current density	200 – 500 mA/cm ²	1000 – 2000 mA/cm ²	300 – 1000 mA/cm ²
Maturity	Commercially available for around 100 years, proven on >100 MW scale	Commercially available for around 30 years, proven on >2MW scale 10 MW https://refhyne.eu/	Demonstration

Efficiency, lifetime, system dynamics, catalyst availability, operating pressure and cost parameters are also required for a full comparison of water electrolysis technologies. However, these characteristics are rapidly evolving and are closely related to the specific engineering, balance of plant and operation management of each machines and not only linked to intrinsic physico-chemical parameters. The specific operation of an alkaline water electrolysis system is detailed in Chapter 5.

Next to water electrolysis, hydrogen can also be obtained electrochemically as a by-product in other processes, in particular during the production of chlorine and caustic soda. Chlor-alkali electrolysis is the electrolysis of brine to produce caustic soda, chlorine gas and hydrogen as a by-product. PVC production and organic synthesis are the main consumers for chlorine [52].

- At the anode $2\text{Cl}^- \rightarrow \text{Cl}_2 + 2\text{e}^-$
- At the cathode $2\text{H}_2\text{O} + 2\text{e}^- \rightarrow \text{H}_2 + 2\text{OH}^-$

Chlor-alkali hydrogen was already used for mobility applications in Switzerland during the hydrogen bus demonstration by Post Auto in 2011-2017. Hydrogen from chlor-alkali represented about 12 % of the total hydrogen consumed during the project, as a complement to the installed on-site electrolyser [53]. The reported performance is 100 kWh of electricity to produce 17 kg of chlorine, 1 kg of hydrogen and 50 liters of a 30% NaOH solution. The respective life cycle inventory allocation to chlorine, caustic soda or/and hydrogen is subject to various appreciations, depending on end-user perspective.

Interestingly, indirect water electrolysis techniques are also developed, decoupling hydrogen evolution from oxygen evolution [54]. In particular we can mention a proof of concept with a dual

circuit redox flow battery, using Mo_2C as a redox mediator for hydrogen evolution and the oxydation of V(II) to V(III) [55]. The electrochemistry of Zinc is also used to decouple hydrogen and oxygen production (www.ergosup.com).

Finally, besides thermochemical and electrochemical conversions, biochemical or microbial conversion (digestion, fermetentation, metabolic processing) [56] and photochemical devices [57] are also developed with limited deployments to date.

1.5 Thesis goals and scope

Moving away from a fossil fuel-based infrastructure requires a major transformation of the ecosystem with vehicles, stations and oil majors as we know today. New players from the gas industry, the power market and electrochemistry are coming into play.

In Chapter 2, the interplay of renewable electricity and the energy demand of electric and hydrogen mobility are assessed.

Chapter 3 addresses the problem of stochastic arrival of BEVs in fast charging stations, and the buffering potential of a local energy storage system.

The design and construction of the grid to mobility demonstrator installed in Martigny is discussed in Chapter 4. The elements installed in the demonstrator represent the experimental set up used to develop the results presented in Chapters 5 and 6.

Chapter 5 covers the purification of electrolytic hydrogen for fuel cell vehicle application and the operating data from a 50 kW alkaline water electrolyser.

Finally, Chapter 6 discusses the compression of hydrogen with air driven gas boosters, the modelling of an hydrogen refueling station and future perspectives for hydrogen costs and distribution.

References

- [1] IEA, World Energy Balances 2019, IEA, Paris, 2019. <https://www.iea.org/reports/world-energy-balances-2019> (accessed February 25, 2020).
- [2] M. Karatayev, G. Movkebayeva, Z. Bimagambetova, Increasing Utilisation of Renewable Energy Sources: Comparative Analysis of Scenarios Until 2050, in: N. Mouraviev, A. Koulouri (Eds.), Energy Security, Springer International Publishing, Cham, 2019: pp. 37–68. https://doi.org/10.1007/978-3-030-01033-1_3.
- [3] United Nations, Department of Economic and Social Affairs, Population Division, World population prospects Highlights, 2019 revision Highlights, 2019 revision, 2019.
- [4] Intergovernmental Panel on Climate Change, Global warming of 1.5°C: Summary for Policymakers, World Meteorological Organization, Geneva, Switzerland, 2018. <http://www.ipcc.ch/report/sr15/> (accessed February 25, 2020).
- [5] S. Pacala, Stabilization Wedges: Solving the Climate Problem for the Next 50 Years with Current Technologies, Science. 305 (2004) 968–972. <https://doi.org/10.1126/science.1100103>.
- [6] United Nations Environment Programme, The emissions gap report 2019, 2019. <https://www.unenvironment.org/resources/emissions-gap-report-2019> (accessed March 11, 2020).
- [7] IEA, Data and statistics, CO2 emissions by sector, World 1990-2017, IEA, Paris, 2019. <https://www.iea.org/data-and-statistics?country=WORLD&fuel=CO2%20emissions&indicator=CO2%20emissions%20by%20sector> (accessed February 25, 2020).
- [8] W. Rosa, ed., Transforming Our World: The 2030 Agenda for Sustainable Development, in: A New Era in Global Health, Springer Publishing Company, New York, NY, 2017. <https://doi.org/10.1891/9780826190123.ap02>.
- [9] Transport & Environment, How European transport can contribute to an EU -55% GHG emissions target in 2030, European Federation for Transport and Environment, Brussels, Belgium, 2020. https://www.transportenvironment.org/sites/te/files/publications/2020_02_TE_EGD_vision_How_EU_transport_can_contribute_minus_55.pdf (accessed March 9, 2020).
- [10] IEA, Energy Technology Perspectives 2017., Organisation for Economic Co-operation and Development., Paris, 2017.
- [11] International Energy Agency, Global EV Outlook 2019: Scaling-up the transition to electric mobility, OECD, 2019. <https://doi.org/10.1787/35fb60bd-en>.
- [12] Y. Ding, Z.P. Cano, A. Yu, J. Lu, Z. Chen, Automotive Li-Ion Batteries: Current Status and Future Perspectives, Electrochem. Energ. Rev. 2 (2019) 1–28. <https://doi.org/10.1007/s41918-018-0022-z>.

- [13] M.A. Hannan, M.M. Hoque, A. Mohamed, A. Ayob, Review of energy storage systems for electric vehicle applications: Issues and challenges, *Renewable and Sustainable Energy Reviews*. 69 (2017) 771–789. <https://doi.org/10.1016/j.rser.2016.11.171>.
- [14] O. Ramström, Scientific Background on the Nobel Prize in Chemistry 2019 - Lithium-Ion Batteries, (2019). <https://www.nobelprize.org/uploads/2019/10/advanced-chemistryprize2019.pdf> (accessed February 27, 2020).
- [15] R. Schmich, R. Wagner, G. Hörpel, T. Placke, M. Winter, Performance and cost of materials for lithium-based rechargeable automotive batteries, *Nat Energy*. 3 (2018) 267–278. <https://doi.org/10.1038/s41560-018-0107-2>.
- [16] B. Cox, C.L. Mutel, C. Bauer, A. Mendoza Beltran, D.P. van Vuuren, Uncertain Environmental Footprint of Current and Future Battery Electric Vehicles, *Environ. Sci. Technol.* 52 (2018) 4989–4995. <https://doi.org/10.1021/acs.est.8b00261>.
- [17] E. Emilsson, L. Dahllöf, Lithium-Ion Vehicle Battery Production - Status 2019 on Energy Use, CO2 Emissions, Use of Metals, Products Environmental Footprint, and Recycling, IVL Swedish Environmental Research Institute, Stockholm, Sweden, 2019.
- [18] International Energy Agency, The Future of Hydrogen - Seizing today's opportunities, IEA, Paris, 2019. <https://www.iea.org/publications/reports/thefutureofhydrogen/> (accessed October 16, 2019).
- [19] H. Barthelemy, M. Weber, F. Barbier, Hydrogen storage: Recent improvements and industrial perspectives, *International Journal of Hydrogen Energy*. 42 (2017) 7254–7262. <https://doi.org/10.1016/j.ijhydene.2016.03.178>.
- [20] E. Rivard, M. Trudeau, K. Zaghbi, Hydrogen Storage for Mobility: A Review, *Materials*. 12 (2019) 1973. <https://doi.org/10.3390/ma12121973>.
- [21] T.Q. Hua, H.-S. Roh, R.K. Ahluwalia, Performance assessment of 700-bar compressed hydrogen storage for light duty fuel cell vehicles, *International Journal of Hydrogen Energy*. 42 (2017) 25121–25129. <https://doi.org/10.1016/j.ijhydene.2017.08.123>.
- [22] E.W. Lemmon, M.L. Huber, J.W. Leachman, Revised standardized equation for hydrogen gas densities for fuel consumption applications, *Journal of Research of the National Institute of Standards and Technology*. 113 (2008) 341.
- [23] D.-Y. Peng, D.B. Robinson, A New Two-Constant Equation of State, *Ind. Eng. Chem. Fund.* 15 (1976) 59–64. <https://doi.org/10.1021/i160057a011>.
- [24] Otto. Redlich, J.N.S. Kwong, On the Thermodynamics of Solutions. V. An Equation of State. Fugacities of Gaseous Solutions., *Chem. Rev.* 44 (1949) 233–244. <https://doi.org/10.1021/cr60137a013>.
- [25] SAE International, J2601: Fueling Protocols for Light Duty Gaseous Hydrogen Surface Vehicles, 2016. http://standards.sae.org/j2601_201407/ (accessed February 14, 2017).

- [26] Z. Lin, S. Ou, A. Elgowainy, K. Reddi, M. Veenstra, L. Verduzco, A method for determining the optimal delivered hydrogen pressure for fuel cell electric vehicles, *Applied Energy*. 216 (2018) 183–194. <https://doi.org/10.1016/j.apenergy.2018.02.041>.
- [27] Y. Wang, D.F. Ruiz Diaz, K.S. Chen, Z. Wang, X.C. Adroher, Materials, technological status, and fundamentals of PEM fuel cells – A review, *Materials Today*. 32 (2020) 178–203. <https://doi.org/10.1016/j.mattod.2019.06.005>.
- [28] European Commission, Regulation (EU) 2019/631 of the European Parliament and of the Council of 17 April 2019 setting CO2 emission performance standards for new passenger cars, 2019. <http://data.europa.eu/eli/reg/2019/631/oj> (accessed March 17, 2020).
- [29] A. Hoekstra, The Underestimated Potential of Battery Electric Vehicles to Reduce Emissions, *Joule*. 3 (2019) 1412–1414. <https://doi.org/10.1016/j.joule.2019.06.002>.
- [30] Nissan Motor Corporation, PR: Nissan Leaf reaching 200 000th sales, (2015). <https://global.nissannews.com/en/releases/release-5c4a425bce43a1fad9e1fe0493003cf6-151210-01-e> (accessed March 16, 2020).
- [31] Transport & Environment, Electric surge: Carmakers’ electric car plans across Europe 2019–2025, (2019). https://www.transportenvironment.org/sites/te/files/publications/2019_07_TE_electric_cars_report_final.pdf (accessed March 17, 2020).
- [32] Toyota Motor Corporation, PR: Toyota to unveil next-generation “Mirai Concept” at 2019 Tokyo Motor Show’s “Future Expo,” (n.d.). <https://global.toyota/en/newsroom/toyota/29933463.html> (accessed March 17, 2020).
- [33] Deloitte, Ballard, Fueling the Future of Mobility - Hydrogen and fuel cell solutions for transportation, (2020). <https://info.ballard.com/deloitte-vol-1-fueling-the-future-of-mobility> (accessed March 17, 2020).
- [34] Avenenergy - Union Pétrolière Suisse, Rapport Annuel 2018, (2019). https://www.avenergy.ch/images/pdf/93090_EV_JB_2018_FR_WEB.pdf (accessed March 17, 2020).
- [35] E. European Parliament and Council of the European Union, Directive 2014/94/EU of the European Parliament and of the council of 22 October 2014 on the deployment of alternative fuels infrastructure, *Official Journal of the European Union*. (2014). http://www.nezeh.eu/assets/media/fckuploads/file/Legislation/RED_23April2009.pdf (accessed January 31, 2017).
- [36] M. Yilmaz, P.T. Krein, Review of Battery Charger Topologies, Charging Power Levels, and Infrastructure for Plug-In Electric and Hybrid Vehicles, *IEEE Transactions on Power Electronics*. 28 (2013) 2151–2169. <https://doi.org/10.1109/TPEL.2012.2212917>.
- [37] L. Rubino, C. Capasso, O. Veneri, Review on plug-in electric vehicle charging architectures integrated with distributed energy sources for sustainable mobility, *Applied Energy*. 207 (2017) 438–464. <https://doi.org/10.1016/j.apenergy.2017.06.097>.

- [38] SAE International, J1772: Electric Vehicle and Plug in Hybrid Electric Vehicle Conductive Charge Coupler, (2016). http://standards.sae.org/j1772_201210/ (accessed February 14, 2017).
- [39] SAE International, J2954: Wireless Power Transfer for Light-Duty Plug-In/Electric Vehicles and Alignment Methodology, (2019). <https://www.sae.org/standards/content/j2954/> (accessed March 11, 2020).
- [40] CharIN e.V., Berlin, CharIN High Power Commercial Vehicle Charging - Task Force Aggregated Requirements, (2019). https://www.charinev.org/fileadmin/HPCCV/High_Power_Commercial_Vehicle_Charging_Requirements_v2.0.pdf (accessed March 11, 2020).
- [41] C. Nelder, E. Rogers, Reducing EV charging infrastructure costs, (2019). <https://rmi.org/ev-charging-costs>. (accessed March 11, 2020).
- [42] J. Smart, S. Schey, Battery Electric Vehicle Driving and Charging Behavior Observed Early in The EV Project, SAE Int. J. Alt. Power. 1 (2012) 27–33. <https://doi.org/10.4271/2012-01-0199>.
- [43] International Organization for Standardization, EN ISO 17268: Gaseous hydrogen land vehicle refuelling connection devices, (2016).
- [44] International Organization for Standardization, ISO 19880-1:2020 - Gaseous hydrogen Fuelling Stations, Part 1: General requirements, (2020).
- [45] D. Apostolou, G. Xydis, A literature review on hydrogen refuelling stations and infrastructure. Current status and future prospects, Renewable and Sustainable Energy Reviews. 113 (2019) 109292. <https://doi.org/10.1016/j.rser.2019.109292>.
- [46] A. Mayyas, M. Mann, Manufacturing competitiveness analysis for hydrogen refueling stations, International Journal of Hydrogen Energy. 44 (2019) 9121–9142. <https://doi.org/10.1016/j.ijhydene.2019.02.135>.
- [47] L. Viktorsson, J. Heinonen, J. Skulason, R. Unnthorsson, A Step towards the Hydrogen Economy—A Life Cycle Cost Analysis of A Hydrogen Refueling Station, Energies. 10 (2017) 763. <https://doi.org/10.3390/en10060763>.
- [48] K. Reddi, A. Elgowainy, N. Rustagi, E. Gupta, Impact of hydrogen refueling configurations and market parameters on the refueling cost of hydrogen, International Journal of Hydrogen Energy. 42 (2017) 21855–21865. <https://doi.org/10.1016/j.ijhydene.2017.05.122>.
- [49] Hydrogen Council, Path to hydrogen competitiveness, A cost perspective, (2020). https://hydrogencouncil.com/wp-content/uploads/2020/01/Path-to-Hydrogen-Competitiveness_Full-Study-1.pdf (accessed March 11, 2020).
- [50] Hydrogen Council, Hydrogen scaling up, A sustainable pathway for the global energy transition, (2017). <https://hydrogencouncil.com/wp-content/uploads/2017/11/Hydrogen-scaling-up-Hydrogen-Council.pdf> (accessed March 11, 2020).
- [51] Prof.Dr.D. Stolten, Dr.B. Emonts, eds., Hydrogen Science and Engineering : Materials, Processes, Systems and Technology, Wiley-VCH Verlag GmbH & Co. KGaA, Weinheim, Germany, 2016. <https://doi.org/10.1002/9783527674268>.

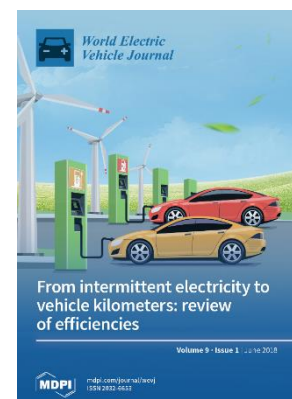
- [52] A. Delfrate, Chlorine-Alkaline Electrolysis - Technology and Use and Economy, in: Prof.Dr.D. Stolten, Dr.B. Emonts (Eds.), Hydrogen Science and Engineering : Materials, Processes, Systems and Technology, Wiley-VCH Verlag GmbH & Co. KGaA, Weinheim, Germany, 2016: pp. 41–56. <https://doi.org/10.1002/9783527674268.ch03>.
- [53] R. Krieger, Brennstoffzellenpostauto & Schweizer Wasserstofftankstelle, Swiss Federal Office of Energy SFOE, Bern, 2017. <https://www.aramis.admin.ch/Dokument.aspx?DocumentID=45619> (accessed May 7, 2020).
- [54] H. Dotan, A. Landman, S.W. Sheehan, K.D. Malviya, G.E. Shter, D.A. Grave, Z. Arzi, N. Yehudai, M. Halabi, N. Gal, N. Hadari, C. Cohen, A. Rothschild, G.S. Grader, Decoupled hydrogen and oxygen evolution by a two-step electrochemical–chemical cycle for efficient overall water splitting, *Nat Energy*. 4 (2019) 786–795. <https://doi.org/10.1038/s41560-019-0462-7>.
- [55] V. Amstutz, K.E. Toghiani, F. Powlesland, H. Vrubel, C. Comninellis, X. Hu, H.H. Girault, Renewable hydrogen generation from a dual-circuit redox flow battery, *Energy Environ. Sci.* 7 (2014) 2350–2358. <https://doi.org/10.1039/C4EE00098F>.
- [56] C.-Y. Lin, T.M.-L. Nguyen, C.-Y. Chu, H.-J. Leu, C.-H. Lay, Fermentative biohydrogen production and its byproducts: A mini review of current technology developments, *Renewable and Sustainable Energy Reviews*. 82 (2018) 4215–4220. <https://doi.org/10.1016/j.rser.2017.11.001>.
- [57] N. Fajrina, M. Tahir, A critical review in strategies to improve photocatalytic water splitting towards hydrogen production, *International Journal of Hydrogen Energy*. 44 (2019) 540–577. <https://doi.org/10.1016/j.ijhydene.2018.10.200>.

Chapter 2

Grid to mobility

The results presented in this chapter were partially published in the following papers:

- R. Frischknecht, C. Bauer, A. Froemelt, S. Hellweg, K. Biemann, T. Buetler, B. Cox, P. de Haan, S. Hoerl, R. Itten, N. Jungbluth, Y. Ligen, N.A. Mathys, S. Schiess, S. Schori, P. van Loon, J. Wang, S. Wettstein, LCA of mobility solutions: approaches and findings—66th LCA forum, Swiss Federal Institute of Technology, Zurich, 30 August, 2017, The International Journal of Life Cycle Assessment. 23 (2018) 381–386. <https://doi.org/10.1007/s11367-017-1429-1>. [1]
- Y. Ligen, H. Vrubel, H. Girault, Mobility from Renewable Electricity: Infrastructure Comparison for Battery and Hydrogen Fuel Cell Vehicles, World Electric Vehicle Journal. 9 (2018) 3. <https://doi.org/10.3390/wevj9010003>. [2]



And presented during the following conferences:

- LCA of Mobility Solutions, Zürich, 30th August 2017, Infrastructure Energy Demand for Battery and Hydrogen Fuel Cell Vehicles
- EVS 30, Stuttgart, October 9-11 2017, Mobility from Renewable Electricity
- EEVC 2018, Geneva, 14th March 2018, Design and Operation of a Grid to Mobility Demonstrator

The interest for electric and hydrogen mobility is closely related to the decrease of the grid carbon intensity and the rise of decentralized renewable energy in the electricity mix. Between 1990 and 2016, the average CO₂ emissions from electricity generation in EU has decreased from 523.6 g CO₂/kWh to 295.8 g CO₂/kWh [3], and even reached 235 g CO₂/kWh in 2019¹. Electrifying the transport sector without a transition to a low carbon electricity mix will not deliver all its potential benefits. On the other hand, moving to a low carbon electricity mix without mobility applications, leaves an untapped potential for a low carbon energy system. A coherent sizing is needed between consumers (vehicles), producers (electricity supply) and delivery infrastructure. In order to fully understand the decarbonization potential of electric mobility, a detailed analysis of BEVs and FCEVs electricity demand is required.

In the first section, the energy intensity from the grid to the final mobility service is analyzed. In a second section, production profiles of renewable energy sources in Martigny (VS, Switzerland) are compared with mobility demand profiles and delivery capacities of service stations.

2.1 Grid to mobility efficiencies

The energy intensity of electric vehicle operation is an essential aspect of their life cycle assessment (LCA). LCA applied to the transport sector is usually broken down in the Well-to-Wheel (WtW) analysis approach [4]. Conceived originally for ICEVs as the reference case, refilling events are not explicitly highlighted, and the methodology doesn't fit to the specificities of EVs. Indeed, Well-to-Tank (WtT) usually covers the energy carrier production and transport and Tank-to-Wheel (TtW) covers the energy consumption of the vehicle, but the distribution of the energy carrier to the vehicle is hidden in the WtT part and is therefore often neglected. The Well-to-Wheels life cycle was schematized by Nordelhof [5] (see **Figure 2.1**). Alternatively, Guzzella and Sciarretta [6] distinguished three steps with upstream energy conversion, on-board energy conversion and vehicle energy consumption, but still without highlighting the energy transfer occurring at the station. For ICE, it is currently estimated that before being burned in a combustion engine (oil extraction and refining), every liter of gasoline has already emitted 630 g of CO₂ [7]. Recalling the numbers from **Table 1.3**, the total emissions from well to wheel amount to 2.95 kg CO₂ /L of gasoline (including 2.32 kg from the fuel combustion).

¹ <https://www.iea.org/reports/european-union-2020>

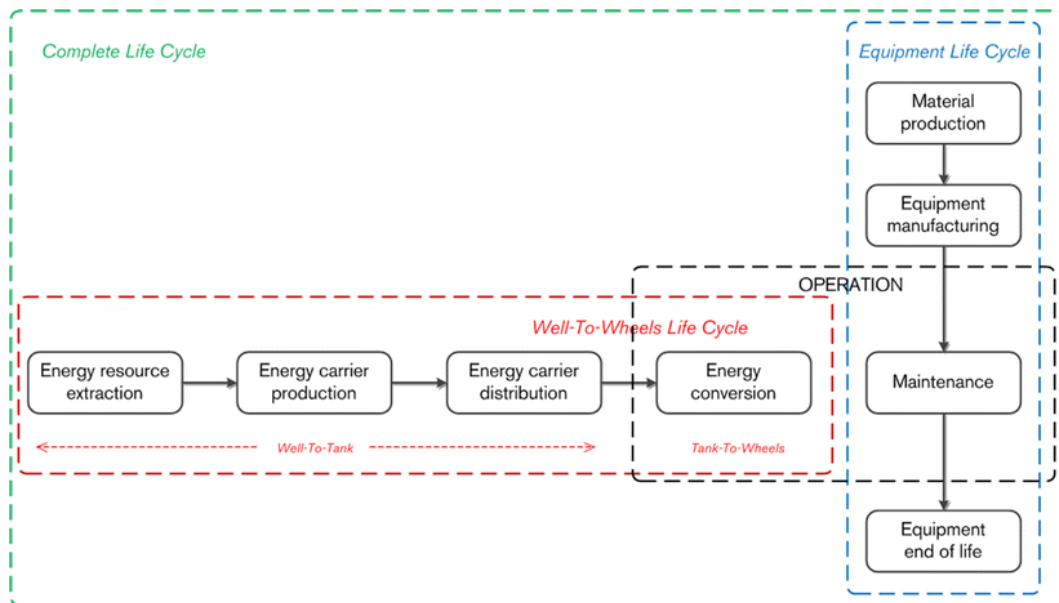


Figure 2.1 - Simplified view of the well-to-wheels and equipment flow by Nordelhöf [5].

An extensive literature is available on BEVs and FCEVs energy balance, with several efficiency comparisons. However, the results are extremely diverse, ranging from BEVs being 1.25 to 3.9 times more energy efficient than FCEVs [8–12]. Car manufacturers have also published their own analysis, but these studies, without peer-reviewing processes are often criticized (VW², Daimler³, Toyota⁴). The main difference originates from the system definition, especially regarding the site of hydrogen production—transport required or not—, the primary energy source and the useful unit considered (energy out of the motor or converted into effective distance driven). In addition, a detailed description of recharging events is often overlooked and the coupling with renewables is not technically addressed.

In previous research, the influence of charging events was mostly considered *via* the charging time or the electricity mix used, and the mode of charging (fast or slow) was anticipated to have an impact on the ageing of batteries but not explicitly on the efficiency [13]. Most of these studies were published prior to 2010, before the momentum towards fast DC charging (the SAE J1772 incorporated DC charging only in its 2012 revision [14]) and the definition and implementation of a standardized hydrogen refueling protocol (the first version of the SAE J2601 was published in 2010 [15]). As a consequence, BEV charging efficiencies are quite accurate when referring to slow charging modes, but inadequate for assessments with fast charging modes. Regarding FCEVs, only a limited energy system analysis of the refilling process has been provided yet with primary data coming from

² <https://www.volkswagen-newsroom.com/en/stories/co2-neutral-id3-just-like-that-5523>

³ <https://www.daimler.com/documents/sustainability/product/daimler-environmental-check-mb-egc-class-org.pdf>

⁴ http://www.toyota-global.com/sustainability/environment/challenge2/lca-and-eco-actions/pdf/life_cycle_assessment_report.pdf

demonstrators [16–18]. In order to address these gaps, we introduced a new segmentation and adapted the WtW approach to EV specificities.

2.1.1 Grid to mobility segmentation

Extremely diverse layouts can be proposed for EV refilling infrastructures coupled with renewables. For illustrative purposes, the minimal layout is represented in the graph below, assuming a HRS with on-site electrolysis. The scope and boundaries of the study are summarized in **Figure 2.2** below.

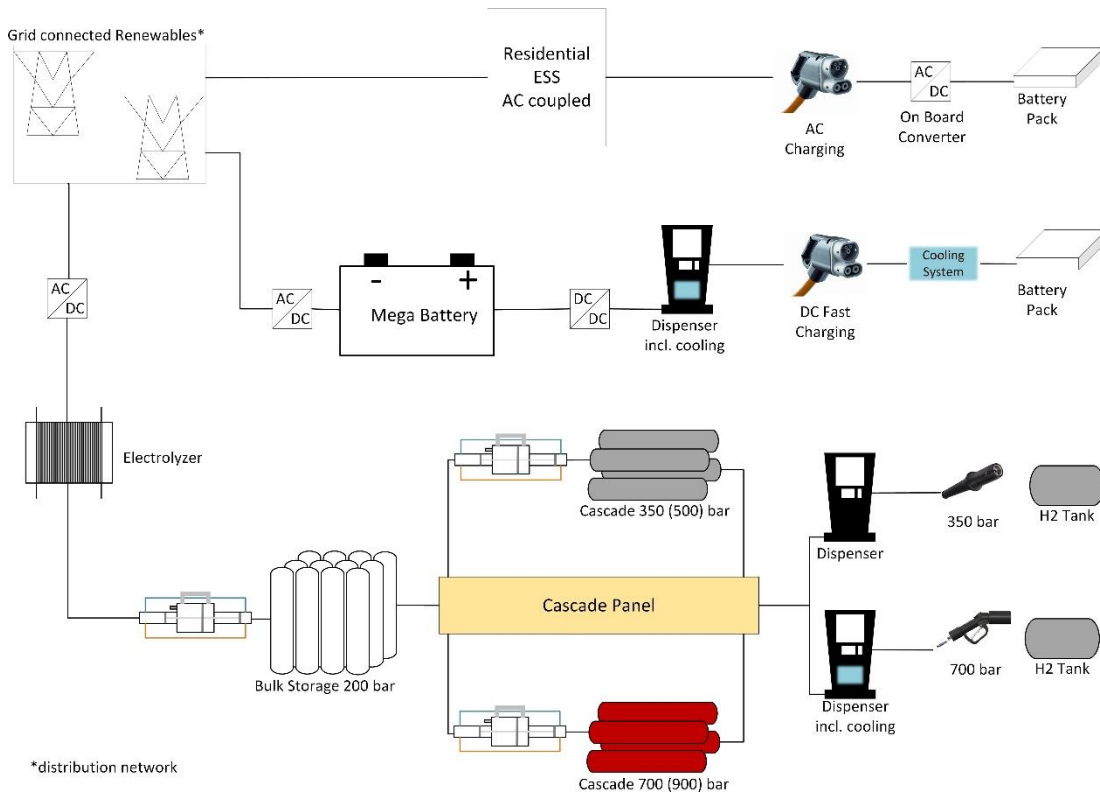


Figure 2.2 – EVs refilling pathways.

Based on the pathways defined in **Figure 2.2**, we can identify a pattern in the conversion of grid electricity to a mobility service for EV drivers.

Grid to useful electricity

Useful electricity is considered as electricity compatible with the main equipment of the refilling infrastructure. Electrochemical devices, either batteries or electrolyzers, operate on DC current, therefore, preliminary AC/DC conversion is usually required, except in the case when a direct DC coupling with solar panels is feasible or if the energy storage system (ESS) includes the converter. For individuals, several manufacturers offer small power packs or residential ESS in the range of 5 to 30 kWh. These systems can be used to store the energy produced with solar panels on the roof to ensure energy autonomy of the household during power cuts or to accommodate time-of-use or demand charge rate schemes. For station operators, buffer batteries offer additional benefits such as lowering the power connection requirements and relaxing the constraints on the grid [19]. The specific role of buffer batteries is detailed in Chapter 3 [19].

Useful electricity to energy carrier

Two different energy carriers are commercially investigated for EVs: electricity stored in batteries or hydrogen. We define the energy carrier as the energy stored in large quantities at the station, for grid independent refueling, at any point in time. It covers the use of megabatteries (MW/MWh), and the operation of electrolyzers and first compression steps for the bulk storage of hydrogen.

Energy carrier to onboard storage

Refilling and recharging events were often neglected for ICEVs due to the extremely simple equipments required and their insignificant energy consumption. However, for EVs, this step can be particularly challenging. For example, both BEVs and FCEVs require thermal management systems. For ICEV and FCEV the energy carrier is physically transferred to the vehicle (with pumps and pressure differential), while for BEV redox species are created during the charge, at the expense of some energy.

On-board storage to mobility

After all the conversions occurring prior to and during charging events, the energy transferred is ultimately converted into a mobility service for the driver. The energy stored on-board is converted into “km driven”, which are assessed on standardized driving cycles such as those conducted by the US Environmental Protection Agency (EPA).

In order to cover all the losses in the grid to mobility pathways, we listed all the equipments and processes involved (see **Table 2.1**). Efficiency estimates are based on literature and published data for commercially available products.

Table 2.1 – Grid to mobility segmentation.

Step	Charging mode		
	BEVs Slow (AC)	BEVs Fast (DC)	FCEVs 35MPa and 70MPa
Grid to useful electricity	No conversion required	AC/DC conversion	AC/DC conversion
Useful electricity to energy carrier	Storage in stationary battery AC coupled	Storage in stationary battery DC coupled	Variable load electrolysis Purification 20 MPa compression
Energy carrier to on-board storage	On-board AC/DC conversion	Dispenser DC/DC conversion Battery Thermal Management	50 MPa cascade compression 90 MPa cascade compression -40°C precooling Dispenser Vent
On-board storage to mobility	EPA combined cycle	EPA combined cycle	EPA combined cycle

2.1.2 BEV charging

We consider AC and DC charging modes in order to evaluate the conversion of kWh of intermittent electricity to km driven with a BEV. Without constraints and incentives to adapt charging schedules, production and consumption cannot match and require therefore the introduction of storage systems.

Stationary storage

For domestic installations, renewable electricity can be locally produced with solar panels. Even if the current produced is already in a DC form, residential ESS are usually AC coupled, requiring the use of inverters. Roundtrip AC efficiencies reported by various manufacturers of lithium-ion residential ESS are comprised between 89% and 92% [20,21]. For commercial installations, batteries in the MWh range are required. Several technologies are available, and we can mention, for example, flow batteries (*e.g.* all Vanadium or Zinc Bromine), lithium-ion, lithium polymer and lithium titanate. Introducing megabatteries in stations with multiple fast chargers has several benefits such as peak shaving, load leveling and buffering as well as relaxing the constraints for grid connection [19,22–24]. A real implementation of a DC fast charging station coupled with a battery storage system was performed by Sbordone et al. [25] with a peak shaving strategy. The system efficiency is highly depending on the chemistry of the battery with reported efficiencies ranging from 65 to 90% [26].

Dispenser and charging events

Losses are also reported during charging events due to power electronics and heat management. AC charging mode involves the use of the charger onboard the vehicle, which is basically an AC/DC converter. The Idaho National Laboratory (INL) performed test bench measurements with various BEVs and reported charging efficiencies in the range of 85 to 92% [27]. The INL also investigated fast DC charges and especially the consumption of the battery management system (BMS). The energy used during fast charge events for the cooling was found to be in the range of 3 to 5% (and up to 10% in hot weather conditions) of the total energy transferred to the battery [27]. These energy expenses are expected to increase with fast charging capabilities, especially above 150 kW, when a cooling system for the charging cord will also be required. Finally, efficiencies reported by fast charger manufacturers are usually accounting for the AC/DC conversion so a typical value of 98% for a DC/DC conversion is used.

Vehicle efficiency

According to EPA measurements, consumption of BEVs varies in the range of 15 to 29 kWh/100km (Hyundai Ioniq to BYD e6) [28]. Similar number are measured for recent cars, with for example 27.2 kWh/100 km for the Audi etron 2019 and 15.4 kWh/100 km for the Tesla Model 3 Long Range.

2.1.3 FCEV refueling

Unlike BEV infrastructures, FCEV infrastructures integrate by construction a storage capacity and some flexibility in the energy carrier production. No simultaneity is required between hydrogen production and hydrogen delivery.

Electrolysis

Commercially available proton exchange membrane (PEM) or alkaline electrolyzers can achieve a system consumption in the range of 4.0 - 5.0 kWh/Nm³ [4,29,30]. Slightly higher values are reported by NOW GmbH and Schmidt [31,32]: in the range of 4.5 - 7.0 kWh/Nm³ expected to go down to 4.3 - 5.7 kWh/Nm³ or 4.1–4.8 kWh/Nm³ within 10–20 years for respectively alkaline and PEM electrolyzers. If electrolysis cannot be performed on site, an additional penalty for transportation in tube trailer would be around 0.6 kWh/kg H₂ transported [33]. A more detailed investigation of electrolysis is available in Chapter 5.

Compression

Empirical compression energy measured varies from 2.7 to 4.2 kWh/kg H₂ [34] for 90 MPa. At the station from the University of California - Irvine (UCI) [17], a consumption of 2.68 kWh/kg H₂ was achieved, and 70 MPa refills exhibited only 11% more compression energy consumption than the 35 MPa refills. At the Empa Move demonstrator, up to 5 kWh/kg was reported for a compression from

0.5 MPa to 44 MPa, but they also confirm industrial scale performance of 2.7 kWh/kg [18]. In order to make the distinction between the compression required for the supply storage (energy carrier stage) and the one required for the refilling (energy carrier to onboard storage) the following conversion efficiencies values were adopted:

- 95% for 20 MPa (nominal pressure of supply storage systems) starting from the outlet pressure of the electrolyser, corresponding to 1.8 kWh/kg H₂.
- 98% and 97% for respectively 35 MPa and 70 MPa refills, corresponding in total to 2.5 kWh/kg H₂ (93%) and 2.8 kWh/kg H₂ (92%) in line with the 11% difference reported by UCI [17] and with the numbers published by Stolten [33].

Efficiency improvements for the compression work are limited by cascade design and thermodynamics: a perfect isothermal compression at 70 MPa would require 2.1 kWh/kg H₂.

Precooling and refilling event

Precooling is one of the critical processes to allow a fast refilling of FCEVs at 70 MPa. High-pressure hydrogen needs to go through a heat exchanger before being transferred to the car *via* the filling nozzle. The cooling block is usually maintained at -40°C in order to keep the station ready at any point of time. As a consequence, the energy requirement for cooling reported per kilogram of hydrogen delivered, ranges from above 20 kWh/kg H₂ (HRS with low frequentation in Germany [35]) to only 1.4 kWh/kg H₂ (HRS with attached fleet [17]). Elgowainy and Reddi [36] estimated that for high HRS capacity utilization, the electricity consumption for H₂ precooling can be even lower than 1 kWh/kg H₂. Based on the measurements performed at the Move demonstrator, Stadelmann reported a cooling energy of 0.5 kWh/kg H₂ in addition to a daily consumption of up to 30 kWh to maintain the cooling block cold [37]. Additionally, another process causes losses during the refilling: the remaining hydrogen in the hose has to be vented in order to release the coupling. Considering a hose of 6 meters under 70 MPa [38], approximately 7g of hydrogen is vented after each refill⁵. This quantity is negligible.

Vehicle efficiency

Similarly, as for BEV, the U.S. EPA also measured efficiencies of the conversion from onboard storage to mobility for FCEVs. The measured figures vary from 0.92 to 1.26 kg H₂/100 km [28], however, the set of commercially available vehicles is still limited.

⁵ We assumed a 6 m hose, with a nominal bore of 3 mm, and 3 m of a 9/16 pipe (7.93 mm inner diameter) before the hose, thus a volume of $1.9 \cdot 10^{-4}$ m³ at 70 MPa.

2.1.4 Results and discussion

The mobility service achievable with 100 kWh of intermittent electricity and the corresponding losses along the grid to mobility pathway is presented in **Figure 2.3**. In order to observe the final conversion into mobility service on the same scale, an arbitrary scaling factor is fixed in order to highlight a typical 46% efficiency of the fuel cell drive train [12].

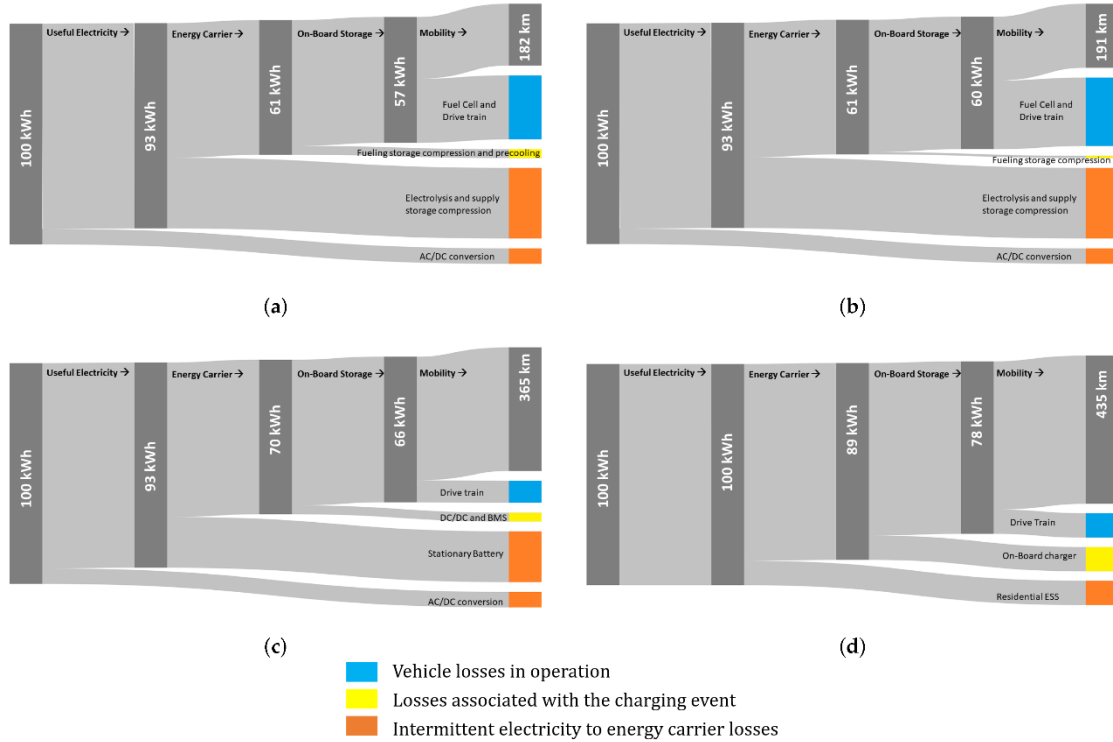


Figure 2.3 – Grid to mobility conversion efficiencies for (a) 70 MPa H2, (b) 35 MPa H2, (c) 50 kW fast charger coupled to a stationary battery, (d) home charger coupled with a residential ESS.

For all modes, most of the infrastructure losses occurs during the conversion from useful electricity to energy carrier. Refilling events (energy carrier to onboard storage) have a minor contribution in the overall efficiency except for home charging. Finally, considering the grid to onboard storage conversion, the fast charging infrastructure for BEVs is only 15% more effective than HRS. The vehicle side conversion is the discriminating criterion. That's why hybrid FCEV concepts with optimized battery size and fuel cell power can offer significant advantages [39]. Interestingly, increasing the delivery pressure from 35 MPa to 70 MPa only costs 5% more energy. The large difference observed between the two BEV modes is mainly due to the fact that a less efficient technology was selected for the megabattery (75%) compared to the residential ESS (89%), to depict likely investment decision of station operators and numbers reported in subsection 2.1.2. The impact of these values is investigated in the sensitivity analysis. For comparison, we can note that

introducing 57 kWh of energy (FCEV 70 MPa case) in the form of gasoline in an ICEV will offer only 100 km of driving range. As an introductory remark for ICE, I mentioned that 630 g of CO₂ emissions should be added to the 2.32 kg of CO₂ resulting from the combustion [7]. In other terms it means that adding Well-to-Tank emissions, corresponds to a 30% mark-up on the Tank-to-Wheel emissions. For BEVs, depending on the charging mode, we are close to this order of magnitude (Grid to On-board storage), but for FCEV it is almost a 70% mark-up based on the energy stored on-board.

As highlighted in subsections 2.1.2 and 2.1.3, some of the major components of EV charging infrastructures exhibit extremely diverse efficiencies. The high uncertainty in the environmental footprint of electric vehicles is a recognized issue [40], and requires additional investigations. To illustrate how some single components of the grid to mobility conversion chain affect the final results, a sensitivity analysis was performed. The results are presented in **Figure 2.4**. Lab and pilot scale installations may report numbers outside of the mentioned ranges, but the general trend is shown in this tornado chart.

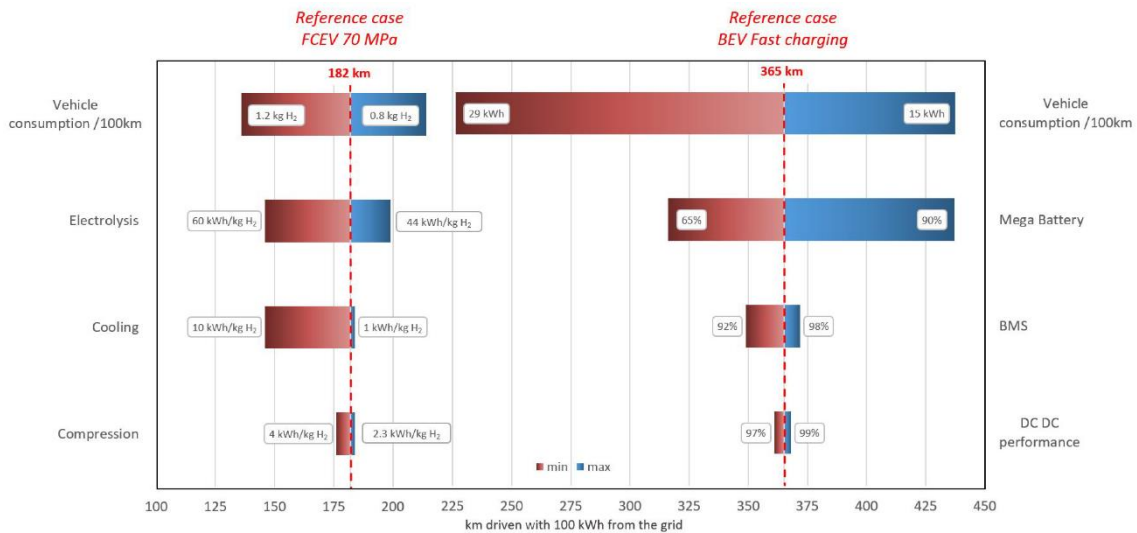


Figure 2.4 – Sensitivity analysis.

The graph presented in **Figure 2.4** is also a way to estimate how future technologies' developments will affect the BEV *versus* FCEV competition. Indeed, the FCEV market and technologies are in an earlier stage of development than BEV and larger efficiency gains, especially on the vehicle side, are expected. On the other hand, the BEV market is going toward longer range and larger vehicles. Thus, we can expect some increase in their energy consumption per kilometer. With BEVs and FCEVs covering more segments of the passenger vehicle market in the future, a more specific comparison could be made. Regarding infrastructure, the efficiency of the electrochemical device used to produce or store the energy carrier is clearly the discriminating parameter. In a sector coupling perspective, the flexibility of this device should also be considered. Finally, limited gains can be made on hydrogen compression, as optimized pressure cascades have a greater impact on economics than on energy

efficiency [41]. Additionally, the energy consumption associated with hydrogen precooling is mostly related to the utilization ratio of the station and not related to technological developments [42]. The expected development of 350 kW ultrafast DC chargers after 2020 will be accompanied with larger losses from the BMS and the cooling of the charging cord should be added in the overall DC/DC efficiency. Even if the performance specifications of ultra-fast chargers are not yet publicly available, the overall picture will remain similar, according to the relative importance of BMS and DC/DC.

Additional considerations such as waste heat utilization and winter effect can heavily affect the energy consumption of BEVs [43] and cannot be observed with traditional TtW approaches. Simulation results performed by Li *et al.* [12] show that with the heating system activated, the onboard storage to mobility efficiency of BEVs goes down from 73% to 45%, as compared with the 46% down to 39% for FCEVs.

2.2 E-Mobility and renewables

For centuries, societies have been powered from renewable energy sources (mainly wood and biomass). The successive industrial revolutions during the 19th and 20th century have dramatically changed the composition of our energy mix with large shares of coal, oil and gas as energy sources for heat, electricity and transport sectors [44]. Wind turbines and solar photovoltaic are often referred as new renewable energies, or Intermittent Renewable Energy Sources (IRES). The low carbon intensity of these IRES make them appealing sources to power an electrified transport sector. The IPCC reviewed 2165 references on LCAs of electricity generation technologies [45]. The results reported in **Table 2.2** clearly highlight IRES as low carbon alternatives to natural gas and coal (the 50th percentile is highlighted: 50% of the studies report values below this number).

Table 2.2 – GHG emissions from electricity generation technologies in g CO₂ eq/kWh.

	Solar PV	Hydropower	Wind Energy	Nuclear	Natural Gas	Coal
25th percentile	29	3	8	8	422	877
50th percentile	46	4	12	16	469	1001
75th percentile	80	7	20	45	548	1130

The carbon intensity of the grid is the sum of all electricity generation technologies emissions weighted by their corresponding share in the mix. Several studies have reported hourly variations of this carbon intensity [46,47]. In addition to the seasonal effects, it means that slow charging during

office hours or during night time will not result in the same CO₂ emissions. Similarly, the carbon intensity of hydrogen mobility is sensitive to the source of electricity for electrolysis and compression [48] and ultimately to the operating hours. One can note that the current low carbon certificate for hydrogen (www.certifhy.com) specifies a limit of 36.4 g CO₂eq/MJ, which, in the case of electrolytic production, corresponds to an electricity supply below 80 g CO₂eq/kWh. CO₂ emissions based on an average mix composition [49] may overlook time based variations and the influence of imports/exports. For example, in 2014, in Switzerland the producer mix was estimated at 29.8 g CO₂eq/kWh but the consumer mix was at 181.5 g CO₂eq/kWh [50]. Energy buffers introduced in section 2.1 allowed us to partially bypass this consideration. In this section, we will analyse IRES production profiles and their suitability to power, alone, BEV and FCEV infrastructure.

2.2.1 Production profiles of intermittent renewable energies

Because IRES profiles are closely related to geographical parameters (see World Bank maps in **Figure 2.5**) we focused here on primary data collected in Martigny, VS (location N 46°06'53.6" E 7°05'03.2"). The data was collected with a one-minute resolution from January 1st 2016 to December 31st 2016 with a weather station Davis Vantage Pro 2.

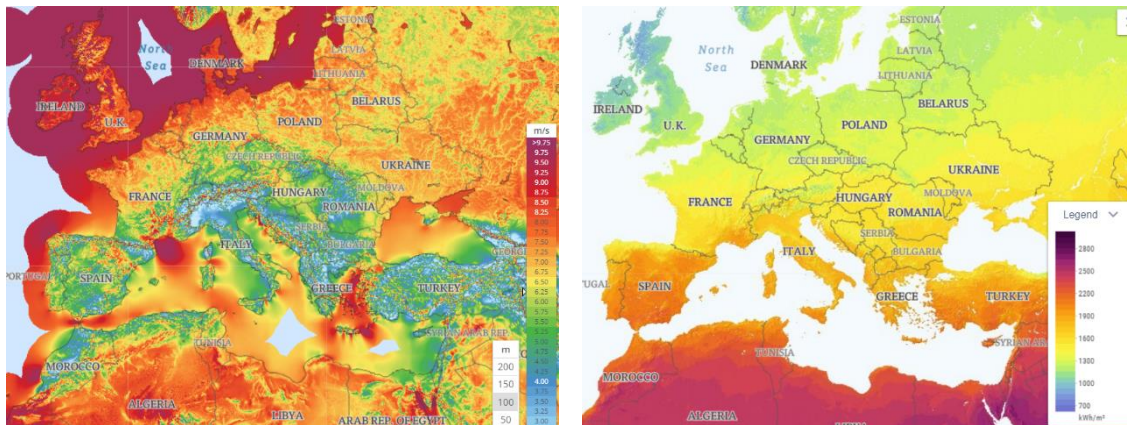


Figure 2.5 – LEFT: Wind atlas (mean wind speed), www.globalwindatlas.info, RIGHT: Solar atlas (tilted irradiation at optimum angle), www.globalsolaratlas.info.

In order to visualize the seasonal variations and to preserve the intrinsic characteristics of the collected data, a medoid clustering methodology was applied [51]. The 52 weeks of the year 2016 are allocated to 3 clusters. Each cluster is centered on a specific week, which minimizes the distance between the weeks in this cluster. By doing this, we avoid an arbitrary selection of one specific week or the use of fictive average weeks. The `kmedoids` function in MATLAB was used with a 52 column matrix as input. Each column contains weather data for one week with a one-minute time step.

The results for solar irradiation are presented in **Figure 2.6** and wind data are reported in **Figure 2.7**. The conversion from solar irradiation to the electric energy produced involves only a multiplication factor. For the rest of the analysis an average module efficiency of 20% was used [52]. The conversion from wind speed to energy harvested involves the turbine power profile function. Based on primary data from a 2 MW wind turbine along the Rhone river, we derived the turbine power profile presented in **Figure 2.8**.

No clear pattern appears from the wind data, except two month of low wind weeks in December and January. For solar, the clustering approach properly reflects the seasonal variations, and the stochastic effects of clouds are still preserved in the exemplary weeks. Considering charging stations, a direct coupling to one or several 2 MW size wind turbine (hub height above 80m) is, due to space constraints, not the most likely scenario. Regarding solar panels, an analysis of 28 gas stations in Switzerland (on the A1 and A9 highway) has shown that, in average, 565 m² are available on the roofs or canopy for solar panels (median 545 m² and standard deviation of 170 m²).

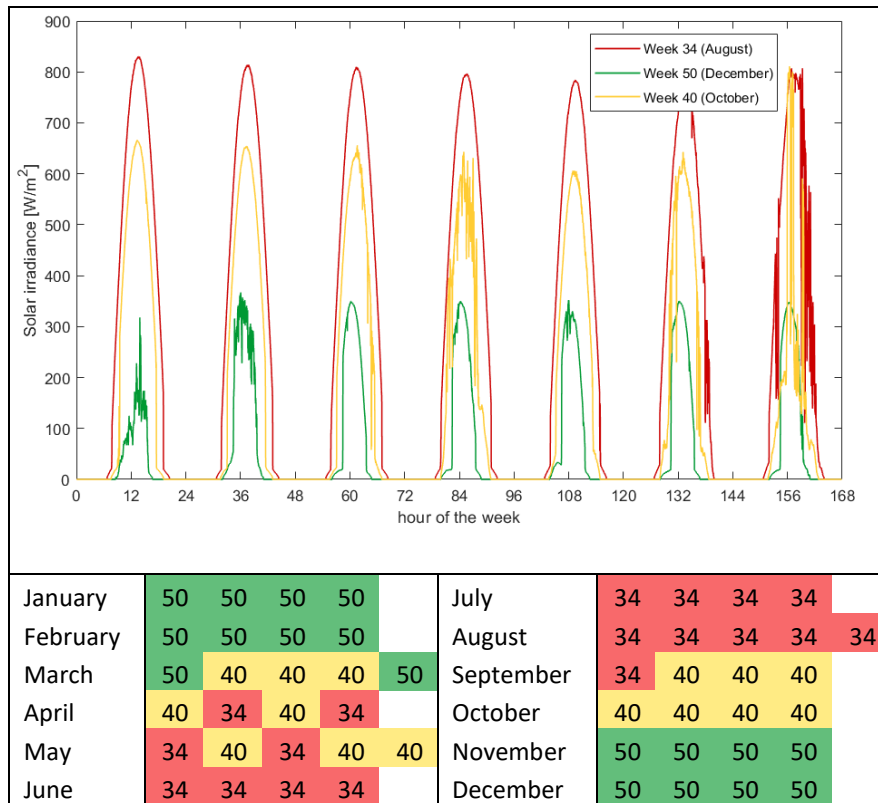


Figure 2.6 – Weekly solar irradiation profiles and clustering. Values per medoid:

Week 50 irradiation: 9.5 kWh/m²
 Week 40 irradiation: 25.7 kWh/m²
 Week 34 irradiation: 43.2 kWh/m²

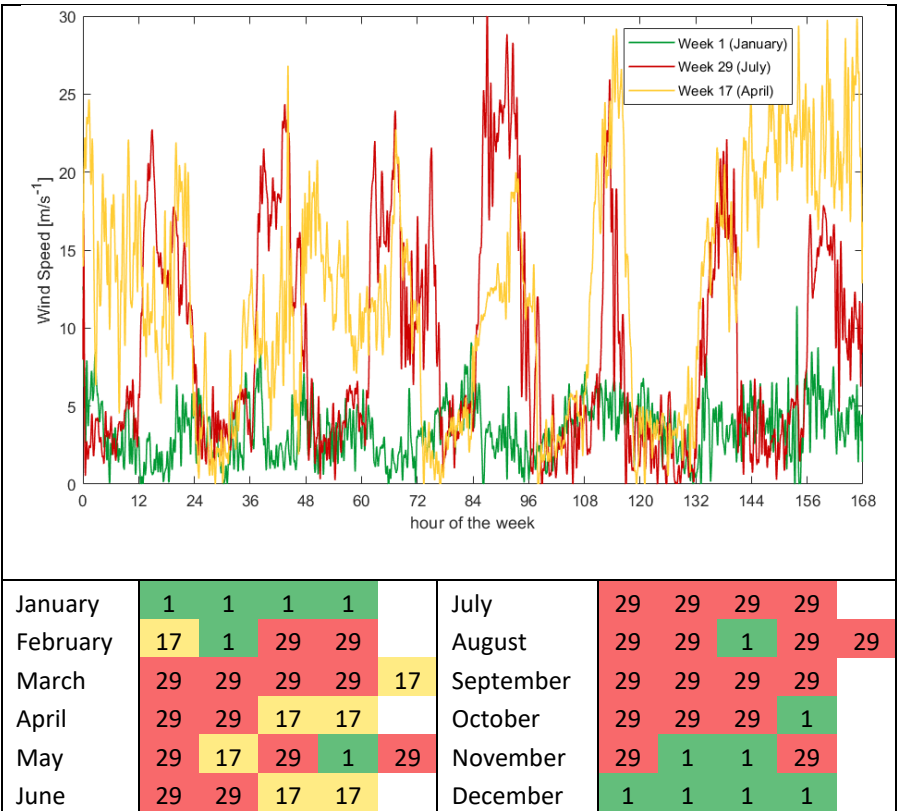


Figure 2.7 – Weekly wind speed profiles and clustering.

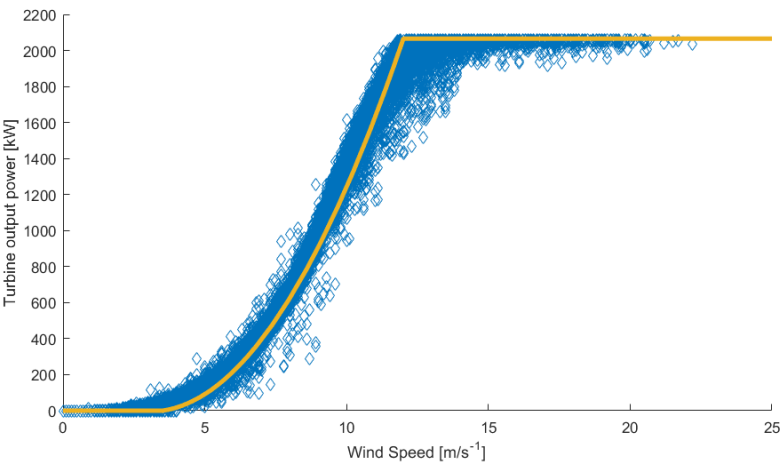


Figure 2.8 – Wind turbine output in MW as a function of windspeed (quadratic function of the windspeed between 3.5 and 12 m/s^{-1}).

2.2.2 Energy demand from charging stations

The annual energy demand for a BEV charging at home (12 000 km⁶ per year per vehicle [53]) is equal to 2.7 MWh. This is roughly equivalent to the annual output of 12 m² of solar panels⁷, which corresponds also to the size of a parking spot. The charging station problem is slightly different. Based on the total annual distance travelled by passenger vehicles in Switzerland and on the number of refilling stations [54], it was determined that each station delivers, each day, in average, the fuel equivalent of 36 000 km of driving range. According to the results from previous section (see **Figure 2.3**), it corresponds to 9.9 MWh consumed by fast chargers or 8.3 MWh with slow chargers. The corresponding solar panel surface required to produce this energy, largely exceeds the available surface at the station as shown in **Figure 2.9** (the station load profile is detailed in Chapter 3). The available surface only covers 10% of the station needs with the summer type profile. With the representative winter week, this value drops to 2%. A 100% self sufficiency requires 5800 m² (football field surface) of solar panels for the summer medoid only and is unrealistic for the winter medoid. This surface represents the active surface area with an ideal orientation. In Switzerland, considering 325 Wp modules (ca. 1 m x 1.65 m), about 10 000 m² are required to install 0.78 MWp of solar panels with a south facing orientation. Thus the required spacing between modules, to prevent shading and allow access for maintenance, reduces the effective density to only 0.08 kWp/m² instead of 0.2 kWp/m² when the module alone is considered. East-West layouts can offer a better coverage or land efficiency (>0.15 kWp/m²), but the yield in kWh/kWp installed is lower [55].

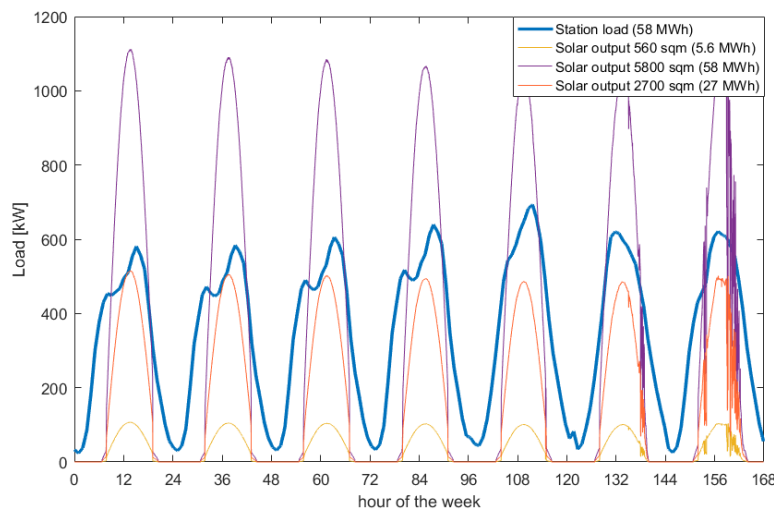


Figure 2.9 – Charging station demand compared to solar output for week 34.

⁶ Due to the lack of more recent data, we assumed arbitrarily a 10% decrease compared to the 2002 value (13 273 km for a gasoline car)

⁷ https://re.jrc.ec.europa.eu/pvg_tools/en/tools.html#PVP, assuming 0.2 kWp/m² (Jinko solar 325 Wp modules : 1 m x 1.65 m)

The performance of PV-Battery systems are often analysed with the self-consumption and self-sufficiency metrics, as defined below [56]:

$$\text{Self consumption} = 1 - \frac{\text{Exports to Grid}}{\text{Total solar Production}}; \quad \text{Self sufficiency} = 1 - \frac{\text{Imports from Grid}}{\text{Total Consumption}}$$

We defined the solar surplus as follows:

$$\text{Solar surplus} = \text{PV production} - \text{Station consumption}$$

Based on this definition, assuming 5800 m² of solar panels, the solar surplus evolution was represented for the week 34 (**Figure 2.10 LEFT**) and a battery operation algorithm was runned for different battery sizes (**Figure 2.10 RIGHT**). We can already observe that we have a negative solar surplus in early morning and late evening. However, because the station load also has a day/night pattern, there is an overall good match. The results of PV-Battery systems are presented in **Figure 2.11**.

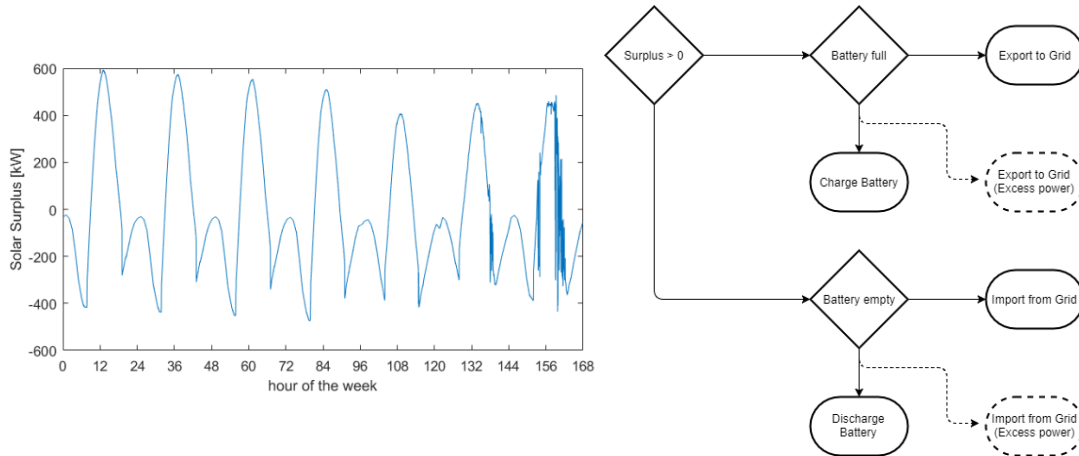


Figure 2.10 – LEFT: Solar surplus distribution over one week. RIGHT: flowchart algorithm for buffer battery operation.

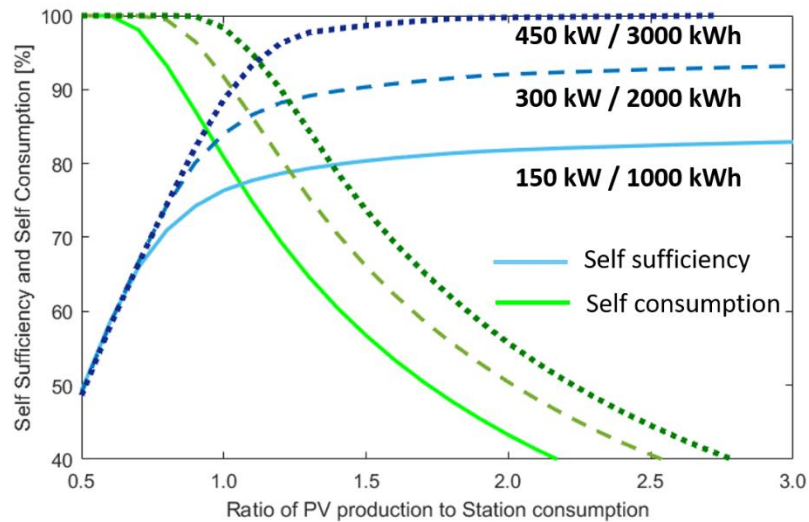


Figure 2.11 – Role of buffer batteries and oversizing solar capacity on the self sufficiency and self consumption metrics.

In order to achieve more than 80% self-sufficiency (in summer time), the PV system should be oversized by a factor 1.5 and a 1 MWh energy storage is required. With this storage system we have only a 60% self consumption, which means that 40% of the energy is either curtailed (off-grid) or reinjected to the grid. A 100% self sufficiency cannot be obtained with a one-to-one ratio between PV production and station consumption due to the charge and discharge efficiency of the storage (values set at 85 %) and improving the self-sufficiency can only be made at the expense of a lower self-consumption. With a 3 MWh battery, and a 1.2 oversize ratio the 94 % mark is reached for both metrics.

2.3 Conclusion

The development of electric mobility is often understood as the development of green mobility. However, the link between renewable electricity and mobility, although well defined in theory, is not always converted into effective measures to guarantee this connection. Moreover, green certificates for electricity contribute to this biased perception. Based on this situation, the scaling of renewable electricity production needs is underestimated and the benefits of hydrogen mobility is blurred. In order to benchmark and compare EV infrastructures coupled with renewables, a grid to mobility approach was introduced. A comprehensive data collection for all components and processes occurring prior and during charging events was performed to ascertain as much realistic efficiencies as possible. First of all, it should be noted that the charging infrastructure is a major contributor to the overall energy efficiency of electric mobility. The exemplary cases presented in this study show that only 57% to 78% of the energy from the grid is effectively transferred to the vehicle.

Additionally, under the assumptions used in this work, it could be shown that up to 15% less energy is transferred to BEVs using fast DC chargers compared to domestic AC chargers. For FCEVs, the penalty linked to the production of the energy carrier is partially compensated by the fact that no stationary battery storage system is required. However, the final conversion occurs onboard the vehicle, within the fuel cell, which caps the overall efficiency of FCEV mobility to about half of the BEV. Cost considerations regarding the infrastructure of electric mobility [57] can bring an additional perspective to this analysis based only on efficiency. Finally, the role of the grid is essential for an infrastructure at scale [58,59]. The effective coupling with intermittent renewable electricity sources faces significant footprint constraints and seasonal limitations. The grid remains an essential aspect for sector coupling while off-grid autonomous (100% self-sufficiency and 100% self-consumption) BEV and FCEV infrastructure appears, with current systems, not appropriate. Other low carbon electricity sources such as hydropower or waste incineration plants with carbon capture should also play a role to electrify the transport sector. The benefits of small buffer batteries for grid integration, in contrast to off-grid buffers, are analysed in the next chapter.

References

- [1] R. Frischknecht, C. Bauer, A. Froemelt, S. Hellweg, K. Biemann, T. Buetler, B. Cox, P. de Haan, S. Hoerl, R. Itten, N. Jungbluth, Y. Ligen, N.A. Mathys, S. Schiess, S. Schori, P. van Loon, J. Wang, S. Wettstein, LCA of mobility solutions: approaches and findings—66th LCA forum, Swiss Federal Institute of Technology, Zurich, 30 August, 2017, *The International Journal of Life Cycle Assessment*. 23 (2018) 381–386. <https://doi.org/10.1007/s11367-017-1429-1>.
- [2] Y. Ligen, H. Vrubel, H. Girault, Mobility from Renewable Electricity: Infrastructure Comparison for Battery and Hydrogen Fuel Cell Vehicles, *World Electric Vehicle Journal*. 9 (2018) 3. <https://doi.org/10.3390/wevj9010003>.
- [3] Eurostat, Electricity generation - CO2 emission intensity, (2018). [https://www.eea.europa.eu/data-and-maps/daviz/co2-emission-intensity-5#tab-googlechartid_chart_11_filters=%7B%22rowFilters%22%3A%7B%7D%3B%22columnFilters%22%3A%7B%22pre_config_ugeo%22%3A%5B%22European%20Union%20\(current%20composition\)%22%5D%7D%7D](https://www.eea.europa.eu/data-and-maps/daviz/co2-emission-intensity-5#tab-googlechartid_chart_11_filters=%7B%22rowFilters%22%3A%7B%7D%3B%22columnFilters%22%3A%7B%22pre_config_ugeo%22%3A%5B%22European%20Union%20(current%20composition)%22%5D%7D%7D) (accessed March 19, 2020).
- [4] R. Edwards, J.-F. Larive, D. Rickeard, W. Weindorf, WELL-TO-TANK Report version 4.a: JEC WELL-TO-WHEELS ANALYSIS, Publications Office of the European Union, 2014. <http://publications.jrc.ec.europa.eu/repository/handle/111111111/31790> (accessed February 1, 2017).
- [5] A. Nordelöf, M. Messagie, A.-M. Tillman, M. Ljunggren Söderman, J. Van Mierlo, Environmental impacts of hybrid, plug-in hybrid, and battery electric vehicles—what can we learn from life cycle assessment?, *The International Journal of Life Cycle Assessment*. 19 (2014) 1866–1890. <https://doi.org/10.1007/s11367-014-0788-0>.
- [6] L. Guzzella, A. Sciarretta, *Vehicle Propulsion Systems*, Springer Berlin Heidelberg, Berlin, Heidelberg, 2013. <https://doi.org/10.1007/978-3-642-35913-2>.
- [7] V. Gordillo, N. Rankovic, A.F.N. Abdul-Manan, Customizing CO2 allocation using a new non-iterative method to reflect operational constraints in complex EU refineries, *Int J Life Cycle Assess.* 23 (2018) 1527–1541. <https://doi.org/10.1007/s11367-017-1380-1>.
- [8] U. Bossel, Does a Hydrogen Economy Make Sense?, *Proceedings of the IEEE*. 94 (2006) 1826–1837. <https://doi.org/10.1109/JPROC.2006.883715>.
- [9] J. Van Mierlo, G. Maggetto, Ph. Lataire, Which energy source for road transport in the future? A comparison of battery, hybrid and fuel cell vehicles, *Energy Conversion and Management*. 47 (2006) 2748–2760. <https://doi.org/10.1016/j.enconman.2006.02.004>.
- [10] S. Campanari, G. Manzolini, F. Garcia de la Iglesia, Energy analysis of electric vehicles using batteries or fuel cells through well-to-wheel driving cycle simulations, *Journal of Power Sources*. 186 (2009) 464–477. <https://doi.org/10.1016/j.jpowsour.2008.09.115>.

- [11] C.E. Thomas, Fuel cell and battery electric vehicles compared, *International Journal of Hydrogen Energy*. 34 (2009) 6005–6020. <https://doi.org/10.1016/j.ijhydene.2009.06.003>.
- [12] M. Li, X. Zhang, G. Li, A comparative assessment of battery and fuel cell electric vehicles using a well-to-wheel analysis, *Energy*. 94 (2016) 693–704. <https://doi.org/10.1016/j.energy.2015.11.023>.
- [13] J. Van Mierlo, M. Messagie, S. Rangaraju, Comparative environmental assessment of alternative fueled vehicles using a life cycle assessment, *Transportation Research Procedia*. 25 (2017) 3435–3445. <https://doi.org/10.1016/j.trpro.2017.05.244>.
- [14] SAE International, J1772: Electric Vehicle and Plug in Hybrid Electric Vehicle Conductive Charge Coupler, (2016). http://standards.sae.org/j1772_201210/ (accessed February 14, 2017).
- [15] SAE International, J2601: Fueling Protocols for Light Duty Gaseous Hydrogen Surface Vehicles, 2016. http://standards.sae.org/j2601_201407/ (accessed February 14, 2017).
- [16] J. Burkhardt, A. Patyk, P. Tanguy, C. Retzke, Hydrogen mobility from wind energy – A life cycle assessment focusing on the fuel supply, *Applied Energy*. 181 (2016) 54–64. <https://doi.org/10.1016/j.apenergy.2016.07.104>.
- [17] T. Brown, S. Stephens-Romero, G. Scott Samuelsen, Quantitative analysis of a successful public hydrogen station, *International Journal of Hydrogen Energy*. 37 (2012) 12731–12740. <https://doi.org/10.1016/j.ijhydene.2012.06.008>.
- [18] C. Bach, M. Brügger, U. Cabalzar, Move, Future Mobility Demonstrator, EMPA, 2017. https://www.empa.ch/documents/146793/239433/Schlussbericht+move_Phase1.pdf/263a5ab0-19e1-4a56-82b6-90d987280d14 (accessed March 18, 2020).
- [19] Y. Ligen, H. Vrubel, H. Girault, Local Energy Storage and Stochastic Modeling for Ultrafast Charging Stations, *Energies*. 12 (2019) 1986. <https://doi.org/10.3390/en12101986>.
- [20] Tesla, Tesla Powerwall 2 - Datasheet, (n.d.). https://www.tesla.com/sites/default/files/pdfs/powerwall/Powerwall%20AC_Datasheet_en_northamerica.pdf (accessed March 18, 2020).
- [21] LG, LG Energy storage ESS Home Datasheet, (n.d.). https://www.lg.com/us/business/download/resources/BT00002151/180830_LG_ESS_Datasheet.pdf (accessed March 18, 2020).
- [22] H. Hõimoja, A. Rufer, G. Dziechciaruk, A. Vezzini, An ultrafast EV charging station demonstrator, in: *Power Electronics, Electrical Drives, Automation and Motion (SPEEDAM)*, 2012 International Symposium On, IEEE, 2012: pp. 1390–1395. <http://ieeexplore.ieee.org/abstract/document/6264617/> (accessed January 31, 2017).
- [23] M. Tsirinomeny, H. Hõimoja, A. Rufer, G. Dziechciaruk, A. Vezzini, Optimizing EV driving-recharge time ratio a under limited grid connection, in: *Power Electronics, Machines and Drives (PEMD 2014)*, 7th IET International Conference On, IET, 2014: pp. 1–6. <http://ieeexplore.ieee.org/abstract/document/6836989/> (accessed January 31, 2017).

- [24] H. Hõimoja, M. Vasiladiotis, A. Rufer, Power interfaces and storage selection for an ultrafast EV charging station, in: *Power Electronics, Machines and Drives (PEMD 2012)*, 6th IET International Conference On, IET, 2012: pp. 1–6. <http://ieeexplore.ieee.org/abstract/document/6242161/> (accessed February 14, 2017).
- [25] D. Sbordone, I. Bertini, B. Di Pietra, M.C. Falvo, A. Genovese, L. Martirano, EV fast charging stations and energy storage technologies: A real implementation in the smart micro grid paradigm, *Electric Power Systems Research*. 120 (2015) 96–108. <https://doi.org/10.1016/j.epsr.2014.07.033>.
- [26] IRENA, Electricity storage and renewables: Costs and markets to 2030, International Renewable Energy Agency, Abu Dhabi, 2017. https://www.irena.org/-/media/Files/IRENA/Agency/Publication/2017/Oct/IRENA_Electricity_Storage_Costs_2017.pdf (accessed March 18, 2020).
- [27] Idaho National Laboratory, Vehicle Testing - Light Duty - Electric | Advanced Vehicle Testing Activity, (n.d.). <https://avt.inl.gov/fuel-type/electric> (accessed February 2, 2017).
- [28] U.S. Environmental Protection Agency, Fuel Economy of Vehicles, (n.d.). <http://www.fueleconomy.gov/feg/> (accessed February 2, 2017).
- [29] K. Ayers, N. Danilovic, R. Ouimet, M. Carmo, B. Pivovar, M. Bornstein, Perspectives on Low-Temperature Electrolysis and Potential for Renewable Hydrogen at Scale, *Annu. Rev. Chem. Biomol. Eng.* 10 (2019) 219–239. <https://doi.org/10.1146/annurev-chembioeng-060718-030241>.
- [30] D. Stolten, World Hydrogen Energy Conference, eds., *Hydrogen and fuel cells: [fundamentals, technologies and applications ; contributions to the 18th World Hydrogen Energy Conference 2010, Essen]*, 2. Reprint, Wiley-VCH, Weinheim, 2011.
- [31] T. Smolinka, M. Günther, J. Garche, NOW-Studie: Stand und Entwicklungspotenzial der Wasserelektrolyse zur Herstellung von Wasserstoff aus regenerativen Energien, Fraunhofer ISE, 2011. <https://www.now-gmbh.de/content/5-service/4-publikationen/4-nip-wasserstoff-und-brennstoffzellentechnologie/now-studie-wasserelektrolyse-2011.pdf> (accessed February 13, 2017).
- [32] O. Schmidt, A. Gambhir, I. Staffell, A. Hawkes, J. Nelson, S. Few, Future cost and performance of water electrolysis: An expert elicitation study, *International Journal of Hydrogen Energy*. 42 (2017) 30470–30492. <https://doi.org/10.1016/j.ijhydene.2017.10.045>.
- [33] D. Stolten, R.C. Samsun, N. Garland, eds., *Fuel cells: data, facts and figures*, Wiley-VCH Verlag GmbH & Co. KGaA, Weinheim, 2016.
- [34] S. Sprik, J. Kurtz, C. Ainscough, M. Jeffers, G. Saur, M. Peters, Hydrogen Station Data Collection and Analysis, (2016). https://www.hydrogen.energy.gov/pdfs/review16/tv017_sprik_2016_o.pdf (accessed February 3, 2017).

- [35] Clean Energy Partnership, Veröffentlichung der Projektergebnisse - Stand 01/2015, (n.d.). https://cleanenergypartnership.de/fileadmin/Assets/user_upload/Veroeffentlichung_Projekte_rgebnisse-11_4_NKBF98.pdf (accessed February 15, 2017).
- [36] A. Elgowainy, K. Reddi, Hydrogen Fueling Station Pre-cooling Analysis, (2015). https://www.hydrogen.energy.gov/pdfs/review15/pd107_elgowainy_2015_o.pdf (accessed February 15, 2017).
- [37] P. Stadelmann, Efficient Hydrogen Fueling (eHF) - Research in the field of gaseous hydrogen fast filling for passenger cars, Empa, 2019. <https://www.aramis.admin.ch/Texte/?ProjectID=40307> (accessed March 18, 2020).
- [38] WEH GmbH Gas Technology, TK17 H2 70 MPa Datasheet, (n.d.). <http://www.weh.com/attachments/file/download/id/1490/> (accessed February 2, 2017).
- [39] A. Jayakumar, A. Chalmers, T.T. Lie, Review of prospects for adoption of fuel cell electric vehicles in New Zealand, IET Electrical Systems in Transportation. 7 (2017) 259–266. <https://doi.org/10.1049/iet-est.2016.0078>.
- [40] B. Cox, C.L. Mutel, C. Bauer, A. Mendoza Beltran, D.P. van Vuuren, Uncertain Environmental Footprint of Current and Future Battery Electric Vehicles, Environ. Sci. Technol. 52 (2018) 4989–4995. <https://doi.org/10.1021/acs.est.8b00261>.
- [41] K. Reddi, A. Elgowainy, N. Rustagi, E. Gupta, Two-tier pressure consolidation operation method for hydrogen refueling station cost reduction, International Journal of Hydrogen Energy. 43 (2018) 2919–2929. <https://doi.org/10.1016/j.ijhydene.2017.12.125>.
- [42] K. Reddi, A. Elgowainy, N. Rustagi, E. Gupta, Impact of hydrogen refueling configurations and market parameters on the refueling cost of hydrogen, International Journal of Hydrogen Energy. 42 (2017) 21855–21865. <https://doi.org/10.1016/j.ijhydene.2017.05.122>.
- [43] S. Karlsson, The variation of BEV energy use and range depending on climate and driving conditions in Sweden, in: Geneva, Switzerland, 2017.
- [44] C. Zou, Q. Zhao, G. Zhang, B. Xiong, Energy revolution: From a fossil energy era to a new energy era, Natural Gas Industry B. 3 (2016) 1–11. <https://doi.org/10.1016/j.ngib.2016.02.001>.
- [45] W. Moomaw, P. Burgherr, G. Heath, M. Lenzen, J. Nyboer, A. Verbruggen, IPCC Special Report on Renewable Energy Sources and Climate Change Mitigation, Annex II: Methodology, Cambridge University Press, 2011.
- [46] I. Khan, M.W. Jack, J. Stephenson, Analysis of greenhouse gas emissions in electricity systems using time-varying carbon intensity, Journal of Cleaner Production. 184 (2018) 1091–1101. <https://doi.org/10.1016/j.jclepro.2018.02.309>.
- [47] D. Vuarnoz, T. Jusselme, Temporal variations in the primary energy use and greenhouse gas emissions of electricity provided by the Swiss grid, Energy. 161 (2018) 573–582. <https://doi.org/10.1016/j.energy.2018.07.087>.
- [48] X. Liu, K. Reddi, A. Elgowainy, H. Lohse-Busch, M. Wang, N. Rustagi, Comparison of well-to-wheels energy use and emissions of a hydrogen fuel cell electric vehicle relative to a conventional

- gasoline-powered internal combustion engine vehicle, *International Journal of Hydrogen Energy*. 45 (2020) 972–983. <https://doi.org/10.1016/j.ijhydene.2019.10.192>.
- [49] A. Moro, L. Lonza, Electricity carbon intensity in European Member States: Impacts on GHG emissions of electric vehicles, *Transportation Research Part D: Transport and Environment*. 64 (2018) 5–14. <https://doi.org/10.1016/j.trd.2017.07.012>.
- [50] A. Messmer, R. Frischknecht, *Umweltbilanz Strommix Schweiz 2014*, Bundesamtes für Umwelt (BAFU), Uster, 2016. https://www.bafu.admin.ch/dam/bafu/fr/dokumente/klima/fachinfo-daten/Umweltbilanz%20Strommix%20Schweiz%202014%20.pdf.download.pdf/589-Umweltbilanz-Strommix-Schweiz-2014-v3_0.pdf (accessed April 16, 2020).
- [51] F. Domínguez-Muñoz, J.M. Cejudo-López, A. Carrillo-Andrés, M. Gallardo-Salazar, Selection of typical demand days for CHP optimization, *Energy and Buildings*. 43 (2011) 3036–3043. <https://doi.org/10.1016/j.enbuild.2011.07.024>.
- [52] M. Kumar, A. Kumar, Performance assessment and degradation analysis of solar photovoltaic technologies: A review, *Renewable and Sustainable Energy Reviews*. 78 (2017) 554–587. <https://doi.org/10.1016/j.rser.2017.04.083>.
- [53] Office fédéral du développement territorial (ARE), Distances parcourues par les véhicules suisses - Résultats de l'enquête périodique sur les prestations kilométriques, (2002). <https://www.news.admin.ch/newsd/message/attachments/1587.pdf> (accessed March 19, 2020).
- [54] Office Fédéral des routes OFROU, *Trafic et disponibilité des routes nationales - Rapport 2015.pdf*, Département fédéral de l'environnement, des transports, de l'énergie et de la communication DETEC, 2015.
- [55] E. Tröster, J.-D. Schmidt, Evaluating the Impact of PV Module Orientation on Grid Operation, in: *Proceedings of the 2nd Solar Integration Workshop*, Lisbon, 2012: p. 6.
- [56] G. Merei, J. Moshövel, D. Magnor, D.U. Sauer, Optimization of self-consumption and techno-economic analysis of PV-battery systems in commercial applications, *Applied Energy*. 168 (2016) 171–178. <https://doi.org/10.1016/j.apenergy.2016.01.083>.
- [57] M. Robinius, P. Kuckertz, D. Stolten, T. Grube, K. Syranidis, M. Reu\ s, P. Stenzel, J. Lin\ s sen, *Comparative Analysis of Infrastructures: Hydrogen Fueling and Electric Charging of Vehicles*, *Elektrochemische Verfahrenstechnik*, 2018.
- [58] T. Gnann, S. Funke, N. Jakobsson, P. Plötz, F. Sprei, A. Bennehag, Fast charging infrastructure for electric vehicles: Today's situation and future needs, *Transportation Research Part D: Transport and Environment*. 62 (2018) 314–329. <https://doi.org/10.1016/j.trd.2018.03.004>.
- [59] M. Robinius, A. Otto, P. Heuser, L. Welder, K. Syranidis, D. Ryberg, T. Grube, P. Markewitz, R. Peters, D. Stolten, Linking the Power and Transport Sectors—Part 1: The Principle of Sector Coupling, *Energies*. 10 (2017) 956. <https://doi.org/10.3390/en10070956>.

Chapter 3

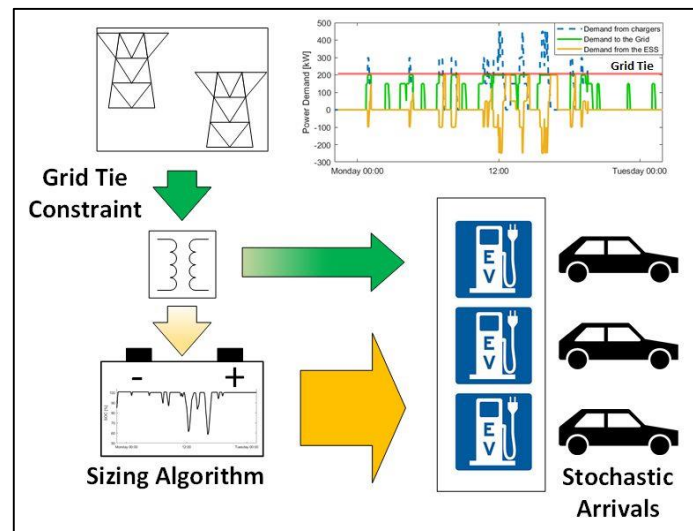
Buffering charging demand

The results presented in this chapter were partially published in the following paper:

- Y. Ligen, H. Vrabel, H. Girault, Local Energy Storage and Stochastic Modeling for Ultrafast Charging Stations, *Energies*. 12 (2019) 1986. <https://doi.org/10.3390/en12101986>. [1]

And presented during the following conference:

- EVS 32, Lyon, May 19-22, How to manage the peak power demand of multi-stall 150 kW charging stations?



Home charging and overnight charging are often referred as the ideal solution for BEV owners. However, the sustained urbanization of the world population (from 55% to 68 % by 2050¹) and long journeys exceeding the vehicle range, support the need for fast charging solutions. While BEVs may represent an asset for grid management and ease the integration of renewables [2], they also represent a challenge in terms of power demand and power connection.

3.1 Problem setting

Nowadays, in most cases, installing multiple charging points without the associated power connection is not an issue. According to the data collected by Fastned™ [3], it appears that fast charging stations are largely underused, with an average of 7.12 charging sessions per station per day reported in June 2018. Under these conditions, a limited number of users will be affected during peak hours if the contracted power does not cover the demand, and power share between stalls is implemented by several charging station operators (CSO). On the other hand, for stations used at full capacity, several studies have pointed out the issues triggered on the electrical grid. Managing the impacts of EVs on the power system is a growing concern [4], and several studies have been conducted to evaluate mitigation techniques via demand side management and power electronics topologies.

Vehicle-to-grid and bidirectional chargers can simultaneously help to support local consumption and contribute to grid regulation, and thus represent particularly relevant solutions for locations with long parking durations. However, they are not considered as appropriate for quick stops at ultra-fast charging stations along transit axes. Indeed, a key condition to implement such schemes is the idle time a vehicle remains attached to a plug, which makes sense at office buildings [5] or at home. A typical example was proposed by Quddus *et al.* [6] with a sector coupling scheme between vehicles, charging stations, and commercial buildings, with hourly operational decisions for energy flows, but it does not address the minute-scale power peak issues of ultra-fast charging stations. From a CSO perspective, the first issues to solve are grid connection requirements and demand charges, rather than grid services such as frequency regulation, which can be implemented in a later stage.

Thus, two major questions are emerging regarding ultra-fast charging stations: how many charging points are required to satisfy a given charging demand, and how to size an energy buffer to reduce grid connection requirements. Because the answer of the first question determines the power demand curve, the questions must be answered sequentially.

¹ <https://www.un.org/development/desa/en/news/population/2018-revision-of-world-urbanization-prospects.html>

The prediction of power demand curves at fast charging stations is a prerequisite for ESS implementation studies. Richard and Petit [7] covered this statistical aspect by running a simulation for 10 years, with three daily peaks (morning, noon, evening) and a normal distribution of state-of-charge (SoC) for a fleet of five different EV types. They claim that waiting times were always below 2 min. Regarding ESS (Energy Storage System) implementation, they limited their investigation to one station configuration (three 120 kW chargers), and two ESS sizes (250 and 650 kWh). Consequently, they decided to modulate the charging power delivered to EVs in order to avoid a complete depletion of the ESS. Gjelač *et al.* [8] used a log normal distribution of daily travel distance to derive the charging needs of EVs with a 50 kWh battery pack. A distinction between workday and holiday was used for the hourly distribution of charging events and stations with up to five charging points at 150 kW were investigated. Queue management details are not provided. The results are presented for a 1-day simulation. A third example of power demand curve derivation is provided by Dominguez-Navarro *et al.* [9]. In this study, they ran a Monte Carlo simulation, considering an average time between two arrivals at the station as a function of the hour of the day. A lognormal distribution of SoC was used, coupled to a distribution of battery capacities ranging from 3.6 to 63 kWh. If all charging points were occupied, vehicles automatically left the station. Various configurations with five 50 kW charging points in combination with renewable power generation were investigated.

While stochastic approaches appear to be well-suited for modeling power demand profiles at fast charging stations, they are rarely used to cover a wide range of station capacities (in terms of vehicles per week) and constraints (in terms of queuing and installed charging points). In the same way, battery assisted charging stations [10] are well covered in the literature, but methods and results may present versatility and universality hurdles for practical implementation. Several products are being commercialized by companies such as Porsche™ [11], ads-tec™ [12], Volkswagen™ [13], and Freewire [14], with modular solutions in the range of 70 to 360 kWh, but no consistent modeling approach is available yet to assess their capabilities. More recently Audi² also reported a container sized system with 8 charging points at 150 kW and a 1 MWh storage system. And Tesla, leverage its stationary energy storage products, using a megapack to power superchargers in selected locations.

Herein, we report a robust stochastic approach, considering various charging station capacities and queuing characteristics, with an appropriate ESS sizing algorithm introduced to address grid connection constraints. Similarly, various implementation scenarii can be investigated for a given battery capacity. The developed methodology is applied for a specific case study, considering a Swiss charging station with the same frequentation as an average gas station.

² <https://www.audi-mediacycenter.com/en/press-releases/audi-provides-sustainable-mobility-and-charging-solutions-at-world-economic-forum-in-davos-12485>

3.2 Stochastic charging demand and charging points

The charging station problem involves different timescales, ranging from the minute, for a charging event, to the year, for seasonal effects. A stochastic approach to model the charging demand at the station is presented, and used in a second phase as input data for an ESS sizing algorithm. Two parameters were considered for the analysis: the number of installed charging points and the contracted power available from the grid, *i.e.* the grid tie.

Several assumptions are required to derive the power demand profile at the station: the duration of charging events, the power profile of individual charging events, and, finally, the hourly distribution of charging events throughout the week and queuing models. Unfortunately, only limited datasets are available for fast charging stations. No 150 kW public station has yet reached its full capacity in terms of frequentation, due to the limited availability of EVs with this charging capability. A stochastic approach was therefore used to model charging datasets as representative as possible of a full scale EV deployment.

3.2.1 Method

The duration of fast charging events is expected to be in the range of 12 to 30 min. The real value depends on many factors related to the vehicle itself, but also to the behavior and preferences of the driver. A random integer value between 12 and 30 min was assumed. During such charging events, 25 to 70 kWh can be transferred to the vehicle. Even if a normal distribution of charging durations was observed in some early measurements [15], this might be a bias due to the limited diversity of vehicles' battery capacities available at this time. Such a distribution will limit the dispersion of the results. A distribution of vehicle's SoC at arrival can be also used to derive charging duration, as previously mentioned [7,8].

While we considered vehicles with a 150 kW charging capability, a constant charging power of 150 kW is not practically implemented in order to prevent excessive battery degradation. A large variety of battery management systems (BMS) and charging strategies are used by car manufacturers, but the general idea is that, at high SoC, the charging power decreases [16]. Thus, based on preliminary protocols, we here assumed that the nominal 150 kW charging power is applied from the beginning until the last 4 min, and from there on linearly decreases down to 50 kW.

The hourly distribution of charging events during the week was based on the measurements made at Nexant™ petrol stations [17]. This typical distribution has been observed in various locations, including EV charging stations [3,18,19], and all regions display morning and an evening peaks. The distribution shape is very similar in the US or in Europe. Some recently data collected in Switzerland have highlighted the same characteristics (https://www.tomtom.com/en_gb/traffic-index/lausanne-traffic). While overnight charging may represent a large share of charging events,

long transit axes with fast charging stations will likely be used in the same way as current petrol stations. It is known that some extreme charging event periods such as Thanksgiving and Christmas will largely overshoot the average frequentation [20], and other seasonal effects have been observed, but these are not considered here. The probability distribution was used to generate the time of arrival of each vehicle during the week. We obtained the power demand curves presented in **Figure 3.1**.

The arrival time of vehicles is generated with the following code in MATLAB:

```
nevents=1000;%number of charging events to distribute over one week
event=zeros(1,nevents);%gives the arrival time for each vehicle
for k=1:nevents
    event(k)=sum(rand >=cumsum([0, prob]));
end
```

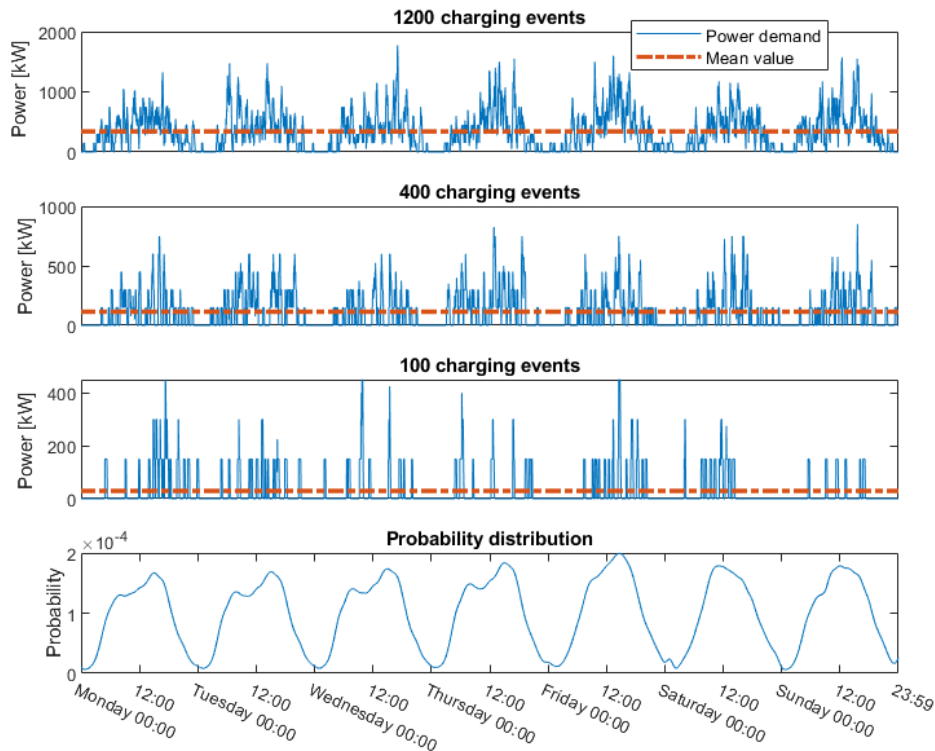


Figure 3.1 - Stochastic distribution of charging events and average power.

The waiting list is introduced as follows (a week contains 1080 minutes):

```
ChargingDuration=randi([8 26],1,nevents);%random integer generation
for a charging session at maximum power during 8 to 26 minutes
RampDown=[125,100,75,50];%lower power demand for the last 4 minutes of
a charging session

TotalChargers=6;%number of charging points
WaitingRecords=zeros(1,nevents);
ChargersInUse=zeros(1,10080).'; %10080 minutes per week
```

```

probaLoad=zeros(1,10080).';
for p=1:nevents
    while ChargersInUse(event(p)+WaitingRecords(p))>TotalChargers-1
        WaitingRecords(p)=WaitingRecords(p)+1;
    end;
    if WaitingRecords(p)>15
        p=p+1; %rejection if waiting time exceeds 15 minutes

    else
        if event(p)+WaitingRecords(p)+ChargingDuration(p)+5<10080
            %5vminutes to include ramp down
            probaLoad(event(p)+1+WaitingRecords(p):event(p)+ChargingDuration(p)+4+
                WaitingRecords(p))=
            probaLoad(event(p)+1+WaitingRecords(p):event(p)+ChargingDuration(p)+4+
                WaitingRecords(p))+[150*ones(1,ChargingDuration(p)),RampDown].';

            ChargersInUse(event(p)+WaitingRecords(p):event(p)+ChargingDuration(p)+
                4+WaitingRecords(p))=
            ChargersInUse(event(p)+WaitingRecords(p):event(p)+ChargingDuration(p)+
                4+WaitingRecords(p))+ones(1,ChargingDuration(p)+4+1).';
        end
    end;
end;

```

Since a limited number of charging points is available at each station, a queuing model was implemented. If all charging points were used, we assumed that a new charging event could be delayed by up to 15 min before being considered rejected, *i.e.* the corresponding user decides not to recharge. Three metrics were used to assess the capacity of the station:

- The percentage of users needing to wait in order to get access to a charging point;
- The percentage of users needing to wait more than 5 min to get access to a charging point;
- The percentage of users rejected (or waiting more than 15 min).

Using these metrics, we defined a minimum number of charging points able to meet the expected demand while keeping acceptable queuing levels. Allowing some queuing at the station can be considered as the first measure to limit the required grid tie for a given number of charging events. The algorithm to compute the demand curve and queuing metrics is presented in **Figure 3.2**.

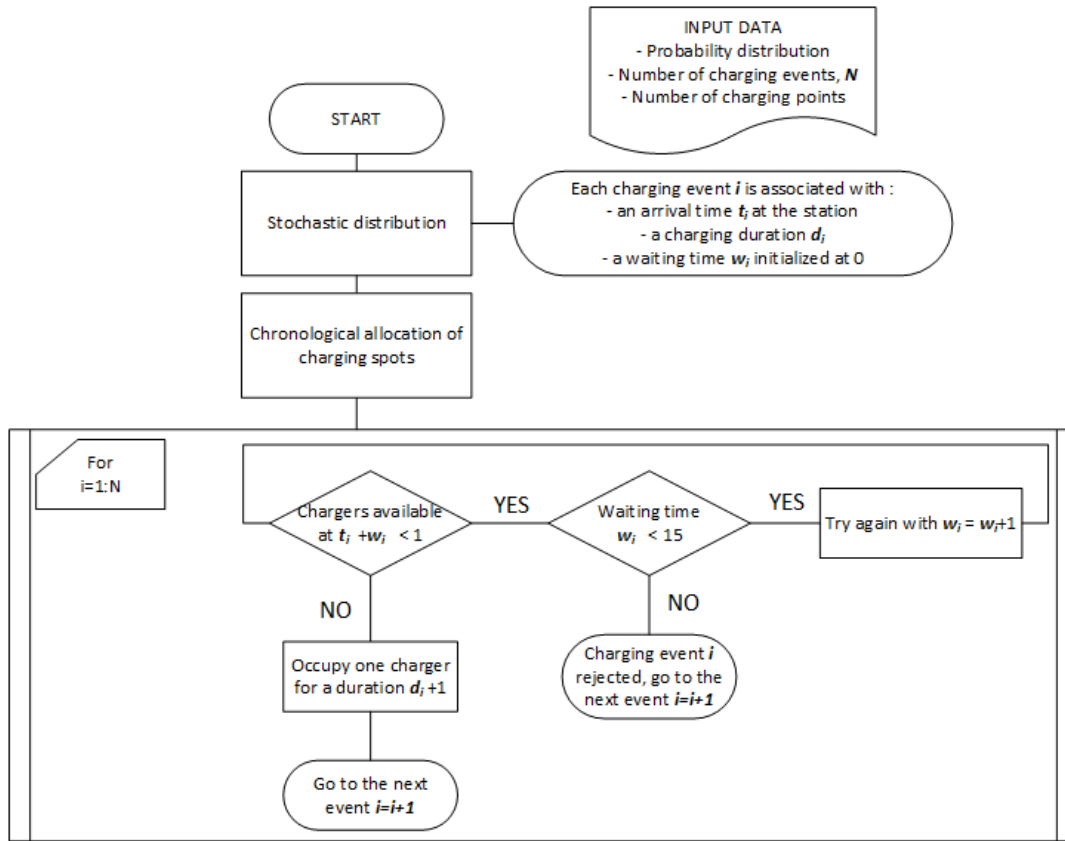


Figure 3.2 - Queuing algorithm flowchart.

3.2.2 Results

The stochastic distribution of charging events throughout the month results in some queuing. For 2 to 12 chargers and from 0 to 3500 charging events, the queuing events were accounted and are presented in **Figure 3.3**. Within the blue region, less than 1% of the users are subject to the respective queuing experience: waiting, waiting more than 5 min, or being rejected. For example, 1000 charging events per week can be provided with only 4 charging points, but with more than 5% of charging events rejected (queuing for more than 15 min). For such demand, six charging points seems to be more appropriate, with 5% of the users waiting more than 5 min and less than 1% rejected. Finally, a higher level of service is offered with 8 charging points for 1000 charging events per week, with only 2% of users needing to wait.

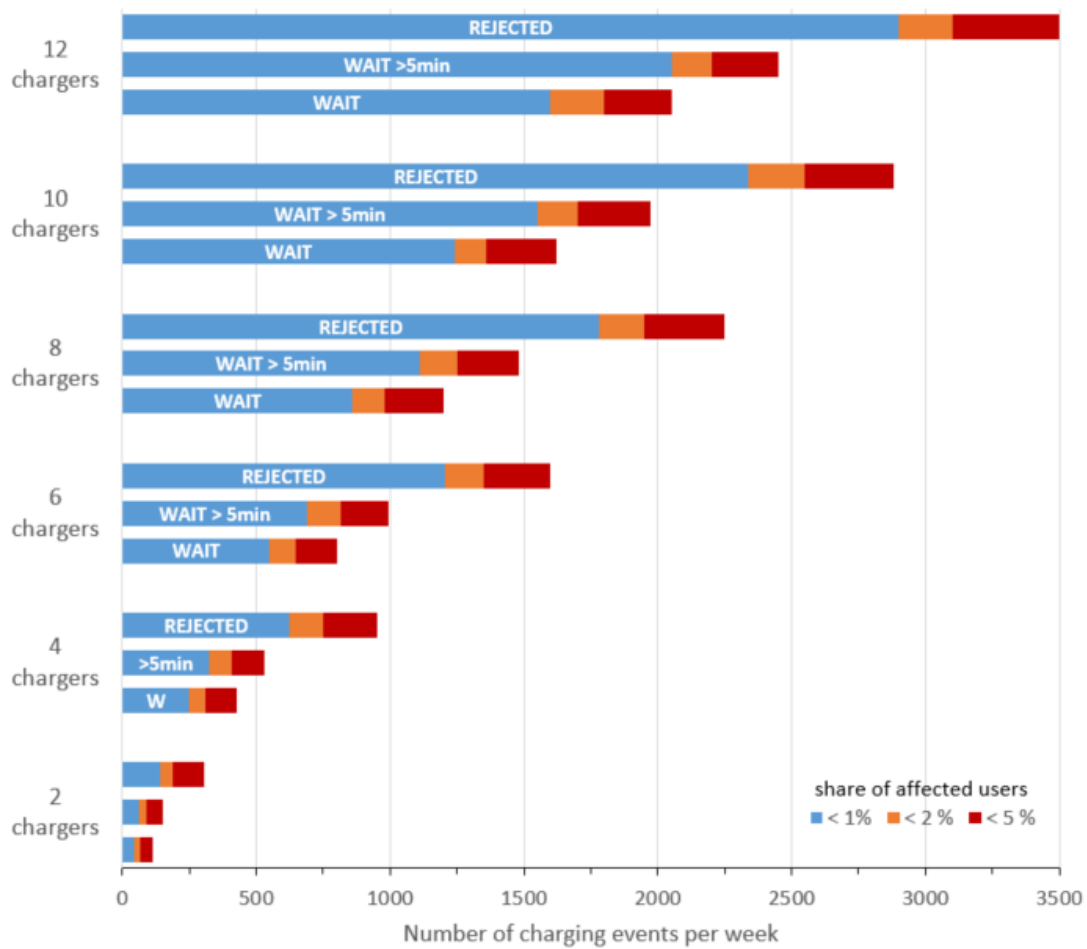


Figure 3.3 – Waiting metrics as a function of the number of charging points and charging events per week.

With four-stall charging stations, Fastned™ expects to deliver 27 MWh per week, and with eight stalls, 55 MWh, corresponding respectively to 550 and 1100 EVs per week [21], which is in line with the numbers presented here.

For the rest of the analysis, we considered a number of charging points sufficient to ensure that less than 5% of the charging events are delayed by more than 5 min. This corresponds to the region on the left of the pink line in **Figure 3.4**. Above this limit, we can consider that the station is undersized, and too many users will be rejected.

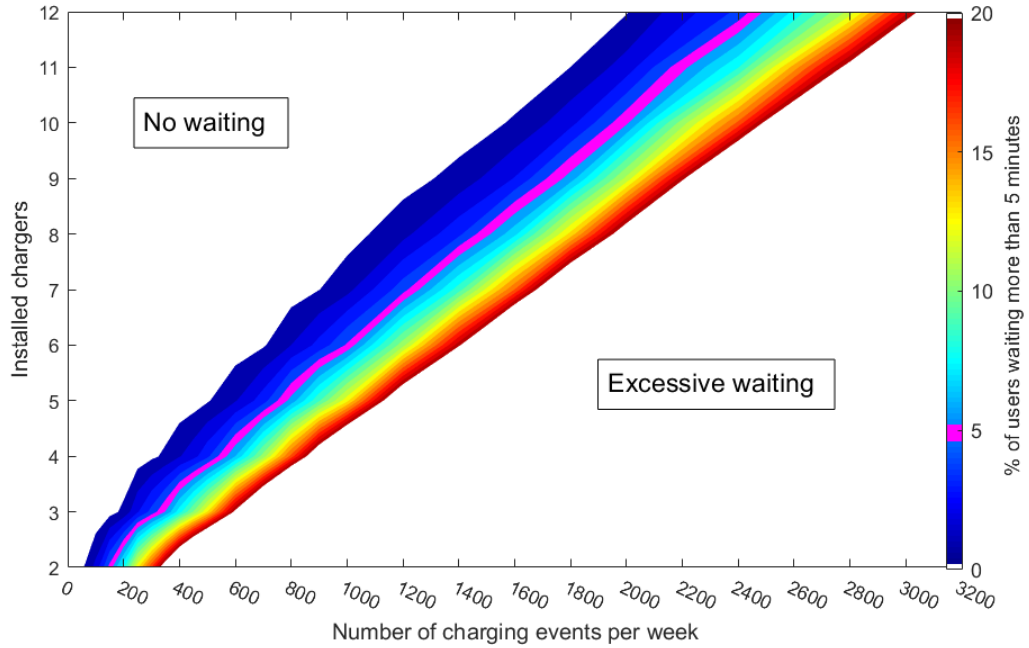


Figure 3.4 – Percentage of users waiting mor than 5 minutes.

3.3 ESS operation and sizing

The most challenging situation corresponds to a station used at full capacity, defined here as 5% of the users waiting more than 5 min. With vehicles queuing to get a charging spot, peak power consumption periods last longer, and, thus, more storage capacity is required. Taking the worst-case scenario for ESS sizing ensures that, as long as the station is used for its designed capacity, the proposed storage capacity will be sufficient.

3.3.1 Method

The modelization from the previous section highlights a considerable potential to reduce peak power requirements considering the average power, as shown in **Figure 3.1**. This characteristic, particularly prominent for small stations, is specific to charging stations with very large peak-to-average power ratios, as presented in **Table 3.1**.

Table 3.1 – Peak-to-average ratio for various stations capacities

Charging Events per Week	Recommended Number of Chargers	Peak Power /kW	Average Power (Full Capacity)/kW	Power Ratio
0–150	2	300	43	7.0
250–550	4	600	157	3.8
600–1000	6	900	287	3.1
1400–2000	10	1500	573	2.6

Without ESS, the grid connection must be dimensioned to cover the peak power, which results in oversized power transformers and expensive demand charges. With an ESS, the required grid connection can approach the average power demand. The ESS provides additional power when the grid connection is not sufficient. Subsequently, the ESS is recharged when the power demand is below the contracted power.

While the ESS capacity, in kWh, requires running of an algorithm with power demand curves, the ESS power requirements are immediately determined by the difference between the peak demand and the grid tie.

Once the number of charging events and the corresponding number of charging points were defined, the stochastic model from the previous section was used to compute the power demand curve. If the grid tie is smaller than the peak power demand but larger than the average demand, an ESS can be installed. The algorithm used to define the appropriate capacity is presented in

Figure 3.5. The ESS capacity was iteratively increased until a full month could be covered without the SoC going below 10%. We also ensured qualitatively that, at the end of the month, the battery could be returned at the same SoC as in the beginning. A charging and a discharging efficiency of 95% was considered (90% round trip). Because of the stochastic nature of the problem, 100 months were simulated in order to ensure the consistency of the results³. The algorithm was stopped if the required ESS capacity exceeded 1.1 MWh.

³ It corresponds to $100 \times 30 \times 24 \times 60 = 4\,320\,000$ minutes simulated

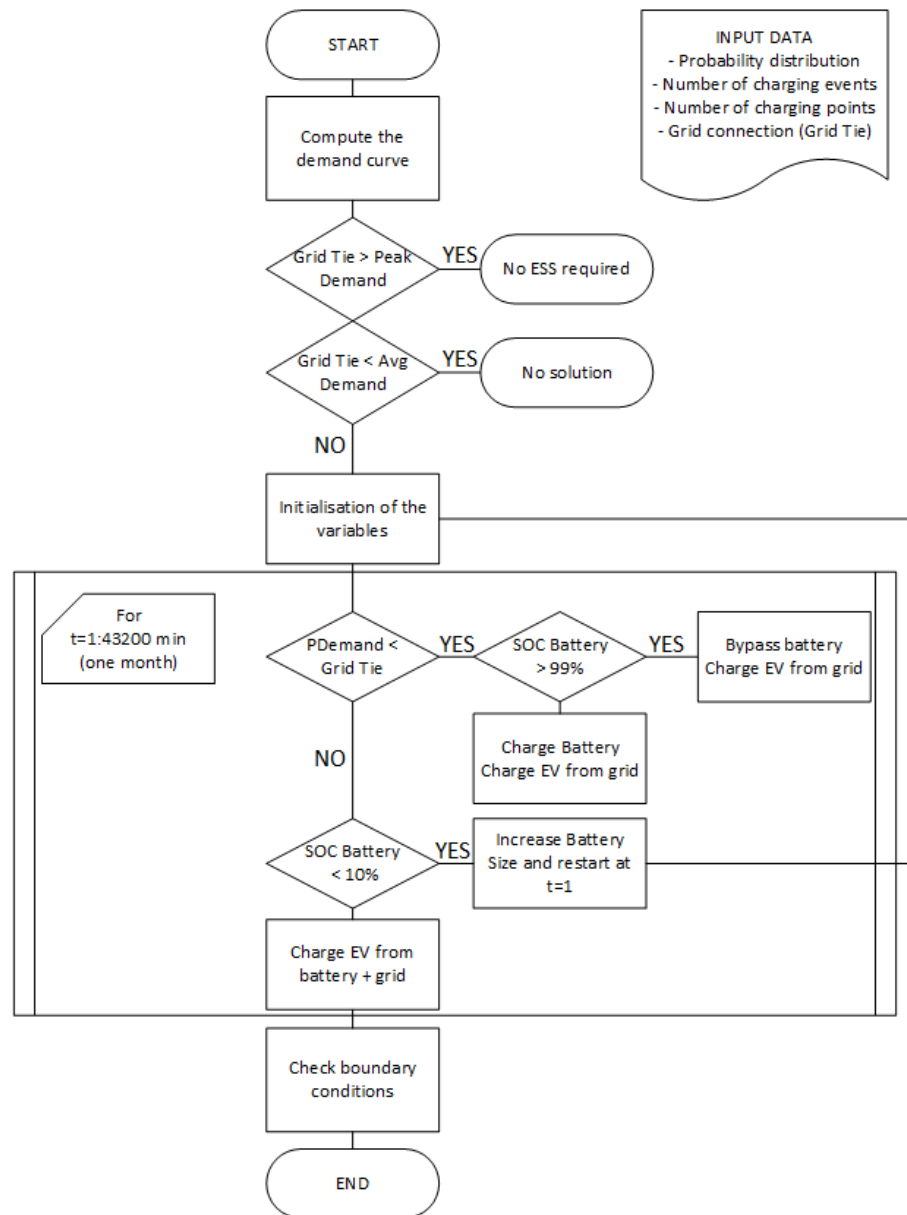


Figure 3.5 – Battery algorithm flowchart.

A typical mode of operation of the ESS during a week is represented in **Figure 3.6**. We can note that the ESS undergoes only a limited number of full discharge cycles, which only occur during peak hours without idle periods to recharge the ESS.

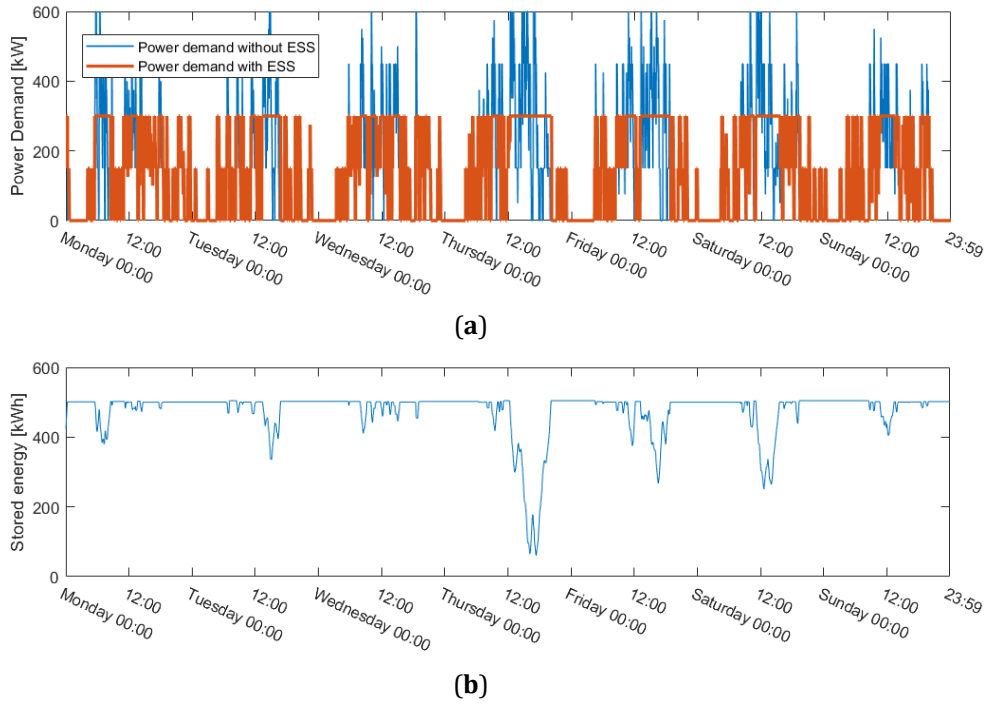


Figure 3.6 – ESS operation (a) and variation of energy level in the ESS (b) during a week with 500 charging events and 4 charging points.

3.3.2 Results

The results of the sizing algorithm are presented in **Figure 3.7**. The red diamond markers represent the peak power demand when all charging points are occupied; it corresponds to the required grid tie when no ESS is installed to provide additional power. It appears that even the smallest ESS considered, 100 kWh, would bring significant savings in terms of required grid tie, with 100 to 200 kW reductions. This is a consequence of the very short duration of peak events, with all chargers occupied, as presented in **Figure 3.1** **Figure 3.1** - Stochastic distribution of charging events and average power.. With a 550 kWh/300 kW ESS, a six-stall charging station can serve up to 1000 users per week with 33% reduction of the grid tie.

Interestingly, it appears that the solution with two modules from the company ads-tec™ (240 kWh/200 kW) [12] is suitable for a two-stall charging station and a 130 kW grid connection. The 360 kWh system with a 30 kW grid connection proposed by VW™ [13] largely covers the needs of a one-stall charging station with up to 22 charging events per week (6 kW average consumption). The present model indicates that 175 kWh would be sufficient. With two stalls, 150 charging events per week, and a 60 kW grid connection, our algorithm recommends a slightly bigger system, with 765 kWh on average instead of 720 kWh. However, the dispersion of the results over the 100 months simulated, presented in **Figure 3.8**, indicates that, for a 60 kW grid tie, the median (red line) ESS

capacity is 720 kWh. The 25th and 75th percentile are, respectively, 660 and 840 kWh, thus the VW™ modules seem also to be adequately sized.

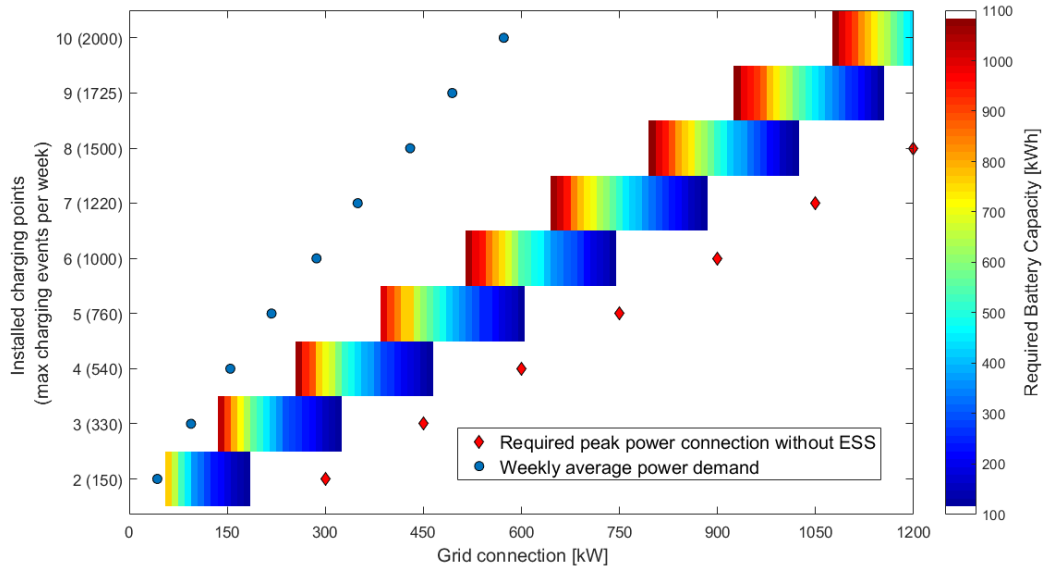


Figure 3.7 – Required ESS capacity as a function of the available grid connection (mean value).

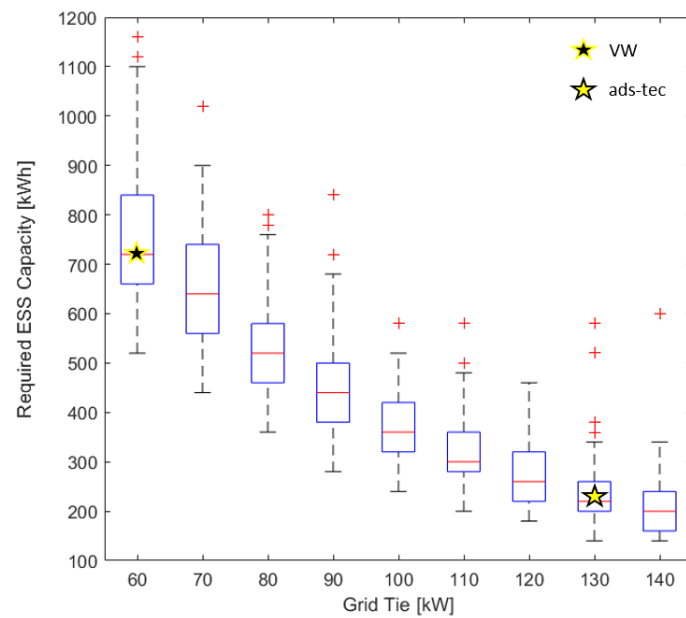


Figure 3.8 – Dispersion of the results for two charging points with 150 charging events per week.

3.4 Case study

In western Switzerland, we have noted demand charges in the range of 4.4 to 15.5 CHF/kW/month, and, in addition to this monthly charge, the initial installation of the grid connection typically costs around 100 CHF/kW. Under these conditions, there is a clear incentive for CSOs to limit the installed grid tie.

We present here a grid tie reduction strategy for CSOs, assuming the frequentation of an average gas station in Switzerland, i.e., 450 charging events per week [22].

The first decision concerns the number of charging points required to satisfy this charging demand. The queuing metrics are reported in **Table 3.2**, including a $\pm 10\%$ variation in the number of charging events per week.

Table 3.2 – Waiting metrics as a function of the number of installed charging points.

Installed charging points	3			4			5		
Charging events per week	-10 %	450	+10 %	-10 %	450	+10 %	-10 %	450	+10 %
Wait %	13.7	17.5	21.2	4.1	5.7	7.6	1	1.6	2.3
Wait > 5 min %	8.2	10.7	13.4	1.9	2.8	3.8	0.3	0.6	0.9
Rejected %	1.3	1.8	2.5	0.1	0.2	0.3	0	0	0
Peak power	450 kW			600 kW			750 kW		

With more than 10% of the users waiting more than 5 min, it appears that a three-stall charging station will not offer a satisfying customer experience, and, in return, it may affect the probability distribution of charging events. Indeed, the 450 charging events per week largely exceeds the rated capacity of 330 charging events per week reported in **Figure 3.4**. For four and five installed charging points, the queuing metrics are below our defined threshold of 5% of users waiting more than 5 min.

In **Figure 3.9**, we can observe the concentration of charging events when a constraint on the available charging points is introduced. With three installed charging points, the station is fully occupied for 1118 min per week (12% of the time). With four and five charging points, the station requests the full power for, respectively, 278 min and 65 min.

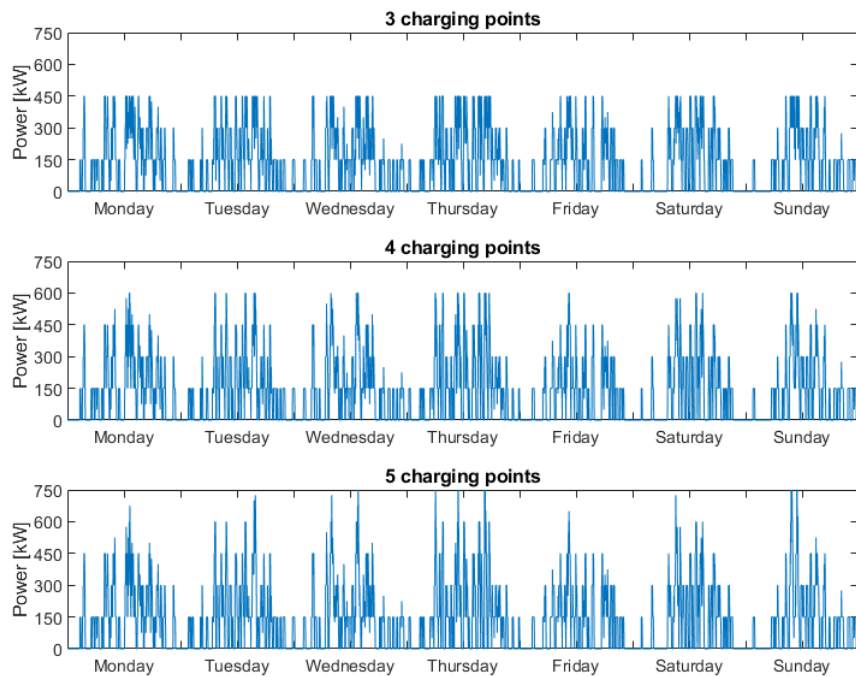


Figure 3.9 – Stochastic distribution of 450 charging events per week for three to five chargers.

Installing four charging points instead of five can already reduce the required grid connection from 750 kW to 600 kW, and thus 15 kCHF can already be saved in initial grid connection fees, and 660–2325 CHF per month in demand charges. In order to further reduce the required grid tie, without affecting queuing time, such as with the three-stalls station, an ESS can be installed. The ESS sizing algorithm presented in **Figure 3.5** was used for 450 charging events per week and four and five charging points. The results are presented in

Figure 3.10. Compared to **Figure 3.7**,

Figure 3.10 indicates smaller battery capacities and lower achievable grid connections. Indeed, Figure 7 was designed for stations used at full capacity (i.e., 5% of users waiting more than 5 min), while we consider here 450 charging events per week in both cases. With a rated capacity of 540 and 760 charging events for, respectively, four and five charging points, there are thus fewer events

where the ESS needs to be used. It highlights that stations used under their nominal capacities have larger demand charge reduction potential and require smaller ESS.

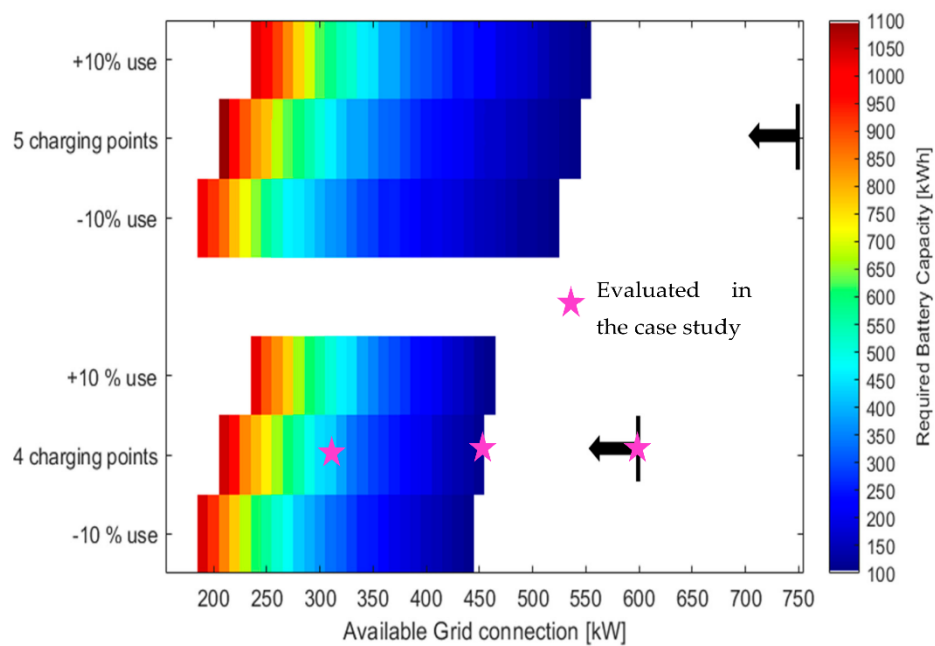


Figure 3.10 – Required ESS capacity as a function of the available grid connection for 450 charging events per week.

Three cases were retained for an economic evaluation of a CSO's business case. The reference case is a direct connection between the grid and the chargers, with 600 kW thus required for four charging points. This reference was compared with a station with a 100 kWh ESS/450 kW grid connection and a 400 kWh ESS/320 kW grid connection.

Based on the economic parameters presented in **Table 3.3**, we evaluated the expected income statement of a CSO. We assumed that the station reached its nominal throughput of 450 charging events per week after five years of operation.

Table 3.3 – Economic parameters for business case evaluation.

Cost Component	Value
----------------	-------

Demand charge	10 CHF/kW/month
Electricity price	0.14 CHF/kWh
Stationary battery (installed)	400 CHF/kWh
Grid connection cost	100 CHF/kW
Fast charging point (installed)	60 000 CHF/unit
Selling price at the charger	0.3 CHF/kWh

Actual rates (without subscription) in one of the current leader in fast charging are at 0.79 CHF/kWh (www.ionity.eu) in Switzerland and 0.30 CHF/kWh at Tesla superchargers.

In **Figure 3.11**, we observe that, despite a larger initial investment, the 100 kWh and the 400 kWh cases are both beneficial due to the cumulative savings in demand charge. In both cases, the energy losses in the ESS represent only 0.3% and 1.1% of the total energy consumed at the station, because power is requested from the ESS only during peak periods. Without ESS, the demand charge represents 32% of the electricity expenses for the CSO compared to 26% with a 100 kWh ESS and 19% with a 400 kWh ESS.

ESS in fast charging stations are subject to less than one full cycle per day, thus, with a reported cycle life above 2000 full cycles [23], an ESS can be easily operated for 8 to 10 years. Considering actual energy installation costs below \$400/kWh for a large variety of technologies, the payback period for the ESS can happen in less than two years. Battery degradation and thermal modeling were studied by Richard and Petit [7]. They concluded that degradation costs can be largely covered by grid services during the night. Efficiency losses will affect marginally affect electricity expenses, considering the 0.3 and 1.1% losses mentioned earlier.

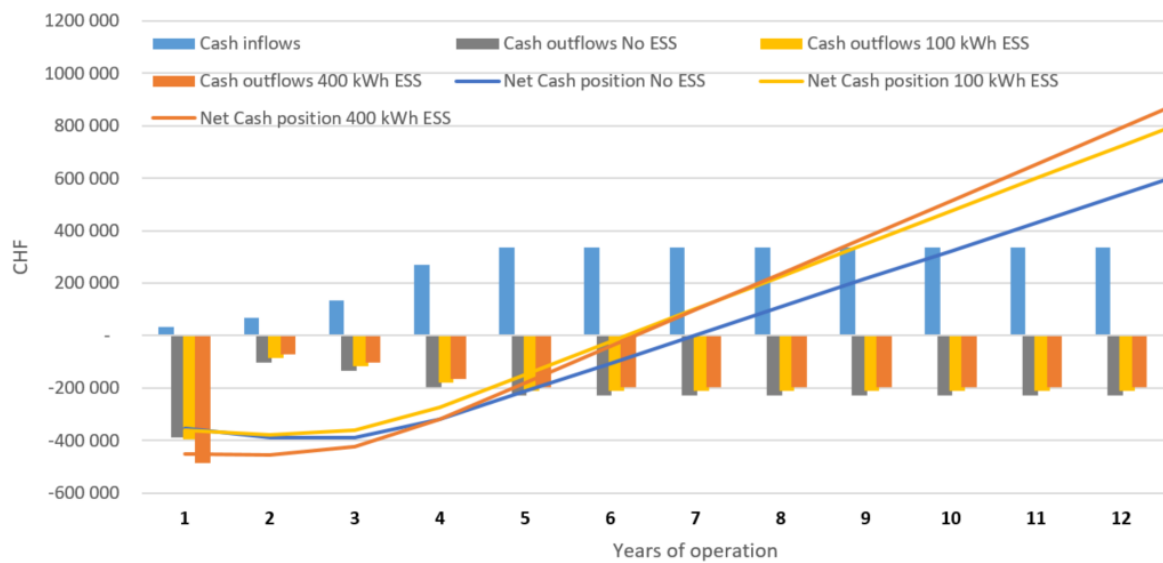


Figure 3.11 – Cash inflows and outflows for a CSO with and without ESS.

3.5 Conclusion

This study provides a tangible method to reduce the required grid tie for multi-stall EV charging stations. The first stage, using a versatile stochastic approach, recommends a number of charging points as a function of the expected capacity.

In a second stage, an ESS is introduced to further reduce the grid tie and associated demand charge. A sizing algorithm, simulating 100 months, shows, for all cases between 150 and 2000 charging events per week, that a 500 kWh ESS can further reduce the grid tie by 200 to 300 kW. Substantial savings are already obtained with 100 kWh ESS, with 100–150 kW reductions.

Finally, the method was applied on a specific case study with 450 charging events per week. It demonstrated that stations used under their nominal capacity present even larger power savings potential. An appropriately sized ESS can help to improve the profitability for CSOs, especially in early EV deployments, ensuring that the nominal power remains available for customers while the monthly demand charge is lowered for the CSO. In addition, new locations become eligible to install fast charging stations, relaxing the existing constraints regarding the grid connection.

We presented here a consistent methodology to assess the relevance of ESS implementation along three parameters: the number of charging points, the available grid connection, and the ESS capacity.

While the electrification of the transport sector has initially targeted passenger vehicles, electric versions of lorries and trucks are becoming available. With different distribution patterns for charging events and higher charging power, the methodology described in this study can be used to

equip motorways with the expected 500 kW [24] charging points, and to limit demand charge for 3 to 6 MW peak installations [25].

The stochastic approach can easily be adapted to other probability distributions, including extreme charging demand periods and various charging modes. Future work could also introduce a constraint on the grid power supply regarding the availability of renewables, and discuss examples such as the 1.5 MWh battery installed to charge EVs in Utrecht, Netherland [26], or the charging test site from ElaadNL with a 138 kWh ESS coupled with vehicle-to-grid V2G capabilities [27]. The aggregation of grid services in low utilization periods would be also relevant for future research [7]. In combination with EV deployments scenarios, electricity grid reinforcement alternatives and local ESS installation can be compared for countrywide transition strategies towards electric mobility.

References

- [1] Y. Ligen, H. Vrabel, H. Girault, Local Energy Storage and Stochastic Modeling for Ultrafast Charging Stations, *Energies*. 12 (2019) 1986. <https://doi.org/10.3390/en12101986>.
- [2] K.M. Tan, V.K. Ramachandaramurthy, J.Y. Yong, Integration of electric vehicles in smart grid: A review on vehicle to grid technologies and optimization techniques, *Renewable and Sustainable Energy Reviews*. 53 (2016) 720–732. <https://doi.org/10.1016/j.rser.2015.09.012>.
- [3] Fastned.nl, Fastned - Financial communication - B.V. € 12,000,000, Bond Programme, (2018). <https://cdn.fastnedcharging.com/uploads/documents/prospectus-fastned-bv-10-october-2018.pdf> (accessed January 17, 2019).
- [4] H. Shareef, Md.M. Islam, A. Mohamed, A review of the stage-of-the-art charging technologies, placement methodologies, and impacts of electric vehicles, *Renewable and Sustainable Energy Reviews*. 64 (2016) 403–420. <https://doi.org/10.1016/j.rser.2016.06.033>.
- [5] D. Thomas, O. Deblecker, C.S. Ioakimidis, Optimal operation of an energy management system for a grid-connected smart building considering photovoltaics' uncertainty and stochastic electric vehicles' driving schedule, *Applied Energy*. 210 (2018) 1188–1206. <https://doi.org/10.1016/j.apenergy.2017.07.035>.
- [6] M.A. Quddus, O. Shahvari, M. Marufuzzaman, J.M. Usher, R. Jaradat, A collaborative energy sharing optimization model among electric vehicle charging stations, commercial buildings, and power grid, *Applied Energy*. 229 (2018) 841–857. <https://doi.org/10.1016/j.apenergy.2018.08.018>.
- [7] L. Richard, M. Petit, Fast charging station with battery storage system for EV: Grid services and battery degradation, in: 2018 IEEE International Energy Conference (ENERGYCON), IEEE, Limassol, 2018: pp. 1–6. <https://doi.org/10.1109/ENERGYCON.2018.8398744>.
- [8] M. Gjela, N.B. Arias, C. Tr, Multifunctional Applications of Batteries within Fast-Charging Stations based on EV Demand-Prediction of the Users' Behaviour, (n.d.) 8.
- [9] J.A. Domínguez-Navarro, R. Dufo-López, J.M. Yusta-Loyo, J.S. Artal-Sevil, J.L. Bernal-Agustín, Design of an electric vehicle fast-charging station with integration of renewable energy and storage systems, *International Journal of Electrical Power & Energy Systems*. 105 (2019) 46–58. <https://doi.org/10.1016/j.ijepes.2018.08.001>.
- [10] M. Aziz, T. Oda, M. Ito, Battery-assisted charging system for simultaneous charging of electric vehicles, *Energy*. 100 (2016) 82–90. <https://doi.org/10.1016/j.energy.2016.01.069>.
- [11] Porsche - Electric Pit Stop, (n.d.). <https://newsroom.porsche.com/en/technology/porsche-e-mobility-fast-charging-modular-building-blocks-system-electricity-grid-visitor-frequency-space-constraints-power-electronics-cooling-unit-pit-stop-missione-taycan-engineering-2018-1-15796.html> (accessed January 17, 2019).

- [12] ads-tec, StoraXe PowerBooster, (n.d.). <https://www.ads-tec.de/energy-storage/industrial-infrastructure/powerbooster/technische-daten.html> (accessed January 17, 2019).
- [13] Volkswagen, Volkswagen Mobile Charging Station, (n.d.). <https://www.volkswagen-newsroom.com/en/press-releases/electrifying-world-premiere-volkswagen-offers-first-glimpse-of-mobile-charging-station-4544> (accessed January 17, 2019).
- [14] Freewiretech, Freewire - Mobi charger series, (n.d.). <https://freewiretech.com/products/dc-boost-charger/> (accessed January 17, 2019).
- [15] T. Oda, M. Aziz, T. Mitani, Y. Watanabe, T. Kashiwagi, Mitigation of congestion related to quick charging of electric vehicles based on waiting time and cost-benefit analyses: A Japanese case study, *Sustainable Cities and Society*. 36 (2018) 99–106. <https://doi.org/10.1016/j.scs.2017.10.024>.
- [16] Fastned.nl, Fast charging curves, (n.d.). <https://support.fastned.nl/hc/en-gb/categories/204629548-Vehicles-charging-tips-> (accessed January 17, 2019).
- [17] T.-P. Chen, Hydrogen delivery infrastructure option analysis, Nexant, Inc., 101 2nd St., San Francisco, CA 94105, 2010.
- [18] M. Neaimeh, S.D. Salisbury, G.A. Hill, P.T. Blythe, D.R. Scofield, J.E. Francfort, Analysing the usage and evidencing the importance of fast chargers for the adoption of battery electric vehicles, *Energy Policy*. 108 (2017) 474–486. <https://doi.org/10.1016/j.enpol.2017.06.033>.
- [19] International Energy Agency, Global EV Outlook 2018, (2018). <https://webstore.iea.org/global-ev-outlook-2018> (accessed September 12, 2018).
- [20] T.S. Bryden, G. Hilton, A. Cruden, T. Holton, Electric vehicle fast charging station usage and power requirements, *Energy*. 152 (2018) 322–332. <https://doi.org/10.1016/j.energy.2018.03.149>.
- [21] Fastned.nl, Fast charging, station capacity and economies of scale, Everything You've Always Wanted to Know about Fast Charging. (n.d.). <https://fastned.nl/en/blog/post/everything-you-ve-always-wanted-to-know-about-fast-charging> (accessed January 17, 2019).
- [22] Union Pétrolière Suisse, Rapport annuel 2015, (n.d.). https://www.erdoel.ch/images/com_evdocs/ev_jb_2015_fr.pdf (accessed February 1, 2017).
- [23] IRENA, Electricity storage and renewables: Costs and markets to 2030, International Renewable Energy Agency, Abu Dhabi, 2017.
- [24] H. Ding, Z. Hu, Y. Song, Value of the energy storage system in an electric bus fast charging station, *Applied Energy*. 157 (2015) 630–639. <https://doi.org/10.1016/j.apenergy.2015.01.058>.
- [25] ACEA - European Automobile Manufacturers Association, Availability of truck-specific charging and refuelling infrastructure in the EU, (2019). https://www.acea.be/uploads/press_releases_files/Infrastructure_alternatively-powered_trucks_January_2019.pdf.
- [26] Jaarbeurs is building a large energy storage facility, (n.d.). <https://www.jaarbeurs.nl/energy-storage-facility> (accessed January 17, 2019).

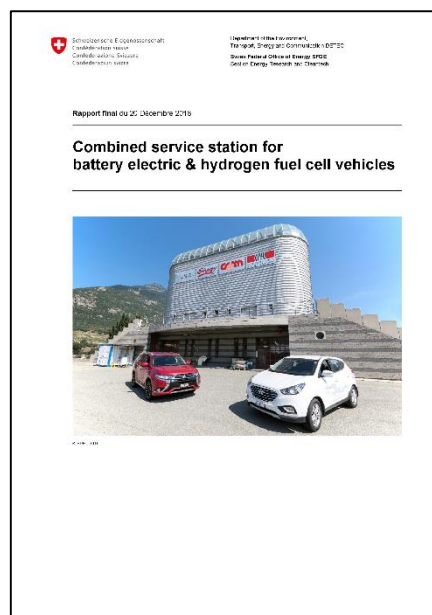
- [27] Alfen, Integrated energy storage solution for EV charging test site of ElaadNL, (n.d.).
<https://alfen.com/en/news/alfen-supplies-integrated-energy-storage-solution-ev-charging-test-site-elaadnl> (accessed January 17, 2019).

Chapter 4

Building a e-mobility infrastructure demonstrator

The results presented in this chapter were partially published in the following report:

- Y. Ligen, H. Girault, J. Rager, Combined service station for battery electric & hydrogen fuel cell vehicles - Final Report, Swiss Federal Office for Energy. (2018).
<https://www.aramis.admin.ch/Dokument.aspx?DocumentID=50166> (accessed November 21, 2019). [1]



In June 2015, the Laboratory of Physical and Analytical Electrochemistry (LEPA) submitted a funding request to the Swiss Federal Office of Energy (SFOE). The project “Combined service station for battery and fuel cell electric cars” was approved in late 2015. From 2016 to early 2020, this research and demonstration platform was designed, built and operated. Also called “Grid to Mobility demonstrator” or “Electromobilis”, the installation made it possible to develop the scientific knowledge presented in this thesis, and in particular the experimental parts presented in Chapter 5 and Chapter 6. Therefore, this chapter is mostly descriptive with limited scientific findings, but with a comprehensive reporting of the engineering issues and implemented solutions.

4.1 Grid to mobility demonstrator layout

The original scope of the demonstrator was organized around three main electrochemical devices: a 200 kW/400 kWh vanadium redox flow battery (VFRB), and two electrolysis systems (see **Figure 4.1**). A complete system for hydrogen processing and dispensing was also developed. Eight programmable logic controllers (PLC) are used to control the different subsystems, and all the data are logged and analyzed in a dedicated control room.

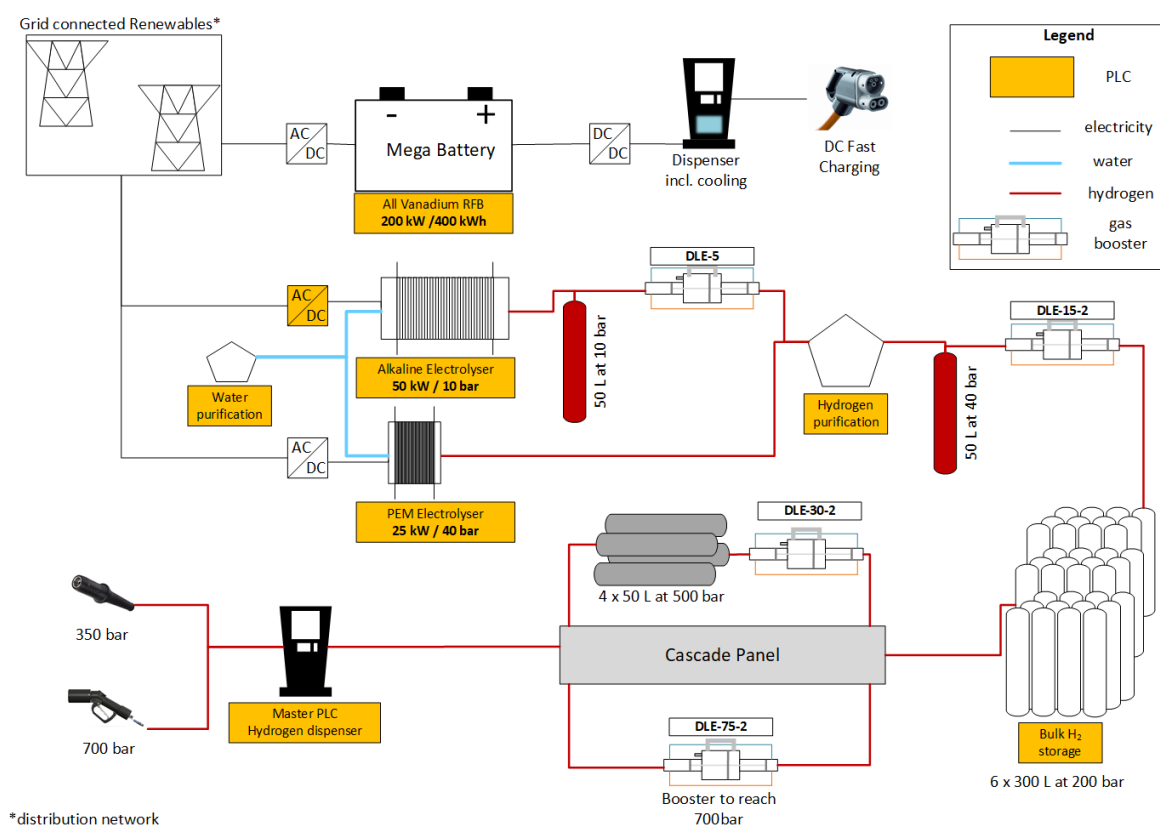


Figure 4.1 - Overview of the systems installed in the demonstrator and corresponding controllers (for readability purposes, the air compressor, which feeds the gas boosters is not represented).

Most of the equipments were mounted on modular aluminium frames from KANYA¹ (standard 50mm profiles). More than 260 pieces were assembled to support cylinders, valves, sensors and electronic cupboards. Electronic systems were assembled on DIN rails in metallic cupboards (Rittal). A Siemens PLC architecture (see **Figure 4.2**), and the programming interface TIA Portal v14 were used for the automation. Temperature measurements are available on dedicated IP addresses with MOXA modules (HRS: 192.168.1.41, PSA and compression: 192.168.1.45). The devices were also equipped with touchscreens or Human Machine Interfaces (HMI) for direct monitoring and interaction. The logging was performed with the OPC server UA Expert². The function GET with the respective IP address of the PLC enables a transfer of process variables and automation signals from one PLC to another.

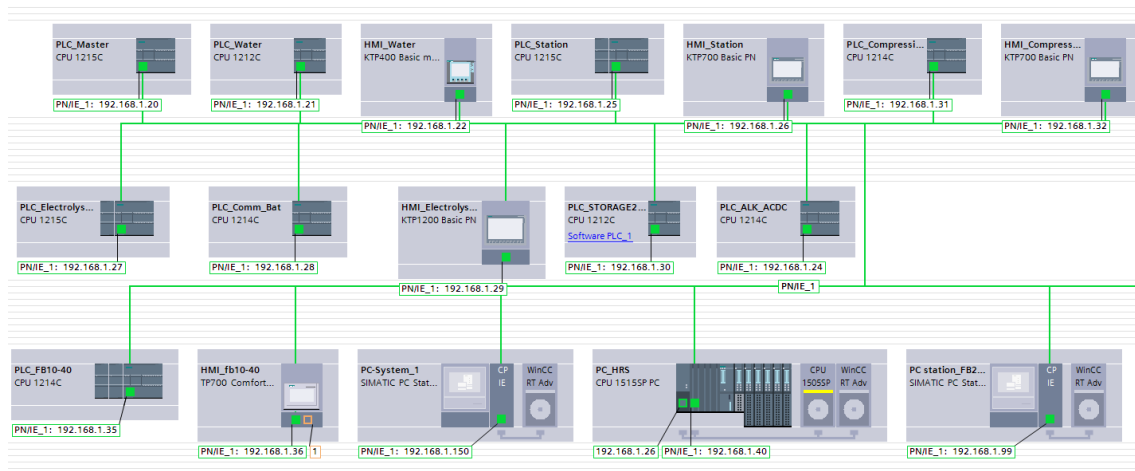


Figure 4.2 – Local network of PLCs in the demonstrator (screenshot from TIA Portal v14).

4.2 Redox Flow battery and DC charger

4.2.1 VRFB fundamentals

All-Vanadium redox flow batteries (VRFB) were developed in the late 80's from an original idea from Rychcik and Skillas-Kazakos [2]. The general scheme in **Figure 4.3** (reproduced from [3]) illustrates the fundamentals of flow batteries, with charge carriers stored in the electrolyte tanks and pumped through electrochemical cells for a charge transfer with an external circuit.

¹ <https://www.kanya.com/fr.html>

² <https://www.unified-automation.com/products/development-tools/uaexpert.html>

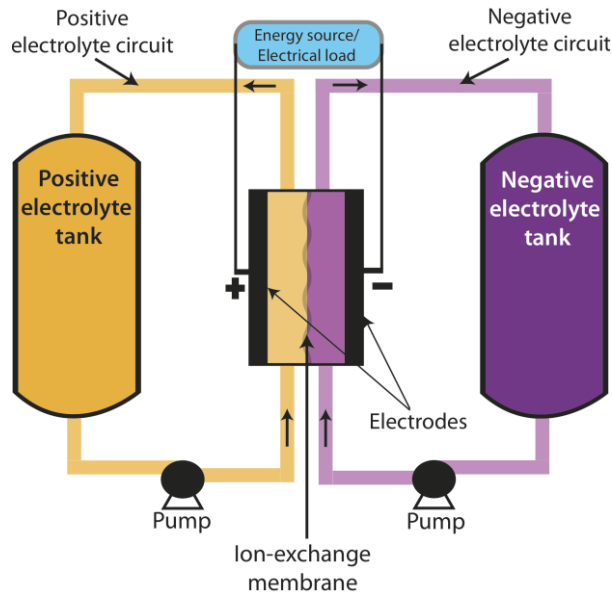
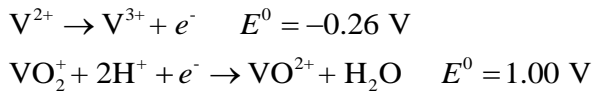


Figure 4.3 – General scheme of a redox flow battery ([3]).

In the case of VRFB, the positive side contains the couple V^{5+}/V^{4+} ions in the form of VO_2^+/VO^{2+} while the negative side is composed of V^{3+}/V^{2+} pair. The species are dissolved in 2M sulfuric acid. The half-reactions during discharge are the following:



Charge levels are limited by the vanadium salts concentration in the solutions, with precipitation occurring on the positive side above 40°C and on the negative side below 10°C [4]. Commercial systems are currently limited to about 1.6 to 2 M vanadium salts concentrations. The initial commissioning electrolyte is a vanadium (III/IV) mixture, requiring a pre-charge from virtually – 50% to 0% during first startup.

Unintentional hydrogen evolution can occur at the negative side while charging at elevated overpotentials or by chemical discharge, catalyzed, for example, on metallic copper. This reaction leads to imbalance of the electrolyte charge levels.

4.2.2 Installation

The VRFB purchased for the Grid to Mobility demonstrator is a 200 kW/400 kWh unit from Gildemeister energy storage GmbH³, referenced as Cell Cube FB 200-400. The purchase order amount was 874 800 € net. This system is arranged in two superposed containers, the lower one containing 26 m³ of acidic vanadium sulfate electrolyte in double walled tanks and the upper one with 80 electrochemical stacks arranged in 4 groups (see **Figure 4.4**). The foundation plate measures 9.25m x 4.70m.

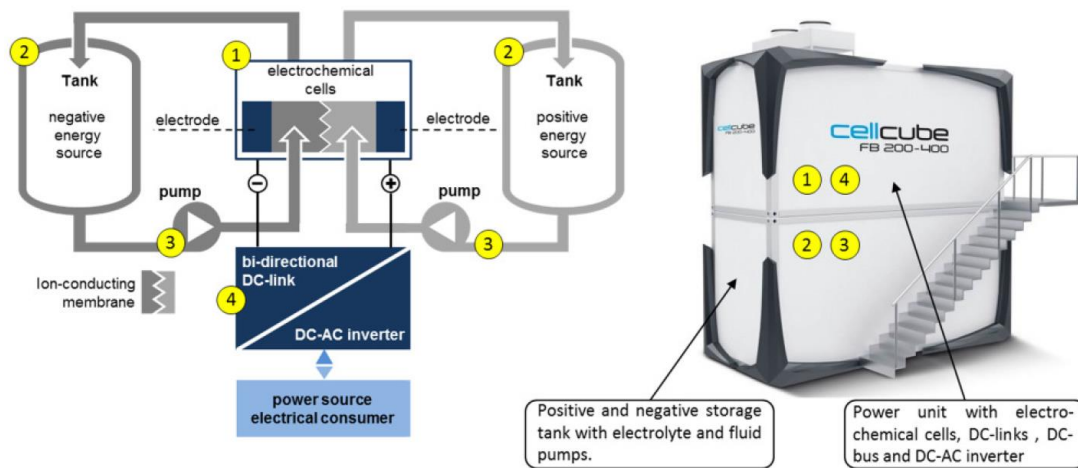


Figure 4.4 – Cell Cube FB 200-400 (illustration from user manual).

The electrical architecture of the CellCube FB 200-400 is based on a DC Bus at 650-750 V, with one DC converter (DC link) per stack. Such a configuration can virtually allow individual stack decoupling. The CellCube FB 200-400 is connected to the 400 VAC 50 Hz network (**Figure 4.5**).

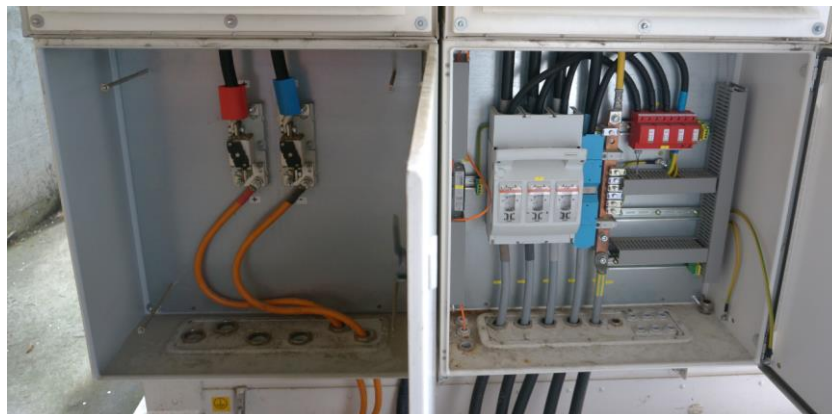


Figure 4.5 – Junction box connections. To the DC charger (left), to the 400 V AC grid (right).

³ Enerox acquired all assets of former Gildemeister energy storage GmbH in May 2018.

Unfortunately, the remote service and monitoring access *via* Modbus, even if included in the scope of purchase, has never been implemented by the supplier. Voltage measurements on one specific stack were performed [5], however limited conclusions can be derived without current measurements.

The VRFB system was connected to a fast DC charger for BEV. The company EVTec AG, arranged a 80kW espresso&charge prototype (unit cost: 70 000 CHF) with a DC/DC converter from Brusa (unit cost 21 000 CHF). An AC connection was still required for the control system and the slow AC charging plug. The initial objective to supply the electrolyser with a direct DC connection from the VRFB was abandoned due to the multiple reliability issues. In addition, the power electronic architecture with a floating high voltage DC line on the battery was particularly challenging regarding available DC/DC converter on the market.

The timeline of events with the VRFB is summarized in **Table 4.1**. The LEPA has deeply investigated the durability issues noticed with this system and developed a dedicated electrolyte purification system [7]. Further work is required on battery management systems to avoid the degradations observed on the stack level.

Table 4.1 - Chronology of events for the Vanadium Redox Flow Battery installed in Martigny.

Date	Event	Comment
14.07.2015	Purchase order	Cell-Cube, same supplier as a 10kW/40kWh system previously operated by LEPA
December 2015	Delivery	
February 2016	Imbalance and high hydrogen levels	
February 2017	Connection of the DC charger by EVTec	
August 2016	Leakages of electrolyte from several stacks	Consecutive to the corrosion of the graphite plates
December 2016 to March 2017	Gildemeister interventions to try to clean the electrolyte, and reduce the rate of hydrogen evolution	Finally the total volume and half of the stacks (40) were replaced.
April 2017	Hydrogen evolution continued	
Summer 2017	Measurement campaign by Declan Bryans	Publication [5]
October 2017	Gildemeister Bankruptcy	
May 2018	Leakage from a damaged hose	
June 2018	Leakage from a stack (old one)	
2019	Multiple exchanges with Enerox to arrange a repair or disposal	No arrangement was obtained

The LEPA has built an extensive experience with VRFB systems from Gildemeister energy storage GmbH thanks to the operation of this CellCube FB 200-400 and a CellCube FB 10-40 during a previous project [6]. The similar stack design and cycling procedures implemented allowed us to notice an important degradation phenomenon. Indeed, the gradual imbalance and hydrogen production is an insidious process occurring in the background with no direct impact on charge/discharge performance. In the initial phase, the battery can still be continuously cycled with no external signs of damage except hydrogen evolution. The gradual degradation of the stack (graphitic plates and current collector) and the consecutive leakages is the first clear external sign of failure. At this stage the electrolyte is fully contaminated and the degradation cannot be stopped without a complete cleaning or replacement of the electrolyte. Thus the battery becomes inoperable.



Figure 4.6 – Aerial view of the VRFB, the electrolysis and the office container during electrolyte replacement.

4.3 Hydrogen Refueling Station

4.3.1 Design

With two vehicles in operation, no more than one refill per day was expected to occur at the demonstrator. When the Grid to Mobility project in Martigny started, limited options were available for HRS with a delivery capacity < 10 kg per day. Later on, a French company, Atawey (<http://atawey.com/>), started to commercialize small units with a peak design capacity of 6 kg/day⁴.

The design of some commercial system and demonstrators is summarized in **Table 4.2**. The indicative cost (installed) for a McFilling 20-350 was ca. 300 000 € with no 700 bar capability and limited modularity and access to measurements for research purpose.

Table 4.2 – Cascade design in commercial systems and demonstrators.

Station	Low pressure source	Compressor	Cascade design
McPhy McFilling 20-350 [8]	600 L bundles at 200 bar	Diaphragm	Two units of 8 x 50 L at 420bar
EMPA [9] With cooling for 70 MPa	6 x 531 L at 30 bar	Piston (Linde) 11 kg/h	6 x 531 L at 440 bar 20 x 50 L at 900 bar
Coop Hunzenschwill With cooling for 70 MPa	87 m ³ at 50 bar underground	Ionic (Linde) 34 kg/h	18 x 50 L at 900 bar Arranged as 8+5+5
Post Auto Brugg	18 m ³ Tube trailer at 200 bar, or electrolyser	Diaphragm (PDC) 5 kg/h	10 x 1200 L at 410 bar
Atawey	50 L at 200 bar	Gas booster 2 kg/day	10 x 50 L at 420 bar
Grid to Mobility demonstrator	6 x 300 L at 200 bar	Gas booster	4 x 50 L at 450 bar 4 x 50 L at 850 bar

One could note that a new design may emerge in the future with bladder accumulators (<http://www.h2ref.eu/>). From the beginning, it was decided not to install a cooling block and thus that the station will not have fast fuelling option at 70 MPa.

LEPA has gained a first experience with air driven gas boosters from the company Haskel during a previous project funded by the SFOE. The easy implementation and high reliability of air driven gas booster were considered a key parameter for the final decision. The final design with two fueling

⁴ One unit was installed in Lausanne for the International Olympic Committee in 2019.

nozzles at 35 and 70 MPa is presented in **Figure 4.7**. The specifications of the selected gas boosters are summarized in **Table 4.3**.

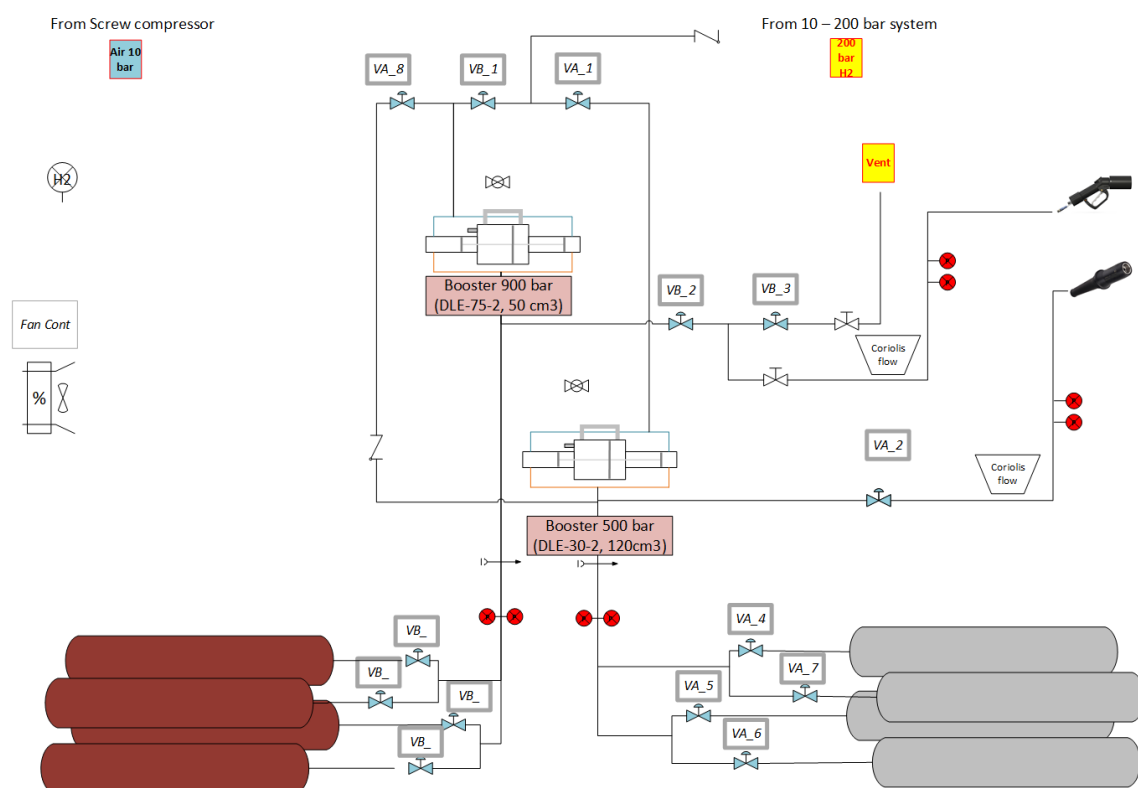


Figure 4.7 – Piping and instrumentation diagram of the Hydrogen Refilling Station.

Table 4.3 – Configuration of the Maximator air driven gas booster installed.

Booster	Inlet	Outlet	Ratio	Stroke	H ₂ quantity per stroke* (20°C)	Unit price
DLE-5	10 bar, from electrolyser	37 bar, to VPSA	3.7	746 cm ³	0.62 g	6440 CHF
DLE-15-2	37 bar, from VPSA	80 - 200 bar, to supply storage	5.4	244 cm ³	0.73 g	8780 CHF
DLE-30-2	80 - 200 bar, from supply storage	200 - 500 bar, cascade storage	6.2	120 cm ³	0.76 - 1.76 g	10 440 CHF
DLE-75-2	200 - 500 bar, from cascade storage	300 - 700 bar, to vehicle	3.5	50 cm ³	0.74 - 1.56 g	11 240 CHF

*volumetric efficiency issues are discussed in Chapter 6

4.3.2 HRS installation

This part of the demonstrator has proven to be very reliable with limited component failures. The O-rings of the spool valve of the gas booster were cleaned and lubricated regularly. No replacement was done in the hydrogen sections. A total of 28.9 kg of hydrogen was delivered with the 350 bar nozzle, and 127.6 kg with the 700 bar nozzle.

About 35 meters of high-pressure pipes and 120 high-pressure fittings were used for the whole installation. Everything was realized on-site with tooling equipments from Maximator (**Figure 4.8**). Therefore, $\frac{1}{4}$ inches (6.34 mm) tubing was preferred for easier bending and for the availability of couplings with sensors and valves without adaptors. The system was assembled in a 10 ft container (**Figure 4.9**).



Figure 4.8 – Processing steps from the delivered pipe to the high-pressure fitting.



Figure 4.9 – Hydrogen refueling station container and dispenser.

The safety concept includes a break away coupling for the nozzles, rupture discs after each compressor, ATEX equipments, normally closed pneumatic-driven valves, compressed air safety buffer, UPS for the control system, continuous ventilation of the container and hydrogen sensor at the top. No crash sensor or accelerometer is included in the dispenser, but an anticollision barrier was installed.

A 3 color control light was installed with the following colour code :

- Green : station ready (nozzle in park position, cascade > 300 bar, compressed air supply ok)
- Flashing Green : dispenser under pressure
- Orange : dispenser not in park position, or cascade < 300 bar, or low compressed air pressure or ventilation failure
- Flashing orange : alarm low H₂ (10 to 25% of LEL)
- Red : pressure measurement out of range (+/- 5bar)
- Flashing Red : alarm H₂ (>25% LEL, flashing faster if level higher)

The Sandia National Laboratories have developed a Hydrogen Risk Assessment Model (HyRAM, <http://hyram.sandia.gov>) which may be used to open the operation of the station to other users. For example, a high flow detection/high pressure variation should be implemented to automatically detect break away, valve or rupture disc failure.

During commissioning, the following tests were performed to ensure the tightness of the elements:

- Pressurization with nitrogen and observable leaks with leak detection foam.
- Helium tracer in nitrogen for leak detection with thermal conductivity detector.
- Multiple purge and vent cycles with Hydrogen 6.0. Overnight control of pressure evolution.

Flow meters for the compressed air were installed during Fall/2018.

Plugs for the 900 bar cylinders were ordered from several workshops with no successful tightness with hydrogen above 400 bar. Teflon tape was applied on the thread and a dynamometric wrench set at its maximum (210 N·m) was used. Since the Spring 2019, 2 of the 4 cylinders are operated at 400 bar maximum. The two other cylinders still presented leaks and were disconnected from the system.

4.3.3 HRS programming

The HRS was programmed with the software Siemens TIA Portal v14, running on a PLC CPU 1515 SP PC, with a 17 inches touchscreen HMI. The total program takes 98 pages and 17 networks in the block format.

For safety reasons, an automated protocol was only programmed for the 35 MPa nozzle. Most of the programming architecture for sequential events is based on the following blocks:

- SR: Set/Reset Box, with priority for the reset input.
- Positive or negative edge detection
- Time pulse

All the valves controls are grouped in a dedicated network with the corresponding opening conditions (see VA1 example in **Figure 4.10**).

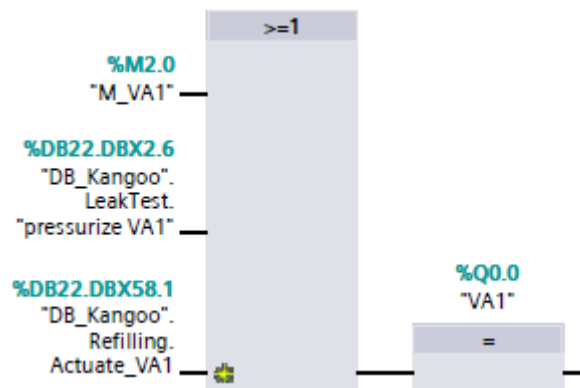


Figure 4.10 – Opening conditions for VA1.

For the automated 35 MPa refill protocol, 4 successive sequences are programmed (see **Figure 4.7** for the corresponding reference to the valve denominations):

- **Leak test:**
 - Initial vent: open VA3 for 3 seconds
 - Open VA1 for 2 seconds
 - Open VA2 for 5 seconds
 - Record the pressure in the dispenser, wait 15 seconds and compare with the new value → if more than 5 bar difference, leak test failed. Else leak test ok, and continue to the next sequence. At this time the initial value of the flowmeter with the total mass transferred is also recorded in order to compute the final value at the end of the refill.
- **Pressure determination:**
 - Open VA2 and VA2 remains opens until the end (stop by pressure or vent)
 - Open VA7 for 1 second, the highest pressure buffer. The goal is to trigger the opening of the check valve of the car, which will close again when the pressure in the pipe is equal to the pressure of the car tank.
 - Wait 5 seconds for a stabilized reading of the dispenser pressure.

- **Supply storage equilibration and cascade:**
 - Based on the determined pressure, the first storage with a pressure $>$ initial car pressure + 20 bar is opened. The decision to move to the next buffer is taken when the mass flow goes below 1.8 g/s and after at least 4 second of opening of the corresponding buffer. The car pressure + 20 bar rule is used for each stage.
 - This sequence terminates when no positive decisions for refill are taken for 3 seconds.
- **Vent:**
 - All valves (including VA2) are closed when this sequence is active.
 - After 0.5 seconds the final pressure and total mass transferred are recorded.
 - After 10 seconds and all valves properly closed, VA3 is open for 3 seconds. In order to limit the noise during this pressurization some stations include a flow limiter and depressurize with several short openings of the valve. This is not implemented here.
 - This sequence terminates when the pressure in the dispenser goes below 2 bar. The final screen with final pressure, total mass transferred and duration is displayed on the HMI.

This protocol results in 5 minutes refills for a 70 L reservoir (see **Figure 4.11**).

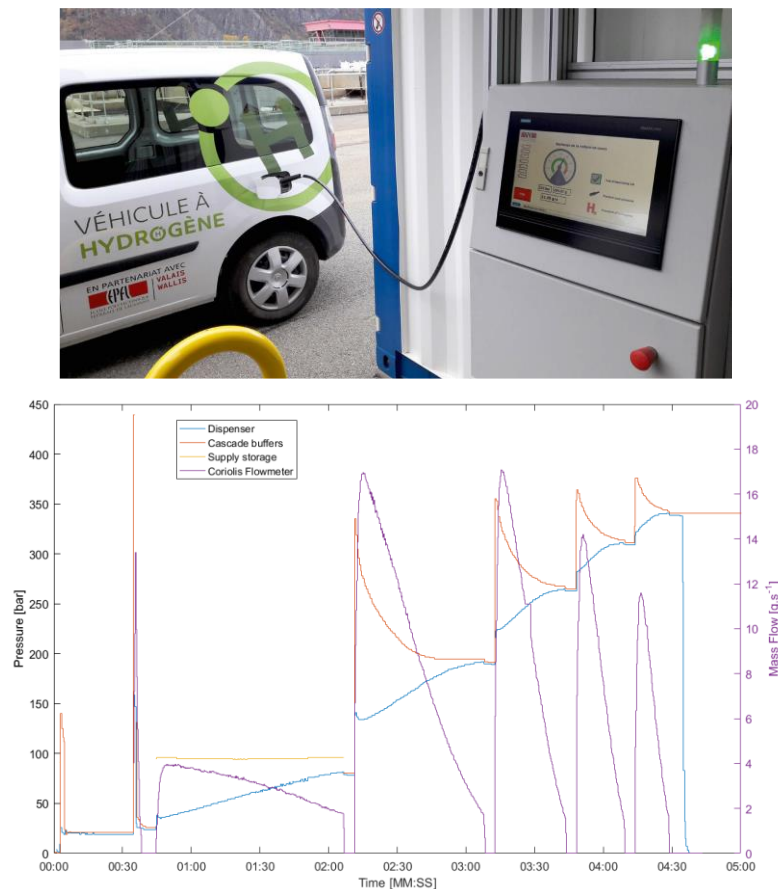


Figure 4.11 – Automated refilling protocol at 35 MPa.

The failures modes in this automated protocol are:

- Leak test failed: more than 5 bar decrease in 15 seconds
- H₂ detection: more than 10% LEL in the container
- Too high pressure in the dispenser: set at 400 bar
- Target pressure of 350 bar not reached
- Non matching pressure measurements for sensors installed in the same location: +/-5 bar
- Emergency Stop Button activation

In the absence of IR communication with the 35 MPa nozzle, no abort signal can be transmitted from the vehicle.

The various screens displayed on the HMI are presented in **Figure 4.12**.

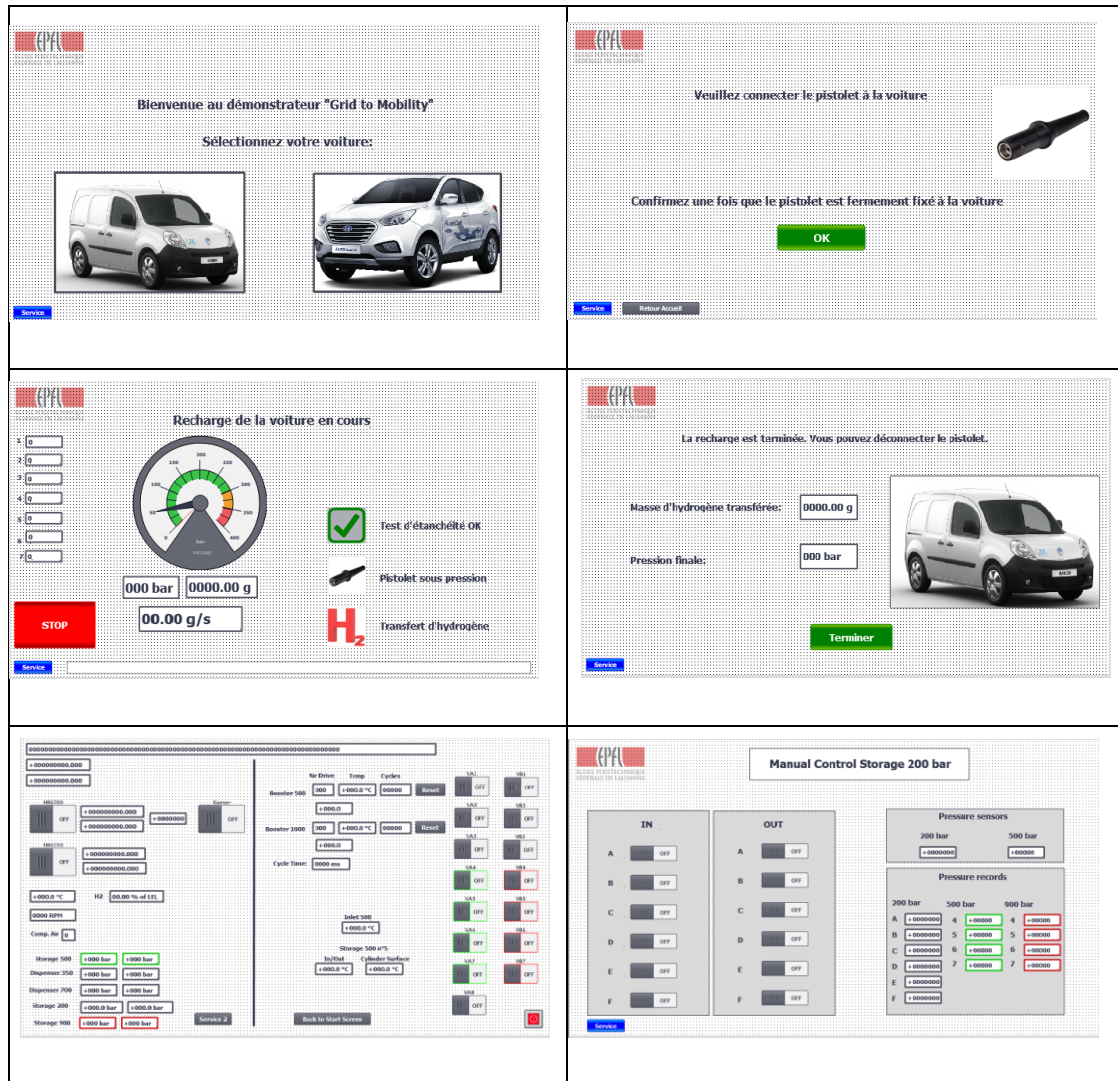


Figure 4.12 – User interface screens (manual controls at the bottom).

One of the main differences with commercial stations is the absence of automatic dynamic flow control devices, thus we can observe in **Figure 4.11** large variations in the flow with up to 18 g/s. The use of small pipes naturally limits the maximum flow. For 35 MPa refills, without communication, the SAE J2601 lookup tables [10] mention pressure ramp rates of 28 to 38 MPa/min, which, in this case corresponds to 23 to 30 g/s.

A pressure regulator would allow to follow average pressure ramp rates as recommended in the SAE J2601 protocol. A quotation at 9000 € was obtained for such a device including an ATEX controller (TESCOM ER5000, similar to the one installed at the EMPA station). Such a device should be installed before a pressure sensor which will provide a feedback signal to the valve controller. Such valves are typically supplied with compressed air at 6-10 bar. In the absence of a regulation of the pressure ramp rate, the HRS can only be used for research purpose and it is not recommended to fill vehicles with type IV reservoirs, which are more prone to temperature damages. More investigations on the cascade topology would allow to determine the cooling demand [11].

Despite of the limitation of the demonstrator for 70 MPa refills, we implemented the IR communication signal reading, according to the SAE J2799 [12]. If the 70 MPa fueling nozzle is not detected in its parking position, the IR communication block is activated. A string signal is sent every 100ms and specific values are extracted for the log. The format is as presented in **Figure 4.13**. To make sure that the scanned string contains enough elements, the received bits are stored in a buffer which is scanned only when it contains at least 69 characters.

Data format According to SAE J2799 / J2601			
Variable	Unit	Range	Format
Protocol Identifier	N/A	SAE J2799	ID=SAE_ J2799
RDI Software Version Number	N/A		VN=##.##
Tank Volume	Liter		TV=####.#
Receptacle Type	N/A		RT=H##
Fill Command	N/A		FC=Dyna
Measured Pressure	MPa		MP=####.#
Measured Temperature	Kelvin		MT=####.#
Optional Data	0-74 characters not including " "		OD=ASDEFINEDINJ2601

Figure 4.13 – IR signal format according to SAE J2799.

The fill command can take the following values:

- Dyna: the dispenser shall dispense fuel based on the table-based communication fueling protocol.
- Stat: shall not be used. If this command is received, the station shall consider non-communication protocol.
- Halt: is optional for vehicles. The dispenser shall pause the fueling process and restart if Dyna is received again for at least 2 seconds or terminate the fueling process if Halt is received for over 60 seconds.
- Abort: the dispenser shall terminate the fueling process within five seconds.

This command value is observed during manual refill procedures with the 700 bar nozzle.

No automation was implemented for the cascade compression. A specific attention is attached to the temperature evolution during such procedures (see Chapter 6).

The list of recorded variables is presented in **Table 4.4**.

Table 4.4 – Recorded variables for the HRS.

Type	Name	Sensor type / supplier
Pressure	Pressure_HRS_200_A	AST
Pressure	Pressure_HRS_500_Stor_A	AST
Pressure	Pressure_HRS_900_Stor_A	AST
Pressure	Pressure_HRS_350_Dis_A	AST
Pressure	Pressure_HRS_700_Dis_A	AST
Pulse	Pulse_Booster_500	Pressure differential
Valve	AO_VPropB500	Analog output
Pulse	Pulse_Booster_1000	Pressure differential
Valve	AO_VPropB1000	Analog output
Gas sensor	H2_sensor_HRS	Cosmos KD12B
Modbus	Mass Flow Grand Total_350	Kem Küppers Coriolis
Modbus	Mass Flow Rate_350	Kem Küppers Coriolis
Modbus	Temperature_350	Kem Küppers Coriolis
Modbus	Mass Flow Grand Total_700	Kem Küppers Coriolis
Modbus	Mass Flow Rate_700	Kem Küppers Coriolis
Modbus	Temperature_700	Kem Küppers Coriolis
IR comm	scaled P bar	IR comm
IR comm	scaled T Celcius	IR comm
Records	Record_P_A4 to Record_P_A7	AST
Temperature	Temp1 to Temp 6	PT100
Counter	Counter_Booster_500	Controller
Counter	Counter_Booster_1000	Controller
Time	CycleTime	Controller
Air flow	M_Airflow500	E+E Elektronik
Air flow	M_Airflow900	E+E Elektronik

4.3.4 HRS PLC wiring diagram

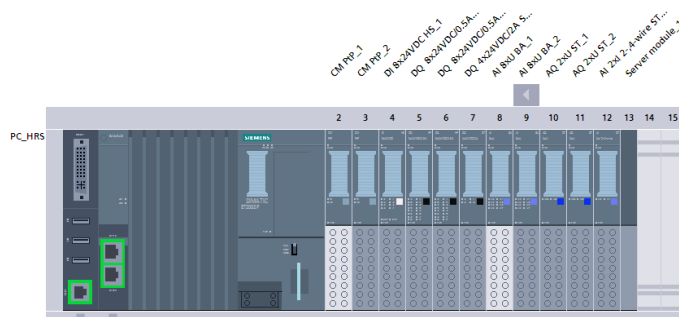


Figure 4.14 – HRS PLC modules.

The main block on the left is receiving temperatures data via Ethernet and is linked to the local supervision network and the HMI. Modules number 2 and 3 are used for communication with the infra-red signal from the 700 bar fueling nozzle (Module 2) and Modbus data from the flowmeters (Module 3).

Digital inputs have addresses starting with %I, digital outputs are starting with %Q, analog inputs with %IW and analog outputs with %QW.

Table 4.5 – HRS PLC modules wiring information.

Module	Adress	Name tag	Description
4	%I16.0	EmergencySTOP	Position of the emergency stop button
4	%I16.1	Tacometer in	
4	%I16.2	CompAir_input	Positive if sufficient air pressure
4	%I16.3	P_H70 at home	Position of the 700 bar fueling nozzle
4	%I16.6	Pulse_Booster_500	Booster impulsions
4	%I16.7	Pulse_Booster_1000	Booster impulsions
5	%Q0.0 to %Q0.7	VA1 to VA8	Pneumatic Valves control
6	%Q1.0 to %Q1.6	VB1 to VB7	Pneumatic Valves control
6	%Q1.7	Alarm_light	Yellow alarm light
7	%Q2.0	GreenLight	3 colors light on the dispenser
7	%Q2.1	OrangeLight	3 colors light on the dispenser
7	%Q2.2	RedLight	3 colors light on the dispenser
7	%Q2.3	IR_Pistolet	
8	%IW17 & %IW19	PSens_HRS500_A & B	Pressure sensors for the 500 bar cascade
8	%IW21 & %IW23	PSens_HRS350_A & B	Pressure sensors for the 350 fueling line
8	%IW25 & %IW27	PSens_HRS900_A & B	Pressure sensors for the 900 bar cascade
8	%IW29 & %IW31	PSens_HRS700_A & B	Pressure sensors for the 700 bar cascade

9	%IW33 & %IW35	PSens_200_A & B	Pressure sensors for the 200 bar storage
9	%IW37	H2_sensor_HRS	
10	%QW3 & %QW5	AO_VPropB500 &1000	Setpoint for the opening of the proportional valves
11	%QW7	AO_Fan_speed	Speed of the ventilation fan
12	%IW49 & 51	AirFlow500 & 900	Flow meter for compressed air input

4.3.5 Dynamic refueling model on MATLAB

Based on the measurements, a dynamic refueling model was programmed on MATLAB in order to estimate the duration, and target pressure achievable for various configurations. The following inputs should be entered by the user:

- Number of steps
- Initial pressure and volume for each step
- Initial pressure and volume of the vehicle tank
- Switching condition (flow, duration, target pressure)

The coefficients for the mass flow calculation are derived from the measurements, the formula is derived from the approach used by Farzaneh-Gord *et al.* [13], the corresponding code is presented below (the index c refers to the car and the index r refers to the buffer reservoir). The equations of state from the SAE J2601 [10] are used.

```

Cd=1;%discharging coefficient of the orifice, stands for
irreversibility. 1 for reversible process
Aorifice=0.55;% scaling factor parameter to adjust to fit to station
data
gamma=5/2;
Pdrop=0.3;%pressure drop in the dispenser lines, in MPa
flowlimit_ratio=0.45;% (2/(gamma+1))^(gamma/(gamma-1)),pressure ratio
threshold for debit limitation, adjusted with experimental data

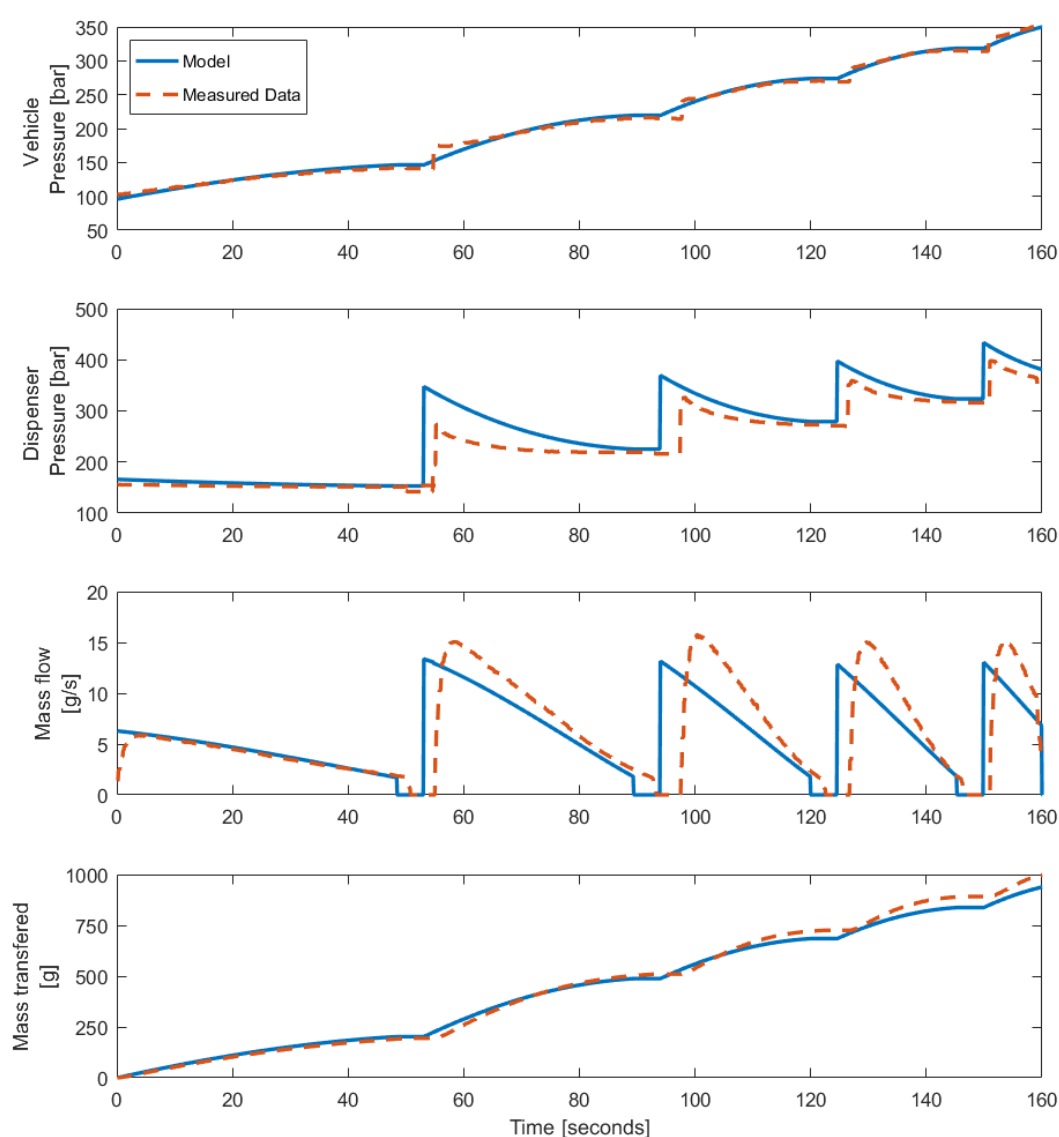
massflow=@(Pc,Pr,Tr) ((Cd*ro(Pr,Tr)*Aorifice*(Pc/(Pr-
Pdrop))^(1/gamma)*((2*gamma/(gamma-1))*((Pr-Pdrop)/ro(Pr,Tr))* (1-
(Pc/(Pr-Pdrop))^(gamma-
1)/gamma)))^(1/2)))).*(Pc/Pr>flowlimit_ratio)+(Cd*sqrt(gamma*(Pr-
Pdrop)*ro(Pr,Tr))*Aorifice*(2/(gamma+1))^(gamma+1)/(2*(gamma-
1)))).*(Pc/Pr<flowlimit_ratio);

```

Once the rules for hydrogen mass flow are defined, the rest of the code consists of iterative mass balances between the source reservoirs and the vehicle. Temperature exchanges with the environment and with the thermal mass of the reservoir is not considered in this simple model, which may explain some differences with the measurements presented in **Table 4.6** and **Figure 4.15** (in addition the model reflects the static pressure, while the measurements are dynamic).

Table 4.6 – Cascade simulation results for a Kangoo refill (22.01.2019 data).

Reservoir	Volume	Initial state	Final state real	Final state model
Kangoo	70 L	96 bar	350 bar	350 bar
Supply storage	300 L	166 bar	154 bar	156 bar
Cascade stage 1	50 L	348 bar	234 bar	228 bar
Cascade stage 2	50 L	370 bar	288 bar	282 bar
Cascade stage 3	50 L	398 bar	330 bar	326 bar
Cascade stage 4	50 L	434 bar	384 bar	386 bar

**Figure 4.15** – Modelling tool for cascade refuelling.

4.3.6 Others uses of the HRS

The high modularity of the station was used to perform tests for the company GreenGT (<http://greengt.com/>) during the development of their endurance racing car Mission H24. Because the station was not designed for such large tanks (3 x 70 L), a multi-stage approach was used as presented in **Figure 4.16**. In addition, single reservoirs were also tested and connected to the station for a partial recycling of the refilled hydrogen, and a connection to our venting system (**Figure 4.17**).

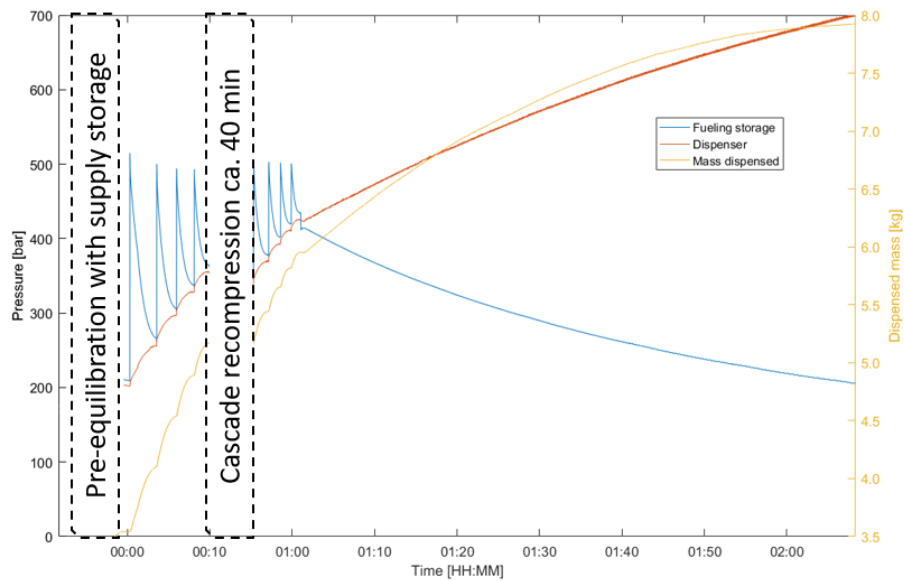


Figure 4.16 – Dispensing of 8 kg of hydrogen with two cascade and a slow refill.



Figure 4.17 – Type IV reservoir testing for GreenGT.

This test campaign, with controlled defueling speed, evidenced the need for thermal studies on the defueling/refueling sequences with steep pressure ramp rates.

4.3.7 Hyundai ix35 Fuel Cell car

The installed datalogger does not provide a readable input and is unfortunately reserved for Hyundai service only.

The car functioned properly during the whole course of the project, including cold starts by -10°C , fast highway driving ($>150\text{ km/h}$ on German highways), city and mountains trips. The first issue came after *ca.* 14 000 km, with a warning about the conductivity of the fuel cell coolant, which may indicate some corrosion issues. The 4 years/15 000 km service consisted in the replacement of the following equipments for a total amount of 1350 CHF (At the time of writing, only one garage in Switzerland is certified for fuel cell vehicles maintenance: Garage Marti AG in Niedergösgen):

- Air filter
- Pollen filter
- Braking fluid
- Ionic filter
- Cooling fluid

Only the lead-acid battery (for lights and on-board electronics) requires a specific attention in the case of slow refills. A depleted 12V battery does not allow to start the car or even to close/open doors.

4.3.8 Costs and hardware suppliers

Hyundai ix 35 Fuel Cell : 60 000 CHF

Hydrogen storage:

- Carbagas: Delivery H60. 855 CHF per 200 bar bundle
- Carbagas: Empty bundle 600 L. 8100 CHF
- Carbagas: storage 500 bar. 1900 CHF per unit 50 L, 210 kg (1.8m, ext diam 244.5 mm)
- Faber industrie: Storage 900 bar. 4500 CHF per unit 50L, 228 kg (1.8 m, ext diam 262 mm)

Others:

- Bürkert: explosion proof rotary actuator. Model 3004. 1500 CHF per unit
- Maximator: 2-way straight valve air operated normally close, for hydrogen, 1050 bar. 848 CHF per unit
- Kem Küppers: Coriolis mass flow meter. Model TCMH 0450 SPPS and SRPS. 6200 € 600 bar, 7800 € for 900 bar + ATEX power supply at 2145 € each.
- Maximator: various high-pressure tubing (1/4) and fittings, rupture disc 81 CHF per disc. 44 CHF per meter of 1/4 tubing

- Stäubli: fueling nozzle for 35 MPa hydrogen. Model CHV08. 3800 CHF (incl. 3.8 m hose, nozzle and break away)
- WEH: fueling nozzle for 70 MPa hydrogen. Model TK17 H2. 900 CHF + 1700 CHF for 4 m hose + 3200 CHF for break away valve
- Kaeser BSD 75 SFC screw compressor for compressed air supply. 33 000 CHF + buffer 900 L 2200 CHF. A heat recirculation system for this 37 kW compressor was installed, however, due to the large volume of the building, the poor insulation and the few number of operating hours (6.6 MWh, i.e. ca. 350 hours at 50%) this had a limited impact.
- American Sensor Technologies: various pressure sensors, from 200 to 900 bar. 200 – 280 CHF per unit
- E+E Elektronik: flow sensor for compressed air. Model EE741-A6D2AC2DN25 – 673 CHF per unit
- A pressure regulator with ATEX electropneumatic controller (not implemented) cost about 8 800 CHF (TESCOM)

Note on safety: Many guidelines and regulations are already in place for hydrogen infrastructure, vehicles and equipments: filling requirements (SAE J2601, SAE J2799, ISO 19880...), vehicles (EC79, ISO 23273, NI 547 ...), reservoirs (ISO 11114) and gas quality (ISO 14687). However, this demonstrator was built and operated as a laboratory equipment, with a design in constant evolution. No formal HAZID (Hazard Identification) and FMECA (Failure Mode Effects and Criticality Analysis) studies were performed, but, under the EPFL guidelines, safety audits were conducted and only users with a deep knowledge and understanding of the systems had access to the installations.

4.4 Electrolyser

A detailed analysis of the collected data is provided in Chapter 5.

4.4.1 Installation

The initial scope of the project included a commercial alkaline electrolyser and a commercial PEM electrolyser. However, due to the events described in **Table 4.7** and the limited capabilities of the delivered system, it was decided to focus on the balance of plant of the alkaline electrolyser. Therefore, no raw data is available for PEM electrolysis, except the stacks supplier specifications.

Table 4.7 – Chronology of events for the McLyzer 10-10 installed in Martigny.

Date	Event	Comment
27.07.2015	Purchase order	McPhy Energy, McLyzer 10-10 (50kW)
22.12.2015	Partial delivery	Control and water pump were delivered later
30.03.2016	First test with McPhy team	Failed, with electrolyte leaks and unexplained detonation
May to July 2016	Unsuccessful attempts to run the electrolyser	Sparks, frozen controls, loss of water via the condensate collector, erratic appearance of error messages, chiller leakages
August to September 2016	Set points adjustments	Frozen controls, sensor failures, lye in production lines
Winter 2016-2017	Disassembly and redesign hardware and software	Excessive degradation of some equipments
2017	Rebuilt	Multiple failures from accessories and sensors
Since September 2017	Operation without purification	Stack exchange in April 2018 after pump failure
Since January 2019	Operation with purification	42.78 MWh consumed in total

The McPhy Italy team, in charge of McLyzer 10-10 series, was experienced on hydrogen production for welding stations. The requirements for hydrogen mobility and renewable energies (gas purity, power modulation, pressure, efficiency) lead probably to some misunderstandings and issues for a reliable operation of our McLyzer 10-10 in an academic research environment. The delivered system was unable to pass the site acceptance tests. The hydrogen and fuel cell center ZBT in Duisburg, Germany, has reported similar issues with a McLyzer 10-10. In their case, it seems that the thermal

stress on the stacks also triggered some leakages. As a general comment, it appears that a Declaration of conformity and CE certificates are insufficient to ensure a smooth commissioning.

4.4.2 Design and construction

An agreement was found with McPhy Energy in order to pursue the commissioning of the McLyzer on our own. For more flexibility, the original electronic cupboard was removed and the automation system on printed circuit boards was replaced and reprogrammed with PLC based modules. A new set of auxiliaries, sensors, gas processing and pipping equipments was installed in order to refurbish the McLyzer 10-10 into a fully instrumented and programmable scientific research equipment.

The original design is presented in **Figure 4.18**. In addition, a dedicated purification and compression unit was installed at the outlet (see Chapter 5). The water purification system was not in the scope of supply, the following equipments were added to obtain a sufficient water quality (conductivity $<1 \mu\text{S}\cdot\text{cm}^{-1}$):

- Pre filter in PTFE
- UV lamp
- Reverse osmosis and activated carbon filter (osmoser type PRF-RO)
- Ion exchange resine (mixed bed from Evoqua)
- Pressurized water reservoir at 5 bar (N.B. due to the volume of air on top of this reservoir, a bladder tank would have been more appropriate to reduce the amount of dissolved gases)

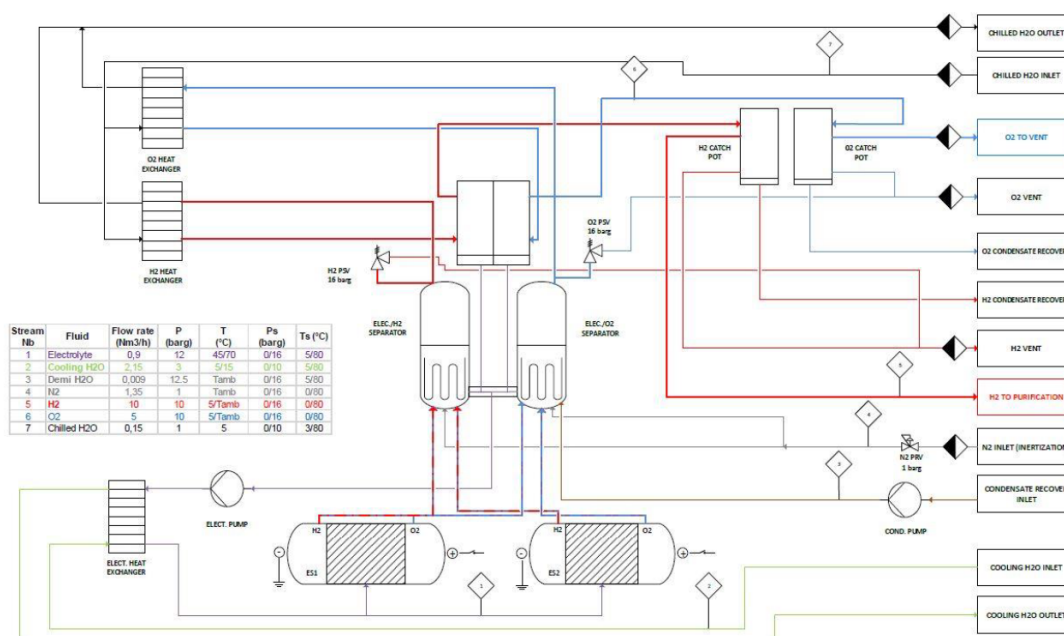


Figure 4.18 – Simplified flow sheet of a McLyzer 10-10.

The major changes during the rebuilt of the electrolyser were:

- remove the condensate recovery system, which brings too much complexity and reliability issues
- add a scrubber to clean the gases, and the overall gas processing strategy
- change NaOH 20 w% for KOH 30w%. The solution (*ca.* 60 liter) was prepared from deionized water and KOH flakes. The final weight concentration was confirmed with a titration using a phenolphthalein indicator. With a measurement of $302 \text{ g}\cdot\text{L}^{-1}$, it corresponds to $5.4 \text{ mol}\cdot\text{L}^{-1}$. Specific temperature, concentration and conductivity graphs were reported by Gilliam *et al.* [14]
- electrolyte pump
- operation strategy for inertization and pressure ramp up
- Introducing PID for the temperature management

The footprint of the system (without control cabinet) is about 1.5 x 1.5 x 2m and weights 850kg. The side panels were removed for direct control, and prevent gas accumulation.

In a cooperative approach with McPhy Energy, spare stacks were delivered. Thus, in order to better understand the system, it was decided to unmount and replace one of the two stacks, even if no defective behavior was noticed. The cell assembly can be observed in **Figure 4.19**. The respective dimensions of the cells' components are reported below:

- Plastic frame and O-ring: 262 g and 34 cm diameter
- Diaphragm: 37g dry, 1.3 mm thick, made from a polysulfone cloth
- Bipolar plates: 226 g and 25 cm diameter (22.5 cm for the active surface). 0.6 mm thick. Some deposits of iron material particles can be observed. We assumed that dissolved iron from the piping and auxiliaries deposits on the cathode surface. This may enlarge the true surface area, but also obstruct the diaphragm. With this demonstrator, insufficient data is available to conclude on the activation role of this deposit [15].



Figure 4.19 – Stack replacement and assembly analysis.

For comparison with a 25kW PEM stack from Giner, the stack characteristics are summarized in **Table 4.8**.

Table 4.8 – Stack comparison of PEM and alkaline electrolyser.

	PEM	Alkaline
Number of cells	14	2 x 115
Active surface area	300 cm ²	370 cm ² (22.5 cm diameter minus the orifices)
Length between end plates	58 mm	703 mm
Cell thickness	4.1 mm	6.1 mm
Diaphragm thickness	-	1.3 mm (dry)
Bipolar plate thickness	-	0.6 mm

In addition to the replacement of most of the hardware, except the stacks, the gas separator and the heat exchangers, a new wiring and control system was built. The electrical cabinet with the AC-DC converter was not changed. The inside of the control cabinet is shown in **Figure 4.20**, with (from top to bottom) frequency controllers (for the cooling fans), PLC, relays, and power supplies.

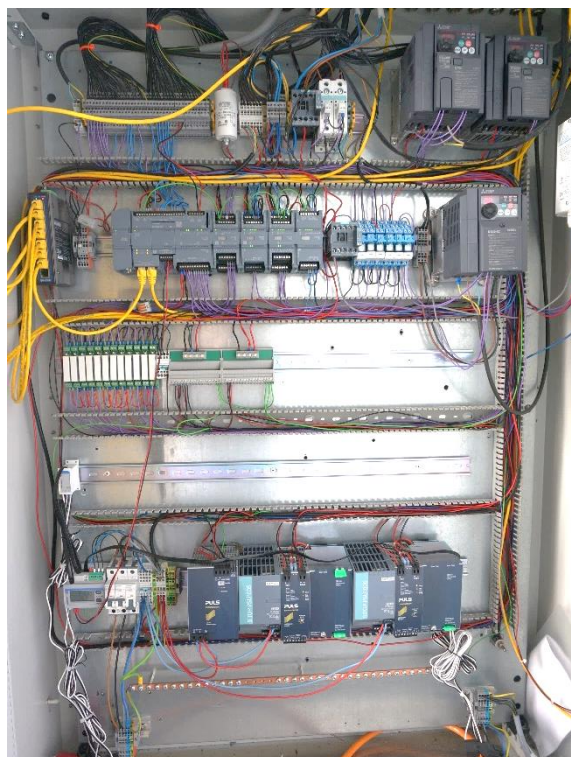


Figure 4.20 – Electrolyser control cabinet.

The overall design after reconstruction is presented in **Figure 4.21**. Redundancy, and sensor failures was one of the main concerns with this electrolyser. This approach was also present in the original design. For example, in the gas separators, in addition to the continuous level sensor, digital switches for the high and low level are included. The pressure operation window is comprised between 8.0 and 11.5 bar. Outlet valves are closed at 8.0 bar and the power supply to the stack is turned off if the pressure reaches 11.5 bar. In addition, mechanical vents will be triggered if the pressure exceeds 16 bar.

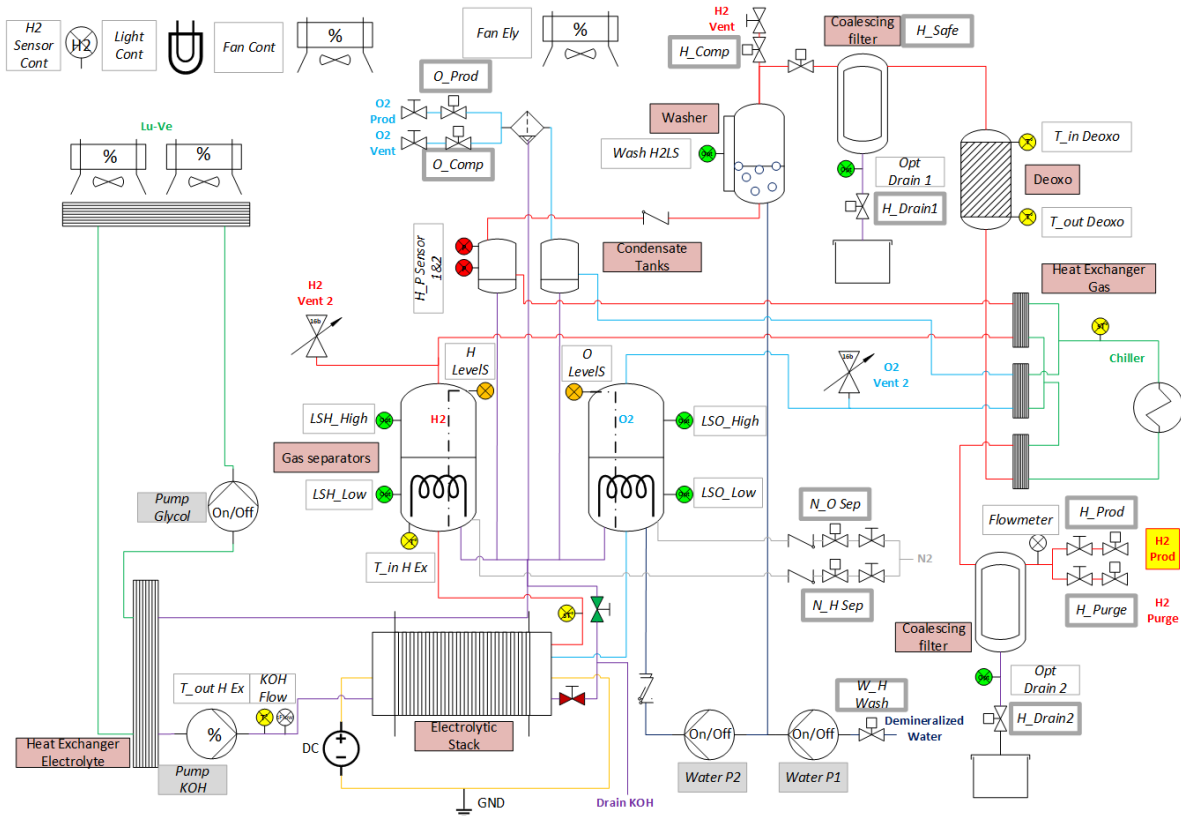


Figure 4.21 – Piping and instrumentation diagram of the electrolyser after redesign.

4.4.3 Electrolyser programming

The electrolyser was programmed with the software Siemens TIA Portal v14, running on a PLC CPU 1214C, with a touchscreen HMI. The total program takes 174 pages and 23 networks in the block format.

5 specific sequences were programmed :

- Pressurization: with N₂ until the system reaches 10bar. The level balance is ensured with separate N₂ inlet on each side. Originally, the nitrogen supply was at 2 bar only and the system was pressurized with the produced hydrogen and oxygen.
- Purge: the stacks are powered, but the production is redirected to a purge outlet due to the low purity of the produced gas, contaminated with nitrogen. During this sequence, the current is limited to 70A. The electrolyte is still at low temperature thus with a low conductivity and high overpotentials.
- Production: nominal operation mode.
- Inertization: when the production sequence is stopped and no more current is applied to the stacks, the system is flushed with nitrogen on both sides.

- Depressurization: Before shut down, the system is cooled down with the fans at maximum speed and depressurized to atmospheric pressure with 2 bar increments.

A hot standby mode was also programmed (no current applied to the stacks, oxygen side periodically purged with nitrogen, electrolyte kept warm with heating jackets), but due to unstabilities in the programming, it was not tested.

During operation, four controls blocks are continuously in operation, they play a critical role for the system safety and stability.

Temperature control

When the electrolyser is not in operation, the electrolyte cools down to ambient temperature. If this temperature goes below 10°C, the electrolyte circulation pump is activated together with the heating jacket. During the start-up sequence, the electrolyte progressively warms-up with the overpotentials. The glycol pump is started when the electrolyte reaches 48°C. Eventually, the fans on top of the container are started when the temperature at the inlet of the heat exchanger reaches 60°C. Finally, a PID adjusts the speed of the fans to reach a target regulation temperature of 52.5°C at the outlet of the heat exchanger. For safety, a temperature switch is set at 72°C at the outlet of the stack, which is supposed to be the hotspot. The current supply to the stack is turned off if this temperature is reached.

Level control in the gas separators

Because the hydrogen and oxygen production lines are not connected, a fine tuning of the proportional relief valves at the outlet is required. Moreover, any variation in the suction of a purification or compression system downstream directly affects the system pressure. In order to adjust the levels in the gas separators, we rely on compensation valves, which, for a short period of time can release part of the pressure (bring the electrolyte level up) on one specific side. Because the separators are interconnected at the bottom, releasing the pressure on the hydrogen side will bring oxygen rich electrolyte into the hydrogen separator. In order to avoid this contamination, it was decided to intentionally restrict the oxygen side in order to force the opening of the compensation valve mainly on the oxygen side. The following hysteresis rules are defined:

- Ocomp is open if:
 - $O\text{ level} < H\text{ level} - 5$ and remains open until $O\text{ level} > H\text{ level} + 3$
- Hcomp is open if:
 - $H\text{ level} < O\text{ level} - 10$ and remains open until $H\text{ level} = O\text{ level}$

Pressure control

With no proportional valve, the only overpressure protection is to cut the current and to rely on pressure relief valves. At low production rates, the level regulation may lead to large pressure losses. Thus, when the pressure goes below 9 bar the outlet valves are closed. However, because the volume of oxygen produced is only half of the volume of hydrogen, closing the valves creates a negative feedback loop on the level control. Currently, at low production rates this regulation has proven to be relatively unstable. Drains are purged with 200 ms pulses (see **Figure 4.22**). This is long enough to push the water out, but short enough to avoid significant pressure losses and level disturbances. The pressure variations in downstream purification and compression processes are partially filtered with a 50 L buffer reservoir at the outlet.



Figure 4.22 – Drain purge system after a coalescing filter (wet sensor and solenoid valve).

Water control

The deionized water introduced in the system is mixed with the electrolyte and a stable concentration of KOH must be ensured to maintain the conductivity characteristics of the system. In this system, two pumps are used to fill both the electrolyte circuit and the scrubber. The electrolyte circuit is filled up when the sum of O and H levels goes below 110. And the corresponding pump (Water pump 2 on **Figure 4.21**) is stopped when it goes above 115. When no current is applied the respective levels for the hysteresis are 80 and 85. In the scrubber, the water pump (P1) is activated if the level switch is in the dry state. The pump is stopped when the level switch remains in the wet position for 10 seconds.

These four control processes can be continuously monitored on the HMI screens presented in **Figure 4.23**. When the automation is deactivated, valves can be opened independently on a dedicated screen, this is particularly useful when no automated procedure is programmed for an unusual failure (see paragraph 4.4.5).

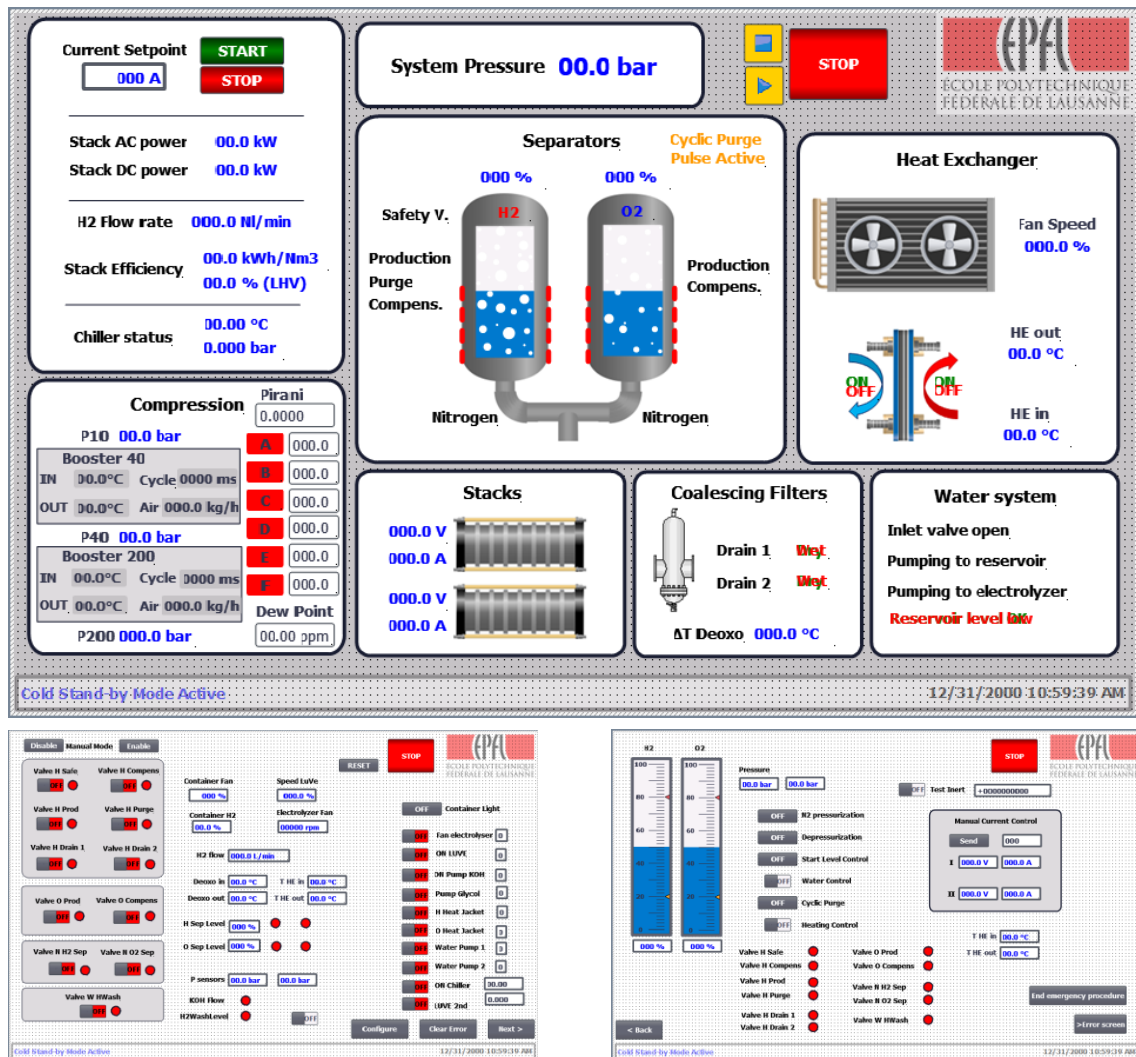


Figure 4.23 – HMI screens for electrolyser control and monitoring.

Table 4.9 – Recorded variables for the electrolyser.

Type	Name	Sensor type / supplier
Power	P1_L1, P1_L2, P1_L3	Carlo Gavazzi Power meter
Power	P2_Tot (Chiller)	Carlo Gavazzi Power meter
Counter	Counter Drain 1	PLC
Counter	Counter Drain 2	PLC
Level	Ely level unbalance	calculation
Pressure	H Psensor1, H Psensor2	Gems sensor
Level	H levelsensor, O level sensor	Valco linear, magnetic float
H ₂ Flow	H2Flow per hour	Redy flowmeter
Current	HMI Stack current Setpoint	PLC input
Power	Power Stack A, Power Stack B	calculation
Power	System Power	AC/DC cabinet controller
Temperature	Tin Deoxo, Tout Deoxo	PT100
Temperature	Tin HE, Tout HE	PT100
Current	current stack A, current stack B	AC/DC cabinet controller
Voltage	voltage stack A, voltage stack B	AC/DC cabinet controller

Table 4.10 – Recorded variables for the compression and purification PSA system.

Type	Name	Sensor type / supplier
Air flow	AFlow_200, AFlow_40	E+E Elektronik
Dew Point	DP_ppm and DP	Michell Easydew
Pressure	P10_A, P_40_A	Gems sensor
Pressure	P200_A	AST
Temperature	Booster200_in, Booster200_out	PT100
Temperature	Booster40_in, Booster40_out	PT100
Time	Cycle_time200	Calculation from counter
Time	Cycle_time40	Calculation from counter
Dew point	DP_ely_ppm and DP_ely	Michell Easydew
Pressure	Pirani_Vacuum_Int	Pirani Gauge

4.4.4 Electrolyser PLC wiring diagram



Figure 4.24 – Electrolyser PLC modules.

The main block on the left is linked to the local supervision network and the HMI. Data from the PSA and compression system and from the AC/DC cabinet are imported to be displayed on the main HMI.

Digital inputs have addresses starting with %I, digital outputs are starting with %Q, analog inputs with %IW and analog outputs with %QW.

Table 4.11 – Electrolyser PLC modules wiring information.

Module	Adress	Name tag	Description
1	%IW64	IW_Pirani_Vacuum	Pirani gauge for the PSA
1	%I0.0	Nothalt	Emergency Stop Button
1	%I0.1	Tachometer_bool	Electrolyser fan
1	%I0.2	KOH_Flow_OK	Electrolyte flow switch
1	%I0.3	LevelSensor_Water	Level switch in the scrubber
1	%I0.4 & 5	Opt_Drain_1 & 2	Drains after coalescing filters
1	%I0.7	T_Switch Stack	Temperature switch for stack protection
1	%I1.0 to %I1.3	LevelSensor_H & O	Level switch for low and high levels in the gas separators
1	%Q0.0	Container_fan	Container's ventilation fan
1	%Q0.1 & 2	WaterPump_1 & 2	Deionized water pumps
1	%Q0.3	Light_Container	ATEX lights in the container
1	%Q0.4	ON_Luve	Cooling fans on top of the container
1	%Q0.5	Vent_Electrolyser	
1	%Q0.6	Pump_Glycol	
1	%Q0.7	Pump_KOH	
1	%Q1.0 & 1	H & O_HeatJackets	Heating elements around the gas separators

2	%Q8.0	V_O_Prod	Solenoid valve (see Figure 4.21)
2	%Q8.1	V_N_HSep	Solenoid valve (see Figure 4.21)
2	%Q8.2	V_N_OSep	Solenoid valve (see Figure 4.21)
2	%Q8.3	V_W_HWash	Solenoid valve (see Figure 4.21)
2	%Q8.4	Luve_2fans	To activate the second cooling fan
2	%Q9.0	V_H_Safety	Solenoid valve (see Figure 4.21)
2	%Q9.1	V_H_Compens	Solenoid valve (see Figure 4.21)
2	%Q9.2 & 3	V_H_Drain_1 & 2	Solenoid valve (see Figure 4.21)
2	%Q9.4	V_H_Prod	Solenoid valve (see Figure 4.21)
2	%Q9.5	V_H_Purge	Solenoid valve (see Figure 4.21)
2	%Q9.6	V_O_Depress	Solenoid valve (see Figure 4.21)
2	%Q9.7	V_O_Compens	Solenoid valve (see Figure 4.21)
3	%IW112	IW_H_LevelSensor	Continuous level sensor in the gas separator
3	%IW114	IW_O_LevelSensor	Continuous level sensor in the gas separator
3	%IW116&8	IW_H_PSensor_1&2	Pressure sensor in the hydrogen side
3	%QW118	QW_speed_KOH	Set point for the electrolyte pump
4	%IW128	IW_FlowMeter	Hydrogen flowmeter in the production line
4	%IW130	IW_H2_Sensor_Container	Hydrogen sensor
4	%QW128	QW_Speed_Vent_Container	
4	%QW130	QW_Speed_Vent_Luve	Speed of the cooling fans, controlled with a PID
5	%IW144	IW_T_In_HE	Electrolyte temperature at the inlet of the heat exchanger
5	%IW146	IW_T_Out_HE	Electrolyte temperature at the outlet of the heat exchanger
5	%IW148	IW_T_In_Deoxo	Gas temperature at the inlet of the Deoxo
5	%IW150	IW_T_Out_Deoxo	Gas temperature at the outlet of the deoxo

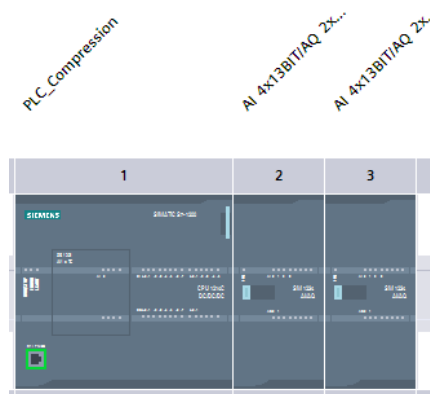


Figure 4.25 – PSA and compression PLC modules.

Table 4.12 – PSA and compression PLC modules wiring information.

Module	Adress	Name tag	Description
1	%IW64 & 66	P200_A&B	Pressure sensors in the outlet line
1	%IO.0	B10to40_pulses	Booster impulsions
1	%IO.1	B40to200_pulses	Booster impulsions
1	%IO.2	Drain_sensor	
1	%IO.3	AFlow40_Pulse	Compressed air flow meter
1	%IO.4	AFlow200_Pulse	Compressed air flow meter
1	%Q0.0 & 1	A & B_Feed	Solenoid valve (see Chapter 5)
1	%Q0.2 & 3	A & B_Vent	Solenoid valve (see Chapter 5)
1	%Q0.4 & 5	B & A_EQ	Solenoid valve (see Chapter 5)
1	%Q0.6 & 7	A & B_Reinject	Solenoid valve (see Chapter 5)
1	%Q1.0	Drain	Solenoid valve (see Chapter 5)
1	%Q1.1	Vacuum	Solenoid valve (see Chapter 5)
1	%IW80	Temp	Ambient temperature
2	%IW96&98	P40_A&B	Pressure sensor after the first booster
2	%IW100	DP	Dew point measurement after PSA
2	%IW102	DP_ely	Dew point measurement at the outlet of the electrolyser
3	%IW112 & 114	P10_A & B	Pressure at the inlet of the PSA system
3	%IW116 & 118	AFlow_200 & 40	Compressed air flow meter
3	%QW112	Booster_40to200	Setpoint for the proportional valve
3	%QW114	Booster_10to40	Setpoint for the proportional valve

4.4.5 Component failures and corrective measures

- **Electrolyte pump:** the original centrifugal pump was damaged by the electrolyte. The mechanical assembly was severely corroded. This failure was detected *via* the electrolyte flow sensor and an abnormal noise during operation. The current supply to the stacks was immediately stopped and the system was extensively purged with nitrogen. In the absence of isolation valves, the whole electrolyte had to be removed in order to replace the pump. In order to avoid corrosive damages, a magnetically coupled pump was installed.
- **Continuous level sensors in the separators:** from the beginning, these sensors, based on a magnetic floater and reed relays, have shown an erratic behaviour with sudden changes to 0. The level sensing in the gas separator is one of the critical measurements to control an alkaline electrolyser. The sensors were replaced (the separators have to be opened from the top). We implemented a small delay to confirm the reading (0.2 seconds), and included a digital signal for top and low levels to avoid false positive low-level signals. Alternative measurement techniques using the reflection on the liquid surface were considered but not implemented due to the uncertainties regarding the behaviour on a foamy and bubbling surface during production.
- **Water level sensor:** For an unknown reason, despite a pressure rating of 25 bars, the level sensor (Honeywell LLN series) for the hydrogen scrubber failed during the operation of the electrolyser. Consequently, the high-level on the scrubber was not detected and fresh water was continuously pumped into the system. Eventually, the scrubber was completely flooded and the next device, the coalescing filter, started to fill up. At this point, the excess water was removed *via* the drain. The systematic opening of the drain valve, in addition to the continuous operation of the water pump allowed us to notice the failure and to shut down the machine for maintenance.
- **Solenoid valve for Oxygen production:** An insufficient flow was coming out of this valve in the open position. Consequently, the level in the oxygen separator went down and triggered multiple openings of the oxygen compensation valve. This behaviour led to a rapid pressure loss in the system, and some KOH was pushed to the compensation line during the O₂ comp openings. As a corrective measure, the oxygen production line was cleaned and the solenoid valve replaced. The orifice at the inlet of the compensation line was reduced in order to prevent sudden pressure drops. The filter is manually purged after operation to prevent electrolyte spills at the outlet. It was found that a lye recovery system after the filter would allow to recover only 40 mL after a day of operation, and adds too much complexity to be implemented at this scale.
- **Cooling system:** During cold winter conditions, and insufficient amount of glycol in the cooling fluid broke the heat exchanger. The corresponding exchanger was replaced and the glycol content was increased.

- **PSA column filter:** The filter at the inlet of the PSA column broke due to the successive shocks with the dessicant beads during the depressurization phase. The whole system was disassembled to remove dessicant particles in the valves and pipes. To prevent another filter failure, the top of the column was filled up with a compressed foam material, which is expected to absorb the depressurization shocks.
- **PSA purge flow capillary:** the vibrations generated by the gas boosters induced a mechanical stress on the capillary which broke prematurely. Some protective tape must be installed to prevent abrasion. The same phenomenon of pipe abrasion, and finally rupture, was observed with the water purification system.
- **24V power supplies:** the power supply for auxiliaries failed two times, when the electrolyser was not in operation. If it happens during operation solenoid valves, water pumps, sensor or control screens will not be powered anymore. Such failure can lead to a critical incident. Each power supply is complemented by a small lead acid battery which can ensure 30 minutes of operation. Automatic response to shutdown the system is not implemented in the automation. Power supply failure is unusual, however due to the outdoor installation and the very windy conditions, a possible explanation would be that dust and particules enter the electronic cupboard and eventually goes through the ventilation grid of the power supply leading to internal short circuits.

Finally, the overall safety concept could be improved with an on-line lye analyser / conductimeter and removable filter to control a contamination of the electrolyte with degraded materials, and prevent small particles to enter the stacks. In terms of software, the monitoring of sudden deviations in temperature profiles or variations in auxiliaries' activation (compensation valves, drains, water pumps...) is also a way to detect potential defects.

4.4.6 Costs and hardware suppliers

McLyser 10-10 system: 175 000 € net for a containerized unit. For reference a 25 kW PEM stack from Giner was purchased at a cost of 46 000 \$, and a magna power DC power supply 23 500 \$








Balance of plant:

- Swagelock 1 gal cylinder for PSA in 304 L steel 124 bar pressure rating. 800 CHF per unit
- Bürkert: various solenoid DC and AC valves for hydrogen production, purification and supply storage. 129 CHF per valve
- AlfaLaval: various brazed plate heat exchangers. 800 – 1200 CHF per unit
- Huber: water chiller. Model Unichiller 055T. 11 500 CHF
- Edwards: vacuum pump. Model nXDS 15i. 6000 CHF
- Sawa pumpen: peripheral pump with magnet coupling. Model MP68 –RKME. 3300 CHF
- Verder: rotary gear pump for deionized water. Model VG50. 2200 CHF

- Michell Instruments: dew point transmitter. Model Easidew. 2800 CHF
- Valco: continuous level sensor. Model LCT EA52. 860 EUR per unit
- Voegtlin: mass flow meter. Model Red-y GSM 10 bar. 1750 CHF
- Baumer: level sensor up to 100 bar. Model CleverLevel LBFI. 250 CHF
- Cosmos: Gas detector to detect explosive atmosphere. Model KD-12B. 1800 CHF
- Gems Sensors&Controls: optical level switch. Model ELS-950. 70 CHF
- Gems Sensors&Controls: various pressure sensors, from 10 to 80 bar
- Honeywell: optical level sensor, up to 25 bar. Model LLN865172-1. 250 CHF

4.5 Hazard identification

List of hazards associated with the chemicals used in the demonstrator.

			
GHS02 - Flammable	GHS04 – compressed gas	GHS05 - Corrosive	GHS06 - Toxic
			
GHS07 - Harmful	GHS08 – Health hazard	GHS09 – Environmental hazard	

Hydrogen gas:

- May displace oxygen and cause rapid suffocation
- May form explosive mixtures with air
- Burns with invisible flame

Nitrogen gas: May displace oxygen and cause rapid suffocation

KOH 30 %

- Acute toxicity (oral), Category 4: H302 Harmful if swallowed
- Skin corrosion/irritation, Category 1B: H314 Causes severe skin burns and eye damage
- Serious eye damage/eye irritation, Category 1: H318 Causes serious eye damage

Vanadium electrolyte (Vanadyl sulfate)

- Acute oral toxicity, Category 4
- Skin Corrosion/irritation Category 2
- Serious Eye Damage/Eye Irritation Category 2
- Specific target organ toxicity (single exposure) Category 3: Target Organs - Respiratory system.

4.6 Conclusion

Building up a full scale demonstrator goes far beyond the expertise of a single scientist and requires the mobilization of skills in various domains from electronics to pipework including mechanical and civil engineering. There has been a good deal of learning-by-doing during the construction and operation of this grid to mobility refuelling station. In the same time that some answers emerged, new questions appeared and the corresponding equipments were adapted and instrumented differently. A design in constant evolution has some advantages in terms of flexibility, and allowed us to perform very specific studies and measurements (fueling and defuelings of a 700 bar type IV tank with gas recycling, performance analysis of gas boosters, redox flow degradation studies...). On the other hand, some topics and metrics, such as long term degradation or availability of the equipments were not investigated due to the absence of stable operating conditions.

Some technological choices are deliberately assumed, in particular the air driven gas boosters. The robust design, the ease of installation and maintenance, and the low cost were decisive parameters compared to more efficient technologies with probably more potential in large scale industrial setups but less potential for scientific investigations at our scale, lower TRL, or jeopardizing safety, gas quality or reliability of the demonstrator.

Nonetheless, some other technological choices were constrained due to difficulties in supplier identification (sensors), component availability or exclusivity arrangements (gas cylinders), or system compatibility (power supplies). In some cases, we deplore the lack of documentation for system integrators (IR communication for 70 MPa fueling nozzle, cylinder plugs).

Finally, this experimental part highlights the importance of exchanges of experience, of the understanding of the working principle of sensors, and of the documentation of manufacturing and assembly processes for the selection of components and the interpretation of their behaviour.



Figure 4.27 – Electrolysis container with hydrogen supply storage on the left.



Figure 4.26 – Exchange of experience at the EMPA Move Demonstrator. Hyundai ix35 fuel cell (2013) side-by-side with a Hyundai Nexo (2018).

References

- [1] Y. Ligen, H. Girault, J. Rager, Combined service station for battery electric & hydrogen fuel cell vehicles - Final Report, Swiss Federal Office for Energy. (2018). <https://www.aramis.admin.ch/Dokument.aspx?DocumentID=50166> (accessed November 21, 2019).
- [2] M. Rychcik, M. Skyllas-Kazacos, Characteristics of a new all-vanadium redox flow battery, *Journal of Power Sources*. 22 (1988) 59–67. [https://doi.org/10.1016/0378-7753\(88\)80005-3](https://doi.org/10.1016/0378-7753(88)80005-3).
- [3] V. Amstutz, Redox flow battery and indirect water electrolysis, EPFL, 2015. <http://infoscience.epfl.ch/record/213651>.
- [4] M. Skyllas-Kazacos, M.H. Chakrabarti, S.A. Hajimolana, F.S. Mjalli, M. Saleem, Progress in Flow Battery Research and Development, *J. Electrochem. Soc.* 158 (2011) R55. <https://doi.org/10.1149/1.3599565>.
- [5] D. Bryans, V. Amstutz, H. Girault, L. Berlouis, Characterisation of a 200 kW/400 kWh Vanadium Redox Flow Battery, *Batteries*. 4 (2018) 54. <https://doi.org/10.3390/batteries4040054>.
- [6] H. Girault, V. Amstutz, Final Report - RFB-HY: redox flow battery pilot installation for hydrogen generation and energy storage, (2017). <https://www.aramis.admin.ch/Texte/?ProjectID=36915>.
- [7] D. Reynard, H. Vrabel, C.R. Dennison, A. Battistel, H. Girault, On-Site Purification of Copper-Contaminated Vanadium Electrolytes by using a Vanadium Redox Flow Battery, *ChemSusChem*. 12 (2019) 1222–1228. <https://doi.org/10.1002/cssc.201802895>.
- [8] HyWay Rapport Final, (2018). <https://www.tenerrdis.fr/uploads/2017/04/rapport-final-hyway-public.pdf> (accessed April 20, 2020).
- [9] U. Cabalzar, Aufbau und Betrieb der ersten Wasserstofftankstellen in der Schweiz mit einem Nenndruck von 70 MPa, Bundesamt für Energie BFE, 2019. <https://www.aramis.admin.ch/Default.aspx?DocumentID=64063&Load=true> (accessed April 20, 2020).
- [10] SAE International, J2601: Fueling Protocols for Light Duty Gaseous Hydrogen Surface Vehicles, 2016. http://standards.sae.org/j2601_201407/ (accessed February 14, 2017).
- [11] E. Talpacci, M. Reuß, T. Grube, P. Cilibrizzi, R. Gunnella, M. Robinus, D. Stolten, Effect of cascade storage system topology on the cooling energy consumption in fueling stations for hydrogen vehicles, *International Journal of Hydrogen Energy*. 43 (2018) 6256–6265. <https://doi.org/10.1016/j.ijhydene.2018.02.030>.
- [12] SAE International, SAE J2799, Hydrogen Surface Vehicle to Station Communications Hardware and Software, (2014).
- [13] M. Farzaneh-Gord, M. Deymi-Dashtebayaz, H.R. Rahbari, H. Niazmand, Effects of storage types and conditions on compressed hydrogen fuelling stations performance, *International Journal of Hydrogen Energy*. 37 (2012) 3500–3509. <https://doi.org/10.1016/j.ijhydene.2011.11.017>.

- [14] R. Gilliam, J. Graydon, D. Kirk, S. Thorpe, A review of specific conductivities of potassium hydroxide solutions for various concentrations and temperatures, *International Journal of Hydrogen Energy*. 32 (2007) 359–364. <https://doi.org/10.1016/j.ijhydene.2006.10.062>.
- [15] A.E. Mauer, D.W. Kirk, S.J. Thorpe, The role of iron in the prevention of nickel electrode deactivation in alkaline electrolysis, *Electrochimica Acta*. 52 (2007) 3505–3509. <https://doi.org/10.1016/j.electacta.2006.10.037>.

Chapter 5

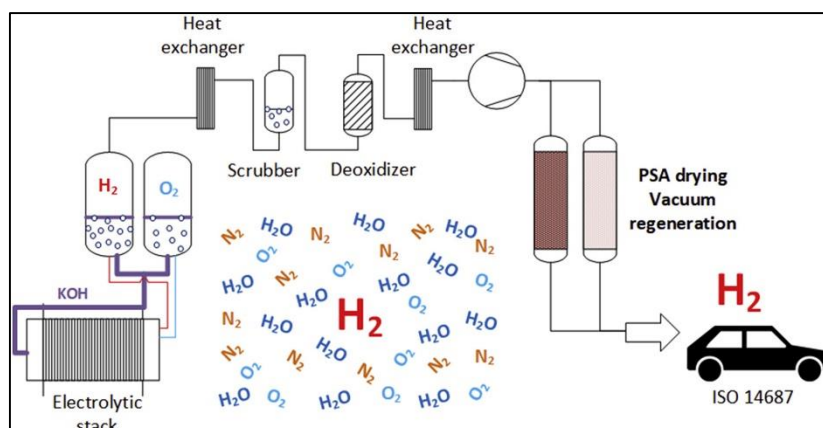
Electrolysis and purification

The results presented in this chapter were partially published in the following paper:

- Y. Ligen, H. Vrubel, H. Girault, Energy efficient hydrogen drying and purification for fuel cell vehicles, International Journal of Hydrogen Energy. 45 (2020).
<https://doi.org/10.1016/j.ijhydene.2020.02.035>. [1]

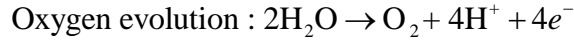
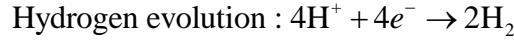
And presented during the following conference:

- ICE 2019, Norway, June 9 -13, Design and operation of a HRS with on-site alkaline electrolysis



5.1 Thermodynamics of alkaline water electrolysis

Water electrolysis is the electrochemical decomposition of water into hydrogen and oxygen. It consists of the two following semi-reactions:



By definition, the standard cell voltage $E_{cell}^{\circ} = -\frac{\Delta G^{\circ}}{n \cdot F} = -\frac{\Delta_r H^{\circ} - T\Delta S^{\circ}}{n \cdot F}$, with n the number of electrons exchanged, $F = 96\,485 \text{ C} \cdot \text{mol}^{-1}$ the Faraday constant, $T = 298 \text{ K}$, the temperature under standard ambient conditions. The Gibbs energy ΔG° corresponds to the maximum work (in absolute value) extractable from the reaction. $\Delta_r H^{\circ}$ is the enthalpy change. $T\Delta S^{\circ}$ corresponds to the energy that can be supplied as heat. Considering, that water is supplied in the liquid form, the higher heating value (HHV) applies and thus we obtain $E_{cell}^{\circ} = 1.23 \text{ V}$, and the thermoneutral voltage $E_{therm}^{\circ} = -\frac{\Delta_r H^{\circ}}{n \cdot F} = 1.48 \text{ V}$.

The equilibrium voltage in non-standard conditions can be obtained with the Nernst equations for each half reactions:

$$\begin{aligned} \Delta E_{eq} &= \left[\left(E_{\text{H}^+/\frac{1}{2}\text{H}_2}^{\circ} \right)_{\text{SHE}} + \frac{RT}{2F} \ln \left(\frac{(a_{\text{H}^+}^{\text{S}})^2}{p_{\text{H}_2}/p_0} \right) \right] - \left[\left(E_{\text{O}_2/\text{H}_2\text{O}}^{\circ} \right)_{\text{SHE}} + \frac{RT}{4F} \ln \left((a_{\text{H}^+}^{\text{S}})^4 \cdot p_{\text{O}_2}/p_0 \right) \right] \\ &= \Delta E^{\circ} - \frac{RT}{4F} \ln \left(\frac{p_{\text{H}_2}^2 \cdot p_{\text{O}_2}}{p_0^3} \right) \end{aligned}$$

With $\left(E_{\text{H}^+/\frac{1}{2}\text{H}_2}^{\circ} \right)_{\text{SHE}}$ and $\left(E_{\text{O}_2/\text{H}_2\text{O}}^{\circ} \right)_{\text{SHE}}$ the standard redox potentials, with the standard hydrogen electrode (SHE) as reference¹. $a_{\text{H}^+}^{\text{S}}$ is the activity of the proton in solution. $R = 8.3145 \text{ J} \cdot \text{mol}^{-1} \cdot \text{K}^{-1}$ the universal gas constant, F the Faraday constant, p_{H_2} and p_{O_2} the partial pressures of hydrogen and oxygen respectively. p_0 is the standard pressure : 1 bar. The equilibrium voltage describes the

¹ The standard hydrogen electrode is defined such as the proton in solution is at unit activity, as well as the hydrogen fugacity ($p_{\text{H}_2} = 1 \text{ bar}$).

electrolysis voltage at equilibrium, thus at zero current and represents the lowest cell voltage value. Once a current is forced through the cell, kinetic and heating losses set in. They translate into overpotentials at the cell level and are the consequences of several phenomena. The following sources of overpotentials can be defined:

- Electrical resistances: ohmic losses relative to the conductivity and thickness of the electrolyte layer and of the diaphragm or membrane.
- Transport related resistances:
 - o bubbles covering the electrode surface, and within the electrolyte solution² [2]
 - o ionic transfer in the electrolyte
 - o ionic transfer across the separator (the separator is theoretically impermeable to gas transport, but gas cross-over can also be included in the modelled losses)
- Electrochemical reaction resistances: overpotential for activation energy, depending on the catalyst. The activation can be expressed *via* the Butler-Volmer equation (or in a reduced form, the Tafel law at high current densities). At the anode, four electrons are involved for the release of one dioxygen molecule, instead of two electrons for one dihydrogen molecule at the cathode. This is one of the reason why the anode side is the most challenging one in terms of electrochemistry, resulting in higher anodic overpotentials compared to cathodic ones [3].

Finally, all the overpotentials contributions sum up into the overpotential η , such as $E = E_{eq} + \eta$, and can be used to model voltage-current polarization curves, the main output of a large variety of modelling approaches [4]. However, the polarization curve at the cell level, can hardly be fully verified at the system level due to limitations on the power supply range, temperature inhomogeneities along the stack, influence of ancilliary equipments and safety control features.

Going to the system level, efficiency is often expressed in kWh/Nm³ or kWh/kg (see Chapter 2). However, the variety of system boundaries and reference values considered by manufacturers and researchers, can lead to comparison issues [5]. The data of interest for the electrochemist, are not always those for the engineer and finally for the operator. To avoid this bias, in the following section, raw data collected on a 50 kW alkaline electrolyser (installation reported in Section 4.4) are reported and discussed to shine some light on cell level implications and control loops on the system level.

² Another side-effect of bubble coverage is the disturbance of electrolyte flow and, consequently, the creation of hotspots on the electrode which can damage the material. This hydrodynamic issue can lead manufacturers to implement software limitations regarding the dynamic power response.

5.2 Alkaline Electrolysis, data collection

5.2.1 Preliminary remarks

The electrolyser was always operated under direct supervision. Thus, no long-term degradation studies were made. The most representative dataset, collected on 05.03.2019, is reported here as an illustrative purpose, but other datasets, from about 40 different runs, are used to ensure the consistency of the reported data. At a larger scale, such resources can be used for data reconciliation, virtual sensor redundancy or system modelling. This issue is investigated in one of the SCCER³ Joint Activity: Coherent Energy Demonstrator Assessment (CEDA)⁴. The pilot plant infrastructure and equipment from six demonstrators across Switzerland are analysed:

- ESI Platform, PSI: PEM electrolysis and fuel cell, methanation
- High Efficiency Power-to-Gas Pilot, Rapperswill: 25 kW PEM electrolysis and methanisation with ambient air carbon capture
- MOVE, EMPA: 180 kW PEM electrolyser and commercial scale refueling station
- NEST, EMPA: research and innovation building
- Ehub: covers the energy flows of mobility, housing and services
- Grid to Mobility, LEPA: demonstrator presented in Chapter 4

Data driven models are developed for thermal systems [6], and the next step might be to develop data driven models for electrochemical devices.

³ Swiss Competence Center for Energy Research

⁴https://www.sccer-mobility.ch/Joint_Activities/CEDA-Coherent-Energy-Demonstrator-Assessment/

5.2.2 Power data

The easiest graphs to interpret are those related to power consumption. With the curves presented in **Figure 5.1**, we can derive the AC/DC conversion efficiency (92 – 94.6%), the respective contribution of auxiliaries (4.7 to 8.5 % of the DC power) and the system efficiency (75.4 kWh per kg or 52.3 % HHV H₂). The same orders of magnitude are reported on a similar scale PEM electrolyser by Stansberry and Brouwer [7]. Indeed, the AC/DC power consumption is in the same range (92.1 – 93.7%), a 2.5 kW power consumption is directed to auxiliaries (compared to 2.7 kW here) and the system efficiency is equal to 46.8% (corrected to 52% before dryer).

The data from the flowmeter is particularly noisy due to rapid fluctuations attributable to the compensation valves. After comparison with pressure evolution in the storage tanks, it appears that the smoothed value leads to an underestimation of the flow of up to 20%. For the calculations, the nominal flow is estimated at 850 g H₂/h. We can also observe spikes every 10 minutes: they correspond to the column switch with the pressure swing system.

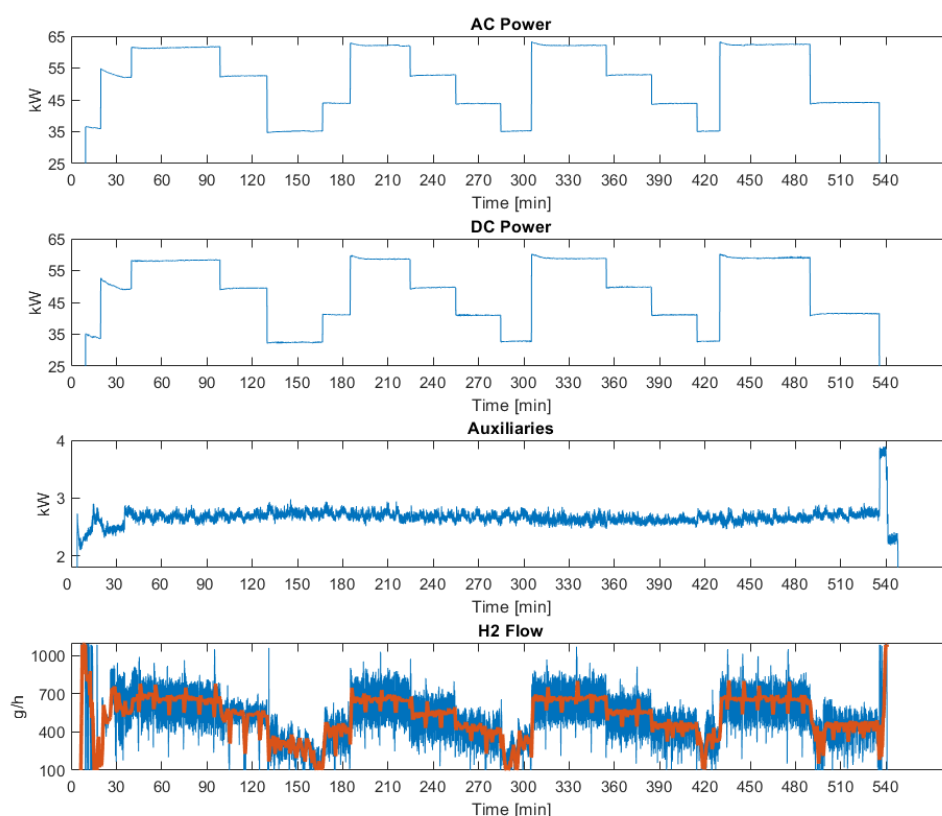


Figure 5.1 – System power consumptions.

A more detailed breakdown of the power consumption from auxiliaries is presented in **Figure 5.2** and **Table 5.1**. A dedicated power circuit supplies all the loads independently from the power supply of the electrolytic stack.

The following decomposition is made:

- Auxiliaries 1, Thermal management (P1_L1): Glycol pump, Fans, Heating jackets. No significant variations, except when the fan speed is set at 100% (see shut down sequence at 540 min). The ambient temperature for this experiment was below 15°C, thus only one of the two fans was activated. A manual switch allows to power the second fan for warmer environmental conditions.
- Auxiliaries 2 (P1_L2): UPS, container lights and fans, KOH pump, compression and 200 bar system. Very stable and dominated by the circulation pump. After ca. 40 minutes, the compression system was activated, which explains the increased consumption (some solenoids and vacuum pump). The 10 min increments are linked to the 10 minutes PSA cycles, and the corresponding variation in the power demand from the vacuum pump.
- Auxiliaries 3 (P1_L3): Control system and screen, all 24 V consumers (includes the water pumps). Each water pump can consume up to 145 W, this is the main reason for the observed variations.
- Chiller (P2): constant load to keep the cooling water for plate heat exchangers at 5°C.

As a general remark, we can note that auxiliaries power consumptions are only weakly affected by load variation on the stack level. Stansberry and Brouwer [7] reported as well the absence of notable correlation with operating conditions and thus the increased percentage of auxiliaries consumption in the system energy share as stack load decreases.

Table 5.1 – Repartition of energy losses in the alkaline electrolyser.

Type	Power under nominal conditions /kW	Energy spent per kg of H ₂ produced /kWh
AC/DC conversion losses	3.1	3.65
DC electricity feeding the stacks	58.3	68.6
Thermal management	0.25	0.29
Circulation pump	1.3	1.53
Control Electronics	0.2	0.24
Chiller	0.97	1.14
Total	63.9	75.4

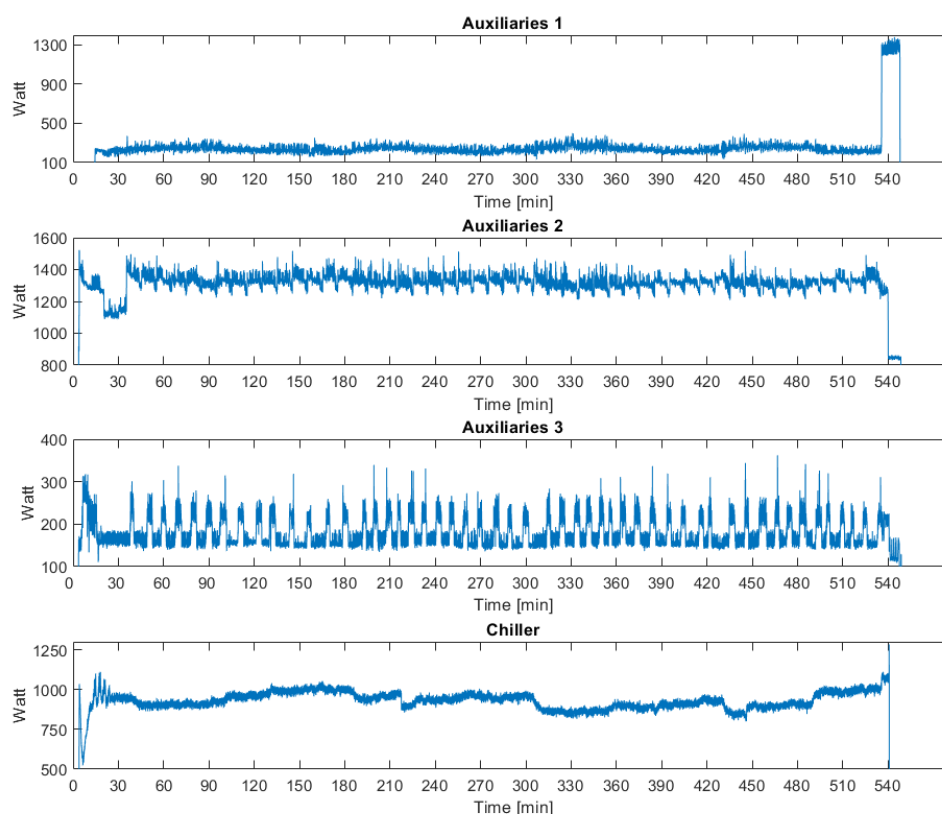


Figure 5.2 – Breakdown of auxiliaries power consumptions.

5.2.3 Cell performance and temperature data

The system consists of two stacks of 115 cells, with an active surface area estimated at 370 cm². Thus, from sytem level measurements, we can derive average cell values as reported in **Figure 5.3**. The power supply is operated in galvanostatic mode, which leads to a stack voltage overshoot during start-up, when the electrolyte is cold (despite the 70A current setpoint fixed by the control system for the cold-start procedure). The non-isothermal operation is also a known issue for the dynamic operation of PEM electrolyzers [8]. Moreover, some thermal gradients are expected due to inhomogeneous electrolyte distribution between the 115 cells (see the stack design in **Figure 4.19**). Indeed, fresh electrolyte is introduced at the bottom of the stacks and collected in the lower part of the gas separators. Average values are reported in

Table 5.2. The stable temperature at the outlet of the heat exchanger (**Figure 5.4**) validates the performance of the PID regulating the speed of the cooling fan. However, for low current densities, even at minimal speed, the cooling power is too high (at *ca.* 150 min, we can notice a sudden variation in the temperature at the outlet of the heat exchanger due to a temporary stop of the fan). In steady state mode, the temperature differential for the stack is about 20°C.

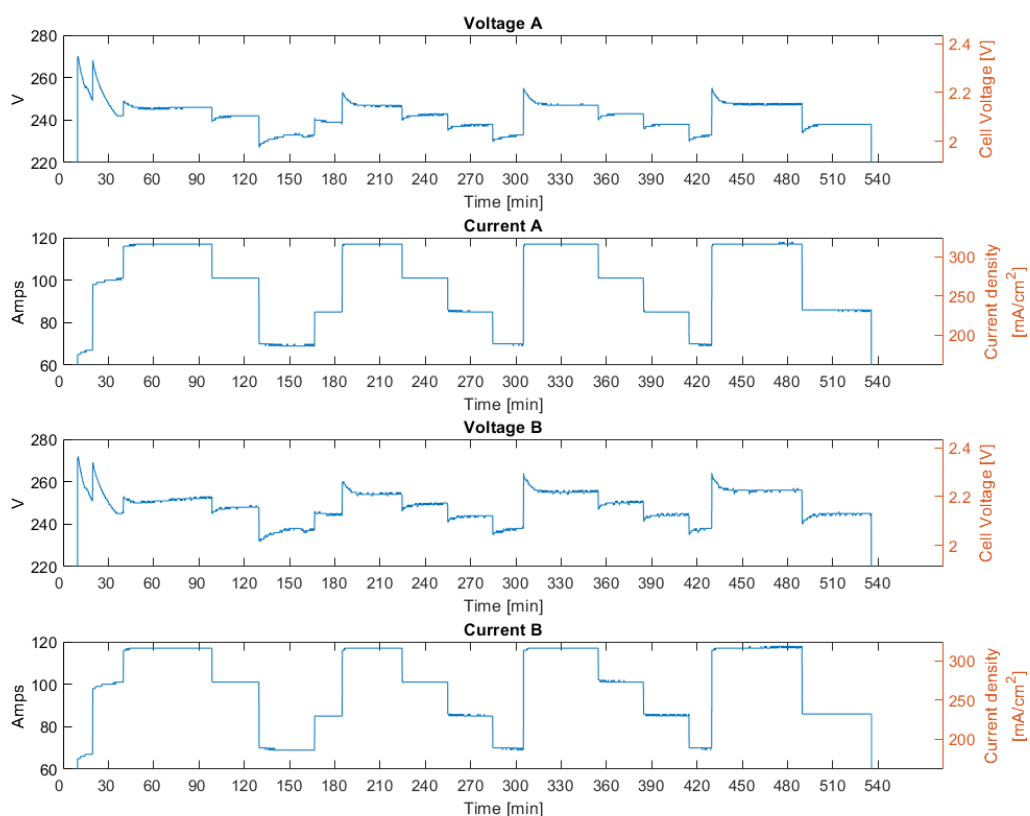


Figure 5.3 – Potential and current measurements.

Table 5.2 – Average cell potential measured under various conditions.

		Current density, mA/cm ²			
		190	230	270	315
Average electrolyte temperature, °C	40	-	-	2.21 V	-
	50	-	-	2.15 V	-
	55	2.02 V	2.07 V	2.12 V	2.21 V
	60	1.98 V	2.03 V	2.09 V	2.15 V

The strong temperature dependency can be correlated with the conductivity of the 30 wt% KOH electrolyte presented in **Table 5.3** (data reported by Gilliam [9]).

Table 5.3 – Conductivity of 30wt% KOH solution.

Temperature in °C	20	30	40	50	60	70	80
Conductivity in S·cm⁻¹	0.5610	0.6831	0.8125	0.9479	1.0885	1.2334	1.3816

As expected, cell voltages are significantly lower in PEM systems (as low as 1.65 V at 200 mA/cm²), which, in addition, operates at larger current densities (2 V at 1.4 A/cm²) [7].

The hydrogen produced in the stack is directed to a deoxidizer to reduce the oxygen content. Regarding the temperature measurements at the inlet of the deoxidizer, the variations can probably be attributed to the variation of ambient temperature and cannot be directly linked with process related events. However, the cooling power provided by chilled water in the plate heat exchangers remains constant; thus we can assume that with lower flows, the gas leaves the heat exchanger at lower temperature. A more precise in flow measurement of the temperature would be required to assess accurately the influence of environmental conditions. In contrast, the temperature at the outlet of the deoxidizer requires further attention. During previous runs, under similar conditions, temperatures at the outlet were measured in the 60 to 70 °C range compared to values in the 40 to 50°C here. Continuous oxygen measurements were not in place at the time of these observations. Two hypotheses can be formulated, however long term temperature, wind and oxygen content measurements would be required for validation. First, this lower temperature can reflect a lower catalytic activity, and thus a degradation of the deoxidizer. Higher oxygen content in outlet gas or post-mortem analysis of the catalyst would be required to validate this hypothesis. Second, even if the electrolyser was installed in a container and delivered with side panels, it was operated most of the time with container doors open and with side panels removed. Thus, the deoxidizer was exposed to the very windy environment of Martigny, which certainly provide some cooling effect. Another point regarding these measurements is the sudden temperature increase after 300 and 420 minutes, which corresponds to the situation where the current setpoint was changed from 70 A to 115 A. The absolute increase of the production flow, leads to more conversion in the deoxidizer and eventually an increased temperature. Thus, a close monitoring of deoxidizer temperature can bring useful information regarding the hydrogen flow variations in quality and quantity.

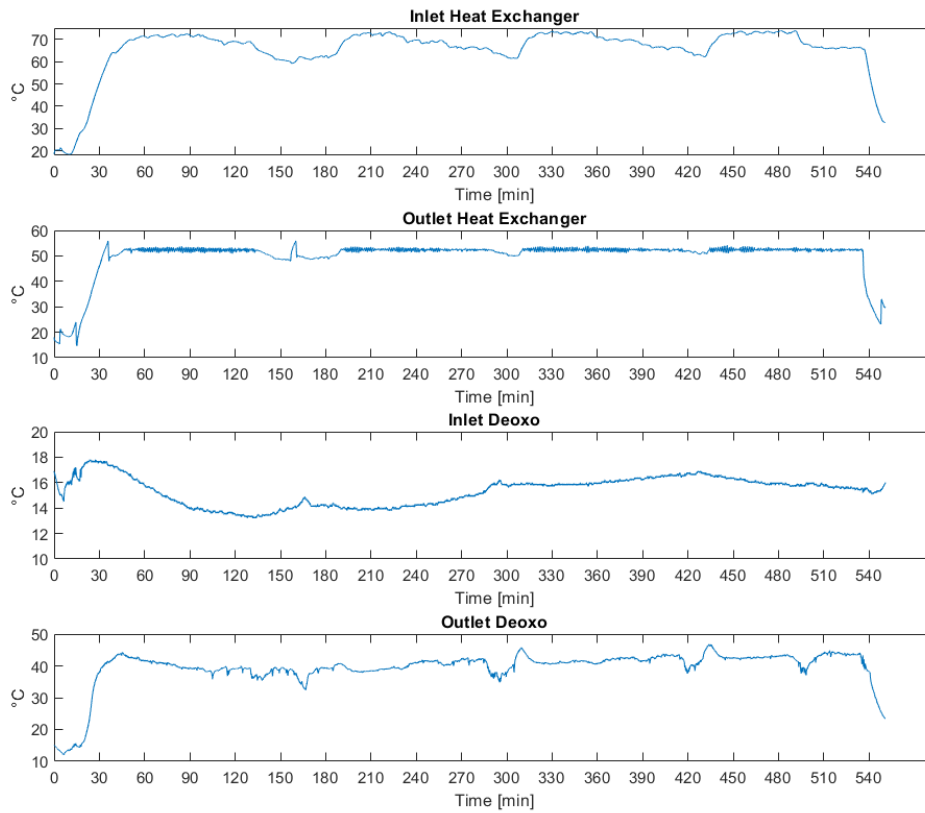


Figure 5.4 – Temperature variations.

5.2.4 Process control observations

The level regulation in the gas separators on the oxygen and hydrogen side performs as expected, but with some issues at low production rates. Indeed, as mentioned in Chapter 4, the pressure losses *via* the oxygen compensation valve directly affects the system stability. Next to 150 and 300 minutes, the lowest pressures are measured, and the highest levels in the oxygen side, meaning that a stronger restriction would be required on this outlet to enable a pressure increase. These events correspond to the 70 A periods (see **Figure 5.3**).

In the beginning, when no current is applied, the respective levels are significantly lower. The rationale here can be given by the nature of the level sensor: it consists of a floating ball moving along a vertical axis, and we can assume that when a current is applied, it creates a foamy turbulent surface in the separators and the ball floats above this foamy surface, thus higher than the surface at rest. In addition, at rest, the stack is 100% filled with electrolyte, however during operation the void fraction (the volume occupied by oxygen and hydrogen bubbles) mechanically lead to a transfer of electrolyte from the stacks to the separators and a corresponding level increase.

The frequency of drain valve openings is not directly exploitable at this stage, it corresponds to the condensed water formed after the second plate heat exchanger (after the deoxo, see Chapter 4, **Figure 4.21**), however each opening does not correspond to the same volume of water expelled. The sensor after the first heat exchanger (after the scrubber) remains dry and thus the first drain is never activated.

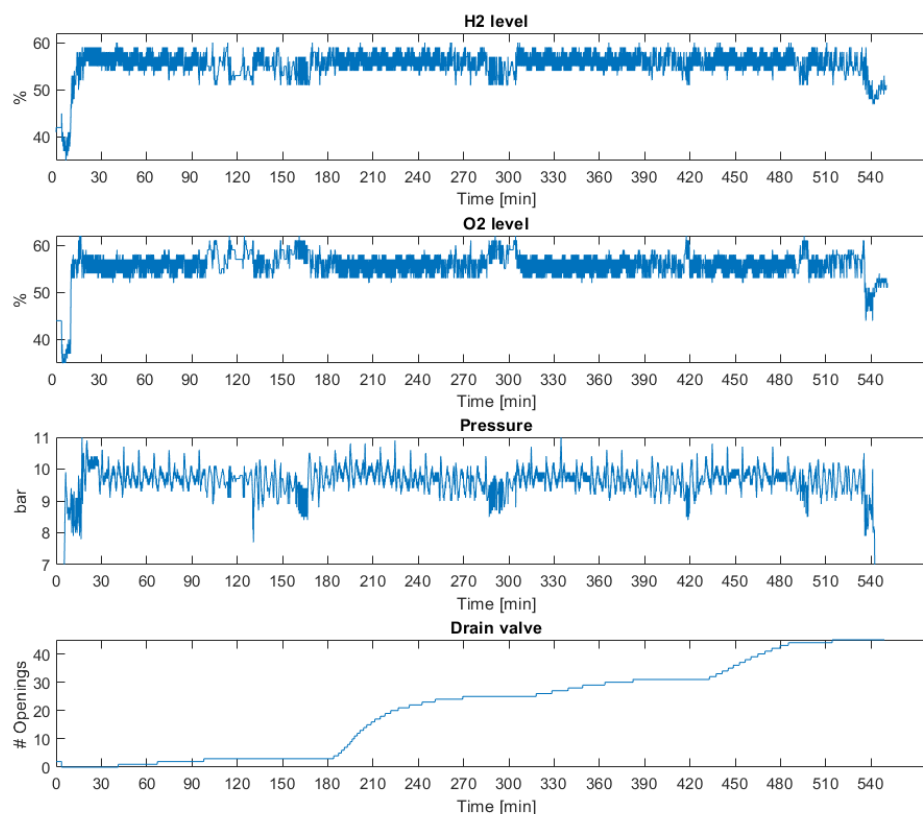


Figure 5.5 – Process control data measurements.

5.3 Electrolytic hydrogen purification

Water electrolysis allows the production of hydrogen with no direct CO₂ emissions, however when the hydrogen gas leaves the stack, some purification steps are still required to condition it into a high-quality energy carrier for PEM fuel cells.

5.3.1 Contaminants

A limited number of contaminants are present in electrolytic hydrogen [10,11]. Carbon monoxide, a particular fuel cell poisoning specie and one of the most critical and expensive to remove [12,13] is unlikely to be produced by water electrolysis processes [14]. Multiple purification processes are able to purify hydrogen gas mixtures such as pressure swing adsorption (PSA), cryogenic distillation, membranes [15,16] and more recently, metal hydrides systems [17]. However, the integration of such processes with electrolyzers and their specific outlet gas composition is rarely documented.

A complex set of instruments is required to ensure full compliance with ISO hydrogen quality standards [18,19] and a pre-screening according to the production mode can be made. In 2018, no European laboratory was able to ensure a full ISO compliance. This capability is currently being developed by the FCH-JU project Hydraite [20], and 3 laboratories are expected to be equipped by 2020. Furthermore, the research program HyCoRa has conducted a risk assessment on fuel cell contaminants [21] and the project MetroHyVe includes work packages dedicated to hydrogen quality assurance, quality control and sampling [22]. Out of the 13 gaseous contaminants specified in ISO 14687:2019, only three are likely to be present in electrolytic hydrogen [10,11]: Nitrogen, Oxygen and Water. Their origin and the corresponding removal methods are summarized in **Table 5.4**. While the hydrogen content in the oxygen stream is extensively modelled and studied in the literature [23], to our knowledge, limited data is available regarding nitrogen and water.

Table 5.4 – Origin of most probable hydrogen contaminants in alkaline electrolysis.

Contaminant	ISO 14687:2019 threshold	Typical content without treatment	Origin	Removal techniques
Nitrogen	300 ppm	< 100 ppm after initial purge	Purge and inertization phases, feed-in water	Venting of initial production
Oxygen	5 ppm	2000 – 6000 ppm	Gas solubility, Cross over	Catalytic recombination
Water	5 ppm	>2000 ppm, saturated at ambient temperature	Process	Gas cooling, PSA or TSA systems

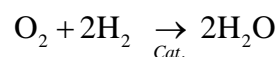
Nitrogen

Nitrogen is often used to purge electrolyzers during maintenance, shut down and/or start up sequences. Nitrogen has a dilution effect on the delivered hydrogen and can affect the accuracy of mass metering instruments. Feeding a fuel cell with high nitrogen concentrations can lead to power losses and affect venting and blower controls [24]. Most of the time, no dedicated post-treatment units are installed for nitrogen removal, and venting the initial production allows to reach ISO 14687:2019 levels. In continuous operation, nitrogen traces can also be attributed to the feed-in water introduced in the electrolyser, which may contain dissolved gases. Pressurized cold water can contain up to 0.09 g/L of dissolved nitrogen, corresponding to 40 ppm of N₂ in the hydrogen outlet flow. This contamination can be avoided if water is properly degassed prior or during the deionization treatment.

Oxygen

PEM fuel cells are tolerant to oxygen content up to 500 ppm and the explosive limit is reached at 4% [25]. Oxygen may affect metal hydride storage materials which are found, to date, only in two-wheelers applications [26]. During water electrolysis, oxygen produced at the anode may pollute the hydrogen stream. The presence of oxygen arises mainly from mixing the oxygen and hydrogen saturated electrolytes [27]. This mixing is directly related to the pump design of the system and to the techniques adopted to balance the electrolyte levels between the oxygen and hydrogen gas separators. Direct gas diffusion through separators is minimal and 0.2 to 0.6% of oxygen in hydrogen are reported for commercial alkaline systems. Similarly, hydrogen is also present in the oxygen stream and was extensively studied for safety concerns under partial load operation [23]. Schug *et al.* measured that the lower explosive limit level is more likely to be obtained on the O₂ side than on the H₂ side [28] due to the higher production rate. For example, when 3000 ppm of O₂ in H₂ were measured (at 100 mA/cm²), up to 1.2 % of H₂ in O₂ were reported. Similar results have also been reported by Sanchez [29].

Oxygen is typically removed using a catalytic recombination:



Because the reaction is exothermic and produces water, it is usually carried before a condensation (cooling & filtering) drying step.

Moisture

The presence of water in hydrogen streams may form ice and affect control components. The 5 ppm limit ensures that water remain gaseous even in high-pressure cylinders at low ambient temperatures, and thus, prevents corrosion of metallic components. In addition, water could carry water soluble contaminants such as K^+ and Na^+ . Potassium and sodium levels below 0.05 ppm are required, because they reduce the proton conductivity of the fuel cell membrane. Nevertheless, PEM fuel cells are tolerant to up to 500 ppm of water, as long as it does not affect internal flows [30]. Hydrogen from alkaline water electrolysis is saturated with water at production temperatures. Large amounts of water can be removed by simply cooling down the hydrogen, but freezing temperatures should be avoided because of ice formation. A dew point of 5°C at 10 and 40 bar corresponds respectively to 1000 and 200 ppm of water, thus further drying is needed to reach 5 ppm. Drying units typically involve temperature swing adsorption (TSA) or pressure swing adsorption (PSA) systems (see **Table 5.5**). Depending on the selected adsorbents, other species such as CO and CO_2 can also be removed [31,32]. The regeneration of adsorbents is favoured at low pressures and high temperatures as presented in **Figure 5.6** [33]. For PSA, a minimum pressure ratio of 4:1 is typically recommended [34], and for TSA the regeneration temperature depends on the adsorbent, with typically $200\text{--}300^\circ\text{C}$ for molecular sieves. Usually, a larger adsorbent loading window is accessible with TSA, due to a regeneration at lower loadings. Nevertheless, a control failure with the heating elements of a TSA may present safety hazards and create hot spots.

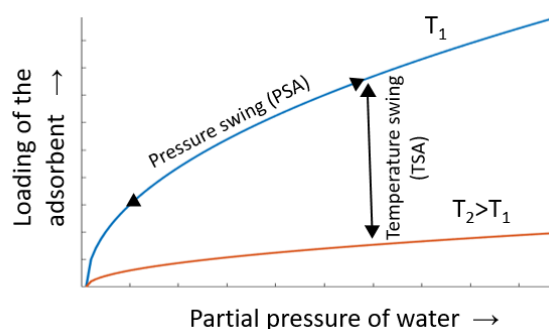


Figure 5.6 – Schematic representation of temperature swing and pressure swing processes (adapted from H.-J. Bart and U. von Gemmingen [33]).

Table 5.5 – PSA and TSA process steps.

Step	PSA	TSA
Drying	Adsorption at high pressure	Adsorption at low (ambient) temperature
Regeneration/Desorption	Depressurization	Temperature increase
	Purging at low pressure	Purging at high temperature
	Pressure build-up	Cooling down

The purging flow is typically implemented *via* a fixed orifice technique, set to 3 to 10% of rated hydrogen output depending on the regeneration mode [35,36]. Stansberry and Brouwer [7] reported a 0.0744 kg H₂/h purge flow at 30 bar for a PSA dryer system installed in a commercial 60 kW PEM electrolyser. It corresponds to 8% of the rated hydrogen output and 5 kW of system power consumption.

For improved purity and lower energy consumption, advanced PSA and TSA systems can be regenerated under vacuum, and are respectively named VPSA and TVSA. For CO₂ capture applications, it was shown that VPSA can consume respectively 4 and 8 times less energy than TVSA and TSA systems [36]. Considering that hydrogen purification is part of the overall grid to mobility pathway [37], product recovery and energy consumption of the drying system are particularly important. Both can be quantified as equivalent recovery rate *via* the equivalent hydrogen that could be produced with the electricity input.

For TSA, the losses can be attributed to the purge flow and the heating requirements. For PSA, in addition to the purge flow, the depressurization of the adsorber bed adds up to the total hydrogen losses [38]. The pressurisation, however, is in any case needed for further use and storage for hydrogen mobility and cannot be considered as a loss for drying purposes. For reference, the conventional TSA system delivered with our electrolyser consists of 3 filters with a total loading of 24 kg of molecular sieves with a rated lifetime of 2 to 6 months.

In the present work, quantitative and qualitative measurements were performed to characterize the purity of the hydrogen stream in a 50 kW commercial alkaline electrolyser and its corresponding purification and drying systems. The time evolution and the influence of various current densities were investigated. The processes in place are discussed to track back the origin of contaminants and the countermeasures to reach the ISO 14687:2019 specifications.

5.3.2 Removal methods and quantification

Electrolyser and purification systems

The alkaline electrolyser used for the measurements is based on commercial stacks from a McPhy McLyzer 10-10. The plant balance, gas management and control system were significantly redesigned and modified for better performance and research purposes [39]. The specifications are summarized in **Table 5.6**.

Table 5.6 – Electrolyser specifications.

Parameter	Value
Nominal Power (DC)	50 kW (2 x 25 kW stacks)
Nominal production rate at 300 mA/cm ²	850 g H ₂ /h
Cells per stack	115
Geometric electrode surface area	370 cm ²
Electrode gap	5.5 mm
Current density	160 – 320 mA/cm ²
Electrolyte	30 wt% KOH (<i>ca.</i> 60 L)
Inertization and pressurization media	Nitrogen 99.999%
Temperature of operation	Stack inlet: 52.5 °C (regulated) Stack outlet: 60 – 75°C
Operating pressure	10 bar
Gas cooling	5°C chilled water with plate heat exchangers

Specific start-up and shut-down procedure were implemented to ensure the repeatability of the measurements, as well as an inert environment for long stand-by periods. Notably, the system is pressurised and purged using nitrogen, before current is applied. The shutdown procedure includes five minutes of system purge with nitrogen, and slow depressurisation to atmospheric pressure.

Three systems, presented in **Figure 5.7**, are installed to purify the hydrogen stream coming from the stacks. First, a scrubber is used for particulate and KOH removal: the wet hydrogen coming from the gas separator is bubbled through the feed-in deionized water. Then, it passes through a deoxygenation reactor where the catalytic recombination of oxygen occurs. The warm outlet gas is cooled down and water removed by a coalescing filter. Finally, hydrogen is further dried in a VPSA unit working at *ca.* 40 bar.

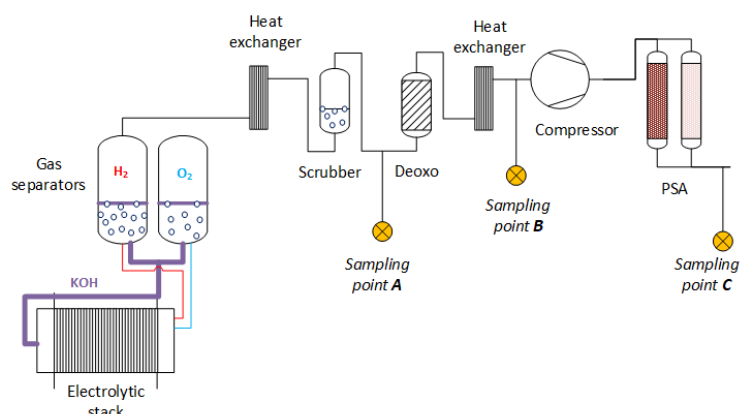


Figure 5.7 – Simplified flowsheet of purification and drying steps installed on a 50 kW alkaline electrolyser.

The deoxygenation system consists of a vessel packed with 3mm beads of Pd/alumina catalyst prepared following a similar route as the one described by Lyubovsky [40] (1.2% Pd loading: 1kg alumina and 25g Palladium acetate).

VP SA design and operation

A VP SA was designed and built to meet ISO purity specifications, with a minimal energetic cost, and gas losses during regeneration. The system was engineered to take advantage of the two compression steps occurring between the electrolyser outlet at 10 bar and the main hydrogen storage of the HRS at 200 bar.

The original Skarstrom PSA cycle was modified to include a regeneration under vacuum, and partial hydrogen recycling. Prior to the vacuum regeneration, 75% of the column gas content are recycled back to the fresh column and the compressor.

A scheme of the main components, valves and measuring instruments of the VP SA is shown in **Figure 5.8**. The compression is performed with air driven gas boosters, and the overall system is controlled *via* a programmable logic controller communicating with both the electrolyser and the storage systems. 15 microns filters are installed at the inlet and the outlet of the columns to avoid the contamination with dessicant particulates.

The design parameters are listed in **Table 5.7**.

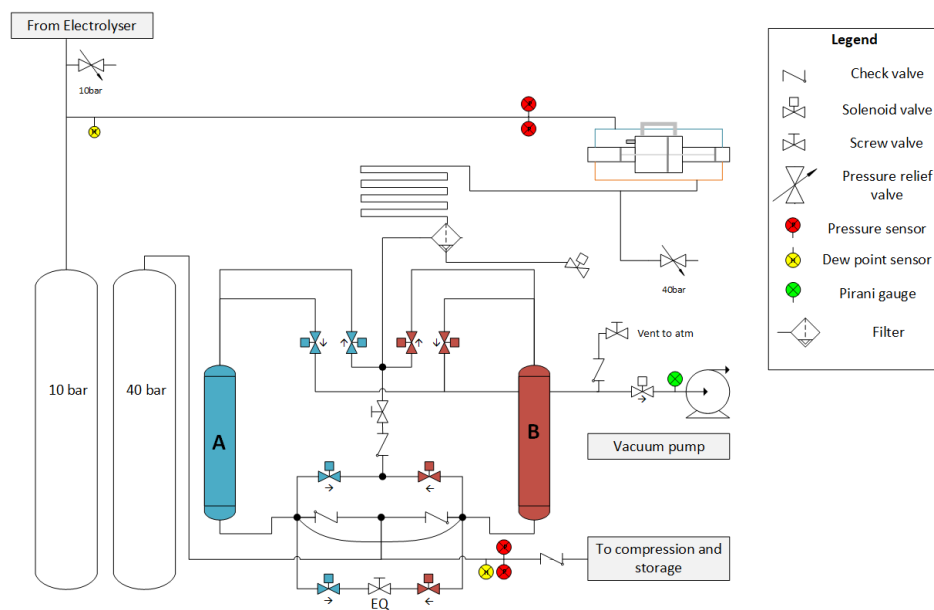


Figure 5.8 – Piping and instrumentation diagram of the vacuum assisted pressure swing adsorption system developed.

Table 5.7 – VPSA specifications.

Parameter	Value
Column volume	3.8 L (1 US gal.) per column, height 60 cm, diameter 9 cm
Column empty volume	2.6 L
Dessicant type	Molecular sieve 4Å, beads 8-12 mesh
Dessicant loading	2.77 kg per column
Operating pressure	35-38 bar, regeneration at 0.1 mbar
Vacuum pump	Edwards nXDS 15i
Purge flow limiter	PEEKsil capillary tubing 50cm, 25 µm internal diameter
Cycle duration	10 minutes

Molecular sieves 4Å was selected as desiccant since it maintains a high adsorption capacity even at low water vapor pressure, allowing lower dew points to be reached when compared to activated alumina or silica gel [41]. Following the two-site Langmuir adsorption isotherm from Jury and Horng [42], a regeneration at 0.1 mbar and 25°C is equivalent to a regeneration at atmospheric pressure and 190°C (Equation 5.1).

$$W(T, P) = \frac{A_L B_L X_h(T, P)}{1 + B_L X_h(T, P)} + \frac{A_h B_h X_h(T, P)}{1 + B_h X_h(T, P)}$$

$$\text{with } X_h(T, P) = \frac{\exp\left(\frac{A}{T}\right)}{\sqrt{T}} \cdot P$$

Equation 5.1 – Adsorption isotherm from Jury and Horng ([42]).

Where the first term represents the mass adsorbed in the clay binder and the second term the mass adsorbed in the zeolite. W corresponds to the mass adsorbed in g/g of pellets. The optimized parameters, with T the dew point in Kelvin and P the water vapour pressure in bar, are [43] $A_h = 0.1579$, $B_h = 6.371 \cdot 10^{-9}$, $A_L = 4.79 \cdot 10^{-2}$, $B_L = 3.095 \cdot 10^{-11}$, $A = 7509$.

Despite a high desiccant loading, it was decided to maintain short pressure swing cycles in order to limit the thermal effects linked to the heat of adsorption and to limit the mass transfer zone to the upper part of the column.

Analytical instruments

Qualitative and quantitative measurements were performed at different points as presented in **Figure 5.7**. Hydrogen samples were compared with a known sample of hydrogen quality 99.9999% by mass spectrometry (MS, Pfeiffer Vacuum OMNIStar GSD 320) and gas chromatography (GC) measurements (see method in **Table 5.8**).

Water was monitored by two online dew point sensors (easidew I.S. - Michell instruments) placed at the outlets of electrolyser and VPSA. Dew point values are converted into ppm(v) values using the formula developed by Buck [44].

$$\text{Water vapour pressure [Pa]} = 611.15 \cdot \exp \left[\frac{(23.036 - T_{dew}/333.7) \cdot T_{dew}}{279.82 + T_{dew}} \right]$$

With T_{dew} , the measured dew point in degree Celsius.

Oxygen is measured with a galvanic fuel cell sensor (GE Panametrics, Oxi iQ). The overall system in operation is presented in **Figure 5.9**.

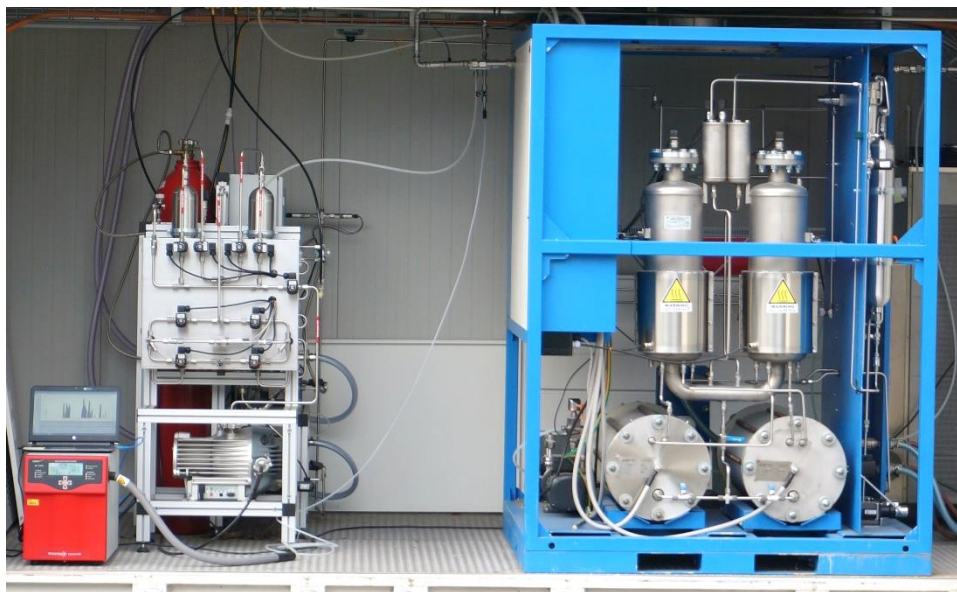


Figure 5.9 – Overall system in operation with continuous MS monitoring, VPSA on the left side and electrolyser on the right side.

Table 5.8 – GC method.

Model type	Perkin Elmer Clarus 500
Carrier gas	Helium 5.0
Sample loop	125 μL
Column type	Metal packed, 1.8m, 60/80 Molecular Sieve 5 A support
Column Flow	12 $\text{mL}\cdot\text{min}^{-1}$
Temperature ramp	50°C (5 min) - +15°C/min - 150 °C (3 min)
Detector	TCD, 150°C
Sample collection	10 mL gas tight syringe

5.3.3 Contaminant removal performance

In nominal operating conditions, GC and MS analyses of the gas at electrolyser outlet confirm the presence of three main contaminants namely water, nitrogen and oxygen as shown in **Figure 5.10**. Systems response to commercial 99.9999% hydrogen was recorded to serve as reference.

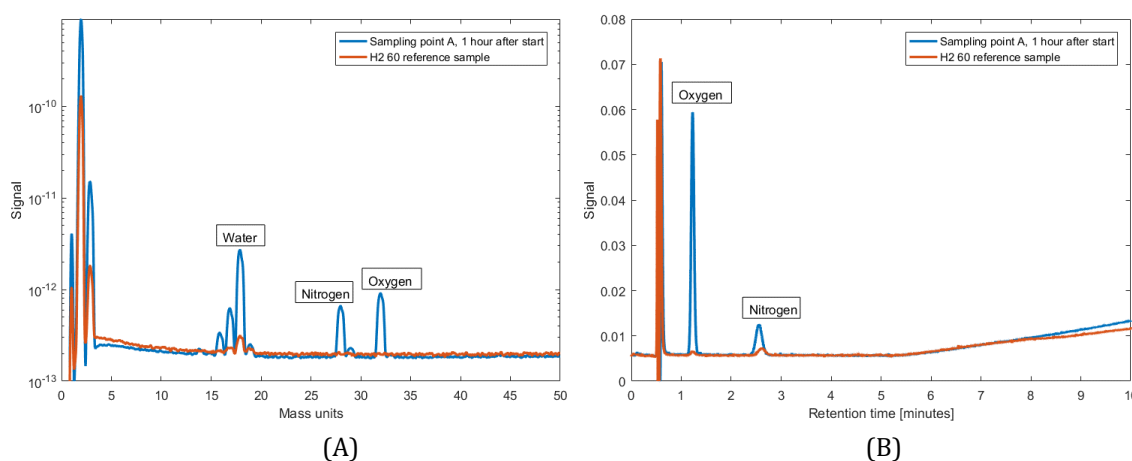


Figure 5.10 – Mass spectrum (A) and Gas chromatograph (B) of untreated hydrogen from alkaline electrolysis.

Nitrogen removal

To validate the hypothesis that the major source of nitrogen comes from the inertization step, nitrogen content was monitored over time by mass spectrometry, as shown in **Figure 5.11**. Nitrogen content decreases over time to reach ISO 14687:2019 levels after 100 minutes from start-up. The remaining signal may be attributed to the sampling method and nitrogen dissolved in feed-in water. Based on these findings, we can easily understand why most electrolyser's manufacturers have developed hot standby modes, and thus avoid nitrogen inertization sequences and long purge times for short stop periods. Finally, in continuous operation, there is no reason to observe an increase of the nitrogen content.

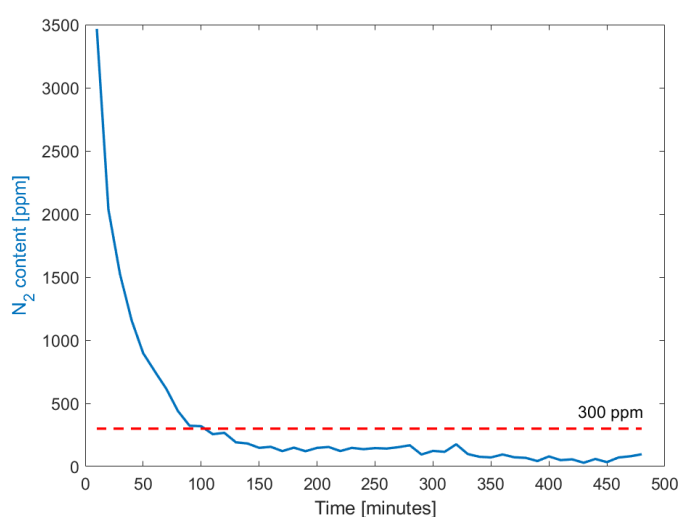


Figure 5.11 – Time evolution of nitrogen content in the outlet stream of the electrolyser measured by mass spectrometry (calibration with dilution samples in autoclaves).

Oxygen removal

Oxygen levels below 4 ppm are obtained after a catalytic recombination in the deoxygenation reactor. Because of the exothermic nature of the reaction (see **Figure 5.12**), further cooling is needed to remove the water produced by the reaction. A close monitoring of the temperature within the deoxygenation reactor can also be a way to detect malfunctions in the process and trigger preventive measures to avoid a contamination of storage tanks.

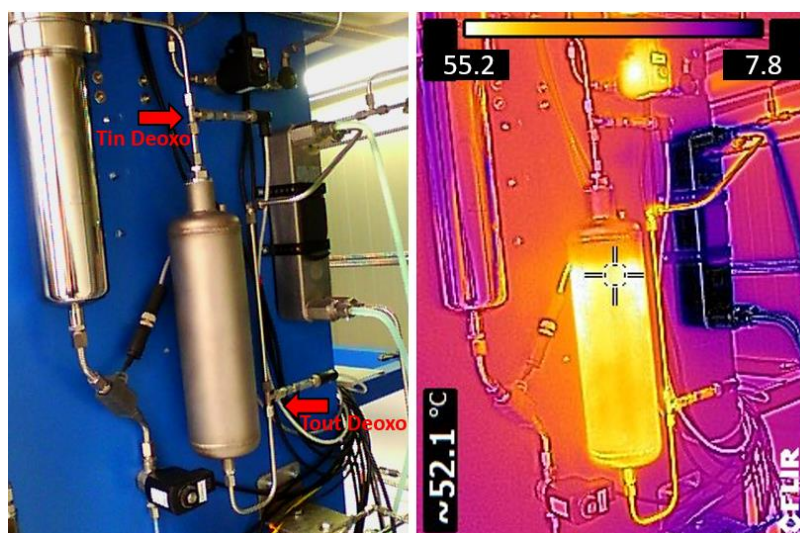


Figure 5.12 – Infrared image of the gas treatment panel, centered on the deoxygenation reactor.

The relative importance of oxygen crossover and electrolyte mixing is higher for low production rates as confirmed by **Figure 5.13**. Analysis of the raw gas before deoxygenation show an almost linear dependence on the applied power, with lower oxygen concentrations obtained at higher production rate. Post deoxidizer levels were always kept between 1 and 4 ppm.

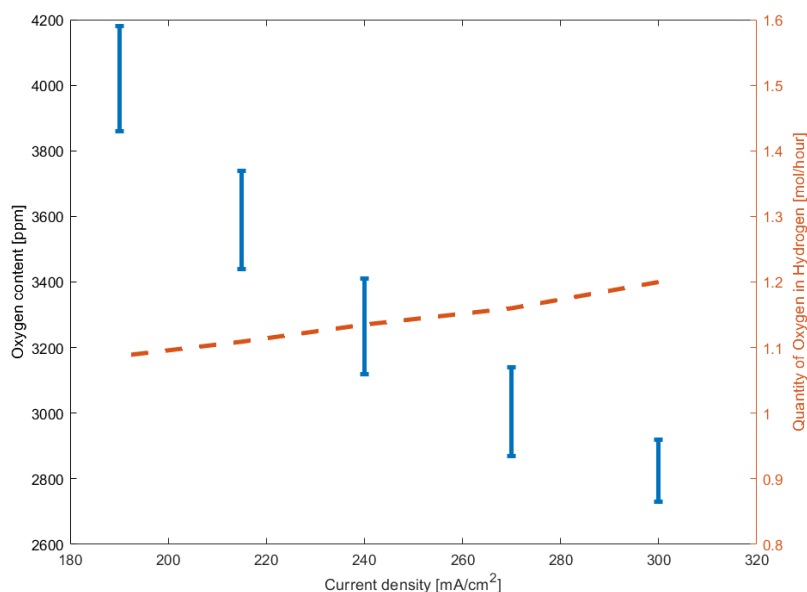


Figure 5.13 – Influence of current density on oxygen contamination.

Because of the catalytic recombination, hydrogen is consumed during this purification step. A recovery rate of 99.2 to 99.4% can be calculated from the measured values.

Water removal

Water is removed from the hydrogen stream by condensation at lower temperatures followed by adsorption in the VPSA system. From the saturated hydrogen leaving the gas separator, 3 successive steps are required to reach ISO levels (see **Figure 5.14**).

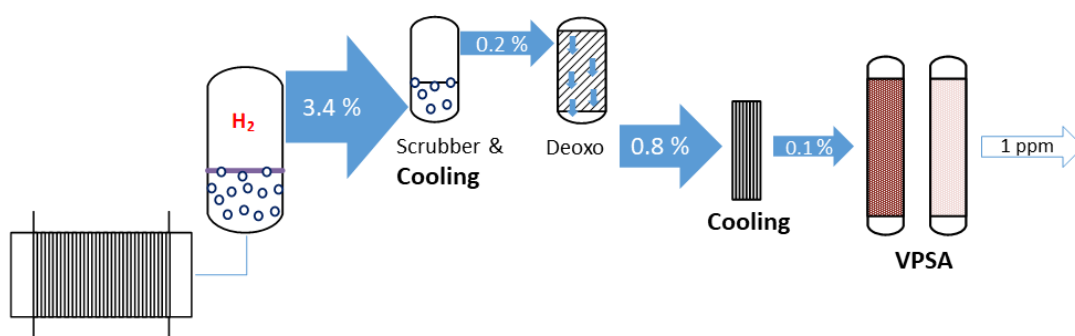


Figure 5.14 – Water removal steps and corresponding water content of the hydrogen stream.

The water formed during the catalytic recombination, adds up to the already saturated hydrogen and leads to the collection of 50-70 mL of water per hour after gas cooling. The collected water is free from KOH, which validates the role of the scrubber, and no water is collected before the deoxidizer, which validates that no water droplets exit the scrubber. Thus, the hydrogen leaving the electrolyser

is saturated at around 5°C at *ca.* 9 bar, which corresponds to *ca.* 1000 ppm, in line with the data reported **Figure 5.15**.

The VPSA is started after 80 minutes of electrolyser operation, and immediately removes water to sub ppm levels, with a dew point of *ca.* -75°C at 38 bar. The dew point sensor is reported to have a 5 minutes response time.

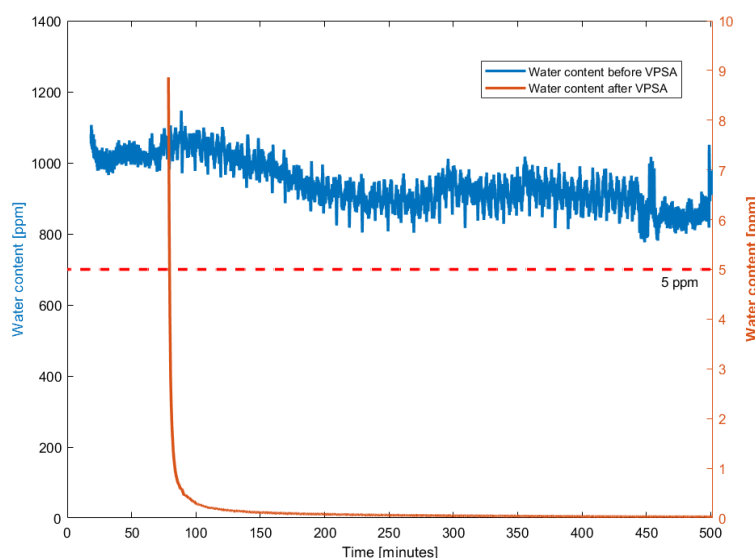


Figure 5.15 – Dew point measurements over time.

After 100 hours of cumulated operation of the VPSA, one column was deliberately saturated to confirm that the column was properly regenerated during these 600 cycles. The used column was able to uptake 21 w% of water before a noticeable increase of the dew point measured on the outlet stream. This confirms that the mass transfer zone was confined to the head of the column and the vacuum assisted regeneration was sufficient to remove the totality of the water adsorbed.

The power consumption of the vacuum pump, control electronics and solenoid valves amount to *ca.* 400 W, which translates to an energy consumption of 0.5 kWh/kg H₂. At this scale, commercial TSA are typically installed with 2 kW heaters operated during 60% of the regeneration time, corresponding to 1.4 kWh/kg H₂. Most of the gains are realised on the product recovery with a purging flow of only 540 mL/h measured through the capillary, and a partial recycling of the depressurized hydrogen, with only 1.6% vented. Finally, the equivalent recovery rate of hydrogen amounts to 97.4% compared to less than 90% reported in equivalent commercial TSA systems. Further improvements can be obtained with asymmetric adsorption/regeneration cycles, but it would require additional characterization of the systems kinetics.

5.4 Conclusion

Alkaline water electrolysis is an old technology but modern modelling techniques and new materials and controls can still improve its efficiency. Despite a relatively simple working principle at the cell level, a massive number of regulation and control loops must be implemented to have a reliable and safe working process at the system level. More than 6.5 kWh/kg H₂ are consumed by auxiliaries and power supplies. In addition, the use of electrolytic hydrogen in fuel cells requires the development of specific purification systems. Indeed, in order to obtain a hydrogen quality fulfilling the ISO 14687:2019 specifications, several procedures and methods must be implemented. Three contaminants require particular attention: nitrogen, oxygen and water. Operating procedures, such as inertization and load modulation, as well as design and regulation techniques, directly impact the relative abundance of contaminants. Hydrogen post-treatment systems for electrolyzers are rarely documented in the literature and mostly remains the in-house expertise of manufacturers. Using a 50 kW - 10 bar alkaline electrolyser, we have designed, documented and characterized all the processes required in the gas management to achieve a hydrogen quality compatible with the ISO 14687:2019 standard.

Nitrogen is the easiest contaminant to remove, requiring appropriate initial purge time and eventually airless pressurized feed-in water tanks. 100 min of purge are here required. Oxygen removal is achieved *via* a catalytic recombination with hydrogen, and thus leads to 0.6–0.8% hydrogen losses.

Finally, the most energy intensive step is the drying. Water coming from the electrolyte and the deoxidizer must be removed to levels below 5 ppm, requiring the use of swing adsorption processes. PSA is usually recognized as more energy efficient than TSA, but rarely used in hydrogen drying applications. An efficient regeneration of the adsorbent was realised using a vacuum pump to reduce the purge flow by 3 orders of magnitude and a hydrogen recycling was implemented to reduce the depressurization losses. A hydrogen recovery performance of 98.4% was achieved, a water content <0.1 ppm, and an energy consumption of 0.5 kWh/kg H₂.

The cumulative losses for purification correspond to 3.6% of the initial equivalent hydrogen stream, compared to 8–20% with temperature-based systems without recycling. Purge flow, desiccant loading and regeneration time implemented here can serve as a reference point for further optimisation, and can be complemented with beads degradation studies. Additional integration leveraging the various heat sources available in the gas management system could also improve the overall efficiency.

References

- [1] Y. Ligen, H. Vrubel, H. Girault, Energy efficient hydrogen drying and purification for fuel cell vehicles, *International Journal of Hydrogen Energy*. 45 (2020). <https://doi.org/10.1016/j.ijhydene.2020.02.035>.
- [2] G. Kreysa, M. Kuhn, Modelling of gas evolving electrolysis cells. I. The gas voidage problem, *J Appl Electrochem*. 15 (1985) 517–526. <https://doi.org/10.1007/BF01059293>.
- [3] K. Ayers, N. Danilovic, R. Ouimet, M. Carmo, B. Pivovar, M. Bornstein, Perspectives on Low-Temperature Electrolysis and Potential for Renewable Hydrogen at Scale, *Annu. Rev. Chem. Biomol. Eng.* 10 (2019) 219–239. <https://doi.org/10.1146/annurev-chembioeng-060718-030241>.
- [4] P. Olivier, C. Bourasseau, Pr.B. Bouamama, Low-temperature electrolysis system modelling: A review, *Renewable and Sustainable Energy Reviews*. 78 (2017) 280–300. <https://doi.org/10.1016/j.rser.2017.03.099>.
- [5] C. Lamy, P. Millet, A critical review on the definitions used to calculate the energy efficiency coefficients of water electrolysis cells working under near ambient temperature conditions, *Journal of Power Sources*. 447 (2020) 227350. <https://doi.org/10.1016/j.jpowsour.2019.227350>.
- [6] X. Li, N. Wang, L. Wang, I. Kantor, J.-L. Robineau, Y. Yang, F. Maréchal, A data-driven model for the air-cooling condenser of thermal power plants based on data reconciliation and support vector regression, *Applied Thermal Engineering*. 129 (2018) 1496–1507. <https://doi.org/10.1016/j.applthermaleng.2017.10.103>.
- [7] J.M. Stansberry, J. Brouwer, Experimental dynamic dispatch of a 60 kW proton exchange membrane electrolyzer in power-to-gas application, *International Journal of Hydrogen Energy*. 45 (2020) 9305–9316. <https://doi.org/10.1016/j.ijhydene.2020.01.228>.
- [8] L. Allidières, A. Brisse, P. Millet, S. Valentin, M. Zeller, On the ability of pem water electrolyzers to provide power grid services, *International Journal of Hydrogen Energy*. 44 (2019) 9690–9700. <https://doi.org/10.1016/j.ijhydene.2018.11.186>.
- [9] R. Gilliam, J. Graydon, D. Kirk, S. Thorpe, A review of specific conductivities of potassium hydroxide solutions for various concentrations and temperatures, *International Journal of Hydrogen Energy*. 32 (2007) 359–364. <https://doi.org/10.1016/j.ijhydene.2006.10.062>.
- [10] T. Bacquart, A. Murugan, M. Carré, B. Gozlan, F. Auprêtre, F. Haloua, T.A. Aarhaug, Probability of occurrence of ISO 14687-2 contaminants in hydrogen: Principles and examples from steam methane reforming and electrolysis (water and chlor-alkali) production processes model, *International Journal of Hydrogen Energy*. 43 (2018) 11872–11883. <https://doi.org/10.1016/j.ijhydene.2018.03.084>.
- [11] ISO Standard, ISO 19880-8, Gaseous hydrogen - Fuelling stations, Part 8: Fuel quality control, (2019). <https://www.iso.org/standard/69540.html>.

- [12] Y.-W. You, D.-G. Lee, K.-Y. Yoon, D.-K. Moon, S.M. Kim, C.-H. Lee, H₂ PSA purifier for CO removal from hydrogen mixtures, *International Journal of Hydrogen Energy*. 37 (2012) 18175–18186. <https://doi.org/10.1016/j.ijhydene.2012.09.044>.
- [13] A. Golmakani, S. Fatemi, J. Tamnanloo, Investigating PSA, VSA, and TSA methods in SMR unit of refineries for hydrogen production with fuel cell specification, *Separation and Purification Technology*. 176 (2017) 73–91. <https://doi.org/10.1016/j.seppur.2016.11.030>.
- [14] B.M. Besancon, V. Hasanov, R. Imbault-Lastapis, R. Benesch, M. Barrio, M.J. Møltnvik, Hydrogen quality from decarbonized fossil fuels to fuel cells, *International Journal of Hydrogen Energy*. 34 (2009) 2350–2360. <https://doi.org/10.1016/j.ijhydene.2008.12.071>.
- [15] N.A. Al-Mufachi, N.V. Rees, R. Steinberger-Wilkens, Hydrogen selective membranes: A review of palladium-based dense metal membranes, *Renewable and Sustainable Energy Reviews*. 47 (2015) 540–551. <https://doi.org/10.1016/j.rser.2015.03.026>.
- [16] L. Schorer, S. Schmitz, A. Weber, Membrane based purification of hydrogen system (MEMPHYS), *International Journal of Hydrogen Energy*. 44 (2019) 12708–12714. <https://doi.org/10.1016/j.ijhydene.2019.01.108>.
- [17] J. Xiao, L. Tong, T. Yang, P. Bénard, R. Chahine, Lumped parameter simulation of hydrogen storage and purification systems using metal hydrides, *International Journal of Hydrogen Energy*. 42 (2017) 3698–3707. <https://doi.org/10.1016/j.ijhydene.2016.11.060>.
- [18] ISO Standard, ISO 21087:2019 Gas Analysis - Analytical methods for hydrogen fuel - Proton exchange membrane (PEM) fuel cell applications for road vehicles, (2019). <https://www.iso.org/standard/69909.html>.
- [19] A. Murugan, A.S. Brown, Review of purity analysis methods for performing quality assurance of fuel cell hydrogen, *International Journal of Hydrogen Energy*. 40 (2015) 4219–4233. <https://doi.org/10.1016/j.ijhydene.2015.01.041>.
- [20] VTT Technical Research Centre of Finland, European Project Hydraite 2018-2020 - Hydrogen Delivery Risk Assessment and Impurity Tolerance Evaluation, (2018). <https://hydraite.eu/> (accessed November 21, 2019).
- [21] HyCoRA - Hydrogen Contaminant Risk Assessment, (2018). <http://hycora.eu/> (accessed January 15, 2020).
- [22] MetroHyVe Metrology for Hydrogen Vehicles, (2020). <https://www.metrohyve.eu/wp-2-hydrogen-quality-assurance/> (accessed January 15, 2020).
- [23] P. Haug, B. Kreitz, M. Koj, T. Turek, Process modelling of an alkaline water electrolyzer, *International Journal of Hydrogen Energy*. 42 (2017) 15689–15707. <https://doi.org/10.1016/j.ijhydene.2017.05.031>.
- [24] ISO Standard, ISO 14687:2019 Hydrogen fuel quality — Product specification, (2019). <https://www.iso.org/standard/69539.html> (accessed January 15, 2020).

- [25] V. Schröder, B. Emonts, H. Janßen, H.-P. Schulze, Explosion Limits of Hydrogen/Oxygen Mixtures at Initial Pressures up to 200 bar, *Chem. Eng. Technol.* 27 (2004) 847–851. <https://doi.org/10.1002/ceat.200403174>.
- [26] J.J. Hwang, Review on development and demonstration of hydrogen fuel cell scooters, *Renewable and Sustainable Energy Reviews.* 16 (2012) 3803–3815. <https://doi.org/10.1016/j.rser.2012.03.036>.
- [27] P. Haug, M. Koj, T. Turek, Influence of process conditions on gas purity in alkaline water electrolysis, *International Journal of Hydrogen Energy.* 42 (2017) 9406–9418. <https://doi.org/10.1016/j.ijhydene.2016.12.111>.
- [28] C.A. Schug, Operational characteristics of high-pressure, high-efficiency water-hydrogen-electrolysis, *International Journal of Hydrogen Energy.* 23 (1998) 1113–1120. [https://doi.org/10.1016/S0360-3199\(97\)00139-0](https://doi.org/10.1016/S0360-3199(97)00139-0).
- [29] M. Sánchez, E. Amores, L. Rodríguez, C. Clemente-Jul, Semi-empirical model and experimental validation for the performance evaluation of a 15 kW alkaline water electrolyzer, *International Journal of Hydrogen Energy.* 43 (2018) 20332–20345. <https://doi.org/10.1016/j.ijhydene.2018.09.029>.
- [30] European Committee for Standardization, EN 17124:2018-10 Hydrogen fuel - Product specification and quality assurance - Proton exchange membrane (PEM) fuel cell application for road vehicles, (2018).
- [31] E.H. Majlan, W.R. Wan Daud, S.E. Iyuke, A.B. Mohamad, A.A.H. Kadhum, A.W. Mohammad, Mohd.S. Takriff, N. Bahaman, Hydrogen purification using compact pressure swing adsorption system for fuel cell, *International Journal of Hydrogen Energy.* 34 (2009) 2771–2777. <https://doi.org/10.1016/j.ijhydene.2008.12.093>.
- [32] S. Sircar, T.C. Golden, Purification of Hydrogen by Pressure Swing Adsorption, *Separation Science and Technology.* 35 (2000) 667–687. <https://doi.org/10.1081/SS-100100183>.
- [33] H.-J. Bart, U. von Gemmingen, Adsorption, in: *Ullmann's Encyclopedia of Industrial Chemistry*, American Cancer Society, 2005. https://doi.org/10.1002/14356007.b03_09.pub2.
- [34] A.L. Kohl, R.B. Nielsen, Chapter 12 - Gas Dehydration and Purification by Adsorption, in: A.L. Kohl, R.B. Nielsen (Eds.), *Gas Purification (Fifth Edition)*, Fifth Edition, Gulf Professional Publishing, Houston, 1997: pp. 1022–1135. <https://doi.org/10.1016/B978-088415220-0/50012-4>.
- [35] M. Peters, H. Dinh, DOE 2016 Annual Progress Report II.B.1 Renewable Electrolysis Integrated Systems Development and Testing, (2016). https://hydrogendoedev.nrel.gov/pdfs/progress16/ii_b_1_peters_2016.pdf (accessed November 21, 2019).
- [36] N. Jiang, Y. Shen, B. Liu, D. Zhang, Z. Tang, G. Li, B. Fu, CO₂ capture from dry flue gas by means of VPSA, TSA and TVSA, *Journal of CO₂ Utilization.* (2019) S2212982019303233. <https://doi.org/10.1016/j.jcou.2019.09.012>.

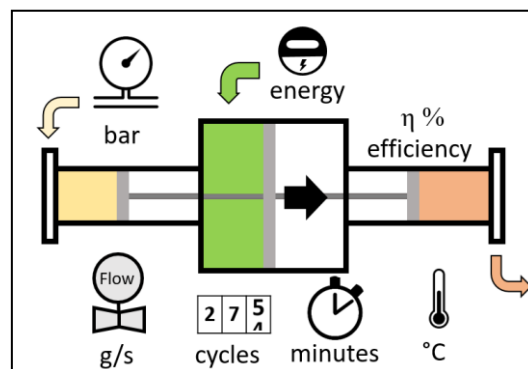
- [37] Y. Ligen, H. Vrubel, H. Girault, Mobility from Renewable Electricity: Infrastructure Comparison for Battery and Hydrogen Fuel Cell Vehicles, *World Electric Vehicle Journal*. 9 (2018) 3. <https://doi.org/10.3390/wevj9010003>.
- [38] G. Tjarks, A. Gibelhaus, F. Lanzerath, M. Müller, A. Bardow, D. Stolten, Energetically-optimal PEM electrolyzer pressure in power-to-gas plants, *Applied Energy*. 218 (2018) 192–198. <https://doi.org/10.1016/j.apenergy.2018.02.155>.
- [39] Y. Ligen, H. Girault, J. Rager, Combined service station for battery electric & hydrogen fuel cell vehicles - Final Report, Swiss Federal Office for Energy. (2018). <https://www.aramis.admin.ch/Dokument.aspx?DocumentID=50166> (accessed November 21, 2019).
- [40] M. Lyubovsky, L. Pfefferle, A. Datye, J. Bravo, T. Nelson, TEM Study of the Microstructural Modifications of an Alumina-Supported Palladium Combustion Catalyst, *Journal of Catalysis*. 187 (1999) 275–284. <https://doi.org/10.1006/jcat.1999.2545>.
- [41] E.M. Robson, The Vacuum Use of Molecular Sieves and other Desiccants, *Vacuum*. 11 (1961) 6. [https://doi.org/10.1016/0042-207X\(61\)90206-8](https://doi.org/10.1016/0042-207X(61)90206-8).
- [42] S.H. Jury, J.S. Horng, The molecular sieve 4-A water vapor sorption therm, *AIChE J.* 19 (1973) 371–372. <https://doi.org/10.1002/aic.690190226>.
- [43] K.F. Loughlin, Water isotherm models for 4A (NaA) zeolite, *Adsorption*. 15 (2009) 337–353. <https://doi.org/10.1007/s10450-009-9189-2>.
- [44] A.L. Buck, New Equations for Computing Vapor Pressure and Enhancement Factor, *Journal of Applied Meteorology*. 20 (1981) 1527–1532. [https://doi.org/10.1175/1520-0450\(1981\)020<1527:NEFCVP>2.0.CO;2](https://doi.org/10.1175/1520-0450(1981)020<1527:NEFCVP>2.0.CO;2).

Chapter 6

Hydrogen at scale and booster modelling

The results presented in this chapter were partially published in the following paper:

Y. Ligen, H. Vrabel, J. Arlettaz, H. Girault, Experimental correlations and integration of gas boosters in a hydrogen refueling station, International Journal of Hydrogen Energy. (2020) S0360319920315652. <https://doi.org/10.1016/j.ijhydene.2020.04.162>. [1]



6.1 Hydrogen storage modes and release

Under ambient conditions, hydrogen is not a suitable energy carrier due to its very low volumetric density (0.08988g/L at 1 bar and 0°C, which translates to ca. 3 Wh/L). Conditioning hydrogen in an energy dense carrier is one of the key challenges for hydrogen mobility and for the hydrogen economy in general. The conditioning method directly influences the energy footprint, the transport and delivery logistics, as well as storage and release constraints. While compressed hydrogen storage is currently the preferred storage mode for road vehicles, some alternatives are still under consideration either for the logistics to the HRS or vehicles with different on-board storage constraints. Three main hydrogen storage families are presented in **Table 6.1**.

Table 6.1 – Hydrogen energy carrier options.

Hydrogen carrier	Volumetric and gravimetric capacity	Conditioning	Release process and device
Compressed Gaseous Hydrogen, 350 – 700 bar	25 – 40 g/L 5 wt.%* (Type IV)	Compression	Expansion Pressure reducer
Liquid hydrogen – 253°C	70 g/L 10 wt.%*	Liquefaction	Vaporisation Heat exchanger
Liquid Organic Hydrogen Carrier (LOHC)	Up to 50 g/L 4 - 10 wt.%*	Hydrogenation	Dehydrogenation Catalytic reactor

*system level

The U.S. Department of Energy (DoE) has set a technical target of 5.5 wt.% and 40g/L at the system level¹. However, each storage mode comes with logistics and scaling challenges discussed in section 6.3.

Methane (ca. 50g H₂/L at 250 bar) and hydrocarbons in general can also be considered as hydrogen carriers with methanation and Fischer-Tropsch process for conditioning, and reforming or gasification for release. However, the hydrogen to hydrogen cycle *via* hydrocarbons is poorly efficient.

Ammonia (17.6 wt.%) is also a promising hydrogen carrier but with remaining challenges for energy efficient, reliable and scalable release and separation of the H₂ product. Large intercontinental hydrogen shipping project often consider ammonia tankers.

¹ <https://www.energy.gov/eere/fuelcells/doe-technical-targets-onboard-hydrogen-storage-light-duty-vehicles>

Another class of materials being developed for hydrogen storage includes metal hydrides and porous materials such as Metal Organic Frameworks (MOF). The first one involves chemical sorption, and the second one is based on physical sorption with weaker binding energies and faster adsorption/desorption kinetics. The formation of hydrogen compounds is exothermic and the release of hydrogen requires heat input. Current research is focused on storage capabilities under room temperature conditions and reversibility [2,3].

6.1.1 Compressed gaseous hydrogen

The compression of hydrogen can be realized by a wide range of mechanical or non-mechanical processes (see **Table 6.2** derived from [4]). The working principle of compressed air driven gas boosters, a derivation of reciprocating piston compressors, is deeply analyzed in section 6.2.

Table 6.2 – Gaseous hydrogen compression technologies.

Mechanical compressors	Advantages	Disadvantages
Reciprocating piston	Mature, large ranges of flow rates	Gas contamination, moving parts
Diaphragm	Low power consumption, no gas contamination	Diaphragm failure risk
Ionic liquid piston	High efficiency, no gas contamination	Liquid handling (leaks, corrosion, cavitation)
Non-mechanical compressors	Advantages	Disadvantages
Metal hydride or MOF https://cosmhyc.eu/cosmhyc-xl-project	Integration with industrial heat, no moving parts	Low efficiency, maturity
Electrochemical	Very high efficiency, no moving parts	Challenges for cell assembly & need for precious metals

With liquid hydrogen at the input of the compression process, cryogenic compression can be implemented. Linde has designed a cryopump system for HRS², which can deliver up to 100 kg H₂/h. The direct compression of liquid hydrogen and the absence of active cooling system reduces the energy consumption to only 0.37 kWh/kg H₂ [5] compared to 2.7 kWh/kg H₂ with the ionic compressor developed by the same company.

² https://www.linde-engineering.com/en/plant_components/hydrogen-fueling-technologies/index.html

The work of compression is directly linked to the compression ratio as presented in **Equation 6-1**. The ideal isothermal compression can not be achieved with mechanical compressors but the electrochemical compression is a promising method to improve the compression efficiency in HRS. Indeed, as presented in **Equation 6-2**, with only 0.054 V the pressure can be increased from 10 to 700 bar at ambient temperature. However, electrochemical compressors are also subject to activation overpotentials and ohmic losses.

Equation 6-1 – Isothermal and adiabatic work of compression.

$$W_{\text{isoth}} = -RT \cdot \ln\left(\frac{P_2}{P_1}\right)$$

$$W_{\text{adiab}} = \frac{\gamma}{\gamma - 1} \cdot \frac{P_1 V_1}{\gamma} \cdot \left[\left(\frac{P_2}{P_1}\right)^{\frac{\gamma-1}{\gamma}} - 1 \right]$$

Equation 6-2 – Electrochemical compression and Nernst equation

$$E_{\text{Nernst}} = \frac{RT}{2F} \ln\left(\frac{p_c}{p_a}\right)$$

6.1.2 Liquid hydrogen

The development of liquid hydrogen is closely related to the need to transport and store large quantities of hydrogen. Most plants are located in North America (11), and only 3 in Europe (Linde-Germany, Air Liquide-France, Praxair-Netherlands) with a total capacity of 19 tons per day³. Thus, the experimentation at small scale is currently limited by the availability of liquid hydrogen at lab scales. Recently, a Korean manufacturer (<http://www.hylium-industries.com/>) has developed a small scale liquefier for 1.5 kg LH₂/day. They report an energy consumption for liquefaction of 50 kWh/kg LH₂. A target efficiency for hydrogen liquefaction near 6 kWh/kg H₂ is assumed to be achievable at large scale by 2022 [6]. The systems in operation are in the 12-15 kWh/kg range [7], but, with current technologies, state of the art liquefiers, can achieve about 10 kWh/kg LH₂ for a daily capacity of 5000 kg LH₂ (*i.e.* the output of ca. 12.5 MW of electrolysis).

With cryogenic on-board storage, the release of hydrogen at ambient temperature to feed the fuel cell requires a complex engineering for the thermal management. However, considering the latent

³<https://www.hysafe.info/wp-content/uploads/sites/3/2018/09/PRESLHY-D2.3-LH2-Installation-description.pdf>

heat of vaporization of hydrogen (450 kJ/kg) and the heat capacity (*ca.* 12 kJ/kg·K), the 7 kWh/kg do not require external energy input if the losses of the fuel cell can be used.

6.1.3 Liquid Organic Hydrogen Carriers

Liquid Organic Hydrogen Carriers (LOHC) are liquid under ambient conditions with hydrogen covalently bound to an organic molecule. They are particularly interesting because the oil based infrastructure and logistics can be used to handle such carriers. Out of the large variety of LOHC [8], the most probable candidates are summarized in **Table 6.3**.

Table 6.3 – Some LOHC options (based on [8]).

LOHC	Storage Density*	Hydrogenation	Dehydrogenation	TRL and limitations
N-ethylcarbazole	5.2 wt %	50-70 bar 130-180°C	53 kJ/mol H ₂ 180 to 270 °C	3 Not fully investigated
Dibenzyltoluene	6.0 wt %	20-50 bar 80-180°C	65.4 kJ/mol H ₂ 290-310 °C	9 Environmental and health hazards
Formic acid	4.1 wt%	1-100 bar 30-100°C	31.2 kJ/mol H ₂ 25-100 °C	3 Flammable, corrosive and toxic
Methanol	10 wt%	20-80 bar	16.5 kJ/mol H ₂ 400°C (fast) 100°C (slow)	9 (high temp.) 3 (low temp.) Flammable and toxic

*capacity reduction due to solvents or concentration limitation included

6.2 Gas booster modelling

6.2.1 Context

Gaseous hydrogen is a promising energy carrier for the transport sector. Forklifts, passenger vehicles and delivery vans are among the first applications being deployed [9]. In order to offer sufficient energy density and driving ranges, the on-board pressure vessels are typically refilled at 350 or 700 bar [10]. This is significantly higher than most on-site hydrogen production solutions (1 to 30 bar) [11] and industrial storage bundles (200 bar) and, thus, refilling points require compression solutions.

Reciprocating compressors represent the most mature technology for hydrogen compression. It involves a back and forth motion in a chamber delimited by a diaphragm or a piston, driven by a hydraulic or pneumatic media [12]. With a lower technology readiness level and smaller flows, electrochemical compressors and thermal sorption systems with hydrides can also be mentioned [13]. Such systems can also contribute to hydrogen purification.

In compressed air gas boosters, the driving force is provided with a flow of air in the drive section (green part of **Figure 6.1**). When the piston reaches one of the sides, the inlet air is automatically redirected to the other side *via* a spool valve and exhaust air is expanded (**Figure 6.1**, inset). In the process gas sections (**Figure 6.1**, red parts), check valves ensure the successive sequences of gas intake and compressed gas output. The iterative motion continues until reaching the equilibrium of the forces exerted by the process and driving gas. It can be noted that the compression chamber is usually built inside of a double jacket to benefit from the cooling capacity of the air drive exhaust.

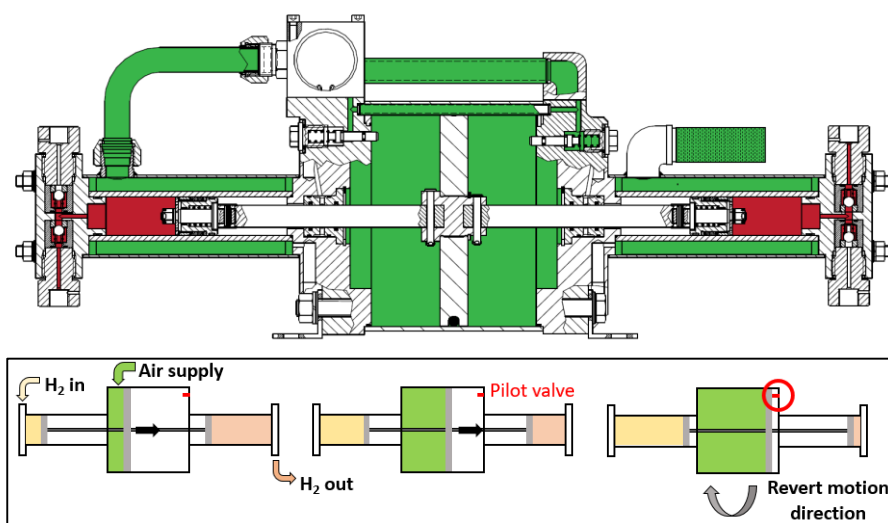


Figure 6.1 – Detailed scheme (top, drawing from Maximator GmbH) and working principle (inset) of a double acting, single stage gas booster.

The mechanical behavior of gas boosters was investigated from various perspectives. A purely mathematical approach was conducted by Li *et al.* [14]. The piston velocity is studied for several parameters such as surface area ratio of piston, piston mass and suction pressure. However, this kinematic study is insufficient to determine macro-scale metrics for hydrogen refueling station applications (HRS). Pneumatic flow constraints for the air drive were introduced by Wang [15]. In a second study [16], instead of differential equations, a discrete cycle approach was used and a dead volume was introduced in the equations. Unfortunately, the absence of temperature considerations and limited developments on the dead volume narrow the applicability of this model. Finally, Shi *et al.* [17] have worked on a new kind of gas booster, leveraging the expansion power of the drive air. This work introduces interesting considerations regarding transmission and expansion power of air.

Broadening the scope of the literature survey to gas production and storage, the experimental characterization of real systems becomes more prominent than pure mathematical and physical modelling. The complete behavior of a grid connected hydrogen energy buffer was studied by Sánchez and González [18]. A Haskel AGT-7/30 with a maximum outlet pressure of 200 bar was used. Because of the variability introduced by a purification process upstream, no accurate correlation between the cycle time and the hydrogen flow was found. Unfortunately, the parameter used for volumetric efficiency was not documented and temperature data was not available. Saadat-Targhi has conducted a detailed thermodynamic analysis of a compressed natural gas refueling station [19], but the developments in the compression section are limited by a constant outlet mass flow rate. In Switzerland, the HEIG-VD has also worked with air driven hydrogen boosters, supplied with an 18 kW air compressor [20]. However, no accurate measurements were produced due to leakages. Guo [21] implemented a flow fitting formula for the booster used for hydrogen gas cycling, without further investigations on the correlations. And finally, in complete energy system analysis of HRS, compressors are often overlooked and mentioned only with constant efficiency and flow parameters [5].

In addition to the academic literature, gas booster suppliers publish some geometrical information along with performance curves (Maximator [22], Haskel [23], Schydraulic [24], Resato [25]) relating flow and outlet pressure. This data, available for a set of air drive pressures and inlet pressures, is insufficient to fully characterize the dynamic system behavior, and derive correlations between the process variables. In 2008-2009, Total Deutschland has operated an HRS with an air-driven hydrogen booster [26]. The hydrogen compression system was supplied with a 22 kW air compressor and arranged in three stages at 200 bar, 450 bar and 850 bar. After 2 years of operation, they concluded that, despite a satisfactory reliability of the compressor, the air supply and outlet flow were too low for the intended use. More recently, the entry level versions (<20 kg H₂/day) of the H2Flow and H2Spring HRS from the French company Atawey are working with air driven hydrogen

boosters [27]. With more than 12 stations of this type deployed with captive fleets, the performance forecasting is a key aspect for users and operators.

Hence, despite the common and successful use of reciprocating compressors in small scale HRS, the prediction of operating variables such as mass flow rate, required cycles, outlet temperature and energy consumption has shown a few caveats.

Herein, the characterization of a commercial hydrogen gas booster is described in order to create a model capable to predict experimental correlations relevant for the implementation in a HRS.

6.2.2 Method

A compression system with an air-driven hydrogen booster could be divided into four components: source reservoir, sink reservoir, air supply and hydrogen compressor. For this study, a double acting, single stage Maximator DLE 30-2 gas booster was used. With a maximum outlet pressure of 600 bar, it can be typically used to refill small HRS pressure cascades from industrial storage bundles at 200 bar (one storage bundle consists of 12 x 50 L cylinders, and the piping was rearranged to have the equivalent of twice 300 L per bundle). This hydrogen booster is part of a larger demonstration setup, including a 50 kW alkaline electrolyser, a 10 – 200 bar compression and purification system [28], and a dual pressure refilling station (see **Figure 6.2** and **Figure 6.3**). The compression step between the bulk storage at 200 bar and the medium pressure cascade at 500 bar, was found to be the most representative of small-scale HRS. Indeed, 200 bar bundles is an industrial standard for hydrogen delivery and storage and most of the small scale HRS are limited to 350 bar dispenser pressure (*i.e.* with buffer storage below 500 bar).

A set of operating variables (see **Table 6.4**) was collected for over 20'000 cycles. The datasets were compiled and analyzed in order to explore correlations between process variables. The rationale for the relationships is detailed below. The derived trendlines were used to build a predictive model for the outlet flow characteristics of the hydrogen booster.

Table 6.4 – Monitored variables and corresponding sensors.

Variable	Sensor	Range and error
Pressure in source and sink storage	American Sensor Technologies	0 – 200 bar \pm 0.5 % 0 – 500 bar \pm 0.5 %
Air flow for gas booster supply	Inline flow meter E+E Elektronik EE741	0.6 – 212 Nm ³ /h \pm 3%
Temperature at the outlet of the gas booster	Thermocouple Pt100 (surface mounted)	-50 – +200°C \pm 0.3°C
Cycle time	PLC calculation based on pulse sensor	500 – 5000 ms \pm 20 ms
Air drive supply pressure	Integrated in the air compressor	5.5 – 15 bar \pm 0.4 bar (due to hysteresis and buffer storage)

**Figure 6.2** - Cascade storage with two gas boosters (center).

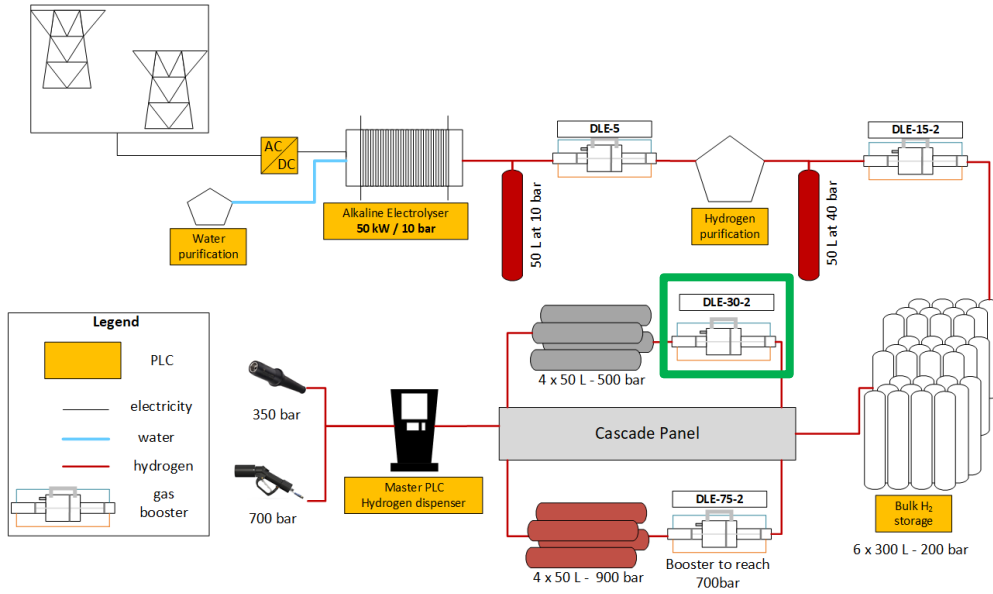


Figure 6.3 – Scheme of the HRS setup used in this study showing the hydrogen booster chosen for characterization (inside green box).

Variables and calculation proxies

One of the first variables of interest for a compressor is the flow rate. The nominal flow rate reported in the supplier's specifications (here 125 Nl/min) refers only to a specific inlet, outlet and air drive pressures triplet. The flow rate can be calculated *via* equation (1):

$$\dot{m} = \frac{\rho_{in} \cdot V_{stroke} \cdot \eta_{vol}}{t_{cycle}} \quad (1)$$

With \dot{m} the mass flow rate, ρ_{in} the inlet gas density, t_{cycle} the cycle time, V_{stroke} the geometrical stroke volume and η_{vol} the volumetric efficiency.

Because the outlet temperature of the gas, T_{out} , can affect the system components and materials, it must be closely monitored. A polytropic relationship with the exponent α is assumed (see equation (2)). Indeed, the compression process in a gas booster lies between a fully adiabatic and a fully isothermal process.

$$T_{out} = T_{in} \cdot \left(\frac{P_{out}}{P_{in}} \right)^{\alpha} \quad (2)$$

Finally, the drive air flow, G_{air} , determines the energy consumption of the system. This air is supplied from a buffered air compressor at a pressure P_{set} and performs work at a pressure P_{drive} (actual pressure inside the hydrogen booster). Due to the pneumatic design, some of the driving air is released without contributing to the compression work, and is denoted as $G_{overflow}$. The air drive overflow, was included as an additional term in equation (3).

$$G_{air} = G_{drive} + G_{overflow} \quad (3)$$

For this study, the compressed air is supplied by a variable speed Kaeser BSD 75 SFC screw compressor, with a nominal power of 37 kW. An average conversion value of 0.0977 kWh/kg of compressed air was measured, in line with current screw air compressors performances.

Equations (1-3) represent the full system to be solved in order to describe and predict the behavior of a gas booster.

Theory and calculation framework used for modelling

The system of equations (1-3) requires further analytical expressions for their parameters. The macroscopic interpretation of transferred volumes and flows is decomposed into more fundamental variables. These variables, introduced in the following subsections, provide not only correlations but also causation principles between the macroscopic, measured, parameters.

The modelling framework is presented in **Figure 6.4**. The experimental work consists of a reverse engineering approach in order to understand and determine the governing parameters. They are validated with the collected data, in order to be used in a model for performance forecasting, and process deviation tracking.

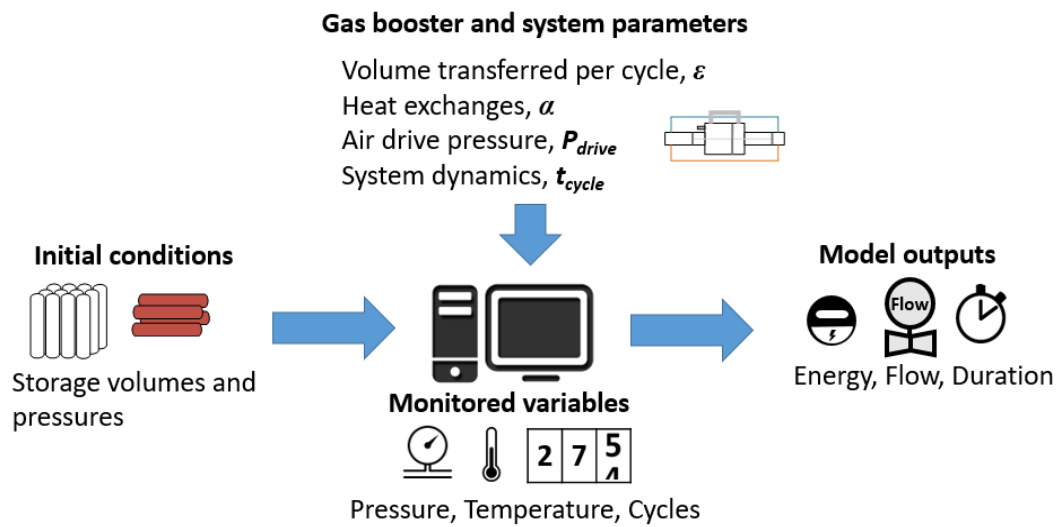


Figure 6.4 - Modelling framework.

The density of hydrogen $\rho(P, T)$ is computed from the thermophysical properties reported in the SAE J2601 [10], accurate within 0.5% to the NIST Standard Reference Database. Driving air was considered as an ideal gas, in the studied pressure range (1-10 bar).

The mass of hydrogen in the reservoirs was calculated from the density $\rho(P, T)$ and the volume of the reservoirs. No direct measurement of the hydrogen temperature inside the reservoir was available. The only measurable temperatures were the ambient temperature and the temperature at

the outlet of the hydrogen booster. Therefore, the external cylinder temperature was used in a thermal resistance model, following the approach of Monde [29].

6.2.3 Variables of interest and governing parameters

Volumetric efficiency and clearance volume

Equation (1) directly relates volumetric efficiency and mass flow. The reasoning is done for one compression cycle in order to decouple the equation from the cycle time. The geometrical construction of both hydrogen and air drive sections creates some dead volumes V_0 , inaccessible to the piston. They have a direct impact on the volumetric efficiency of the compressor and are schematically described in **Figure 6.5**. In addition, it appears that the reversing point of the piston varies with the operating conditions. The piston does not travel the full course of the chambers and creates an offset volume V_ε . The distance from the geometrical end position - the piston offset - is denoted ε . Together with the equipment supplier, the authors formulated the hypothesis that, because the pilot valve is triggered before the end position, the remaining distance travelled depends on the piston velocity at this point. It directly affects the volume of gas transferred per cycle. The sum of the dead volume and the offset volume is called the clearance volume V_{cl} (see equation (4)).

$$V_{cl} = V_0 + V_\varepsilon \quad (4)$$

The DLE 30-2 is a dual acting gas booster, meaning that the left and the right chambers are in phase opposition regarding the compression-expansion sequences. The model is developed here for one chamber.

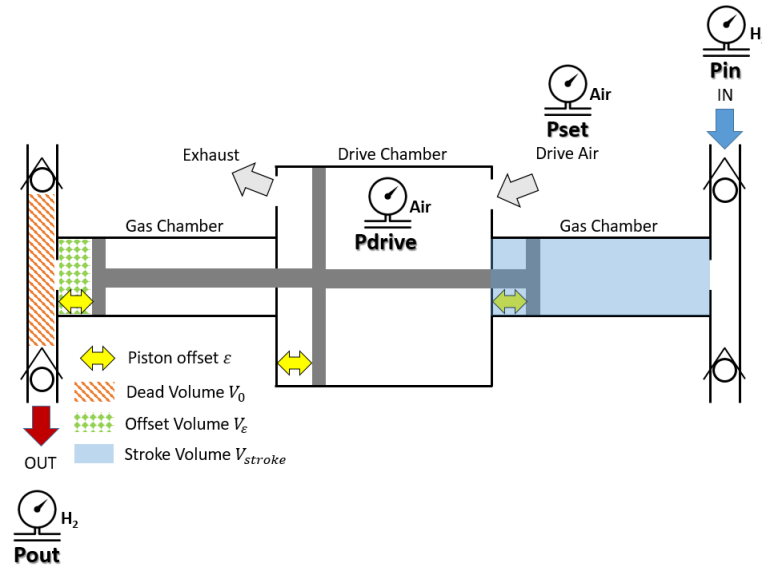


Figure 6.5 - Gas and drive chambers, dead volume and offset volume in a double acting gas booster, represented at the end of a compression cycle on the left side.

At the beginning of a compression cycle i , the clearance volume, from the previous cycle $i - 1$, will first expand until reaching the supply pressure $P_{in,i}$. Re-expansion of this unswept volume is a penalty for the gas intake. The intake proceeds until the whole chamber volume will be filled up except for the offset volume at the other end (second chamber) of the piston stroke. The total available volume for fresh gas intake can be described as the following:

$$V_{intake,i} = V_{stroke} + V_0 - (V_0 + V_\varepsilon) \cdot \frac{\rho_{out,i-1}}{\rho_{in,i}} - V_\varepsilon \quad \text{and, by definition:} \quad \eta_{vol,i} = \frac{V_{intake,i}}{V_{stroke}} \quad (5)$$

At this stage, the mass of hydrogen contained in the gas chamber is equal to

$$m_{booster,i} = \rho_{in,i} \cdot (V_{stroke} + V_0 - V_\varepsilon) \quad (6)$$

Finally, for one cycle, the mass transferred is described by equation (7):

$$m_{in,i} = m_{booster,i} - V_{cl} \cdot \rho_{out,i-1} \quad ; \quad m_{out,i} = m_{booster,i} - V_{cl} \cdot \rho_{out,i} \quad (7)$$

The parameters V_{stroke} and V_0 can be obtained from the supplier ($V_{stroke} = 60 \text{ cm}^3$ [22] and $V_0 = 3.39 \text{ cm}^3$ [30]). The mass conservation is applied iteratively on the complete system in order to derive the offset volume V_ε , and consequently, the piston offset ε .

Air drive model and effective drive pressure

The drive air flow, G_{air} , is measured at the inlet of the gas booster and thus can be plotted for all experiments. Following the clearance volume considerations, we have the following relationships:

$$V_{drive} = V_{stroke,air} - 2 \cdot V_{\varepsilon,air} \quad ; \quad m_{drive} = (G_{air} - G_{overflow}) \times t_{cycle} \quad (8)$$

In collaboration with the booster supplier, and based on experiments with long cycle times, $G_{overflow}$ was determined to be roughly equal to 25% of the total flow.

For the driving air, being modeled as an ideal gas, the following relationship applies:

$$P_{drive} \cdot V_{drive} = \frac{m_{drive}}{M_{air}} \cdot RT_{drive} \quad ; \quad T_{drive} = T_{amb} \cdot \left(\frac{P_{drive}}{P_{set}} \right)^\alpha \quad (9)$$

P_{drive} is defined as the actual working pressure of drive air in the chamber. Indeed, the movement of the air piston occurs before the air chamber reaches P_{set} . Thus, by definition, $P_{stall} < P_{drive} < P_{set}$ with P_{stall} , the stall pressure, corresponding to the equilibrium pressure for the drive air:

$$P_{stall} = \frac{P_{out} - P_{in}}{i} \quad (10)$$

with i the compression ratio provided by the supplier, defined as the ratio between the air drive section and the high-pressure section, corrected with a friction factor.

Cycle time

The motion of the piston during a cycle can be studied in order to define the cycle time. Shi [17] has developed the Newton law of motion for a gas booster piston, but no direct measurements are available for friction forces. In a first order approximation, it can be assumed that the main parameters involved are the difference $P_{\text{drive}} - P_{\text{stall}}$ and the offset, ε , which is directly related to the distance travelled by the piston. Considering an industrial installation with a compressed air network, the air drive pressure setpoint is not expected to change under dynamic operations. Some data was recorded after manually adjusting the discharge pressure of the screw compressor. Cycle time can be forced by the user by adding a flow restriction in the air supply.

6.2.4 Results and discussion

Experimental correlations

Based on the equations formulated in previous subsection, the collected data are graphically represented to highlight trendlines (see **Figure 6.6**). The specific findings are detailed below.

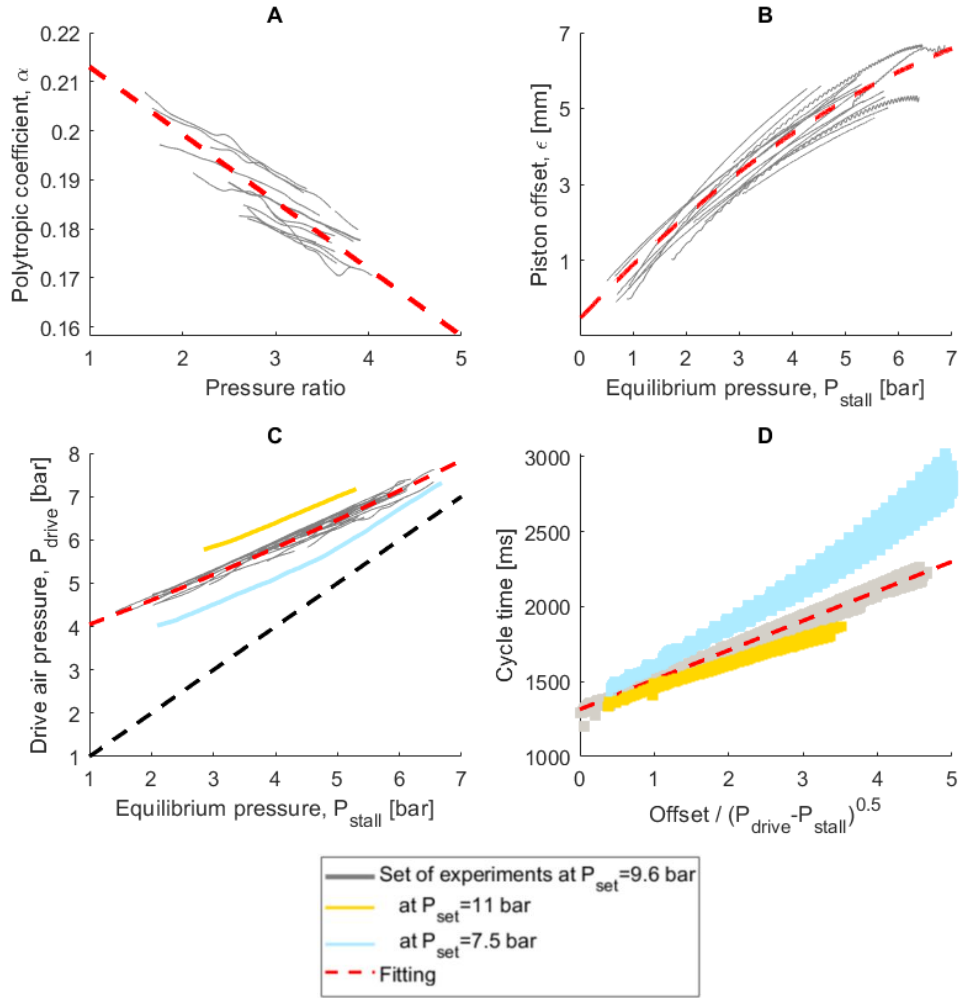


Figure 6.6 - Experimental validation for the proposed correlations regarding (A) polytropic coefficient, (B) piston offset, (C) drive air pressure, (D) cycle time.

Polytropic coefficient, α

A high variability was observed for temperature measurements, since no direct measurement of the gas temperature was available. Nevertheless, the assumed polytropic relationship is in good accordance with the collected data, and a linear relationship with the pressure ratio was found.

$$\alpha = 0.227 - 0.0137 \cdot P_{\text{out}}/P_{\text{in}} \quad ; \quad R^2 = 0.797$$

It was experimentally confirmed that compressions with high ratios, *i.e.* slow processes, exchanged more heat with the environment and thus, the polytropic coefficient decreases. The model is valid for

a cycle time below 2500 ms. Longer cycles are not in the scope of the study and differ significantly from the use case in HRS. For the considered pressure ratio range, α is comprised between 0.16 and 0.21. An upper bound of 0.29 is mentioned in the operating instructions for adiabatic conditions. Because the temperature is measured at the outlet of the hydrogen booster, the cooling capacity of the expanded air (see **Figure 6.1**) is already included in the measurement. Depending on atmospheric conditions, ice formation can be observed on the cooling cylinders, which are wrapping the hydrogen side.

Piston offset, ε

Based on the volume and mass balance detailed in subsection 6.2.3, the piston offset value was calculated from the pressure and temperature evolution. The evolution of the piston offset (in mm) was found to follow a quadratic expression of the pressure differential (in bar) between source and sink pressure.

$$\varepsilon = -0.068 P_{\text{stall}}^2 + 1.49 P_{\text{stall}} - 0.55 \quad ; \quad R^2 = 0.948$$

With small differences between inlet and outlet pressures, the piston can freely move to its end position and the offset is minimal. With larger pressure differentials, the piston faces larger resistances and cannot reach its end position after triggering the pilot valve. The results show that the piston movement could be reduced by up to 7 mm on a total course of 970 mm.

Drive air pressure, P_{drive}

The motivation to introduce the drive air pressure variable was to find a representative variable for the driving force of the compression. The drive air pressure was found to increase linearly with the stall pressure, with the highest correlation coefficient of all the expressions studied here.

$$P_{\text{drive}} = 0.637 P_{\text{stall}} + 0.0855 P_{\text{set}} + 2.49 \quad ; \quad R^2 = 0.972$$

Cycle time, t_{cycle}

Because the cycle time depends on both the distance travelled by the piston and the velocity of the piston, it is appropriate to introduce the ratio $\varepsilon / \sqrt{P_{\text{drive}} - P_{\text{stall}}}$.

$$t_{\text{cycle}} = 197 \varepsilon / \sqrt{P_{\text{drive}} - P_{\text{stall}}} + 1315 \quad ; \quad R^2 = 0.899$$

The cycle time (in ms) was found to increase linearly with this ratio. Further analysis is required to determine a more detailed expression of the slope, including the supply air pressure as a variable. Above 2500ms, the variability observed in the measurements is too high to propose an accurate model.

6.2.5 Integration of the results and engineering variables for HRS

Based on the correlations described in subsection 6.2.4, an engineering tool was programmed in MATLAB® in order to solve the system summarized in **Table 6.5**.

Table 6.5 - Input and output variables for the predictive hydrogen booster model.

Input variables	Output variables
Source reservoir : Pressure, Volume	Outlet temperature of the hydrogen booster
Sink reservoir : Pressure, Volume	Pressures : sink and source reservoirs
Ambient temperature	Number of cycles and total duration
Air drive supply pressure	Compressed air consumption

The HRS demonstrator is designed to perform two back-to-back refills at 350 bar on a Renault Kangoo modified fuel cell car with a 70L tank [31]. The pressure cascade consists of 4 x 50 L cylinders at 450 bar. The 700 bar fueling line, used for engineering purposes on vehicle tanks, is out of the scope of this paper.

Herein, half of the cascade, 2 x 50 L, initially at 200 bar and recompressed from a 600 L supply storage is considered. For consistency reasons, the volumes of the reservoirs are not changed, because they represent an intrinsic characteristic of the station. However, the operational conditions may affect the supply pressure, therefore, four different initial pressures are simulated for the supply storage: 200, 160, 120 and 80 bar (see **Figure 6.7**). The iterative addition or removal of hydrogen in the reservoirs (based on equation (7)) is used to compute the evolution of pressures in the source and sink reservoirs (**Figure 6.7**, subplot a).

With the model described above, the target pressure of 450 bar is forecasted to be reached after respectively 24 minutes (905 cycles), 34 minutes (1169 cycles) and 54 minutes (1720 cycles). With a supply at 80 bar, the simulation was interrupted when the outlet hydrogen temperature limit of 100°C was attained. Experimentally, with a supply storage at 165 bar, the target pressure of 450 bar was reached after 34 minutes and 1071 cycles, in good accordance with the model.

Increasing the inlet pressure reduces the pressure differential and thus results in a higher volumetric efficiency, a higher outlet flow, and a lower outlet temperature. Interestingly, the scenario with the highest outlet temperature does not result in higher temperatures in the sink reservoir (**Figure 6.7**, subplot c). Indeed, less hydrogen is transferred (low flow) and the thermal mass of the sink reservoir has more time to dissipate the heat to the environment.

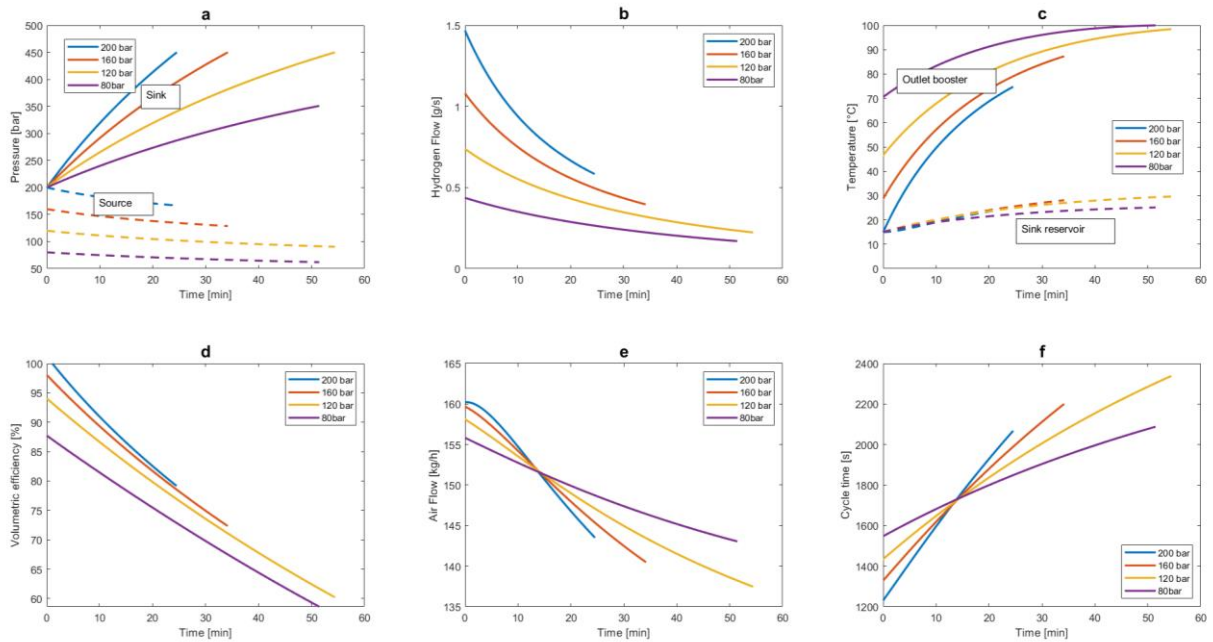


Figure 6.7 – Calculated dynamic variation of process variables when increasing the pressure from 200 bar to 450 bar in a 100 L reservoir, using a 600 L supply storage at different initial pressures.

Regarding volumetric efficiency, clearance volumes are reported in the range of 4 to 16% [32]. Here, including the piston offset, the clearance volume represents 5 to 12% of the stroke chamber, but can lead to more than 25% of volumetric losses due to its re-expansion (**Figure 6.7**, subplot d). High compression ratios are detrimental for efficiency, flow and temperature. For example, comparing the results for a source at 160 bar and a source at 80 bar, the hydrogen flow is not divided by a factor 2 but by 2.5 and the outlet temperature is more than 40°C higher (**Figure 6.7**, subplots b and c).

The simulation of the drive air flow (**Figure 6.7**, subplot e) allows the total consumption of compressed air to be computed and, consequently, the energy consumption. Starting with a source at 200, 160 and 120 bar, the target pressure of 450 bar is reached (ca. 1.4 kg transferred), and the corresponding air consumption estimates are as follows: 62.5 kg (6.1 kWh), 85.5 kg (8.3 kWh) and 133 kg (13 kWh). It translates to 4.4 to 9.3 kWh/kg of hydrogen compressed. For 35 MPa fills in full scale HRS, reported compression energies are much lower, with ca. 2.5 kWh/kg H₂ for a source at 13 bar [33]. Although compressed air is a commodity in many industrial set-ups, it is not an energy efficient media for gas compression. From 200 bar, a 20% decrease in the initial supply pressure

leads to a 37% increase in energy consumption and 42% in duration. Furthermore, from 160 bar a 25% decrease leads to 56% more energy consumption and is 59% longer.

Finally, the cycle time (**Figure 6.7**, subplot f) can be used to analyze the mechanical stress on the moving parts. With more than 60% increase over the course of the modelled experiment, the cycle time is one of the most tangible variables. However, this variable alone is insufficient to assess the speed of compression or a mechanical failure and must be considered globally in a combination with pressure, volumetric efficiency and temperature.

The accuracy of the model was assessed *via* a comparison with experimental data. For a given target pressure, the duration, the number of cycles and the energy consumption were predicted with a precision of +/- 5 %.

6.3 Hydrogen at scale

Building up a hydrogen infrastructure requires three interconnected systems: hydrogen production, hydrogen distribution, and hydrogen transport and logistics. Each part comes with associated costs and challenges for upscaling, which are discussed in the following sub-sections.

6.3.1 Levelized cost of hydrogen production

The economics of hydrogen production is a critical topic and estimates can vary by more than one order of magnitude [34]. For a better understanding of the cost structure of hydrogen, some parameters of the levelized cost of hydrogen (LCOH), based on **Equation 6-3** are discussed.

Equation 6-3 – Levelized cost of hydrogen.

$$LCOH = \frac{LHV}{\eta} \times \left[\left(\frac{i \times (1+i)^n}{(1+i)^n - 1} + \text{Maintenance} \right) \times \frac{CAPEX / kW}{\text{Annual Load hours}} + \text{Electricity price} \right]$$

$$\text{Efficiency : } \frac{LHV}{\eta}$$

The ratio of the Lower Heating Value (LHV) over efficiency (η) corresponds to the electrical energy required to produce one kilogram of hydrogen.

$$\text{Capital recovery factor : } \left(\frac{i \times (1+i)^n}{(1+i)^n - 1} \right)$$

n is the amortization period in years and i the interest rate. This formula gives the fraction of the initial investment which has to be reimbursed each year. For the examples discussed below, with $i=5\%$ and $n=10$ years, the capital recovery factor is equal to 0.13. Which means that for a 1 M€ loan, 10 annual payments of 0.13 M€ are required.

CAPEX

The CAPEX corresponds to the capital expenditures or initial investment. Hydrogen mobility projects cover a wide range of systems from the 0.1 MW scale to multi-MW. Based on various quotations for alkaline systems, we notice a very strong scale effect on the cost per kW. As a rule of thumb an increase of factor 10 for the capacity leads to a decrease by a factor 2 of the cost per kW. In **Table 6.6** we report the latest publicly available system costs, significantly higher than the 750€/kW at the 2 to 5 MW scale reported in the review [35] used in the IEA report [36]. The rule of six-tenths holds relatively well with electrolyzers: a 10 times larger unit is typically $10^{0.6} = 4$ times more expensive.

Table 6.6 – Electrolyser system costs.

System power	System cost (installed)	Cost per kW	Reference
100 kW	>0.4 M\$	4000 \$	Quotations from various suppliers
2 MW	>3 M\$	1500 \$	NEL purchase order from H2Energy 25.02.2019 ⁴
85 MW	>30 M\$	350 \$	NEL purchase order from Nikola 03.06.2020 ⁵

The learning rate for electrolyzers and fuel cells is estimated at about 18% [37]. By definition, it means that the costs decrease by 18% each time the cumulative installed capacity is doubled. Similar learning rates are reported for Li-ion batteries [38].

In late 2019, the annual manufacturing capacity of ITM Power, Thyssenkrup, NEL hydrogen and Areva H2gen is respectively 1 GW, 1 GW, 360 MW (alkaline) and 60 MW. The Nationale Organisation Wassertstoff in Germany (NOW) suggests that a stable level of sales of 20 to 50 MW per year and per

⁴ <https://news.cision.com/nel-asa>

⁵ <https://news.cision.com/nel-asa>

manufacturer is necessary for industrialisation and will allow the electrolysis sector to become a gigawatt industry by 2030 [39].

Annual load hours and electricity price

Annual load hours and average electricity price are interlinked *via* the annual price duration curve of the electricity market presented in **Figure 6.8**. Partial load operation at lower current density, allows some efficiency gains, and thus lower electricity expenses. The conversion into full load hours equivalents reflects this trend.

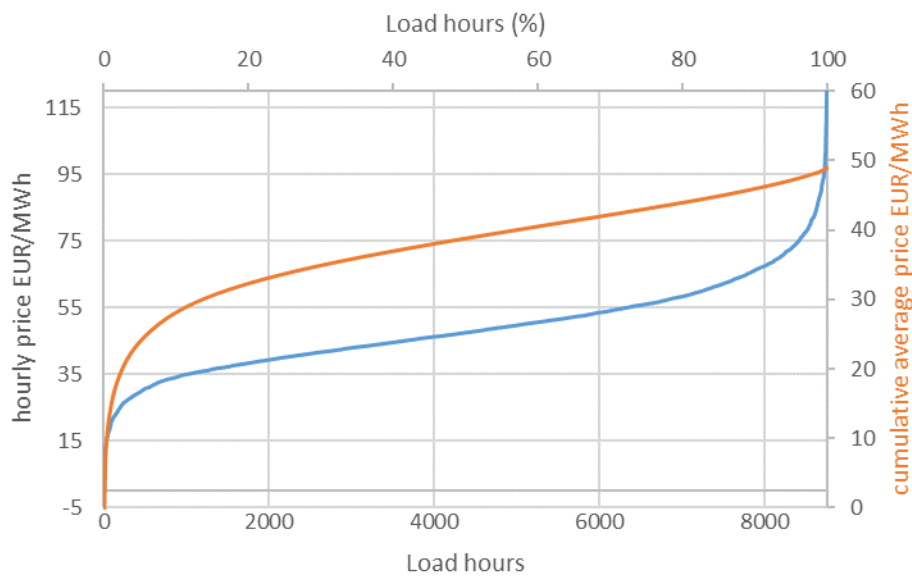


Figure 6.8 – Day ahead auction prices 2019 for electricity based on nordpool data (<https://www.nordpoolgroup.com/historical-market-data/>).

Results

Using the **Equation 6-3** and the electricity price profile from **Figure 6.8**⁶, we obtain the results presented in **Figure 6.9**. For small systems, the CAPEX is clearly the largest cost contributor in LCOH, with a strong incentive to maximize the full load hours and a minor role of the electricity price. For larger systems, the tradeoff between lower amortization costs or lower electricity price can be obtained with less hours of operation. In the presented example, for a 500 CHF/kW system, the

⁶ Assumptions: electricity consumption: 60 kWh/kg H₂, discount rate: 5%, amortization period: 10 years, annual maintenance cost: 5% of CAPEX, Electricity price range: 5.8 to 9.2 cts CHF/kWh (cumulative average).

lowest LCOH is obtained for 5000 hours of operation. At large scale, significant cost reductions can only be achieved with cheaper electricity or efficiency gains.

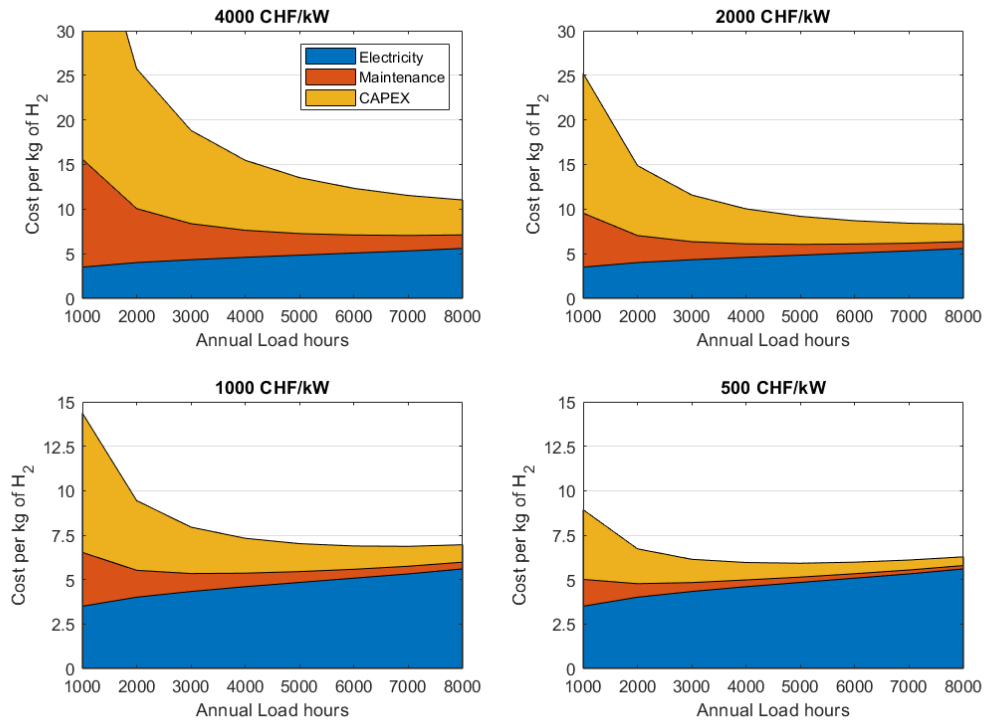


Figure 6.10 – Levelized cost of hydrogen from electrolysis.

The results from **Figure 6.9** can be rearranged next to each other in **Figure 6.10**, and we observe the strong advantage for large operators, and the importance to plan demand growth due to the cost penalty of small systems.

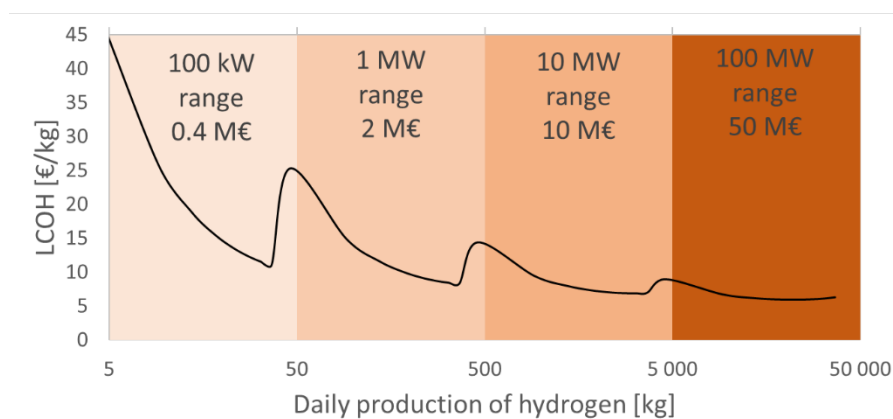


Figure 6.9 – LCOH as a function of daily production capacity.

The competition with Steam Methane Reforming (SMR) is a key question for the competitiveness of hydrogen mobility, and in particular how CO₂ certificates, Carbon Capture and Storage and guarantee

of origin for green hydrogen (<https://www.certifyh2.eu/>) will be handled. In the Hydrogen Roadmap Europe [40], electrolysis is expected to reach 50% of the hydrogen supply mix by 2035 with more than 3/4 in centralized locations.

6.3.2 Refueling stations

Current stations in Europe are designed for 200 to 400 kg H₂/day, which is enough for a local fleet of 50 to 100 passenger vehicles. Each passenger car is estimated to create a daily demand of 0.4 kg of hydrogen at the station, while the daily consumption of heavy duty vehicles is closer to 30 to 40 kg of hydrogen. To date, the UC Irvine station in California, with an average of 246 kg/day over one week, holds the record of hydrogen demand⁷. The low quantities of hydrogen delivered strongly affect the cost of the delivered hydrogen. For a station with 500 kW on site electrolysis, for about 6 bus, the current cost estimates in Europe are:

- 650 k€ per bus and 200 k€ for a 10 years service and maintenance contract
- 1.6 M€ for a 500 kW electrolyser (200 kg/day)
- 1.6 M€ for the station allowing 6 consecutive refills (0.25 M€ for the 450 bar cascade storage, total 10m³, and 190 m³ back up storage at 30 bar)⁸

Smaller scale stations in the 20 to 40 kg/day range are available for *ca.* 300 000 € with only 350 bar capability. At high utilization ratios, they remain competitive for demonstration projects. Assuming 180 kg/day from Monday to Saturday (6760 full load hours equivalent) over 10 years we obtain the following cost distribution:

- CAPEX and maintenance for electrolyser: 5.10 €/kg
- CAPEX and maintenance for the station: 5.10 €/kg (in line with numbers from Mayyas and Mann [41])
- 1.2 to 8.5 €/kg for electricity (depending of the electricity price in the 2 to 14 cts/kWh range)

Finally, it results in a cost of hydrogen at the pump of 11.4 -18.7 €/kg. An average price of 16.3 \$/kg is reported in the U.S.⁹, with delivery, compression and dispensing representing half of the costs. A cost at the pump below 10\$/kg is projected once 10 million vehicles are on the road [42].

⁷ Air Liquide stations in Paris, which are used by the hydrogen taxi fleet Hype, do not disclose publicly their numbers

⁸ Same order of magnitude in Korea : Nel purchase order from HyNet Korea, 28.08.2019: 1.5 M€ for a 200-400 kg/day HRS

⁹ <http://www.energy.ca.gov/2017publications/CEC-600-2017-011/CEC-600-2017-011.pdf>

While the annual load hours is a critical cost parameter for the cost of hydrogen production, the cost of hydrogen distribution is also strongly linked to the utilization ratio as presented by Reddi *et al.* [43] (Figure 6.11).

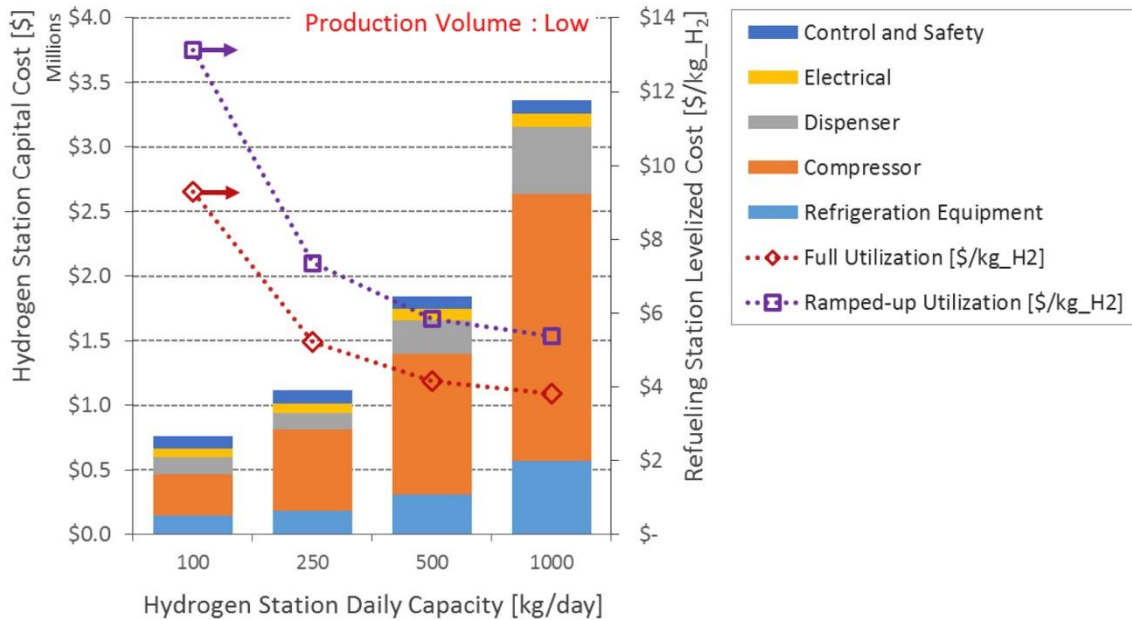


Figure 6.11 - The impact of station utilization and economies of scale of hydrogen (from Reddi *et al.* 2017 [43]).

In order to follow ramped-up utilization scenario, most suppliers offer modular designs with several components upgrades:

- Low pressure storage for back up capacity
- High pressure storage for more successive refills
- Electrolyser and compressors for daily capacity

For reference, the modular unit proposed by Linde for HRS based on gaseous storage is limited to 450 kg/day (IC90/30-S), and the modular unit based on liquid hydrogen has a daily capacity of 2400 kg/day (CP90/100-XL). Because the usage profile of the station and the topology of users directly affect the design of the pressure cascade, various systems are deployed depending on user demand. The main difference is the delivery pressure and tank volumes for passenger vehicles (700 bar, up to 250 L) and heavy-duty vehicles (350 bar and up to 2500 L). For the latter, the refueling protocol is still under development [44], and preliminary simulations are performed for a capacity of 1400 L (33.6 kg at 350 bar).

Station designs with delivery capacities in the ton per day range are closer to mini factories and cannot fit in an urban environment. For example, a station for a bus depot (2000 kg/day for 60 buses) requires at least the daily capacity as supply storage, which corresponds to 460 m³ at 50 bar. NEL and Nikola have announced a plan to deploy 8000 kg/day stations in the U.S. with a concomitant deployment of stations and vehicles. In such a case, 20 MW of on-site electrolysis would be required. It corresponds to the size L in the 2050 scenario in Germany and is 8 times higher than the L size considered in the same country in 2010 [45,46].

A full cost perspective should also include the cost of land, insurances and staff, however, attributing all the cost of the infrastructure to the price of hydrogen can be discussed, considering that the business case of refilling stations also relies on services such as convenience store and car wash.

6.3.3 Hydrogen dispensing and transport logistics

Until now, it appears difficult to achieve high demand on a single location, the strong economies of scale for electrolysis incentivize the deployment of centralized production. Thus, the network of refueling stations has to be supplied regularly with hydrogen similarly as the current network of liquid hydrocarbons. In Switzerland, 2600 conventional stations are in operation, in France it is about 11 000 stations and 14 400 in Germany. However, the analogy with gasoline and diesel rapidly highlights the shortcomings of hydrogen logistics. Indeed, liquid tanker trucks can deliver 30'000 liters of fuel in a single trip, corresponding to *ca.* 600 passenger car refills. 600 FCEV refills would correspond to roughly 3 tons of hydrogen.

The first delivery system currently deployed is the transport of compressed hydrogen in tube trailers. A typical example is the 20ft system supplied by Umoe and used by Hydrospider in Switzerland, which contains 350 kg of hydrogen at 350 bar (see **Figure 6.12**). The cost components for the truck delivery include:

- CAPEX: Hydrogen storage system (*ca.* 255 000 €), towing truck
- OPEX: driver and trained personnel, fuel and taxes

Based on our estimates, a delivery in a 100km radius can add 2 to 2.5 CHF/kg of hydrogen in Switzerland (CAPEX *ca.* 25%, fuel 15% and personal 60%). For a 200kg per day station (as discussed in 6.3.2), truck delivery is economically favorable if the centralized location has access to electricity at least 3cts/kWh cheaper or if the price per kW of the electrolyser drops from 3200 €/kW to 2000 €/kW.



Figure 6.12 – Hydrogen transport with 350 bar cylinders in a 20ft container (from Martin Osterwalder on linkedin).

The second option is the delivery in liquid form. Liquid hydrogen trailers can transport up to 3.5 tons of hydrogen in one trip. LH_2 can also be transported by ship or by rails. For LOHC at this stage, it is unclear if the dehydrogenation will occur in large terminals or directly at the station. With liquid hydrogen, centralized production in the multi-ton per day range is required for efficiency [6]. However, the liquid delivery directly affects the station design and is not interchangeable with gaseous deliveries. Liquid hydrogen offers significant gains on the station side (footprint and delivery), but the overall pathway (including liquefaction and transport) represents 5.57-8.57 kWh/kg H_2 delivered compared to 4.21 kWh/kg for gaseous hydrogen [5,47]. Liquid hydrogen storage on-board some vehicles may change the perspective.

Finally, pipelines at low or high pressure may represent a suitable solution for large flow in dense urban areas or transport over long distances. With a power grid network analogy, we can imagine a transport network over long distances at low pressure and centralized compression stations with local distribution to HRS in high-pressure pipelines. Such a system will reduce the traffic to supply HRS, reduces compression and storage equipments in the HRS, and consequently the footprint and cost.

The low pressure part is already deeply investigated by gas grid operators to leverage their assets from the natural gas [48].

The high pressure pipeline concept was investigated at NREL [49] with an economic perspective. The “Hyline” system encompasses an intra-urban network of high pressure pipelines at 15'000 psi (ca. 1000 bar). The advantage over lower pressure pipelines and truck delivery is confirmed in dense areas. Delivery to a network of up to 24 HRS with a capacity of 1500 kg/day each is assessed. The reduced footprint of HRS and the increased reliability is not assessed in this study. Operating

pipelines at a pressure more than ten times higher than industrial standards requires extensive work on codes and standards. However, one should note that such pipelines, for a few tens of meters are already in place between dispensers and cascade storages. A 1.7 km pipeline has been successfully in operation in Germany for 3 years in the 2007-2010 period [50] and has proven the technical feasibility. In Geneva, we identified 5 Tamoil sites within a 4 km radius, much lower than the 60 km of pipelines considered in the HyLine study. Further work on pipeline architecture with stations in series (HyLine study, inner diameter 1.6 inches with 208 kg/h dispensing rate) or in parallel in a star network are required. For pipelines, with an analogy to the electrical grid, the power *i.e.* the peak flow is the expensive sizing factor, so storage on site can reduce the stochastic peak demand on the network (see Chapter 2).

6.4 Conclusion

Hydrogen mobility faces today two opposing trends. On the one hand, demonstrations with working systems in the 100 – 200 kg/day range are required to convince investors and authorities. On the other hand, economically and energetically efficient systems are foreseen with systems that are at least one order of magnitude larger. The current risk for policy makers is the risk of technological lock-in, for example with compressed gas transport and the 700 bar standard. Indeed, for some clusters with a high concentration of FCEV, 500 bar can be a better option in terms of costs [51]. In general, encouraging technological diversity is beneficial to achieve long-term economic efficiency and the resilience of the energy system [52]. The stations designed today are probably not the ones for a fully scaled up hydrogen mobility, in the same way that pharmacies are not selling gasoline anymore as they were doing in the beginning of the automobile industry in the early 1900s. However, small scale solutions are a great way to democratize hydrogen technologies and develop skills and knowledge.

Experimental data from over 20 000 compression cycles were used to build a simulation tool for an air driven hydrogen booster and, by extension, for a small scale hydrogen refueling station. With this tool, based on mechanical and geometrical considerations, the dynamic evolution of pressures, flows, temperatures and volumetric efficiency can be determined for any initial configuration. Such models can be used for various purposes such as failure detection when measurements deviate from simulation, displaying estimated remaining time for compression or adjusting reservoir switching conditions depending on time or economic constraints. Despite being developed for a small scale compressor, the specific metrics and variables introduced here offer an interesting methodology to analyse other systems.

The second take-home message from this chapter is that hydrogen can hardly be economically competitive if considered only within the road mobility sector. Larger demand in mobility will be driven by rail and/or marine applications and industrial hydrogen will remain the largest consumer

for decades. System integration [53], grid services [54] and sector coupling at large scale are key to enable the access to low priced electricity [55]. System integration also ensures the resilience of business cases. Interestingly, some of the leading regions for low carbon and low price electricity production are also the one exporting oil today. The next scale for the green hydrogen sector will be enabled by the implementation of transnational import/export logistics.

References

- [1] Y. Ligen, H. Vrubel, J. Arlettaz, H. Girault, Experimental correlations and integration of gas boosters in a hydrogen refueling station, *International Journal of Hydrogen Energy*. (2020) S0360319920315652. <https://doi.org/10.1016/j.ijhydene.2020.04.162>.
- [2] K.K. Gangu, S. Maddila, S.B. Mukkamala, S.B. Jonnalagadda, Characteristics of MOF, MWCNT and graphene containing materials for hydrogen storage: A review, *Journal of Energy Chemistry*. 30 (2019) 132–144. <https://doi.org/10.1016/j.jechem.2018.04.012>.
- [3] L. Ouyang, K. Chen, J. Jiang, X.-S. Yang, M. Zhu, Hydrogen storage in light-metal based systems: A review, *Journal of Alloys and Compounds*. 829 (2020) 154597. <https://doi.org/10.1016/j.jallcom.2020.154597>.
- [4] G. Sdanghi, G. Maranzana, A. Celzard, V. Fierro, Review of the current technologies and performances of hydrogen compression for stationary and automotive applications, *Renewable and Sustainable Energy Reviews*. 102 (2019) 150–170. <https://doi.org/10.1016/j.rser.2018.11.028>.
- [5] A. Bauer, T. Mayer, M. Semmel, M.A. Guerrero Morales, J. Wind, Energetic evaluation of hydrogen refueling stations with liquid or gaseous stored hydrogen, *International Journal of Hydrogen Energy*. 44 (2019) 6795–6812. <https://doi.org/10.1016/j.ijhydene.2019.01.087>.
- [6] U. Cardella, L. Decker, H. Klein, Roadmap to economically viable hydrogen liquefaction, *International Journal of Hydrogen Energy*. 42 (2017) 13329–13338. <https://doi.org/10.1016/j.ijhydene.2017.01.068>.
- [7] M. Aasadnia, M. Mehrpooya, Large-scale liquid hydrogen production methods and approaches: A review, *Applied Energy*. 212 (2018) 57–83. <https://doi.org/10.1016/j.apenergy.2017.12.033>.
- [8] M. Niermann, A. Beckendorff, M. Kaltschmitt, K. Bonhoff, Liquid Organic Hydrogen Carrier (LOHC) – Assessment based on chemical and economic properties, *International Journal of Hydrogen Energy*. 44 (2019) 6631–6654. <https://doi.org/10.1016/j.ijhydene.2019.01.199>.
- [9] A. Alaswad, A. Baroutaji, H. Achour, J. Carton, A. Al Makky, A.G. Olabi, Developments in fuel cell technologies in the transport sector, *International Journal of Hydrogen Energy*. 41 (2016) 16499–16508. <https://doi.org/10.1016/j.ijhydene.2016.03.164>.
- [10] SAE International, J2601: Fueling Protocols for Light Duty Gaseous Hydrogen Surface Vehicles, 2016. http://standards.sae.org/j2601_201407/ (accessed February 14, 2017).
- [11] K. Ayers, N. Danilovic, R. Ouimet, M. Carmo, B. Pivovar, M. Bornstein, Perspectives on Low-Temperature Electrolysis and Potential for Renewable Hydrogen at Scale, *Annu. Rev. Chem. Biomol. Eng.* 10 (2019) 219–239. <https://doi.org/10.1146/annurev-chembioeng-060718-030241>.
- [12] S. Metz, Linde pioneers hydrogen compression techniques for fuel cell electric vehicles, *Fuel Cells Bulletin*. 2014 (2014) 12–15. [https://doi.org/10.1016/S1464-2859\(14\)70266-4](https://doi.org/10.1016/S1464-2859(14)70266-4).

- [13] P. Bouwman, Electrochemical Hydrogen Compression (EHC) solutions for hydrogen infrastructure, *Fuel Cells Bulletin*. 2014 (2014) 12–16. [https://doi.org/10.1016/S1464-2859\(14\)70149-X](https://doi.org/10.1016/S1464-2859(14)70149-X).
- [14] Z. Li, Y. Zhao, L. Li, P. Shu, Mathematical modeling of compression processes in air-driven boosters, *Applied Thermal Engineering*. 27 (2007) 1516–1521. <https://doi.org/10.1016/j.applthermaleng.2006.09.012>.
- [15] H. Wang, W. Xiong, Z. Li, Dynamic Simulation And Experimental Research On Charge Of Gas Booster, *Proceedings of the JFPS International Symposium on Fluid Power*. 2008 (2008) 419–422. <https://doi.org/10.5739/isfp.2008.419>.
- [16] H. Wang, W. Xiong, X. Wang, Research on the static characteristics of air driven gas booster, *Proceedings of the JFPS International Symposium on Fluid Power*. 2008 (2008) 715–718. <https://doi.org/10.5739/isfp.2008.715>.
- [17] Y. Shi, M. Cai, Working characteristics of two kinds of air-driven boosters, *Energy Conversion and Management*. 52 (2011) 3399–3407. <https://doi.org/10.1016/j.enconman.2011.07.008>.
- [18] C. Sánchez, D. González, Experimental characterization of a grid-connected hydrogen energy buffer: Hydrogen production, *International Journal of Hydrogen Energy*. 38 (2013) 9741–9754. <https://doi.org/10.1016/j.ijhydene.2013.05.096>.
- [19] M. Saadat-Targhi, J. Khadem, M. Farzaneh-Gord, Thermodynamic analysis of a CNG refueling station considering the reciprocating compressor, *Journal of Natural Gas Science and Engineering*. 29 (2016) 453–461. <https://doi.org/10.1016/j.jngse.2016.01.027>.
- [20] J.-F. Affolter, S.D. Marques Dos Santos, P. Morey, H2Ports - Hydrogène dans les ports, (2010). <https://www.aramis.admin.ch/Default.aspx?DocumentID=62629&Load=true> (accessed March 31, 2020).
- [21] J. Guo, L. Xing, Z. Hua, C. Gu, J. Zheng, Optimization of compressed hydrogen gas cycling test system based on multi-stage storage and self-pressurized method, *International Journal of Hydrogen Energy*. 41 (2016) 16306–16315. <https://doi.org/10.1016/j.ijhydene.2016.05.076>.
- [22] Maximator GmbH - Gas Boosters Catalog, (2007). <http://www.maximator.de/assets/mime/993e777b8b67789fe5508d0497a8a25a/MAXIMATOR%20Gas%20Boosters%2004-2007.pdf> (accessed January 23, 2020).
- [23] Haskel - Pneumatic & Hydraulic Driven Gas Booster, (2015). <https://www.haskel.com/wp-content/uploads/190706-Gas-Booster-Booklet-ENG-GB-1.pdf> (accessed January 23, 2020).
- [24] Schydraulic - Gas Booster Performance Chart, (2019). <https://schydraulic.com/GBDSeries-SingleStage-DoubleActing.php> (accessed January 23, 2020).
- [25] Resato - Air Driven High Pressure Pumps, (2006). http://resato.dk/pdf/Pumper_eng.pdf (accessed January 23, 2020).
- [26] Clean Energy Partnership (CEP), TOTAL Deutschland GmbH, Aufbau, Erprobung und temporärer Betrieb einer mobilen 700bar-Betankungseinrichtung am Standort Margarete-Sommer-Straße, (2009) 8. <https://doi.org/10.2314/GBV:76783139X>.

- [27] Atawey, Stations de recharge d'hydrogène vert, H2Spring, H2Flow. (2020). <http://atawey.com/fr/domaine-intervention/installations-industrielles.html> (accessed March 31, 2020).
- [28] Y. Ligen, H. Vrabel, H. Girault, Energy efficient hydrogen drying and purification for fuel cell vehicles, *International Journal of Hydrogen Energy*. 45 (2020). <https://doi.org/10.1016/j.ijhydene.2020.02.035>.
- [29] M. Monde, P. Woodfield, T. Takano, M. Kosaka, Estimation of temperature change in practical hydrogen pressure tanks being filled at high pressures of 35 and 70 MPa, *International Journal of Hydrogen Energy*. 37 (2012) 5723–5734. <https://doi.org/10.1016/j.ijhydene.2011.12.136>.
- [30] T. Christians, Information on gas booster DLE 30-2 - Maximator GmbH, Engineering Components, e-mail communication, 2019.
- [31] A. Closset, Hydrogen fuel cell range extender for Renault Kangoo ZE - Integration and testing, Swiss Federal Office of Energy SFOE, 2018. <https://www.aramis.admin.ch/Dokument.aspx?DocumentID=49938> (accessed January 30, 2020).
- [32] H. P. Bloch, J. J. Hoefner, Reciprocating compressors and their applications, in: *Reciprocating Compressors*, Elsevier, 1996: pp. 1–43. <https://doi.org/10.1016/B978-088415525-6/50002-X>.
- [33] T. Brown, S. Stephens-Romero, G. Scott Samuelsen, Quantitative analysis of a successful public hydrogen station, *International Journal of Hydrogen Energy*. 37 (2012) 12731–12740. <https://doi.org/10.1016/j.ijhydene.2012.06.008>.
- [34] R.S. El-Emam, H. Özcan, Comprehensive review on the techno-economics of sustainable large-scale clean hydrogen production, *Journal of Cleaner Production*. 220 (2019) 593–609. <https://doi.org/10.1016/j.jclepro.2019.01.309>.
- [35] J. Proost, State-of-the art CAPEX data for water electrolyzers, and their impact on renewable hydrogen price settings, *International Journal of Hydrogen Energy*. 44 (2019) 4406–4413. <https://doi.org/10.1016/j.ijhydene.2018.07.164>.
- [36] International Energy Agency, The Future of Hydrogen - Seizing today's opportunities, IEA, Paris, 2019. <https://www.iea.org/publications/reports/thefutureofhydrogen/> (accessed October 16, 2019).
- [37] S.M. Saba, M. Müller, M. Robinius, D. Stolten, The investment costs of electrolysis – A comparison of cost studies from the past 30 years, *International Journal of Hydrogen Energy*. 43 (2018) 1209–1223. <https://doi.org/10.1016/j.ijhydene.2017.11.115>.
- [38] B. Nykvist, F. Sprei, M. Nilsson, Assessing the progress toward lower priced long range battery electric vehicles, *Energy Policy*. 124 (2019) 144–155. <https://doi.org/10.1016/j.enpol.2018.09.035>.
- [39] T. Smolinka, F. Lehner, S. Kiemel, Studie IndWEde - Industrialisierung der Wasserelektrolyse in Deutschland: Chancen und Herausforderungen für nachhaltigen Wasserstoff für Verkehr, Strom und Wärme, Nationale Organisation Wasserstoff und Brennstoffzellentechnologie - MOW GmbH,

- Berlin, 2018. https://www.now-gmbh.de/content/service/3-publikationen/1-nip-wasserstoff-und-brennstoffzellentechnologie/indwede-studie_v04.1.pdf (accessed April 22, 2020).
- [40] Fuel Cells and Hydrogen 2 Joint Undertaking, Hydrogen roadmap Europe: a sustainable pathway for the European energy transition., 2019. http://publications.europa.eu/publication/manifestation_identifier/PUB_EG0618327ENN (accessed June 14, 2020).
- [41] A. Mayyas, M. Mann, Manufacturing competitiveness analysis for hydrogen refueling stations, *International Journal of Hydrogen Energy*. 44 (2019) 9121–9142. <https://doi.org/10.1016/j.ijhydene.2019.02.135>.
- [42] E.L. Miller, S.T. Thompson, K. Randolph, Z. Hulvey, N. Rustagi, S. Satyapal, US Department of Energy hydrogen and fuel cell technologies perspectives, *MRS Bull.* 45 (2020) 57–64. <https://doi.org/10.1557/mrs.2019.312>.
- [43] K. Reddi, A. Elgowainy, N. Rustagi, E. Gupta, Impact of hydrogen refueling configurations and market parameters on the refueling cost of hydrogen, *International Journal of Hydrogen Energy*. 42 (2017) 21855–21865. <https://doi.org/10.1016/j.ijhydene.2017.05.122>.
- [44] C. Due Sinding, E. Vyazmina, F. Ammouri, A. Charolais, Q. Nouvelot, N. Hart, S. Quong, Deliverable D3.1, Report on the characteristics of the cases to be studied in the preliminary simulations, (2020). https://prhyde.eu/wp-content/uploads/2020/05/PRHYDE_Deliverable-D3-1_final_revised.pdf (accessed June 5, 2020).
- [45] P.K. Rose, F. Neumann, Hydrogen refueling station networks for heavy-duty vehicles in future power systems, *Transportation Research Part D: Transport and Environment*. 83 (2020) 102358. <https://doi.org/10.1016/j.trd.2020.102358>.
- [46] M. Robinius, P. Kuckertz, D. Stolten, T. Grube, K. Syranidis, M. Reu\’s s, P. Stenzel, J. Lin\’s sen, Comparative Analysis of Infrastructures: Hydrogen Fueling and Electric Charging of Vehicles, *Elektrochemische Verfahrenstechnik*, 2018.
- [47] T. Mayer, M. Semmel, A. Bauer, M. Guerrero-Morales, K. Maria, J. Wind, Techno-economic evaluation of hydrogen refueling stations with trucked-in gaseous or liquid hydrogen, in: Stuttgart, 2017: p. 20.
- [48] W. Liemberger, D. Halmschlager, M. Miltner, M. Harasek, Efficient extraction of hydrogen transported as co-stream in the natural gas grid – The importance of process design, *Applied Energy*. 233–234 (2019) 747–763. <https://doi.org/10.1016/j.apenergy.2018.10.047>.
- [49] M. Penev, J. Zuboy, C. Hunter, Economic analysis of a high-pressure urban pipeline concept (HyLine) for delivering hydrogen to retail fueling stations, *Transportation Research Part D: Transport and Environment*. 77 (2019) 92–105. <https://doi.org/10.1016/j.trd.2019.10.005>.
- [50] H. Lienkamp, A. Rastogi, Achievements and Lessons Learnt in the EU Project Zero Regio, *Procedia - Social and Behavioral Sciences*. 48 (2012) 2201–2210. <https://doi.org/10.1016/j.sbspro.2012.06.1193>.

- [51] Z. Lin, S. Ou, A. Elgowainy, K. Reddi, M. Veenstra, L. Verduzco, A method for determining the optimal delivered hydrogen pressure for fuel cell electric vehicles, *Applied Energy*. 216 (2018) 183–194. <https://doi.org/10.1016/j.apenergy.2018.02.041>.
- [52] L. Haelg, M. Waelchli, T.S. Schmidt, Supporting energy technology deployment while avoiding unintended technological lock-in: a policy design perspective, *Environ. Res. Lett.* 13 (2018) 104011. <https://doi.org/10.1088/1748-9326/aae161>.
- [53] D. Parra, L. Valverde, F.J. Pino, M.K. Patel, A review on the role, cost and value of hydrogen energy systems for deep decarbonisation, *Renewable and Sustainable Energy Reviews*. 101 (2019) 279–294. <https://doi.org/10.1016/j.rser.2018.11.010>.
- [54] G. Matute, J.M. Yusta, L.C. Correias, Techno-economic modelling of water electrolyzers in the range of several MW to provide grid services while generating hydrogen for different applications: A case study in Spain applied to mobility with FCEVs, *International Journal of Hydrogen Energy*. 44 (2019) 17431–17442. <https://doi.org/10.1016/j.ijhydene.2019.05.092>.
- [55] G. Glenk, S. Reichelstein, Economics of converting renewable power to hydrogen, *Nat Energy*. 4 (2019) 216–222. <https://doi.org/10.1038/s41560-019-0326-1>.

Concluding remarks and perspectives

A few days before the submission of this thesis, the European Commission released its hydrogen strategy for a climate-neutral Europe, recognizing hydrogen as “essential to support the EU’s commitment to reach carbon neutrality by 2050”¹. The previous year, the same Institution expressed its strategic approach to batteries, recognizing batteries as “one of the key enablers” for the transition to carbon neutrality, especially for grid stabilization and the roll-out of clean mobility². Thus, electrochemistry, a science which truly emerged in the 19th century, appears to be one of the most relevant science to face the challenges of the 21st century, while internal combustion systems will remain the archetypes of the fossil fuel era. This paradigm shift leverages a new set of questions, in particular regarding the electrochemical systems for hydrogen fuel cell and battery electric vehicle infrastructure.

Indeed, upstream processes for energy carrier production, storage, conditioning and delivery are found to induce 22 to 34% of energy losses for battery electric vehicles and up to 43% for hydrogen fuel cell vehicles. It is a common misconception to consider efficiency as the only appropriate metric and as a self-sufficient indicator to judge the relevance of future transport technologies. This thesis has pointed out part of the large scope of other issues that future transport sector technologies must address. For example, BEV adoption with no home charging option or vehicle availability constraints is one of the first hurdle that many ICE drivers face today. For FCEV, ICE-like pit stops require complex upstream processes to use the lightest element on earth as a dense energy carrier, but enable a spatial and temporal decoupling of production and demand. And in both cases, off-grid and intermittent renewable energy powered infrastructure is often presented as a realistic and ideal solution. Though, based on real production profiles of wind turbines and solar panels, we have reaffirmed the value of existing networks (gas and electricity) and low carbon electricity sources (hydropower and nuclear) as important assets to enable a large electrification of the transport sector.

Using a stochastic modelling of charging stations, I have emphasized the role that energy storage can play to boost locally and temporarily the capacity of the power grid. Stationary buffer batteries in the sub MWh scale are economically efficient to reduce the stress on the grid and power transformation costs. In the same time, they enable to develop the self-consumption of intermittent renewable

¹ EU Commission 2020, A hydrogen strategy for a climate-neutral Europe, Brussels, 08.07.2020

² EU Commission 2019, on the Implementation of the Strategic Action Plan on Batteries: building a Strategic Battery Value Chain in Europe, Brussels, 09.04.2019

energy sources. To avoid distortions of the carbon market, new mechanisms must be developed for time dependent certificates of origin, for net energy metering and vehicle-to-grid concepts.

While electrochemistry is basically the control of chemical reactions with a power input/output knob, the realization of a full-scale demonstrator has highlighted the major role of auxiliaries and control systems for efficient, reliable and stable operation of electrochemical devices. Scientists can develop fully optimized solutions, but engineers are constrained by a limited set of off-the-shelf products, and diverging user goals. The full range modulation of electrolyzers is one of the examples where engineers can hardly find the right equipments such as power supply, cooling systems and compressors to satisfy an ideal scientific concept. The practical implementation of systems has underlined the cornerstone role of integrators to ensure the build up of compatible system interfaces, and trigger the development of tailor-made products when required. In an ever-changing world, beyond optimized solutions, resilient and robust solutions are needed.

Consequently, the electrochemical challenges of electric mobility infrastructure are now slightly overtaken by process engineering, logistics, social acceptance and economical challenges for competitive solutions at scale. Infrastructure development receives most of the attention and funding but, considering the life cycle of vehicles and equipments, the supporting infrastructure must not be overlooked, especially regarding the user experience. I experienced the lack of maintenance staff and workshops for hydrogen fuel cell vehicle service. The companies I talked to, experienced the lack of trained staff for both technicians and managers. The engineers I met, were disappointed by non-mandatory but strongly recommended guidelines, instead of clear and updated regulations. The projects managers I worked with, complained about the non-standardized approval processes. Also, the public expresses many others questions that they, rightfully or not, perceive as related to electric mobility: material recycling (even if most of the current EV rolling stock will still be on the roads for the next decade), material sourcing (with mislabeled conceptions of resources and reserves), autonomous driving, vertical take-off and landing drones... All in all, this is a clear sign that electric mobility represents a paradigm shift: habits, structures and systems have to change.

Hydrogen, a commodity used for decades in the industry, has to become a low carbon commodity with new standards and protocols. Indeed, electrolyzers with power modulation capacity and reduced footprint are now a must for hydrogen production technologies. Scientific progress in catalysis and materials, has improved the efficiency and lifetime at the cell level. However, auxiliaries still represent a significant burden on the overall system in terms of reliability, flexibility and efficiency. In our system, auxiliaries, power supply and purification already consume 10% of the energy of the system and were responsible of 100% of the failures. Unprecedented requirements are also imposed on downstream processes such as purification and compression. The gas purity is a particularly important parameter to ensure the durability of PEM fuel cells. The combined use of vacuum and heat offers great opportunities to improve the efficiency of pressure swing adsorption systems. Regarding compression, gas boosters powered with compressed air, a widely available

media in industrial setups, are unfortunately poorly efficient to represent a viable solution at scale. However, an in-depth analysis of working volumes in the different chambers has shown how macro-scale metrics can be modelled from geometrical characteristics.

When it comes to economics, the latest H2@Scale funding by the DoE, a good indicator of remaining industrial hurdles, is centered on manufacturing capacity in the Gigawatt scale (electrolysers and fuel cells) and advanced materials (for storage tanks and membranes). While the CAPEX is still a major cost contributor in demonstration projects with low utilization rates, the availability of low-price electricity will become the dominant factor to achieve competitive LCOH at scale. Logistics is at the core of the tradeoff between large centralized production with good economic parameters but complex transport to delivery point and small decentralized production with footprint and grid fees constraints. Compressed gaseous tube trailers are probably only a temporary solution before the development of bulkier alternatives such as liquid hydrogen, low- and high-pressure pipelines, and LOHC. Electric mobility is also affecting the business model of station operators: the footprint of services such as car wash and convenience store is being cannibalized by hydrogen storage or power transformers. In the same time, parking spots with chargers are becoming a source of revenue.

Gas distributors, electricity providers, fuel retailers are forced to join their forces to enable the electrification of the transport sector. They represent an opportunity to foster a holistic approach for sector coupling, beyond the optimisation that can be done in academic research labs. The journey to climate change mitigation with the physical constraints of our finite world is certainly rough and brutal: required cut in emissions are now 2.7% per year for the 2°C goal³.

Finally, a particular prominence to the Avoid-Shift-Improve framework is currently given by the Covid-19 crisis. We are experiencing the impact of avoid and shift strategies on our mobility needs: finding alternatives for discretionary travel (video-conferencing, holiday locally) and rediscovering the benefits of clean air and the efficiency of light modes (cycling, walking). However, the last pillar, “Improve”, appears to be essential for long-lasting benefits and hard-to-abate modes. A low carbon resilient infrastructure can be built around batteries and hydrogen, and support the take-off of electric mobility.

³ UNEP (2019). Emissions Gap Report 2019. Executive summary. United Nations Environment Programme, Nairobi. <http://www.unenvironment.org/emissionsgap> (accessed on 26 July 2020)

Numbers and orders of magnitude

Universal constants

Avogadro's constant $N_A = 6.022 \times 10^{23} \text{ mol}^{-1}$

Elementary charge $e = 1.602\,176\,634 \times 10^{-19} \text{ C}$

Faraday's constant $F = eN_A \approx 96\,485 \text{ C} \cdot \text{mol}^{-1}$

Boltzmann's constant $k = 1.980\,649 \times 10^{-23} \text{ J} \cdot \text{K}^{-1}$

Ideal gas constant $R = N_A k \approx 8.314\,462 \text{ J} \cdot \text{K}^{-1} \cdot \text{mol}^{-1}$

Thermodynamics

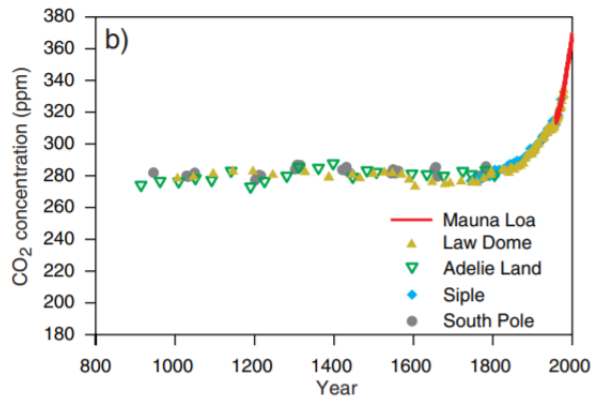
	Enthalpy (at 298.15 K) $\Delta_f H^\circ \text{ (kJ} \cdot \text{mol}^{-1})$	Entropy (at 298.15 K) $\Delta S^\circ \text{ (J} \cdot \text{mol}^{-1} \cdot \text{K}^{-1})$
$\text{H}_2\text{O}_{(l)}$	-285.83 (HHV)	69.95
$\text{H}_2\text{O}_{(g)}$	-241.82 (LHV)	188.83
H_2	0	130.68
O_2	0	205.15

Data from:

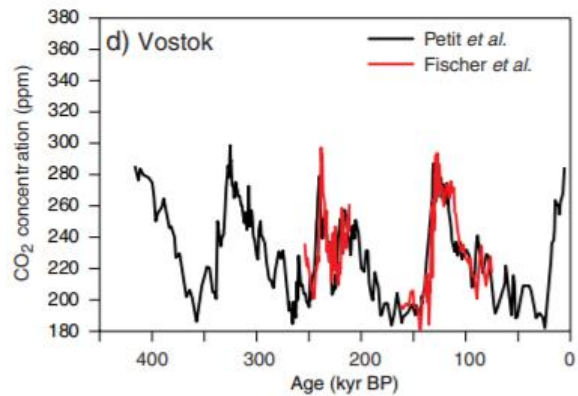
"CODATA Key Values for Thermodynamics", in *CRC Handbook of Chemistry and Physics*, David R. Lide, ed., CRC Press, Boca Raton, FL, 2005.

CO₂ emissions

In June 2020, the monthly average value in Mauna Loa reached 416 ppm CO₂.



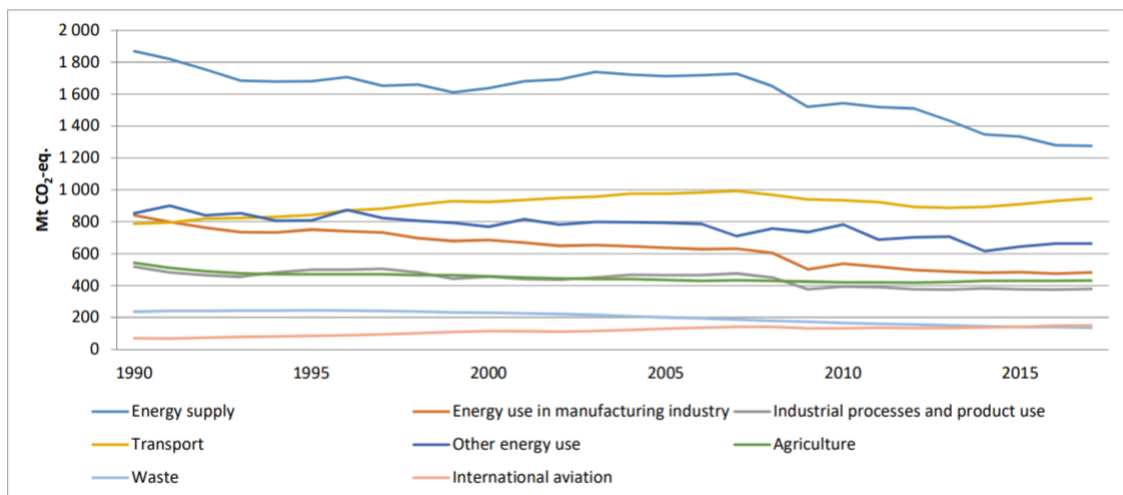
<https://www.esrl.noaa.gov/gmd/ccgg/trends/ets/uploads/2018/02/TAR-03.pdf>



and

<https://www.ipcc.ch/site/assets/uploads/2018/02/TAR-03.pdf>

EU CO₂ emissions by sector:



https://ec.europa.eu/clima/sites/clima/files/strategies/2050/docs/long-term_analysis_in_depth_analysis_figures_20190722_en.pdf

Energy dependency in Switzerland

Fig. 1 Endenergieverbrauch 1910–2019 nach Energieträgern
Consommation finale 1910–2019 selon les agents énergétiques

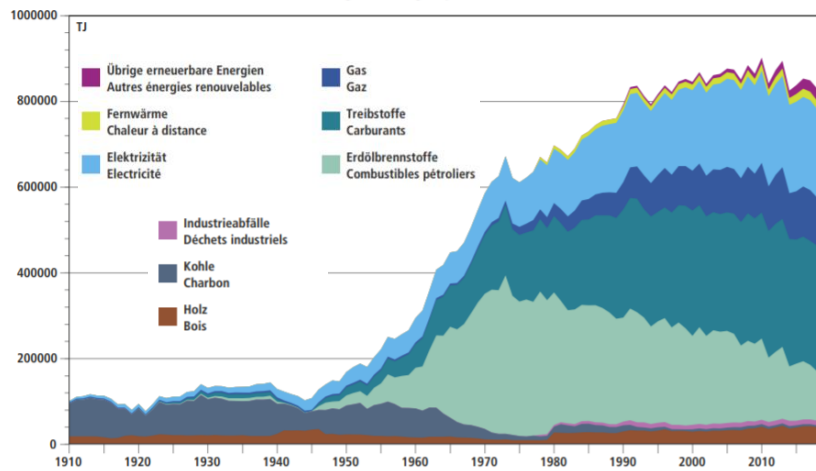
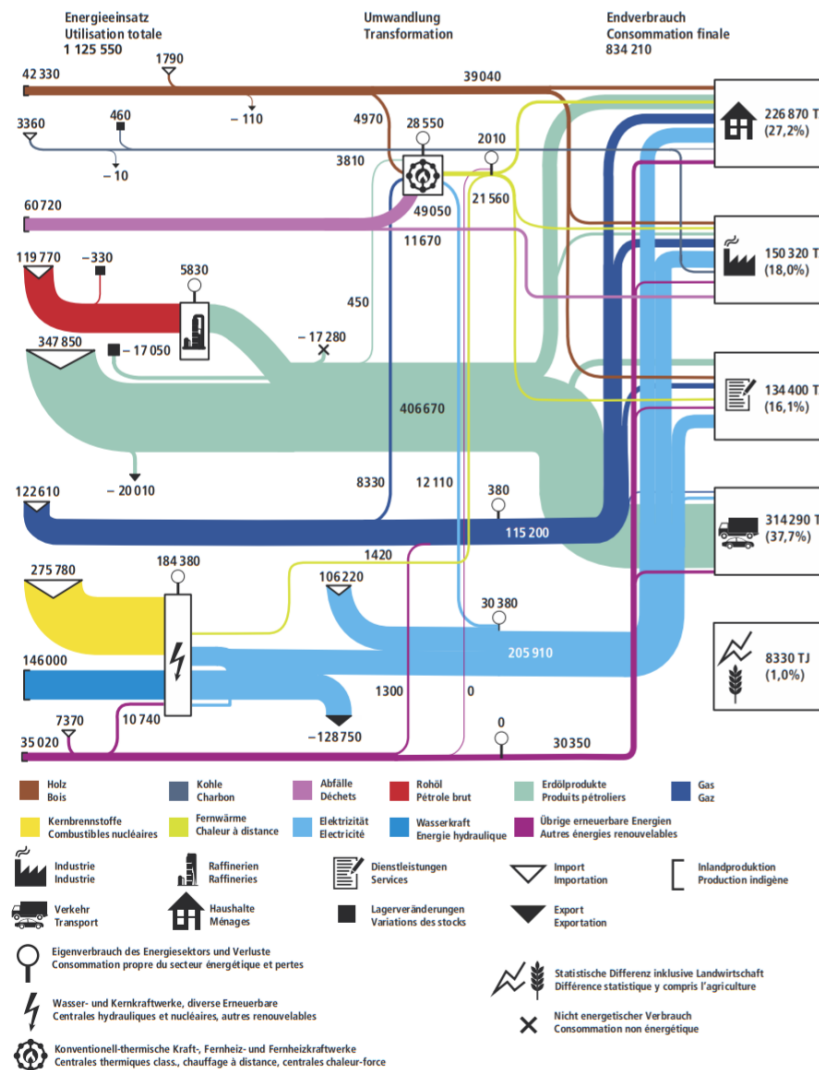


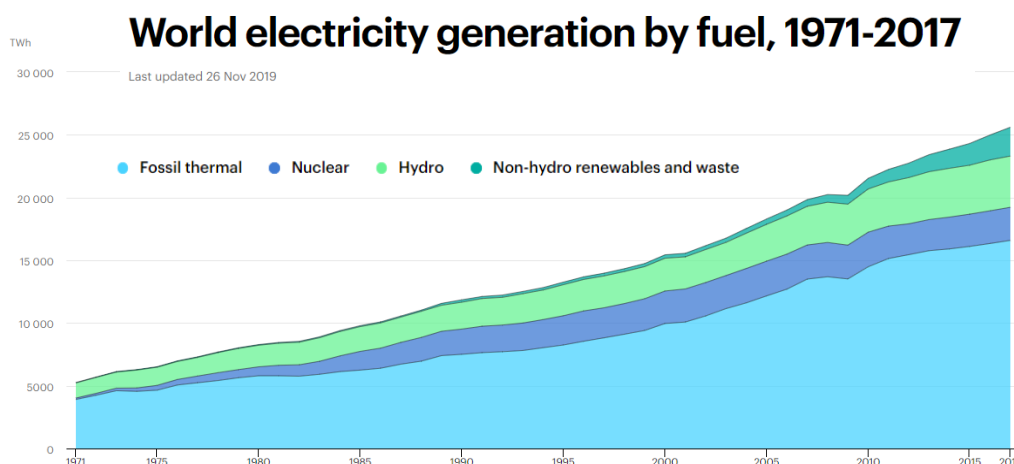
Fig. 5 Detailliertes Energieflussdiagramm der Schweiz 2019 (in Tj)
Flux énergétique détaillé de la Suisse en 2019 (en Tj)

BFE, Schweizerische Gesamtenergiestatistik 2019 (Fig. 5)
OFEN, Statistique globale suisse de l'énergie 2019 (Fig. 5)



<https://www.bfe.admin.ch/bfe/en/home/supply/statistics-and-geodata/energy-statistics/overall-energy-statistics.html>

Electricity sector



<https://www.iea.org/data-and-statistics/charts/world-electricity-generation-by-fuel-1971-2017>

Energy and electric mobility

The following techno-economic properties are presented for reference purpose only. The values mentioned are, as much as possible, consistent with the current technological development at the time of redaction. The reader must not place undue reliance on these numbers without a broader context analysis. The information is presented to allow the reader to understand the techno-economic context.

Diesel and Gasoline

Property	Diesel	Gasoline
Average chemical formula	$C_{12}H_{24}$	C_8H_{18}
Density	0.83	0.75
Gravimetric energy content	42.8 MJ/kg	42.5 MJ/kg
Volumetric energy content	9.87 kWh/L	8.85 kWh/L
Price at the station (Shell 2019 average)	1.75 CHF/L	1.63 CHF/L
Consumption (VW Golf 110 ch)	5.5 L/100km	7.2 L/100km
Consumption bus or truck	ca. 35L/100km	-
Transport	Liquid tanker truck up to 30'000 L	
CO ₂ emissions from combustion	2608 g CO ₂ eq/ L	2316 g CO ₂ eq/ L
CO ₂ emissions upstream*	533 g CO ₂ eq/ L	618 g CO ₂ eq/ L

*from Gordillo, V., Rankovic, N. & Abdul-Manan, A.F. Customizing CO₂ allocation using a new non-iterative method to reflect operational constraints in complex EU refineries. Int J Life Cycle Assess 23, 1527–1541 (2018). <https://doi.org/10.1007/s11367-017-1380-1>

Hydrogen

Density at 1 bar, 20°C	Density at 200 bar, 20°C	Density at 350 bar, 20°C	Density at 700 bar, 20°C	Density liquid, -253°C	Energy content
0.0826 g/L	14.7 g/L	23.7 g/L	39.7 g/L	70 g/L	33.3 kWh/kg or 120 MJ/kg

Loading capacity of trailers:

- 200 bar: 23m³, 338 kg
- 350 bar: in 20 ft multi element gas container, 15 m³, 356 kg
- Liquid: in 50 m³ cryogenic tank, 3500 kg

H₂ content in type IV storage tanks: 4 to 5 w%, no significant difference at small scale between 350 and 700 bar.

Consumption per 100 km: 1kg H₂ (passenger car), 8-10 kg H₂ (Bus or truck)

Price at the station: 10.90 CHF/kg (Hydrospider 2020)

Electrolysis

100 kW (DC) electrolysis can be approximated to *ca.* 2 kg H₂/h, 40 kg/day, 12 tons per annum

System energy consumption for small scale commercial systems (<0.5 MW): 65 kWh/kg H₂

Stack lifetime 80 000 h (1 year = 8 760 hours)

Degradation rate (0.15%/1000 h)

Batteries

Weight of a battery pack: 330 kg for 50 kWh in a Peugeot e-208, in average 7 to 8 kg per usable kWh

Consumption per 100 km: 18 kWh (passenger car)

Charging rates:

- 3.7-7.4 kW (16-32 A home charging)
- 11 kW (16 A three-phase current AC charger)
- 50 kW (fast charger)
- > 100 kW (ultrafast charger)

Price at ultra-fast charging stations: 0.79 CHF/kWh (Iionity 2020), 0.30 CHF/kWh (Tesla 2020)

Price at home: 0.182 CHF/kWh (average 2020 value in Valais, CH <https://www.prix-electricite.elcom.admin.ch/Map/ShowSwissMap.aspx>)

Photovoltaics in Switzerland

Annual solar irradiance: 1200 kWh/m²

Module performance: 0.2 kWp/m²; Ground surface needed: 6-10 m²/kWp

Yearly production: 1100 kWh/kWp (65% produced in summer)

Electricity production from a photovoltaic module⁴:

The electricity production from a Photovoltaic module, P_{pv} , can be expressed as follows

$$P_{pv} = P_{Max} * \frac{I_s}{I_{STC}} * [1 - \gamma_s * (T_{cell} - T_{STC})]$$

where

P_{max} : Installed capacity [W]

I_s : Solar radiation [W/m²]

I_{STC} : Radiation at standard conditions (1000 W/m²) [W/m²]

γ_s : Temperature coefficient for module efficiency [-]

T_{cell} : Operation cell temperature [°C]

T_{STC} : The cell temperature at standard conditions (25 °C) [°C]

The operation cell temperature is calculated by the following formula (Antonio Luque and Steven Hegedus (2003)):

$$T_{cell} = T_a + I_s * \left(\frac{NOCT - 20^\circ C}{800 W / m^2} \right)$$

where

T_{at} : Ambient temperature

$NOCT$: Nominal Operating Cell Temperature

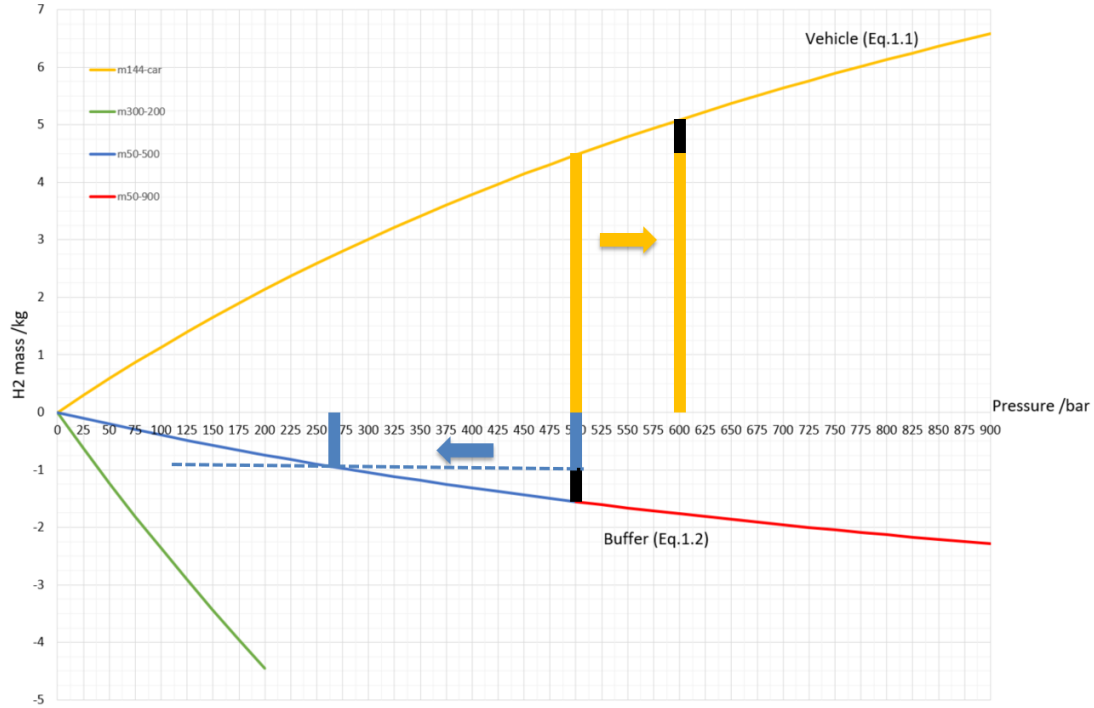
Hereto comes losses from the PV-module to the grid, λ_{misc} , such as miscellaneous PV array losses and other power conditioning losses.

The power production at grid becomes:

$$P_{elec} = P_{pv} * (1 - \lambda_{misc})$$

⁴ From energyPRO Software, from EMD International Denmark

Mass and pressure equilibrium plot



The pressure and mass equilibrium levels can be graphically predicted using the graph presented above. This graph is the representation of the equation of state functions for the corresponding volumes of the reservoirs involved. On the vertical axis, the mass contained in each reservoir can be read (positive for the vehicle side and the opposite for the station side). The mass repartition and the pressure at equilibrium can be graphically predicted, using a vertical segment [$m_{\text{buffer}} + m_{\text{vehicle}}$] and translating it until it fit exactly into the two curves based on Eq.1.1 and Eq.1.2 as presented in equation Eq.1.3. It can be applied for both compression (pressure difference increase) or refills (pressures converging).

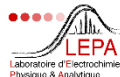
$$f(p, V_{\text{vehicle}}, T_0, m_{\text{vehicle}}) = 0 \quad (\text{Eq.1.1})$$

$$f(p, V_{\text{buffer}}, T_0, m_{\text{buffer}}) = 0 \quad (\text{Eq.1.2})$$

$$f(p, V_{\text{buffer}} + V_{\text{vehicle}}, T_0, m_{\text{buffer}} + m_{\text{vehicle}}) = 0 \quad (\text{Eq.1.3})$$

Conference posters

Demonstrator presentation



ELECTROMOBILIS - Energy research demonstrator in Martigny

Hardware and Software design, construction and operation of electrochemical equipments

Vanadium Redox Flow

- Electrolyte purification
- Direct DC coupling with charging station for electric cars
- Advanced expertise with stack degradation
- Controlled discharge for hydrogen production

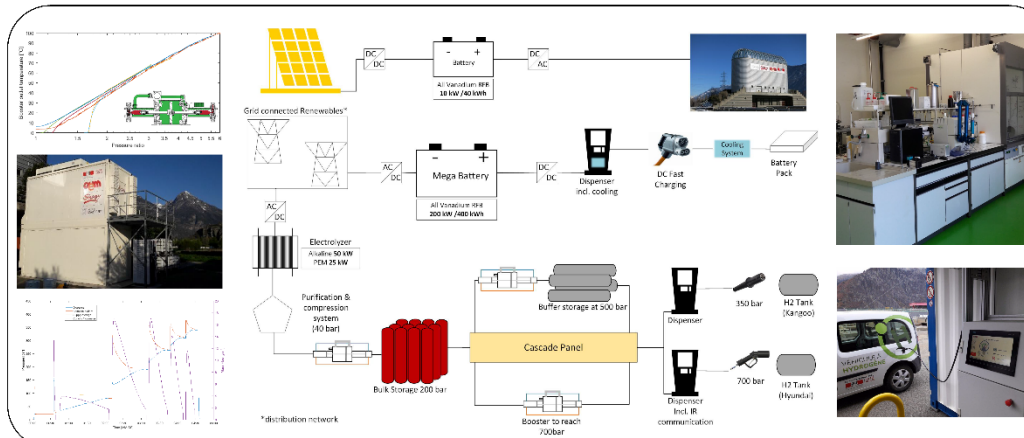


Hydrogen

- Electrolysis PEM and Alkaline
- Advanced catalyst proof of concept
- Compression and distribution up to 700 bar
- Custom refilling protocols development

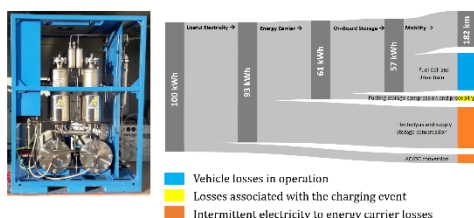


Chemical Lab and Large Scale Energy Demonstrator

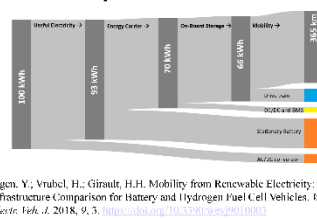


Energy efficiency of Grid to Mobility pathways

Hydrogen Fuel Cell Vehicle



Battery Electric Vehicle



Ligen, Y.; Vrubel, H.; Girault, H.H. Mobility from Renewable Electricity: Infrastructure Comparison for Battery and Hydrogen Fuel Cell Vehicles. *World Electr. Veh. J.* 2018, 9, 3. <https://doi.org/10.3390/wevj9010003>

Partners



www.electromobilis.ch

<https://lepa.epfl.ch/>



@LEPA_EPFL

EVS 32 2019, France


EPFL

Local Energy Storage for Ultrafast charging stations

P4M35

Yorick Ligen, Heron Vrabel, Hubert Girault
Ecole Polytechnique Fédérale de Lausanne
yorick.ligen@epfl.ch

How to manage peak power demands of multi-stall 150 kW charging stations ?

Challenges

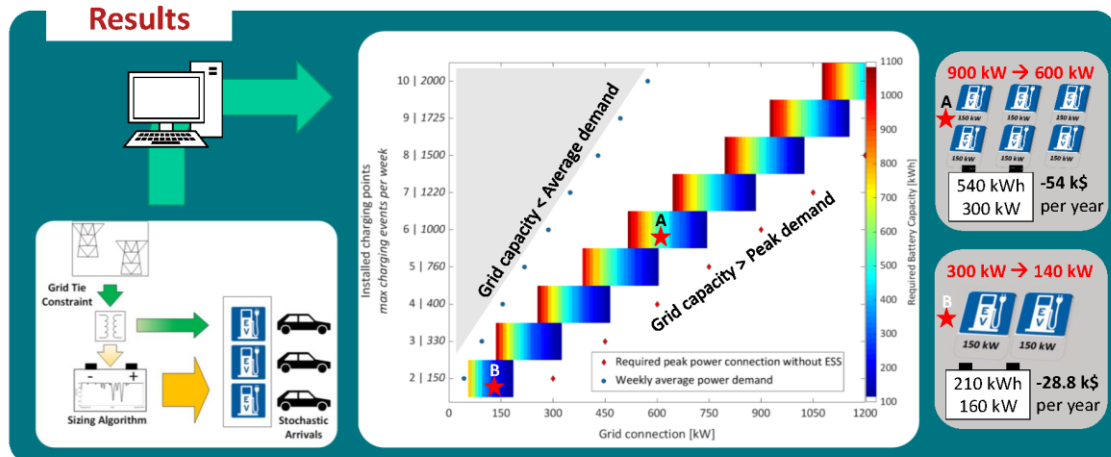
- Limited availability of high power connection
- High demand charge costs for power peaks, median US value > 180 US \$ /kW/year
- Peak power >> average power

Methods

- **Stochastic** arrival of vehicles and queuing
- Iterative sizing algorithm with a 1 min time step - **100 months simulated**
- 50 kW to 1.2 MW grid connections
- 150 to 2000 charging events per week

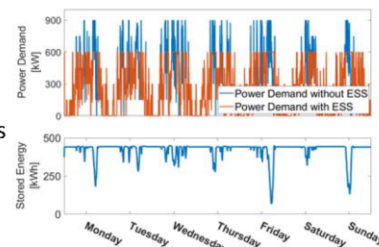
A consistent sizing methodology for local energy storage with grid constraints

Results



Discussion

- Station capacity defined to ensure that less than 5% of users have to wait more than 5 minutes
- Less than one full cycle per day → long life time
- Lower OPEX + lower transformer costs: payback time < 4 years
- <1% of energy losses due to charging/discharging efficiency
- **A versatile approach applicable to various usage profiles**



Funded by



Schweizerische Eidgenossenschaft
Confédération suisse
Confederazione Svizzera
Confederaziun svizra

Department of the Environment, Transport,
Energy and Communication DETEC
Swiss Federal Office of Energy SFOE
Section Energy Research and Cleantech

ICE 2019, Norway


EPFL

Design and operation of a HRS with on-site alkaline electrolysis

Yorick Ligen, Heron Vrabel, Hubert Girault
Ecole Polytechnique Fédérale de Lausanne
Laboratory of Physical and Analytical Electrochemistry
yorick.ligen@epfl.ch

Poster n°63



50 kW alkaline electrolysis : from a stack to a supply system for a refilling station



Control and supervision

- Electrolysis, Purification, Compression and Storage in one system
- > 70 IN/OUT signals monitored
- 4 modes of operation: production, hot stand-by, inertization, purge
- Purification via a compact pressure swing adsorption system designed and built in-house

Challenges

- Thermal management and inertia of the system
- Synchronisation of the compression system for all production rates
- Modulation in the 70 – 120 % range

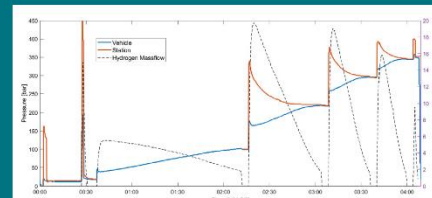
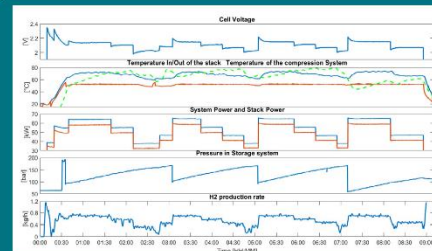
350 and 700 bar refilling station

Design and capabilities

- Operation with Hydrogen supply in the 60 – 200 bar range
- Compression with air driven gas boosters
- 4 x 50 L cascade at 500 and 900 bar
- 350 bar refills in 4 minutes
- 700 bar refills in < 1 hour



Measurements



Funded by



Schweizerische Eidgenossenschaft
Confédération suisse
Confederazione Svizzera
Confederaziun svizra

Department of the Environment, Transport,
Energy and Communication DETEC
Swiss Federal Office of Energy SFOE
Section Energy Research and Cleantech

Curriculum Vitae

<h2>Yorick Ligen</h2> <h3>Energy and Mobility Engineer</h3>		Rue du Praillon 5 1920 Martigny Switzerland Tel. : +41 78 610 85 28 / +33 6 48 77 61 35 email : yorick.ligen@gmail.com
 <p>Citizenship</p> <p>French</p> <p>Born on 04.01.1989 in Quimper (29)</p> <p>Languages</p> <p>French : mother tongue</p> <p>English : TOEFL iBT 101</p> <p>German : Goethe Zertifikat C1</p> <p>Softwares</p> <p>MS Office</p> <p>Matlab</p> <p>Siemens TIA Portal</p> <p>Hobbys</p> <p>Mountain and water sports Trail running, ski touring, mountaineering, sailing</p> <p>Music Celtic harp player since 1994</p>	<p>Professional experience</p> <p>2016 – 08.2020 PhD in Energy Ecole Polytechnique Fédérale de Lausanne</p> <p>Electrochemical systems for hydrogen fuel cell and battery electric vehicle infrastructure. Advisor: Prof. Hubert Girault. Co-advisor: Dr. Heron Vrubel. Technical expertise for hydrogen projects in Western Switzerland (Geneva, Lausanne, Aubonne, Collombey).</p> <p>2015 – 2016 Project Engineer Hydrogen TOTAL Deutschland, DE</p> <p>Deployment of hydrogen refilling stations (HRS) for fuel cell vehicles in Germany. Planning and integration in conventional gas stations. Certifications procedures. Coordination with equipment and car manufacturers. Construction work supervision. Operation management of existing HRS.</p> <p>2012 Innovation consultant InExtenso, FR</p> <p>Technology transfer, Strategy consulting, Funding of innovation, Technology watch, Business & market analysis, Competitive intelligence.</p> <p>Education</p> <p>2013 – 2014 Master of Science MTEC ETH Zürich, CH</p> <p>Master in management, economy and energy Master thesis, Paul Scherrer Institut: Environmental (LCA) and economic (TCO) assesment of current and future freight transport technologies.</p> <p>2010 – 2013 Ingénieur des Arts et Manufactures Ecole Centrale Paris</p> <p>Industrial engineering and energy science. Gap year 2012-2013 : Innovation consultant in France followed by a Workshop Manager position in Cambodia.</p> <p>2007 – 2010 Classes préparatoires PCSI/PC* Lycée Ste Geneviève</p> <p>Intensive preparation in Math, Physics and Chemistry for the competitive entrance exams to the French Grandes Ecoles.</p> <p>2007 Baccalauréat Scientifique, with highest honour</p> <p>Publications</p> <p>Y. Ligen, H. Vrubel, and H. Girault, "Mobility from Renewable Electricity: Infrastructure Comparison for Battery and Hydrogen Fuel Cell Vehicles," World Electric Vehicle Journal, vol. 9, no. 1, p. 3, May 2018. https://doi.org/10.3390/wevj9010003</p> <p>Y. Ligen, H. Vrubel, and H. Girault, "Combined refuelling station for electric cars either with batteries or fuel cells," Swiss Federal Office for Energy, Grant SI/501286, Final Report, December 2018. https://www.aramis.admin.ch/Texte/ProjectID=36923</p> <p>Y. Ligen, H. Vrubel, and H. Girault, "Local Energy Storage and Stochastic Modeling for Ultrafast Charging Stations," Energies, vol. 12, no. 10, p. 1986, May 2019. https://doi.org/10.3390/en12101986</p> <p>Y. Ligen, H. Vrubel, H. Girault, "Energy efficient hydrogen drying and purification for fuel cell vehicles," International Journal of Hydrogen Energy. 45 (2020). https://doi.org/10.1016/j.ijhydene.2020.02.035</p> <p>Y. Ligen, H. Vrubel, H. Girault, "Experimental correlation and integration of gas booster in a hydrogen refueling station," International Journal of Hydrogen Energy. 45 (2020). https://doi.org/10.1016/j.ijhydene.2020.04.162</p>	